Alalawi, Huda A., Ph.D., December 2023 NUCLEAR/PARTICAL PHYSICS

THEORY AND APPLICATION OF FAR-FROM-EQUILIBRIUM HYDRODYNAMICS AND KINETIC THEORY (221 pp.)

Director of Dissertation: Michael Strickland

In the field of high-energy nuclear physics, ultrarelativistic heavy-ion collisions serve as a one-of-a-kind laboratory for investigating the extreme properties of matter. These collisions involve massive nuclei, such as lead or gold, colliding with energies in the trillions of electron volts per nucleon range. These collisions produce an environment where the strong force, as described by quantum chromodynamics (QCD), is the dominant force. In particular, the collisions generate a state of matter known as the quark-gluon plasma (QGP), which is characterized by a state of quarks and gluons that is not confined inside hadrons such as protons and neutrons. The QGP is an intriguing state of matter that provides insights into the behavior of dense astrophysical objects and the early universe. It is produced when the energy density of the collision reaches a critical threshold, resulting in the transition from the confined to the unconfined state of quarks and gluons. The QGP is a hot and dense system, with temperatures on the order of trillions of Kelvin and densities several orders of magnitude greater than the density of atomic nuclei in ordinary matter.

In the initial phases of a heavy-ion collision, the system is far from thermal equilibrium and possesses a highly anisotropic pressure. The pressure anisotropy results from the longitudinal expansion being more rapid than the transverse expansion. The dynamics of the system cannot be adequately described by ideal hydrodynamics, which assumes local

isotropic thermal equilibrium at all times. To account for the pressure anisotropy and non-equilibrium nature of the QGP, a framework known as anisotropic hydrodynamics has been developed. Anisotropic hydrodynamics (aHydro) is a useful tool for describing the evolution of the QGP, especially during the early non-equilibrium evolution of the QGP. It goes beyond the ideal hydrodynamic limit by incorporating dissipative transport coefficients, such as shear viscosity, which are essential for accurately modeling the system's dynamics. aHydro accounts for the anisotropic character of the pressure tensor and permits a more accurate description of the evolution of the QGP.

In addition, the introduction of the quasiparticle formulation of anisotropic hydrodynamics (aHydroQP) is a recent development in the field. This formulation integrates the concept of quasiparticles and extends the aHydro framework to a full 3+1D framework with a realistic equation of state. Quasiparticles are effective degrees of freedom that arise in the QGP as a result of strong interactions. The aHydroQP method provides a more exhaustive description of the QGP's behavior, enabling a phenomenological analysis of heavy-ion collision data at various energies. Significant emphasis has been placed on conformal theories in hydrodynamics, where the equations of motion exhibit scale invariance. In conformal systems, the existence and properties of hydrodynamic attractors have been the subject of extensive investigation. These attractor solutions are insensitive to the initial conditions of the system and describe the approach of the system towards thermal equilibrium. Understanding the behavior of conformal systems has yielded significant insights into the dynamics of non-equilibrium relativistic systems. However, the study of hydrodynamic attractors in non-conformal kinetic theories remains an open question. Non-conformal systems possess additional scales, thereby destroying the scale invariance of conformal theories. Exploring the behavior of non-conformal systems is crucial for gaining a comprehensive understanding of dynamics in far-from-equilibrium situations that are more phenomenologically realistic.

In this dissertation, the primary objective is to increase our knowledge of the non-equilibrium dynamics of the QGP in ultrarelativistic heavy-ion collisions. Because of that, we intend to develop an improved ansatz for the distribution function in anisotropic hydrodynamics, aiming specifically for a more precise representation of moments with $l = 0$. Due to the inadequacy of the early assumption of ideal hydrodynamics and local isotropic thermal equilibrium in capturing the complex dynamics of the QGP, the canonical formulation of aHydro provided adequate descriptions of moments with nonzero longitudinal momentum ($l > 0$). However, it failed to describe moments with $l = 0$ accurately. This inadequacy was attributed to the limitations of a single ellipsoidal form in representing the two-component nature of exact solutions to the Boltzmann equation in the relaxation time approximation.

To address this limitation, a revised ansatz is proposed that incorporates an explicit separation of free-streaming and equilibrating contributions in the distribution function. This study demonstrates that this improved ansatz yields much better agreement with exact results available in the literature for the evolution of moments, especially those that do not contain power of the longitudinal momentum. By obtaining more precise dynamical equations and extracting the non-equilibrium attractor associated with this enhanced ansatz, a more accurate representation of the non-equilibrium dynamics of the QGP is obtained. As result, this research has the potential to enhance our understanding of the behavior of the QGP and enhance the theoretical frameworks used to investigate ultrarelativistic heavy-ion collisions. By refining the description of non-equilibrium dynamics, it contributes to the development of more precise models and a deeper understanding of the QGP's complex phenomena.

Moreover, experiments conducted at the Relativistic Heavy Ion Collider (RHIC) and the Large Hadron Collider (LHC) are designed to recreate conditions comparable to those in the early universe and during astrophysical mergers. Under these conditions of high

temperatures and net baryon densities, nuclear matter undergoes a phase transition from quarks and gluons confined within hadrons to the deconfined QGP state. Calculations based on lattice quantum chromodynamics (LQCD) have determined the temperature at which this deconfinement transition occurs, yielding important insights into the QCD equation of state. For modeling the spatiotemporal dynamics of the QGP in ultrarelativistic heavy-ion collisions, relativistic viscous hydrodynamics has proven to be an indispensable instrument.

For a more accurate description, it became apparent that dissipative transport coefficients, such as shear viscosity, must be included. This resulted in the development of second-order viscous hydrodynamics, which effectively incorporated dissipative effects and allowed for constraints on the shear viscosity to entropy density ratio. However, the application of second-order viscous hydrodynamics to the early phases of the collision, where the system is far from equilibrium and exhibits significant pressure anisotropy along the beam-line direction was problematic. Early on, it was difficult for fixed-order truncations of viscous hydrodynamics to accurately represent the large viscous corrections.

To address these issues, aHydro was used, employing a distribution function that assured probability positivity and non-negativity. The original formulation was centered on boost-invariant conformal Bjorken expansion, but subsequent work has expanded it to incorporate more realistic characteristics associated with heavy-ion collisions. This part of the research endeavor has dual objectives. The first objective of the project is to demonstrate that aHydro automatically includes an infinite series of terms when expanded as a power series in the inverse shear Reynolds number, thereby providing an infinite order resummation of viscous contributions to all orders. The second focus of the research is aHydroQP in a full 3+1D framework, which surpasses traditional approaches and allows for phenomenological applications to heavy-ion collision experiments at RHIC and LHC energies. By refining the theoretical frameworks used in ultrarelativistic heavy-ion collision studies, this research

seeks to describe various bulk observables of the QGP using anisotropic hydrodynamics and compare the results with experimental data at different collision energies. This will contribute to a more thorough characterization of the QGP and provide valuable insights into the physics at play.

Understanding the success of aHydro has led researchers to consider the topic of dynamical hydrodynamic attractors. Extensive research has been conducted on the existence of hydrodynamic attractors in conformal theories but less so in non-conformal theories. Important insights into the behavior of relativistic systems have been gleaned from studies of conformal systems. However, the existence of hydrodynamic attractors in non-conformal kinetic theories remains unanswered. This raises the intriguing issue of whether or not hydrodynamic attractor theories extend beyond conformal theories. Exploring the behavior of non-conformal systems is crucial for gaining a comprehensive understanding of dynamics in situations far from equilibrium that are phenomenologically relevant. In addition, the influence of a realistic mass- and temperature-dependent relaxation time on the behavior of an attractor has not been studied in detail. Understanding the interaction between relaxation dynamics and the emergence of attractor solutions can cast light on the evolution of non-conformal systems at the macroscopic level. In addition, we plan to investigate the impact of initial conditions on the time-dependent evolution of integral moments of the one-particle distribution function. We aim to investigate how the initial momentum-space anisotropy and initialization time influence the emergence and persistence of hydrodynamic attractors.

Our findings indicate the existence of an attractor for the scaled longitudinal pressure, but not for the shear and bulk viscous corrections separately. Additionally, our results provide evidence for both early- and late-time attractors for all moments of the one-particle distribution function containing greater than one power of the longitudinal momentum squared. By answering these questions, we aim to shed light on the behavior of non-conformal kinetic

theories, reveal the role of relaxation dynamics, and examine the sensitivity of the system to initial conditions. This research contributes not only to the fundamental understanding of far-from-equilibrium dynamics, but also to the description of relativistic systems in diverse physical contexts.

THEORY AND APPLICATION OF FAR-FROM-EQUILIBRIUM HYDRODYNAMICS AND KINETIC THEORY

A dissertation submitted to
Kent State University in partial
fulfillment of the requirements for the
degree of Doctor of Philosophy

by
Huda Alalawi
December, 2023

Dissertation written by

Huda Alalawi

B.S., Umm Al-Qura University, 2011

M.S., Kent State University, 2018

Ph.D., Kent State University, 2023

Approved by

_____ , Chair, Doctoral Dissertation Committee
Dr. Michael Strickland

_____ , Members, Doctoral Dissertation Committee
Dr. Declan Keane

_____
Dr. Mina Katramatou

_____
Dr. Diana Goncalves Schmidt

_____ , Graduate Faculty Representative
Dr. Ruoming Jin

Accepted by

_____ , Chair, Department of Physics
Dr. Michael Strickland

_____ , Dean, College of Arts and Sciences
Dr. Mandy Munro-Stasiuk

Table of Contents

List of Figures

List of Tables

List of Publications

Journal Papers

1. **H. Alalawi** and M. Strickland, "An improved anisotropic hydrodynamics ansatz", *Physical Review C* 102, 064904, (2020), arXiv:2006.13834.

2. **H. Alalawi**, M. Alqahtani, and M. Strickland, "Resummed relativistic dissipative hydrodynamics", *Symmetry* 2022, 14(2), 329, arXiv:2112.14597 [nucl-th].

3. **H. Alalawi** and M. Strickland, "Far-from-equilibrium attractors for massive kinetic theory in the relaxation time approximation", *Journal of High Energy Physics.* 2022, 143, arXiv:2210.00658 [nucl-th].

4. **H. Alalawi** , J. Boyd, C. Shen, and M. Strickland, "The impact of fluctuating initial conditions on bottomonium suppression in 5.02 TeV heavy-ion collisions", *Physical Review C* 107, L031901, (2023), arXiv:2211.06363 [nucl-th].

Acknowledgments

I am profoundly grateful to the individuals whose support, guidance, and encouragement have been instrumental in the successful completion of this dissertation on "Theory and Application of Far-From-Equilibrium Hydrodynamics and Kinetic Theory." Foremost, my deepest appreciation goes to my advisor, Dr. Michael Strickland. Their remarkable mentorship, profound expertise, and unwavering commitment to my academic development have been the guiding light of this research journey. Dr. Strickland's invaluable insights and constructive feedback have not only refined the course of this dissertation but have also deepened my understanding of the subject matter. I extend my appreciation to Dr. Mubarak Alqahtani for their invaluable contributions to this dissertation. Engaging discussions and insightful insights during our research deliberations have greatly enriched my comprehension of the subject.

My heartfelt gratitude extends to my family, my parents, Ahmed and Fawziah, who have been unwavering pillars of support from the very beginning. Their unending encouragement, boundless belief in my abilities, and sage advice have been the bedrock upon which my academic pursuits have thrived. To my beloved sisters, Rahmmah and Hayat, your unwavering support, understanding, and words of motivation have been a constant source of strength. To my husband, Naif, I owe a debt of gratitude that words cannot fully express. Your patience, unflagging support, and belief in me have been my refuge throughout this challenging journey. Your unwavering faith in my abilities has spurred me on to excel academically while maintaining a balanced life. My sons, Hattan, Luai, and Kinan, have been a wellspring of joy and inspiration. Your curiosity, boundless energy, and playful spirits have not only brought joy to my life but have also reminded me of the importance of perpetual learning and exploration.

Lastly, I would like to express my gratitude to the broader academic community whose groundbreaking work in the field of hydrodynamics and kinetic theory has indirectly contributed to this endeavor. Your research has been a constant source of inspiration. In conclusion, the culmination of this dissertation represents a collective effort, and I want to acknowledge the pivotal roles played by my family, my advisor, and the entire academic community. Their unwavering support, wisdom, and contributions have been instrumental in shaping both my academic and personal growth.

I offer my heartfelt thanks to each and every one of you for your steadfast support, encouragement, and belief in my journey.

Chapter 1

Introduction

In the early moments of the universe, after the Big Bang, a quark-gluon plasma (QGP) was formed, consisting of weakly-interacting quarks, the building blocks of matter, and gluons, the carriers of the strong force. This mixture was dominated by high-speed particles in an incredibly hot and dense soup. To recreate these conditions, powerful accelerators collide heavy ions, such as gold or lead resulting in a tiny but extremely hot fireball in which everything melts into a QGP. This plasma cools rapidly, and the individual quarks and gluons reform into ordinary hadronic matter that flies away, leaving behind debris that contains particles such as pions, kaons, protons, and neutrons, as well as antiprotons and antineutrons, etc. The momentum distribution and energy of this debris can reveal much about the plasma, which behaves almost like a perfect fluid with little viscosity.

To observe QGP on Earth, high-energy particle collisions are required. These collisions take place at the Relativistic Heavy Ion Collider (RHIC) at Brookhaven National Laboratory or the Large Hadron Collider (LHC) at CERN in Switzerland, where fast-moving lead or gold nuclei collide at high speeds, creating a short-lived plasma that can be studied. The properties of the QGP can also be explored through theory, using quantum chromodynamics (QCD) to describe the interactions between quarks and gluons. However, due to the vast number of variables involved, solving these complex interactions requires advanced parallel computing resources.

For many years, experimental physicists have been attempting to create QGP and finally reported success about two decades ago. During this time, theorists have also been developing the equations that govern this state of matter and have worked alongside experimentalists

to better understand it.

In this introduction, we delve into the basics of the Standard Model, which describes the interactions between the fundamental building blocks of matter that are governed by four fundamental forces. We start by providing a succinct overview of Quantum Chromodynamics (QCD), the underlying theory of strong interactions. Next, we take a closer look at the structure of hadrons, made up of quarks and gluons, with a special emphasis on confinement and phase transitions. We then proceed to define the quark-gluon plasma (QGP) and explore the circumstances under which hadrons can disintegrate into deconfined quarks and gluons. To better understand the properties of QGP, we explain high-energy heavy-ion collisions, which provide a unique opportunity to study this state of matter in a laboratory setting. We also examine the most promising experimental signatures of the QGP produced in nucleus-nucleus collisions. Finally, we conclude by considering the future of quark-gluon plasma research and what we can expect from future accelerators.

1.1 The Standard Model

Since the 1930s, the theories and discoveries of thousands of physicists have led to an amazing understanding of the basic structure of matter: everything in the universe is made of a small number of basic building blocks called fundamental particles, which are controlled by four fundamental forces. The Standard Model of particle physics is the best way to explain how these particles and three of the forces relate to each other [20–25]. Since it was created in the early 1970s, it has been able to explain almost all experimental results and make accurate predictions concerning a wide range of phenomena. The Standard Model has been proven to be an excellent theory of physics over time and through many experiments [26–28].

1.1.1 Matter particles

The Standard Model of particle physics provides a framework for understanding the interactions of the fundamental constituents of matter. In this model, quarks and leptons are the two main categories of elementary particles that make up everything in the universe. There are six types of particles in each category, arranged into three generations. The first generation, which is made up of the lightest and most stable particles, includes the "up" and "down" quarks and the "electron" and "electron neutrino." The second and third generations are composed of heavier and less stable particles, but they can still contribute to the stability of matter in various ways. For example, the heavier particles can quickly decay into lighter and more stable particles, and the resulting particles can be a part of stable matter. Additionally, the heavier particles can participate in the formation of composite particles such as hadrons, which are made up of quarks and gluons, and can be stable. Quarks come in three "colors" and can only combine in such a way as to result in colorless objects, such as hadrons. Leptons, on the other hand, can be electrically charged or neutral, and they have varying amounts of mass. For example, the "electron," "muon," and "tau" are charged and have significant mass, while the corresponding neutrinos are electrically neutral and have very little mass.

1.1.2 Forces and carrier particles

The four fundamental forces operating in the universe are the strong force, weak force, electromagnetic force, and gravitational force. These forces each have unique strengths and operate within different ranges. Gravity is the weakest of the four forces, but it has an infinite range. The electromagnetic force is stronger than gravity and has an essentially infinite range as well. The strong and weak forces only operate over short distances and are dominant only at the level of subatomic particles. The strong force is the strongest of the four fundamental forces.

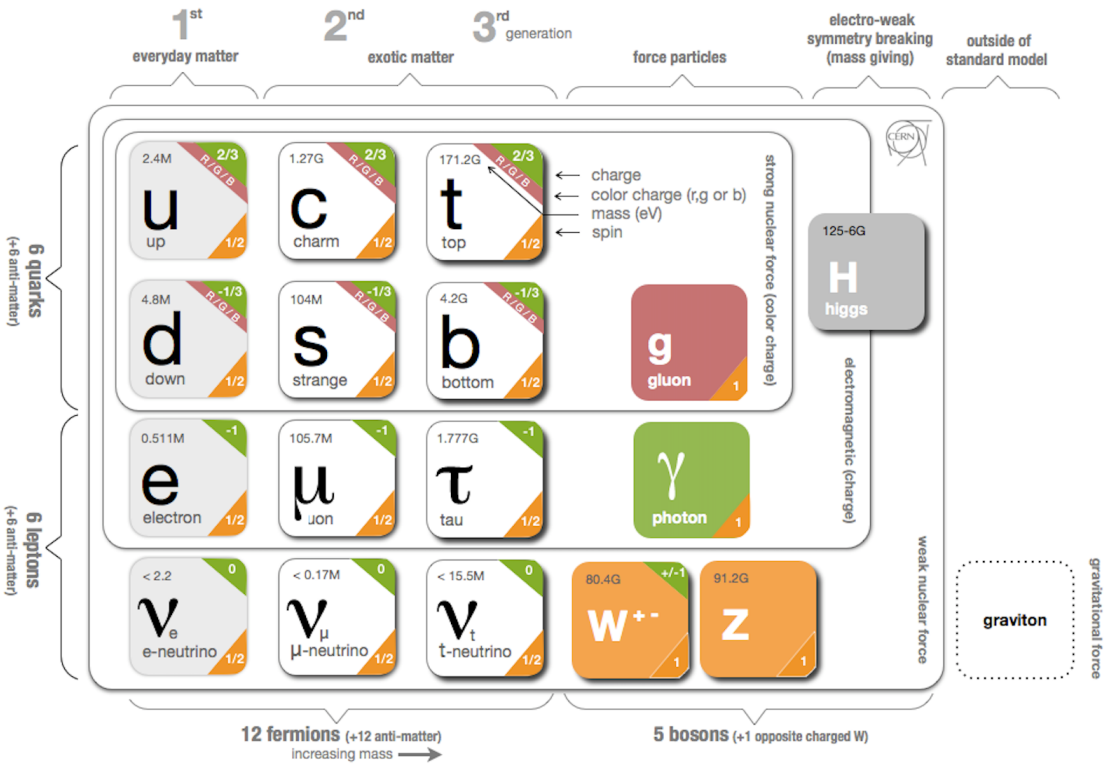

Figure 1: The Standard Model in Heavy Ion Collisions illustrates the fundamental building blocks of the universe. *Source: CERN.*

The interaction between matter particles and the forces they experience is facilitated by the exchange of bosons, also known as force-carrier particles, which means matter particles can exchange specific amounts of energy. The strong force is carried by the gluon, the electromagnetic force by the photon, and the weak force by the W and Z bosons. The hypothetical[1] boson carrying the force of gravity is called the graviton, but it has not yet been discovered.

The Standard Model of particle physics includes the electromagnetic, strong, and weak forces, as well as their respective bosons. It explains the interactions between the force carriers (boson) and matter particles (fermions). However, gravity is not included in the

[1]The graviton is described as "hypothetical" because it has not been experimentally observed or detected. In physics and scientific research, a "hypothetical" particle or entity is one that has been predicted or proposed by theoretical models and equations but has not yet been explicitly observed or confirmed by experimental evidence.

Standard Model as it has been difficult to incorporate within the framework due to the mathematical incompatibility between the general theory of relativity and quantum theory, which describe macro and micro phenomena, respectively [29–33]. Nevertheless, the influence of gravity on particles is typically so small that it can be ignored in the context of particle physics. The gravitational effect only becomes significant when matter is in bulk, such as planets or large objects like the human body.

1.2 Quantum chromodynamics

Quantum chromodynamics (QCD) is a fundamental theory of particle physics that explains the strong nuclear force. It describes the interaction between quarks and gluons, which are the building blocks of matter. The strong force holds quarks together to form protons and neutrons and keeps these particles bound within the atomic nucleus. As a result, strongly interacting matter can exist in a variety of phases, including a nuclear liquid phase, a hadronic gas phase, and the quark-gluon plasma phase [34–37]. In this way, QCD plays a crucial role in understanding the properties and behavior of matter in the universe.

1.2.1 The Lagrangian of QCD

The QCD Lagrangian is a mathematical equation that describes the interactions between quarks and gluons. It consists of a combination of terms that describe the different types of interactions between quarks and gluons. It includes terms that describe the kinetic energy of quarks and gluons, as well as terms that describe the interactions between quarks and gluons via the exchange of gluons. The QCD Lagrangian also includes a term known as the "color charge" term, which describes the fact that quarks come in three different "colors" (red, green, and blue) that are related to the strong force. This term is important because it allows quarks and gluons to interact with one another via the exchange of gluons, which carry the strong force between them. The complex phenomenology of the strong interaction

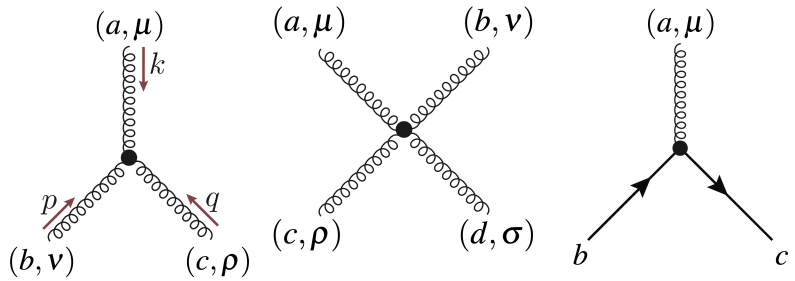

Figure 2: Illustration of a quark-gluon, 3- and 4-gluon vertices vertex in QCD [1].

is represented in an apparently straightforward Lagrangian [36,38–40]. The QCD Lagrangian is

$$\mathcal{L}_{\text{QCD}} = \sum_{f}^{N_f} \bar{q}_f^c (i\gamma^\mu D_\mu - m_f) q_f^c - \frac{1}{4} G^a_{\mu\nu} G_a^{\mu\nu} \,, \tag{1.1}$$

- $\mathcal{L}_{\text{QCD}}$: This is the symbol for the Lagrangian density which is a mathematical function that describes the dynamics of quarks and gluons. It consists of two main terms: the quark term and the gluon term.

- $\sum_f^{N_f}$: This indicates a sum over all flavors f, where N_f is the number of quark flavors. In this Lagrangian, there are N_f different quark fields, each with its own mass m_f.

- $\bar{q}_f^c$: This is the conjugate of the quark field q. The subscript $c = 1, \ldots, N_c$ with $N_c = 3$ being a color index, which indicates that quarks come in three different colors (red, green, and blue). The subscript f is the quark/anti-quarks flavor index, which distinguishes between different types of quarks where $f = up, down, strange, charm, bottom, top$.

- γ^μ: This is a Dirac matrix that expresses the vector nature of the strong interaction with the matrix encoding the spin properties of the quark field. The symbol μ is a Lorentz four vector index.

- D_μ: This is the covariant derivative of the quark field, which describes how the quark field changes as it moves through space-time. The covariant derivative acting on the

quark fields is

$$D_\mu = \partial_\mu - ig_s A^a_\mu \frac{\lambda^a}{2}\,, \tag{1.2}$$

where g_s the strong coupling (related to α_s by $g_s^2 = 4\pi\alpha_s$; we return to the strong coupling in more detail below), A^a_μ is the gluon fields which is a vector field labeled by an adjoint color index $a = 1, \ldots, 8$. The octet of gluon fields can be used to construct a matrix valued field $A_\mu = A^a_\mu \frac{\lambda^a}{2}$, where λ^a is a set of traceless, Hermitian, 3×3 matrices. Additionally, local gauge invariance, which is a fundamental symmetry in gauge theories, is preserved by the covariant derivative in the QCD Lagrangian.

- m_f: This is the mass of the quark. The mass of a quark determines its behavior, and is one of the parameters that must be specified in order to fully describe the quark field.

- $G^a_{\mu\nu} G^{\mu\nu}_a$: This represents the gluon term. It describes the gluon self-interactions and the energy of the gluon field. It is proportional to the square of the field strength tensor. The factor of $-\frac{1}{4}$ is sets the magnitude of the gluon term and is specified uniquely at the Lagrangian level.

- $G^a_{\mu\nu}$: This is the field strength tensor for the gluon field. It is defined by the equation

$$G^a_{\mu\nu} = \pm \frac{1}{ig_s}[D_\mu, D_\nu] = \partial_\mu A^a_\nu - \partial_\nu A^a_\mu + g_s f^{abc} A^b_\mu A^c_\nu\,, \tag{1.3}$$

and $f^{abc} = 4i\,\mathrm{Tr}([\lambda^a, \lambda^b]\lambda^c)$ is a set of numbers called the $SU(3)$ structure constants. The gluon field is the field that mediates the strong force between quarks. The field strength tensor describes the strength and direction of the gluon field at a given point in space-time. The superscript a is an index that distinguishes between different types of gluons. Since gluons consist of all possible combinations of color and anti-color charge which possess a total color charge there are eight of them (in general, $N_c^2 - 1$)

1.2.2 Confinement and Asymptotic Freedom in QCD

The two central features of QCD are confinement and asymptotic freedom, which play a crucial role in understanding the behavior of the strong force.

- **Confinement** in QCD is a fundamental property that characterizes quark and gluon behavior at low energies or long distances. It refers to the property that quarks and gluons are permanently confined inside hadrons at low energy or large distances and cannot be isolated as individual particles [41, 42]. Instead, as quarks are separated, the energy in the system rises, which causes new quark-antiquark pairs or gluon pairs to spontaneously form out of the vacuum. These newly formed quarks and gluons are immediately joined to create new hadrons, ensuring their confinement within color-neutral bound states.

- **Asymptotic Freedom** is the property of QCD which states that the interaction between quarks and gluons becomes weaker at high energies or short distances. This means that as the energy of a quark-gluon system increases, the particles are free to move more independently, whereas at lower energies they are more strongly bound. This property was first predicted by theorists (particularly by David Gross, Frank Wilczek, and David Politzer) in the 1970s and has since been experimentally confirmed, leading to its acceptance as a key aspect of the theory of QCD [43, 44], which resulted that David Gross, Frank Wilczek, and David Politzer were awarded the Nobel Prize in Physics in 2004 for their contributions to the understanding of the strong force and Asymptotic Freedom.

1.2.3 The coupling constant in QCD

In QCD, the coupling constant, also known as the strong coupling constant, is a fundamental dimensionless parameter that describes the strength of the strong interaction between

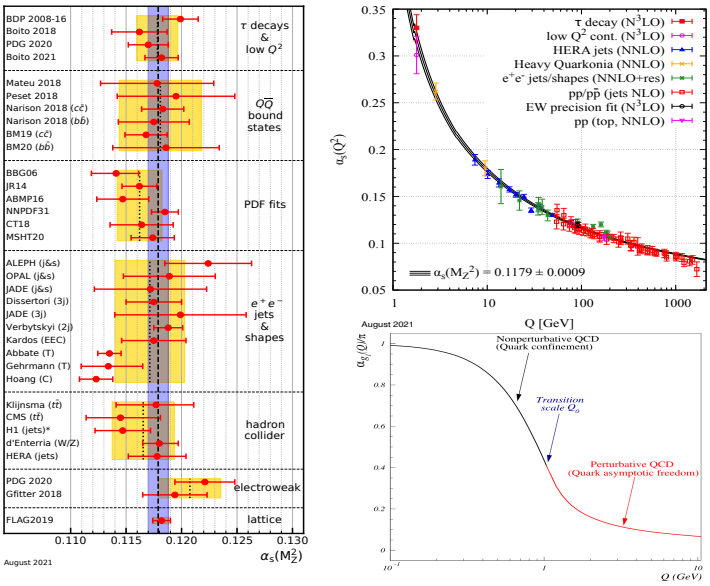

Figure 3: (Left) The average value of $\alpha_s(M_Z^2)$ and its uncertainty for seven sub-fields [2]. (Top) Summary of measurements of α_s as a function of the energy scale Q where depending on the energy scale, the strength of the strong force can be either weak or strong [2]. (Bottom) the running coupling constant is divided into two regions perturbative and non-perturbative, each with its own characteristics [3].

quarks and gluons as a function of energy. Therefore, it determines the behavior of the particles at different energy scales. The strong interaction is responsible for binding quarks together to form protons and neutrons, and these, in turn, make up the atomic nucleus. The value of the coupling constant determines the range of the strong force and the rate at which energy is exchanged between strongly interacting particles.

This parameter is denoted by the symbol α_s and is related to the QCD scale parameter, denoted by Λ_{QCD}. The coupling constant in QCD at the momentum scale Q is approximately

$$\alpha_s(Q^2) = \frac{g^2}{4\pi} = \frac{\alpha_s(\Lambda^2)}{1 + \frac{\alpha_s(\Lambda^2)}{4\pi}(11 - \frac{2N_f}{3}) \ln \frac{Q^2}{\Lambda^2}} \tag{1.4}$$

where N_f is the number of flavors and $\Lambda \approx 100$ MeV is the QCD scale parameter. The value of α_s is proportional to the strength of the interaction and it decreases with increasing energy. The scale parameter Λ sets the momentum below which the theory becomes confining.

The running coupling constant in QCD has a divergence at a scale known as Λ_{QCD} [2], which is the characteristic energy scale of the strong interaction. At this scale, the value of the coupling constant becomes large, signaling the breakdown of perturbative methods. The fact α_s becomes large at low momentum is a key feature of QCD and is related to the confinement of quarks and gluons, meaning that they cannot exist as free particles at low energies. Instead, they must be bound together in hadrons, such as protons and neutrons. The value of the running coupling constant α_s changes over the mass range of typical particles (the energy scale), and it can be described in terms of two regions: perturbative and non-perturbative as illustrated in Fig. 3 at the bottom. Depending on the energy scale, the strength of the strong force can be either weak or strong.

In the perturbative region, where the energy scale is much higher than the confinement scale Λ_{QCD}, the behavior of α_s can be described by perturbative QCD (pQCD) calculations, which are based on the expansion of the QCD Lagrangian in powers of the coupling constant. In this region, α_s is small and the strong force can be treated as a weak perturbation which reflects the asymptotic freedom. This means that at high energies, quarks and gluons interact weakly and can be treated as nearly free particles. In this region, the interactions can be treated as a series of small corrections to the free particle motion. In the non-perturbative region, where the energy scale is close to or lower than Λ_{QCD}, the behavior of α_s cannot be described by perturbative calculations and must be studied using non-perturbative methods such as lattice QCD simulations or effective field theories. In this region, α_s is large and the strong force results in significant interactions between quarks and gluons and to confinement of quarks and gluons inside hadrons.

Eq. (1.4) shows that the coupling constant is small when $Q^2 \gg \Lambda^2_{QCD}$. Therefore the interactions with a large momentum transfer can be treated in the perturbative way. The

[2]It is worth noting that Λ_{QCD} is a scale parameter in QCD that separates the perturbative and non-perturbative regions. It is not a physical mass, but rather a parameter that determines the energy scale at which the transition from perturbative to non-perturbative behavior occurs.

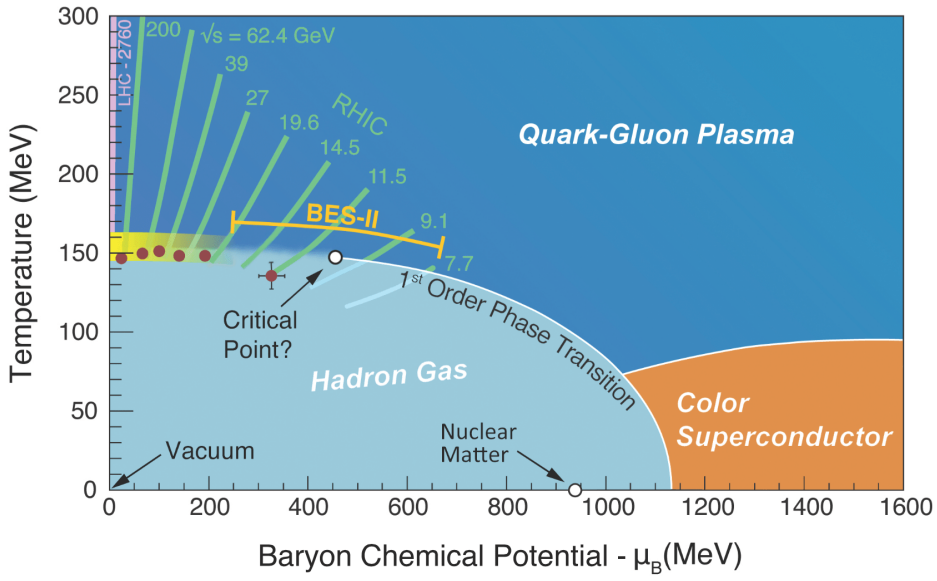

Figure 4: The QCD phase diagram illustrates the phases of strongly interacting matter, such as quarks and gluons, at different temperatures and densities [4].

value of α_s is known, and it is estimated to be around 0.12 at high energies (Q = mass of the Z boson)and around 0.5 at low energies as shown in figure 3 at the top. It is determined experimentally through a variety of means, including deep-inelastic scattering experiments, lattice QCD simulations, and studies of hadronic spectra. In Fig. 3 on the left we provide an overview of recent measurements of $\alpha_s(M_Z^2)$ from several sub-fields and experiments.

1.2.4 QCD phase transition and its diagram

The Quantum Chromodynamics phase diagram is a graphical representation that uses the temperature T and baryon chemical potential μ_B as coordinates to depict the different phases of strongly interacting matter, such as quarks and gluons, as predicted by the theory of QCD. The baryon chemical potential in this context is a measure of the imbalance between quarks and anti-quarks, i.e., the relative abundance of matter vs antimatter. The phase diagram is particularly important in the study of nuclear matter, which is composed of protons and neutrons which themselves are made up of quarks and gluons.

The QCD phase diagram is roughly divided into three regions: the hadronic phase, the

quark-gluon plasma phase (QGP), and the color superconducting phase as shown in figure 4.

- The quark-gluon plasma phase is the region where quarks and gluons are no longer confined inside hadrons and can move approximately freely (the particles are highly energetic) because the strong force, which is responsible for the confinement of quarks and gluons within hadrons is effectively screened.[3] This phase is characterized by high temperatures and/or densities. It was studied at Brookhaven National Laboratory's Relativistic Heavy Ion Collider (RHIC) and CERN's Large Hadron Collider (LHC). It is thought that this phase of matter may have existed in the early universe, for a few microseconds after the Big Bang, when it was hot enough for quarks and gluons to be weakly-interacting independently. In this phase the quarks and gluons are deconfined and chiral symmetry is restored [45].

- The hadronic phase is characterized by low temperatures and densities, and it corresponds to the vacuum state of QCD. In this region the matter is composed of strongly interacting protons and neutrons, which are made up of quarks and gluons, which are confined inside hadrons because of the strong coupling at low energies. In other words, the strong force becomes less screened. In this phase, the system undergoes a second-order phase transition, in which the confinement of quarks and gluons within hadrons is observed. This phase transition is also associated with the restoration of chiral symmetry, which is broken in the hadronic phase due to the formation of a condensate of quark-antiquark pairs. The hadronic phase is characterized by the presence of bound states of quarks and gluons, such as protons, neutrons, and mesons, which are

[3] In this context, "screened" refers to the reduction in the strength of the strong force at short distances due to the presence of other charges in the system. The screening of the strong force in the plasma phase is due to the presence of free color-charged particles in the plasma, which can interact with the gluons that carry the strong force. This interaction can cause the gluons to "dress" or acquire an effective mass, which reduces the strength of the strong force at short distances.

analogous to the matter that comprises the macroscopic world we observe in everyday life.

- The color superconducting phase occurs at extremely high densities and low temperatures. It is believed that quarks and gluons may bind together into a more tightly bound state. In this phase, quarks are expected to form pairs and behave like a fluid, resulting in unusual properties such as the ability to conduct color currents without resistance.

Moreover, the phase diagram consists of several key components, including a crossover transition, a first-order phase transition, a critical point, and a line of first-order phase transitions.

- At intermediate temperatures and chemical potentials, the system exhibits a crossover behavior (yellow strip) in figure 4, where there is a smooth, continuous transition between the hadronic phase and the QGP phase without the need for a discontinuous phase transition. In a crossover transition, the properties of the system change smoothly as the temperature or density is increased or decreased.

- On the other hand, a first-order phase transition is a transition between two phases that is marked by a discontinuous change in properties of the system (abruptly), such as the energy density and the pressure, and there is a clear boundary between the two phases.

- The critical point in the QCD phase diagram separates the regions where the transition between QGP and hadronic matter is smooth (crossover transition) and abrupt (first-order phase transition) depending on the temperature and density. At high densities before one gets the critical point, the transition is characterized by a sharp change because the properties of the system, such as the energy density and the pressure change rapidly. However, at the critical point the transition becomes a second-order

phase transition, where thermodynamic quantities are continuous but their derivatives may be discontinuous. The critical point has not been experimentally found yet, but it is a subject of active research.

In conclusion, the QCD phase diagram is a complex and active area of research, as scientists are still trying to understand the properties and behavior of quarks and gluons at different temperatures and densities, and to locate the critical point and understand the properties of the QCD vacuum. It is important to note that the QCD phase diagram is still not fully understood, and many aspects of it remain a subject of active research.

1.3 High energy and heavy ion collision

The field of physics that studies ultra-relativistic heavy-ion collisions brings together the principles of high-energy particle physics and nuclear physics. The term "heavy-ions" refers to heavy atomic nuclei, while the term "ultra-relativistic energy" indicates an energy regime where kinetic energy is a large multiple of the rest energy [46, 47]. In high-energy particle physics, interactions between single particles (such as leptons, quarks, and hadrons) are derived from first principles, while in nuclear physics, interactions are modeled through effective models for more complex objects like nuclei. In the field of ultra-relativistic heavy-ion collisions, the goal is to understand the properties of hot and dense nuclear and hadronic matter in terms of fundamental interactions. This includes searching for new phases of hadronic matter, identifying phase transitions, and reconstructing the phase diagram of strongly interacting matter over a wide range of thermodynamic parameters such as temperature, baryon chemical potential, and isospin chemical potential. Relativistic heavy-ion experiments began to create a droplet of Quark-Gluon Plasma (QGP) through high-energy collisions of ions. Initially, experiments with lighter ions did not show significant differences from proton-proton collisions, but heavier ions later revealed new flow patterns. Currently,

the world's leading experimental facilities for this field are the Relativistic Heavy Ion Collider (RHIC) at Brookhaven National Laboratory and the Large Hadron Collider (LHC) at CERN. Gold and lead ions are typically used in these experiments, with gold being the heaviest monoisotopic element. The process of these experiments involves heating the intended element, vaporizing it, and accelerating it to ultrarelativistic speeds through multiple stages. While RHIC was previously the dominant apparatus for QGP discoveries, the LHC now has the highest collision energy. Currently, RHIC is focused on beam energy scans and is planned to be transformed into an electron-ion collider to better understand the 3D wave functions of hadrons and nuclei, as well as to better understand the role of gluons in the building blocks of matter.

1.3.1 Stages of a heavy ion collision and theoretical tools

Relativistic collisions of heavy ions provide one of the few opportunities to investigate nuclear matter in extreme laboratory settings. The center-of-mass collision energy per nucleon pair $\sqrt{s}$ and the shape of the colliding nuclei are the defining characteristics heavy-ion collisions. Once the center-of-mass energy is more than the rest mass of the nuclei, or if $\sqrt{s}/2$ is greater than the nucleon mass, the collisions are considered relativistic. This indicates that the nuclei move at a significant fraction of the speed of light c. Therefore, this implies that the typical nucleons Lorentz contraction factor γ of the collision might be approximated as

$$\gamma = \frac{m\gamma c^2}{mc^2} = \frac{E^{\text{total}}}{m_p} \simeq \frac{\sqrt{s}}{2 \text{ GeV}}\,, \tag{1.5}$$

where this equation shows the Lorentz factor that quantifies the relativistic effects experienced by the nucleons during the collision with m_p is the rest mass of a proton $m_p = 938.6$ MeV $\simeq 1$ GeV with 1 GeV $= 10^9$ eV being the unit of energy used in high-energy physics. In modern experiments, collision energies are in the TeV range, which means that

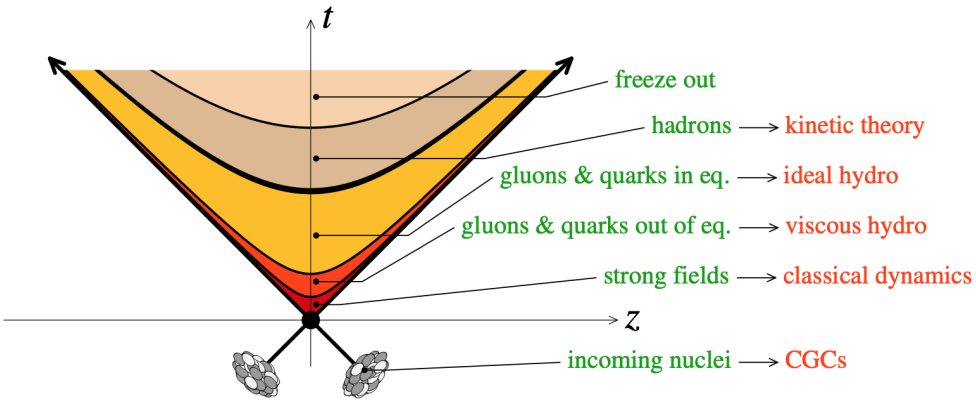

Figure 5: The stages of a heavy ion collision [5].

$\gamma \gg 1$. This means that nucleons move at speeds very close to the speed of light, and that kinetic energy, not rest mass energy, is the main source of energy when they collide with one other. Moreover, high Lorentz contraction factors mean that the shape of nuclei appears different in the center-of-mass frame compared to their shape at rest. A picture that is often used to explain this is that a nucleus moving at relativistic speed looks more like a "pancake" than a roughly spherical object due to relativistic length contraction

1. The initial stage denoted by the notation $\tau < 0$ (before the collision). For Au+Au collisions at RHIC, the two beams of Lorentz-contracted gold nuclei were accelerated in opposite directions in the RHIC ring and brought to collide (on the light-cone defined by positions $z = \pm t$) once they reached their target energies which correspond to a speed greater than 99.9% of the speed of light. The collision takes place at $t = z = 0$, and any remnants of the nuclei that do not take part in the collision process leave the collision region on the forward and backward light-cones. Interacting matter will lead to energy deposition in the center of the collision region, close to $z \simeq 0$. Initially, this deposited energy will be far from equilibrium, and this early stage can be characterized by a dense ensemble of gluons walls known as the Color Glass Condensate (CGC) at sufficiently high collision energies, which could conceivably be reached at RHIC [48].

Therefore, early after the collision the evolution in the directions transverse to the initial beam direction (the "transverse plane") can be assumed to be static, and the dynamics is dominated by the longitudinal expansion of the system. Being interested in the bulk dynamics of the matter created in a relativistic heavy-ion collision as well as the primary theoretical methods used to explain or simulate these events, one can divide the evolution into four stages in proper time $\tau = \sqrt{t^2 - z^2}$, shown schematically in figure 5.

2. Pre-equilibrium stage and thermalization: The energetic collision of the two heavy nuclei excites the QCD vacuum and forms a dense pre-equilibrium matter composed of quarks, anti-quarks, and gluons. This stage is followed by thermalization. The pre-equilibrium bulk matter requires around 1 fm/c $\simeq 10^{-23}$ seconds for it to attain local thermalization and create the quark-gluon plasma.

3. QGP expansion and hadronization: The QGP rapidly expands and cools due to thermal pressure gradients. When it reaches the critical temperature T_c (which is around 155 MeV), it hadronizes and transforms into hadronic matter, which is made up of a combination of stable and unstable hadrons and hadron resonances. Throughout the QGP expansion period, hadronization occurs continuously at the edge of the QGP fireball. It takes roughly 10 fm/c for the QGP fireball to spread and entirely convert to hadronic matter in central Au+Au collisions at RHIC.

4. Hadronic expansion and decoupling: The hadronic matter continues to expand until it becomes highly diluted. Once the local effective temperature of the system drops below a certain limit ($T \sim 150 - 180$ MeV), partons become confined within colorless hadrons in a process known as hadronization, which occurs at $\tau \sim 10$ fm/c. The system then transforms into an interacting hot hadron gas for several fm/c. At $\tau \sim 20$ fm/c, the hadrons undergo chemical freezeout, where they stop interacting strongly and colliding

inelastically, but the particle number remains conserved. This is followed by kinetic freezeout, where the hadrons stop having any kind of collisions, and their momenta remain constant. Finally, the hadrons move freely (free streaming) on straight lines until they reach the detector, marking the end of the hadronic decoupling process. The entire process, from the growth of the hadronic matter until the hadrons fly freely to the detector without undergoing any further collisions, takes another $5 - 10$ fm/c for it to completely freeze out.

In the field of ultra-relativistic heavy-ion collisions, scientists study what happens when heavy atomic nuclei collide with each other at very high energies. This creates a large number of particles, much more than the number of particles that existed before the collision (exceeding the number of initial nucleons by a factor of 10-100). To study these collisions, scientists use different methods such as mathematical modeling and computer simulations. When analyzing the effects of ultra-relativistic heavy-ion collisions, scientists often make predictions based on thermodynamic (related to heat and temperature) or statistical (related to probability) considerations. However, the systems of particles produced in these collisions are not stationary and change over time, so a more dynamic approach is necessary. This is where transport theories come in. These theories are used to describe processes that are not in equilibrium. The matter produced in these collisions has a short lifespan, so there is a growing interest in using these theories to understand what is happening.

In addition, researchers use microscopic Monte-Carlo simulations to make predictions. These simulations are based on models of low energy hadron-hadron collisions and are used as an extrapolation, or prediction, of what may happen in these types of collisions. Furthermore, there is also research being done to understand the effects of these collisions on the behavior of particles and how they interact with each other. This involves using theories from quantum physics, such as quantum field theory in and out of equilibrium. By using

these methods, scientists hope to get a better understanding of the properties of the matter created in these collisions and how it behaves. Overall, the field of ultra-relativistic heavy-ion collisions is interdisciplinary and requires a combination of different approaches, including thermodynamics, statistical methods, hydrodynamics, kinetic theory, field theory at finite temperature and density, non-equilibrium field theory, and Monte-Carlo simulations to fully understand the effects and properties of these collisions.

1.3.2 Quark-gluon plasma

The Quark-Gluon Plasma (QGP) is a state of matter that is hot, dense, and has strong interactions. Unlike the normal hadronic state, where the partons (quarks and gluons) are confined in colorless hadrons held together by the strong force, in QGP, the partons are deconfined and free to move around [49]. This is due to the large population of color charge carriers, leading to long-range color charge conductivity. To better understand the properties of QGP, let's consider a thought experiment. At low temperatures, the system is composed of a gas of colorless hadrons, which are the eigenstates, or ground states, of the QCD Hamiltonian at zero temperature. However, as the temperature increases and the hadron interactions become more intense, the hadronic states no longer provide an adequate description of the medium. At temperatures around 155 MeV and above, the system transforms into QGP, where the degrees of freedom are the quarks and gluons.

There are two ways to generate the Quark-Gluon Plasma (QGP), a state of matter that consists of free-moving quarks and gluons:

1. **At extremely high densities:** By squeezing a large number of baryons into a small space, their wave functions start to overlap and they eventually dissolve into a system of degenerate quark matter. This occurs at a critical baryon density, ρ_c, which is typically several times the nuclear saturation density ($\rho_0 = 0.16\,\mathrm{fm}^{-3}$). This type of matter can be found in compact stars such as white dwarfs, neutron stars, and quark

stars. If the density at the center of neutron stars reaches 5 -10 ρ_0, the neutrons could potentially melt into cold quark matter.

2. **At extremely high temperatures:** QGP can be generated by heating up the QCD vacuum without the need for nuclear matter. At low temperatures, hadrons are thermally excited from the vacuum. But at higher temperatures, the interactions between the hadrons become so intense that they overlap and eventually transform into quark and gluon degrees of freedom at a critical temperature ($T \gtrsim 150$ MeV). The only way to generate QGP in the laboratory is through Ultra-Relativistic Heavy Ion Collisions (URHICs), which rely on this mechanism. Furthermore, Friedman's solution of Einstein's equation suggests that the universe experienced an expansion from a singularity at time zero, which has been confirmed by the red shift of distant galaxies observed through Hubble's law. By extrapolating these observed properties of the universe backwards in time, it is believed that the universe became hotter and denser and crossed the QCD phase transition ($T \sim 155$ MeV) about $\sim 10^{-5}$ seconds after its inception. This phase transition was preceded by the electroweak phase transition at ~ 200 GeV.

It has been shown that QGP's behavior can be described by hydrodynamic equations with a small specific shear viscosity, making it similar to a liquid with low shear viscosity, based on its flow properties [50–53]. However, the QGP is a complex system that may exhibit either weak or strong coupling, depending on the scale being considered. Short wavelength modes, such as thermodynamic functions, are dominated by asymptotic freedom, resulting in a weakly-coupled system of quarks and gluons at high temperatures ($T \gg \Lambda_{\mathrm{QCD}}$). On the other hand, long wavelength modes, such as static magnetic color fields, are strongly coupled, even in the limit $T \gg \Lambda_{\mathrm{QCD}}$. Despite its strongly-coupled character, the non-perturbative sector of the QGP does not significantly contribute to its thermodynamic properties.

1.3.3 The evidence for the existence of QGP at RHIC

The existence of the QGP has been confirmed at RHIC through a combination of experimental observations and theoretical predictions. Experimentally, evidence for the QGP at RHIC includes:

1. **Suppression of high transverse momentum hadrons:** RHIC and LHC experiments have observed a significant suppression of high transverse momentum hadrons, which is consistent with the idea that these hadrons are losing energy as they traverse the hot, dense QGP [54–56].

2. **Elliptic flow:** The RHIC and LHC experiments have also observed a large elliptic flow, which is a measure of the anisotropy in the momentum distribution of particles. This observation can be explained by the hydrodynamic expansion of the QGP, in which the pressure gradients cause the matter to flow and distribute momentum anisotropically [57–59].

3. **Jet quenching:** The RHIC and LHC experiments have observed a strong suppression of high-energy jets, which are collimated beams of particles produced in high-energy collisions. This suppression can be explained by the energy loss of the jets as they traverse the hot, dense QGP [60].

4. **Strangeness enhancement:** RHIC and LHC experiments have also observed an enhancement of strange hadrons, which can be explained by the creation of a hot, dense environment in which strange quarks can be produced more efficiently.

Theoretically, the evidence for the QGP at RHIC is also supported by numerical simulations of heavy-ion collisions that incorporate the principles of quantum chromodynamics (QCD), the theory of the strong interaction. These simulations have been able to reproduce many

of the experimental observations, such as the suppression of high-energy hadrons and the elliptic flow, and provide further support for the creating of a QGP at RHIC and LHC.

1.4 The overview and outline of my dissertation

In my PhD dissertation, I explored the study of the Quark-Gluon Plasma (QGP) created in heavy-ion collisions using a non-equilibrium hydrodynamics framework, called the anisotropic hydrodynamics (aHydro) framework. I aimed to improve the elementary aHydro framework to enable the study of QGP phenomenology. Throughout the study, I utilized two primary methods to evaluate the aHydro framework: exact solutions to the Boltzmann equation and experimental data. The exact solutions of the Boltzmann equation, obtained for specific symmetrical cases, were frequently used as a reference for comparisons between the aHydro framework and other frameworks. The experimental data from ultrarelativistic heavy-ion collisions was also used to verify the phenomenological predictions of the aHydro model.

Therefore, in Chapter 2, I introduce the fluid dynamic and the system of kinetic equations and investigate their moments, which leads to the establishment of Landau matching conditions related to energy-momentum conservation. In Chapter 3 of this dissertation, I delve into a comprehensive exploration of the Glauber model, that enables us to gain insights into the spatial arrangement of nucleons in colliding nuclei which is consider as a crucial factor in understanding the initial stages of heavy-ion collisions. Also, the Bjorken model which guides our understanding of the early moments of high-energy nuclear interactions and shedding light on the parton distribution functions and the energy density of the quark-gluon plasma formed in such collisions. In Chapter 4, an improved form for the anisotropic hydrodynamics distribution function is introduced and demonstrated to better reproduce exact results from literature. The non-equilibrium attractor associated with this improved

form is also extracted. In Chapter 5, the existence of early and late time attractors in non-conformal kinetic theories is explored by computing the time-evolution of moments of the one-particle distribution function. I extend previous attractor studies by using a mass- and temperature-dependent relaxation time that is realistic and varying the initial momentum-space anisotropy and initialization time. In Chapter 6, the motivation for using relativistic anisotropic hydrodynamics to study ultrarelativistic heavy-ion collisions is presented and highlights the main ingredients of the 3+1D quasiparticle anisotropic hydrodynamics model, including the underlying symmetry assumptions. I also present phenomenological comparisons with experimental data, which show that anisotropic hydrodynamics can describe many bulk observables of the quark-gluon plasma. Finally, in Chapter 7, I conclude and summarizes the key results of the dissertation and provides an outlook for future research.

Part I

Background of Theory

Chapter 2

Fluid Dynamics and Kinetic Theory in Heavy Ion Collisions

2.1 Hydrodynamics

Hydrodynamics, also known as fluid dynamics, is a theoretical framework that describes the behavior of fluids which is a continuous system on large distance scales. In fluid dynamical descriptions individual particles are not explicitly considered and instead one makes use of macroscopic variables. This discipline endeavors to understand the fundamental nature of matter and energy transfer by deciphering the complex patterns and behaviors that emerge in fluid motion. In the context of heavy ion collisions, fluid dynamics plays a crucial role in elucidating the complex dynamics of the quark-gluon plasma (QGP) and hadronic matter created in the collisions, over spatial scales orders of magnitude smaller than those of conventional matter. The transformation of the kinetic energy of colliding ions into thermal energy and the rapid expansion of the QGP produce conditions resembling those of the universe just microseconds after the Big Bang. These conditions deviate greatly from our everyday experiences and from conventional physics, making their study especially difficult.

Hydrodynamics offers an efficient method for describing the collective behavior of quarks and gluons in this medium that arise during plasma expansion and cooling. One of fluid dynamics primary benefits is its simplicity and generality. By focusing on a few macroscopic variables that characterize the state of the fluid such as energy density, pressure, temperature, and flow velocity, fluid dynamics simplifies the complex behavior of the system. The thermodynamic properties (such as the equation of state that relates pressure, energy density, and temperature) and transport coefficients (such as viscosity and thermal conductivity) contain all the microscopic information. On macroscopic scales (large distances

and long times), the intricate microscopic behavior is no longer detectable. Most microscopic variables (such as the positions and velocities of individual particles) exhibit rapid spatial and temporal variation. These rapid fluctuations result in negligible changes to average values, which have no appreciable impact on the macroscopic dynamics. These variables that change slowly over time and space are often associated with conserved quantities (like total energy or momentum), which play a significant role in the macroscopic dynamics. Therefore, using hydrodynamics enables a simpler and more computationally tractable description of the evolution of the system.

Generally, a fluid is a continuous system and each small volume element in this system is called fluid element. It is traditionally assumed that each fluid element needs to be sufficiently large on a microscopic scale to be close to thermodynamic equilibrium. This is considering as the basic principle of fluid dynamics where the system evolves while remaining close to local thermodynamic equilibrium. Even as the system expands and evolves, it is presumed that the interactions between particles are sufficient to maintain local equilibrium, thereby permitting the application of fluid dynamics equations. This is where fluid dynamics steps in as a powerful theoretical framework for understanding the matter in heavy ion collisions. Likewise, each fluid element must be sufficiently small on a macroscopic scale to preserve the continuum approximation. Consider fluid dynamics in a heavy-ion collision for the QGP as an illustration where the system has very differing length scales. The component particles (quarks, gluons, etc.) interact with one another over extremely small distances when observed at the microscopic level. However, when you zoom out to the macroscopic level, fluid dynamics—which concentrates on the typical characteristics of huge volumes—describes the behavior of the entire system.

As a result, hydrodynamics provides a link between the microscopic interactions of quarks

and gluons and the macroscopic observables that can be measured in experiments. By modeling the QGP as a relativistic fluid with strong interactions and analyzing the evolution of it with hydrodynamic equations, scientists are able to make predictions about the distribution of particles, their momenta, and other observables that can be compared to experimental data collected at particle colliders such as the Large Hadron Collider (LHC) at CERN or the Relativistic Heavy Ion Collider (RHIC) at Brookhaven National Laboratory.

In the following sections, we will delve further into this basic kind of fluid and its hydrodynamical framework, examine the subtleties of the effects of viscosity in heavy-ion collisions, and learn how the interaction between theoretical knowledge and actual experiments has aided in our understanding of the novel properties of the QGP and how it evolves over time. This investigation will help us understand the very first moments of the universe and provide new information concerning how matter behaves in the most extreme situations we can envisage.

2.2 From perfect-fluid hydrodynamics to the viscous hydrodynamics framework

As heavy ion collisions occur, the initially created state of the QGP undergoes a rapid hydrodynamic expansion, which is the flow of matter from regions of high energy density to regions of lower energy density. This expansion causes the matter to cool down and eventually transforms the QGP into hadronic matter. Because the QGP is a relativistic fluid that behaves as a nearly perfect fluid with low viscosity, we will discuss two primary categories of fluids: ideal and viscous.

2.3 Relativistic perfect-fluid hydrodynamics

Ideal fluids are a simplified model that depict the frictionless and adhesion-free behavior of fluids. In a relativistic perfect fluid, particles move without encountering any internal resistance. This simplified perspective is beneficial for comprehending fundamental fluid

dynamics and can shed light on fluid motion under specific conditions. The relativistic ideal hydrodynamic equations serve as the foundation for characterizing the evolution of the QGP during its early expansion phases. These equations presume that the fluid is in thermal equilibrium at the local level, i.e., all fluid elements must be exactly in thermodynamic equilibrium within each local fluid cell but not necessarily in global thermal equilibrium [61, 62]. The condition of a fluid governed by relativistic principles can be fully defined by the densities and flow of conserved quantities, which include the energy-momentum tensor, denoted $T^{\mu\nu}$, and the four-current associated with particle number (net particles minus anti-particles), denoted N^{μ}.

2.3.1 Derive the energy-momentum tensor

To establish a comprehensive description of these quantities for an ideal fluid, it is necessary to first determine the energy-momentum tensor, $T^{\mu\nu}_{LRF}$ in the fluid local rest frame (LRF) where in this frame the fluid is not in motion $u^{\mu} = (1, \mathbf{0})$, so the energy-momentum tensor, particle four-current, and entropy four-current should exhibit the distinct characteristics of a system in static equilibrium. The definition of the energy- momentum tensor is a mathematical object that describes the distribution of energy and momentum in a physical system with certain transformation properties under coordinate transformations. Therefore, the energy-momentum tensor is the four-momentum component in the μ direction per three-dimensional surface area perpendicular to the ν direction. Thus $T^{\mu\nu}$ has dimensions of energy per volume. Thus we have differential four-momentum components $\Delta p = (\Delta E, \Delta p_x, \Delta p_y, \Delta p_z)$ associated with differential space-time four-vector $\Delta x = (\Delta t, \Delta x, \Delta y, \Delta z)$. For $\mu = \nu = 0$, one obtains

$$T^{00}_{R} = \frac{\Delta E}{\Delta x \Delta y \Delta z} = \frac{\Delta E}{\Delta V} = \epsilon \,, \tag{2.1}$$

and for $\mu = \nu = 1$ (the x coordinate), one obtains

$$T_R^{xx} = \frac{\Delta p_x}{\Delta t \Delta y \Delta z} = \frac{\Delta f_x}{\Delta A} = P\,. \tag{2.2}$$

Here, $\frac{\Delta p_x}{\Delta t} = \Delta f_x$ is the force in the x direction acting on a surface of area $\Delta A = \Delta y \Delta z$ with a normal vector perpendicular to the force and the force exerted per area is the pressure P. Observing an ideal fluid from its LRF reveals the following properties: there is no energy transfer ($T^{i0}_{LRF} = 0$), the force per unit surface element is the same in all directions (the pressure is isotropic $T^{ij}_{LRF} = \delta^{ij} P$), and there is no net flow of particles or entropy ($\vec{N} = 0$ and $\vec{S} = 0$). Thus, in the fluid rest frame, an ideal fluid has

$$T^{\mu\nu}_{LRF} = \begin{pmatrix} \epsilon & 0 & 0 & 0 \\ 0 & P & 0 & 0 \\ 0 & 0 & P & 0 \\ 0 & 0 & 0 & P \end{pmatrix} . \tag{2.3}$$

Now, we can generalize to the moving frame by using a Lorentz transformation when we consider these quantities from the viewpoint of the LRF. These components are linked to fluid velocity (u^μ) and the metric tensor ($g_{\mu\nu}$). The possible forms of these quantities can be inferred from particular conditions, such as the symmetry of the energy-momentum tensor and the consistent transformation properties under Lorentz transformations. The following can be used to determine the most general form for the energy-momentum tensor of an ideal relativistic fluid (denoted $T^{\mu\nu}_{(0)}$) that meets these requirements and using the hydrodynamic degrees of freedom, namely two Lorentz scalars (ϵ, p):

$$T^{\mu\nu}_{(0)} = \epsilon \left(c_0 g^{\mu\nu} + c_1 u^\mu u^\nu\right) + P \left(c_2 g^{\mu\nu} + c_3 u^\mu u^\nu\right) \ . \tag{2.4}$$

In the LRF, one requires the $T^{00}_{(0)}$ component to represent the energy density ϵ of the fluid. Similarly, in this frame, the momentum density should be vanishing $T^{0i}_{(0)} = 0$, and the space-like components should be proportional to the pressure, $T^{ij}_{(0)} = P\,\delta^{ij}$. Imposing these conditions onto the general form (2.4) leads to the equations

$$(c_0 + c_1)\epsilon + (c_2 + c_3)P = \epsilon, \qquad -c_0\epsilon - c_2 P = P, \tag{2.5}$$

which imply $c_0 = 0, c_1 = 1, c_2 = -1, c_3 = 1$. Therefore, the energy-momentum tensor of an ideal relativistic fluid becomes

$$T^{\mu\nu}_{(0)} = (\epsilon + P)\; u^\mu u^\nu - P\; g^{\mu\nu}. \tag{2.6}$$

To simplify this equation, we introduce a projection operator $\Delta^{\mu\nu} = g^{\mu\nu} - u^\mu u^\nu$ that focuses on the space-like part of a tensor in the LRF. For any metric $g_{\mu\nu}$, the $\Delta^{\mu\nu}$ operator is orthogonal to the fluid four velocity, meaning $\Delta_{\mu\nu}u^\nu = \Delta_{\mu\nu}u^\mu = 0$. Moreover, it obeys $\Delta_{\mu\nu}\Delta^\nu_\rho = \Delta_{\mu\rho}$, and $\Delta^\mu_\mu = 3$. With this operator, we can rewrite Eq. (6.22) as

$$T^{\mu\nu}_{(0)} = \epsilon u^\mu u^\nu - P\Delta^{\mu\nu}. \tag{2.7}$$

In Minkowski space-time, a Lorentz transformation to the LRF leads to $u^\mu_{LRF} = (1, \mathbf{0})$, which means $\Delta^{\mu\nu}_{LRF} = \mathrm{diag}(0, -1, -1, -1)$. This explicit representation highlights Δ's focus on space-like properties. Similarly, u^μ can be understood as a time-like projection operator. Now, to describe the behavior of an ideal fluid, we keep track of energy, momentum, and particle number. These conservation principles are expressed through equations involving the flow of these quantities. When a system has no net conserved charges (vanishing chemical potential), the ideal hydrodynamic evolution of the system can be described by local

conservation of energy and momentum, which is expressed by the equation

$$\partial_\mu T^{\mu\nu}_{(0)} = 0\,. \tag{2.8}$$

These equations use the mathematical tool ∂_μ to compute how objects change through time and space, and this equation means that the total energy and momentum in the system are conserved, and any changes in one part of the system must be compensated by changes in other parts of the system. Additionally, it fully consistent with the Lorentz invariance principles, which describe how objects appear to move when viewed from various moving frames.

For practical calculations, we use the projection operator $\Delta^{\mu\nu}$ and the fluid's four velocity u^μ. This makes it easier to divide the direction of change into components that are either parallel ($u_\nu \partial_\mu T^{\mu\nu}_{(0)}$) to the fluid's velocity or perpendicular ($\Delta^\alpha_\nu \partial_\mu T^{\mu\nu}_{(0)}$) to it. For the first projection the co-moving time-like components of Eq. (2.8), one finds

$$\begin{aligned}
u_\nu \partial_\mu T^{\mu\nu}_{(0)} &= u_\nu \partial_\mu [\epsilon u^\mu u^\nu - P\Delta^{\mu\nu}]\,, \\
&= u_\nu [(\partial_\mu \epsilon) u^\mu u^\nu + \epsilon (\partial_\mu u^\mu) u^\nu + \epsilon u^\mu (\partial_\mu u^\nu) - (\partial_\mu P)\Delta^{\mu\nu} - P(\partial_\mu \Delta^{\mu\nu})]\,, \\
&= u_\nu (\partial_\mu \epsilon) u^\mu u^\nu + u_\nu \epsilon (\partial_\mu u^\mu) u^\nu + u_\nu \epsilon u^\mu (\partial_\mu u^\nu) - u_\nu (\partial_\mu P)\Delta^{\mu\nu} - u_\nu P(\partial_\mu \Delta^{\mu\nu})\,, \\
&= u^\mu (\partial_\mu \epsilon) + \epsilon\,(\partial_\mu u^\mu) + \epsilon\, u_\nu u^\mu (\partial_\mu u^\nu) - P\, u_\nu (\partial_\mu \Delta^{\mu\nu})\,, \\
&= u^\mu (\partial_\mu \epsilon) + \epsilon\,(\partial_\mu u^\mu) - P\, u_\nu (\partial_\mu \Delta^{\mu\nu})\,, \\
&= u^\mu (\partial_\mu \epsilon) + \epsilon\,(\partial_\mu u^\mu) - P\, u_\nu [\partial_\mu (g^{\mu\nu} - u^\mu u^\nu)]\,, \\
&= u^\mu (\partial_\mu \epsilon) + \epsilon\,(\partial_\mu u^\mu) + P\, u_\nu \partial_\mu (u^\mu u^\nu)\,, \\
&= u^\mu (\partial_\mu \epsilon) + \epsilon\,(\partial_\mu u^\mu) + P\,[u_\nu u^\nu (\partial_\mu u^\mu) + u^\mu u_\nu (\partial_\mu u^\nu)]\,, \\
&= (\epsilon + P)\partial_\mu u^\mu + u^\mu \partial_\mu \epsilon = 0\ ,
\end{aligned} \tag{2.9}$$

where the identity $u_\nu u^\nu = 1$ and $u_\nu \partial_\mu u^\nu = \frac{1}{2}\partial_\mu (u_\nu u^\nu) = \frac{1}{2}\partial_\mu 1 = 0$ are used. For the other projection the co-moving space-like components of Eq. (2.8) one obtains

$$\begin{aligned}
\Delta^\alpha_\nu \partial_\mu T^{\mu\nu}_{(0)} &= \Delta^\alpha_\nu (\partial_\mu \epsilon) u^\mu u^\nu + \Delta^\alpha_\nu \epsilon (\partial_\mu u^\mu) u^\nu + \Delta^\alpha_\nu \epsilon u^\mu (\partial_\mu u^\nu) - \Delta^\alpha_\nu (\partial_\mu P)\Delta^{\mu\nu} - \Delta^\alpha_\nu P(\partial_\mu \Delta^{\mu\nu}) \,, \\
&= \epsilon\, u^\mu \Delta^\alpha_\nu \partial_\mu u^\nu - \Delta^{\mu\alpha}(\partial_\mu P) + \Delta^\alpha_\nu P \partial_\mu (u^\mu u^\nu) \,, \\
&= \epsilon\, u^\mu \Delta^\alpha_\nu \partial_\mu u^\nu - \Delta^{\mu\alpha}(\partial_\mu P) + P[u^\nu \Delta^\alpha_\nu (\partial_\mu u^\mu) + u^\mu \Delta^\alpha_\nu (\partial_\mu u^\nu)] \,, \\
&= \epsilon\, u^\mu \Delta^\alpha_\nu \partial_\mu u^\nu - \Delta^{\mu\alpha}(\partial_\mu P) + P\, u^\mu \Delta^\alpha_\nu \partial_\mu u^\nu \,, \\
&= (\epsilon + P)\, u^\mu \partial_\mu u^\alpha - \Delta^{\mu\alpha}\partial_\mu P = 0 \,. \qquad (2.10)
\end{aligned}$$

where in the first line $\Delta^\alpha_\nu u^\nu = 0$, and $\Delta^\alpha_\nu \Delta^{\mu\nu} = \Delta^{\mu\alpha}$. Now, by introducing

$$D \equiv u^\mu \partial_\mu, \qquad \nabla^\alpha = \Delta^{\mu\alpha}\partial_\mu, \qquad \theta \equiv \partial_\mu u^\mu, \qquad (2.11)$$

for the projection of derivatives parallel and perpendicular to u^μ, equations (2.9), and (2.10) can be written as

$$\begin{aligned}
D\epsilon + (\epsilon + p)\theta &= 0 \,, \qquad (2.12) \\
(\epsilon + p) D u^\alpha - \nabla^\alpha p &= 0 \,. \qquad (2.13)
\end{aligned}$$

These are the fundamental equations for an ideal relativistic fluid. Note that there are four quantities used to characterize an ideal fluid: energy density (ϵ), pressure (P), particle number density (n), and fluid velocity (u_μ). These quantities represent six distinct fluid properties such as u^μ has three independent components. However, only five equations result from analyzing how these quantities change over time (conservation laws). This leaves our understanding of the fluid's behavior incomplete. To solve this, we employ a state equation ($P = P(n, \epsilon)$). This equation connects the pressure to other thermodynamic properties,

"closing" the equations. The presence of this equation is ensured by the assumption that the fluid is in local thermal equilibrium. With this equation of state, the equations of ideal fluid dynamics become a complete framework for describing the behavior of fluids in a variety of situations.

2.4 Relativistic viscous-fluid hydrodynamics

When a fluid is not in ideal local thermodynamic equilibrium, it is subject to dissipative effects that result in irreversible thermodynamic processes during its motion. Due to the nature of dissipative processes, no fluid can maintain precise local thermodynamic equilibrium throughout its entire dynamics. This implies that some elements of the fluid may not be in equilibrium with the rest of the fluid, and that they must interchange heat with their surroundings in order to achieve equilibrium. In addition, the movement of fluid elements and the friction between them can also result in energy loss. To accurately describe the behavior of a relativistic fluid, these features must all be taken into account. This kind of fluid is called a viscous fluid, and possesses a degree of "stickiness," or viscosity. In heavy-ion collisions, the viscosity becomes crucial for understanding how the created matter evolves. Therefore, with accounting for viscosity, we have to consider additional term called viscous corrections that add to the ideal term.

The viscous corrections play a significant role in describing the collective behavior of the system. It can be expressed in terms of moments of the one-particle distribution function, which allows for a more convenient way of describing the collective behavior of the system and can be used to extract information about the properties of the fluid. Here, the energy-momentum tensor, $T^{\mu\nu}$, describes the macroscopic state of the system. It can be expressed in terms of a single-particle phase-space distribution function and decomposed into

hydrodynamic degrees of freedom as following

$$T^{\mu\nu} = T^{\mu\nu}_{(0)} + T^{\mu\nu}_{(1)} = T^{\mu\nu}_{(0)} + \Pi^{\mu\nu}, \tag{2.14}$$

$$\begin{aligned} T^{\mu\nu} = \int dP\, p^\mu p^\nu f(x,p) &= \epsilon u^\mu u^\nu - P\Delta^{\mu\nu} + \Pi^{\mu\nu} \\ &= \epsilon u^\mu u^\nu - (P+\Pi)\Delta^{\mu\nu} + \pi^{\mu\nu}\,, \end{aligned} \tag{2.15}$$

with $\int dP$ is the integration measure and $\Pi^{\mu\nu} = \pi^{\mu\nu} + \Pi\Delta^{\mu\nu}$. In this equation, the tensor decomposition includes the energy density ϵ, thermodynamic pressure P, bulk viscous pressure Π, and shear stress tensor $\pi^{\mu\nu}$. These quantities describe how the system behaves under different conditions, such as changes in temperature or pressure. Moreover, $\Pi^{\mu\nu}$ is the viscous stress tensor, and decomposes in two parts: a traceless part $\pi^{\mu\nu}$ and a part with non-vanishing trace $\Delta^{\mu\nu}\Pi$.

- **The traceless part ($\pi^{\mu\nu}$)** corresponds to the shear stress tensor, which captures the departures from ideal fluid dynamics due to small anisotropic deviations from local thermal equilibrium. In other words, shear viscosity is comparable to the friction that occurs when fluid layers with various velocities move against one another. Shear viscosity functions as a brake, slowing the differences in motion between various parts of the fluid. This effect is crucial because it facilitates a more uniform flux of matter, allowing it to evolve collectively. This part of the stress tensor is symmetric $\pi^{\mu\nu} = \pi^{\nu\mu}$, and $\pi^\mu_\mu = 0$. As a result, the traceless part of the stress tensor captures the anisotropic pressure-like effects due to the deviations from equilibrium.

- **The non-vanishing trace ($\Delta^{\mu\nu}\Pi$)** is called the bulk pressure that contributes to the pressure of the system. It is responsible for the behavior of the system in cases of uniform expansion or contraction that means it is linked to how the fluid's volume

changes when it gets isotropically squished or stretched. To see this, consider a fluid element that is expanding or contracting uniformly in all directions, with no net flow of matter. In this case, the stress tensor must be isotropic, meaning that it is proportional to the metric tensor: $\Delta^{\mu\nu}\Pi = -Pg^{\mu\nu}$. When it comes to heavy-ion collisions, as matter expands, the pressure and temperature undergo rapid fluctuations. The bulk viscosity influences the expansion rate, potentially delaying or speeding it up. This influences the evolution of matter and the production of particles as the system cools. The bulk pressure can be related to the thermodynamic pressure of the fluid, but it is not necessarily equal to it, especially in non-equilibrium situations. In general, it depends on the gradients of the fluid velocity, temperature, and other thermodynamic variables, and it can be determined from the equations of motion of the fluid, such as the Navier-Stokes equation for a viscous fluid.

Taking the proper projections of the conservation equations of the energy momentum tensor yields the fundamental equations of viscous fluid dynamics that describe how the energy-momentum tensor changes and evolves due to the presence of viscosity in a fluid

$$u_\nu \partial_\mu T^{\mu\nu} = D\epsilon + (\epsilon + P)\partial_\mu u^\mu + u_\nu \partial_\mu \Pi^{\mu\nu} = 0\,, \tag{2.16}$$

$$\Delta^\alpha_\nu \partial_\mu T^{\mu\nu} = (\epsilon + P) Du^\alpha - \nabla^\alpha P + \Delta^\alpha_\nu \partial_\mu \Pi^{\mu\nu} = 0\ . \tag{2.17}$$

The first equation represents energy and momentum conservation in the direction of fluid movement. It states that the sum of the variations in the fluid's energy (ϵ), the energy and pressure terms ($\epsilon + p$) associated with its expansion or compression ($\partial_\mu u^\mu$), and the contribution from the bulk pressure tensor ($\Pi^{\mu\nu}$) must equal zero. The third term in Eq. (2.16) is simplified using $u_\nu \partial_\mu \Pi^{\mu\nu} = \partial_\mu \left(u_\nu \Pi^{\mu\nu}\right) - \Pi^{\mu\nu}\partial_{(\mu} u_{\nu)}$, and by using the identity $\partial_\mu = u_\mu D + \nabla_\mu$

that connects the partial derivative to the convective derivative D, the equation can be further simplified as well by using the fact that in the Landau frame, $u_\mu \Pi^{\mu\nu} = 0$ with

$$A_{(\mu} B_{\nu)} = \frac{1}{2} \left(A_\mu B_\nu + A_\nu B_\mu \right) \ .$$

Furthermore, the second equation focuses on the energy and momentum conservation in directions orthogonal to the fluid flow. Consequently, the essential equations for viscous fluid dynamics in relativistic theory are

$$\begin{aligned} D\epsilon + (\epsilon + p)\partial_\mu u^\mu - \Pi^{\mu\nu} \nabla_{(\mu} u_{\nu)} &= 0 \,, \\ (\epsilon + p) D u^\alpha - \nabla^\alpha p + \Delta^\alpha_\nu \partial_\mu \Pi^{\mu\nu} &= 0 \ . \end{aligned} \tag{2.18}$$

Now, to derive the expressions for the viscous stress tensor $\Pi^{\mu\nu}$, we start by using the basic equilibrium thermodynamic relations for a system without conserved charges (or zero chemical potential)

$$\epsilon + p = Ts, \qquad Tds = d\epsilon \ . \tag{2.19}$$

We know that, in equilibrium, the entropy of the system remains constant or increases. In contrast, out of equilibrium, the entropy of the system will always tend to increase. It means that the second law of thermodynamics can be rewritten in the form

$$\partial_\mu s^\mu \geq 0 \,, \tag{2.20}$$

where the entropy 4-current s^μ in equilibrium is given by $s^\mu = s u^\mu$. The thermodynamic

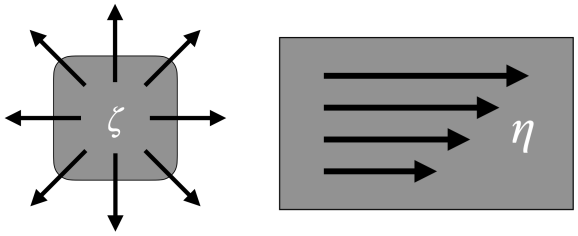

Figure 1: Illustration of viscosity components in relativistic hydrodynamics: ζ (bulk viscosity) resists expansion, while η (shear viscosity) opposes flow gradients.

relations (2.19) allow to rewrite the second law as

$$\begin{aligned}
\partial_\mu s^\mu &= \partial_\mu(su^\mu) = (u_\mu D + \nabla_\mu)(su^\mu) \\
&= u_\mu D(su^\mu) + \nabla_\mu(su^\mu) = Ds + s\partial_\mu u^\mu \\
&= D[(\epsilon+p)/T] + [(\epsilon+p)/T]\partial_\mu u^\mu \\
&= \frac{1}{T}D\epsilon + \frac{\epsilon+p}{T}\partial_\mu u^\mu \\
&= \frac{1}{T}[D\epsilon + (\epsilon+p)\partial_\mu u^\mu] \\
&= \frac{1}{T}\Pi^{\mu\nu}\nabla_{(\mu}u_{\nu)} \geq 0 \ , \qquad (2.21)
\end{aligned}$$

Because $\Pi^{\mu\nu} = \pi^{\mu\nu} + \Delta^{\mu\nu}\Pi$ has a traceless part and a remainder with non-vanishing trace, we introduce a notation for the traceless part of $\nabla_{(\mu}u_{\nu)}$,

$$\nabla_{<\mu}u_{\nu>} \equiv 2\nabla_{(\mu}u_{\nu)} - \frac{2}{3}\Delta_{\mu\nu}\nabla_\alpha u^\alpha \ , \qquad (2.22)$$

Therefore, Eq. (2.21) becomes

$$\partial_\mu s^\mu = \frac{1}{2T}\pi^{\mu\nu}\nabla_{<\mu}u_{\nu>} + \frac{1}{T}\Pi\nabla_\alpha u^\alpha \geq 0 \ . \qquad (2.23)$$

The ultimate goal is to ensure that the inequality that is representing the second law is satisfied. This is achieved by defining specific quantities ($\pi^{\mu\nu}, \Pi, \eta,$ and ζ) that guarantee the

inequality holds and by imposing constraints that these quantities are non-negative. Here, ζ is the bulk viscosity, which measures the resistance to expansion, and η is shear viscosity, which measures the resistance to flow gradients for the traceless part of the derivative of the 4-velocity (see Fig. 1). This notation allows for a more compact representation of certain terms.

$$\pi^{\mu\nu} = \eta \nabla^{<\mu} u^{\nu>}, \quad \Pi = \zeta \nabla_\alpha u^\alpha, \quad \eta \geq 0, \quad \zeta \geq 0, \tag{2.24}$$

because then $\partial_\mu s^\mu$ is a positive sum of squares.

In the next sections, we will dive deeper into the models and simulations used to study these viscous effects, and we will explore how experimental data and theoretical predictions come together to provide a clearer picture of the behavior of matter in these extraordinary conditions.

2.5 Hydrodynamic modeling and experimental insights in high-energy heavy ion collisions

During heavy-ion collisions, the particles begin to behave like a fluid very rapidly. This indicates that they undergo a process known as "hydrodynamization". Once "hydrodynamized", the particles begin to exhibit "collective behavior." Hydrodynamics enables us to comprehend how these particles interact and move collectively which provides insight into the properties of the QGP.

In section (1.3.1), we introduced how the journey of the intensely hot and dense matter created in heavy-ion collisions unfolds in distinct stages. To comprehend these stages, sophisticated hydrodynamic models that simulate the evolution of matter are required. These models are analogous to virtual laboratories, allowing us to investigate conditions that are almost impossible to reproduce in reality. To capture the effects of viscosity and other factors, researchers use specialized relativistic viscous hydrodynamics equations that take into

account how matter flows and how it reacts to pressure gradients and viscosities. Then, in order to perform these simulations, we must provide initial conditions – essentially, the initial state of the matter immediately following the collision. After that, they use the equation of state to describe the relationship between pressure, energy, and temperature in the evolving matter. Next, to solve these equations, it is necessary to conduct numerical simulations using sophisticated numerical methods. These simulations allow us to observe the evolution of matter over time. Nonetheless, they present obstacles, such as coping with the complex geometry of the collision region and modeling the effects of viscosity accurately.

Extracting hydrodynamic information from the experimental data acquired from heavy-ion collisions enables scientists to unravel the mysteries surrounding these energetic events. For example, the elliptic flow pattern observed in the particle emission is caused by the almond-shaped overlap region created when nuclei collide. Scientists can establish a relationship between the observed elliptic flow and the viscosity of the created matter using hydrodynamic simulations and they find that lower viscosity enables particles to behave collectively, resulting in an elliptic flow pattern. Also, the types and energies of emitted particles provide vital information regarding the conditions and stages of the evolution of matter. By analyzing the spectra of emitted particles, scientists can determine the temperature at which particles "freeze out" – that is, cease interacting and are no longer affected by strong multi-particle interactions. This temperature provides insight into the transition between the QGP and hadronic matter.

Comparing experimental data with hydrodynamic simulations helps validate the models and adjust their parameters. When the simulated patterns of particle emission and other observables closely match experimental data, it indicates that the hydrodynamic model accurately captures crucial aspects of the collision's dynamics. However, there are limitations, including the models' simplified assumptions and sensitivity to initial conditions. Scientists

can obtain insight into the properties of the matter formed in heavy-ion collisions through this comparison. This includes parameters such as the QGP's initial temperature viscosity, and its equation of state. Moreover, discrepancies between experimental results and simulations can indicate gaps in our current understanding, steering future research and model refinement.

After looking at how complicated relativistic viscous hydrodynamics is and how important it is to understanding how matter behaves in extreme conditions, we now turn our attention to the interesting field of anisotropic hydrodynamics. Even though relativistic viscous hydrodynamics has been helpful, the development of anisotropic hydrodynamics gives us a new way to look at systems with large differences in momentum in different directions.

2.6 Anisotropic hydrodynamics

Anisotropic hydrodynamics is a non-perturbative reorganization of relativistic hydrodynamics intended to explain the large momentum-space anisotropies observed in ultrarelativistic heavy-ion collisions [6]. These collisions generate substantial imbalances or anisotropies in momentum space, which undermine the traditional hydrodynamic assumption of isotropic (nearly) thermodynamic equilibrium. Anisotropic hydrodynamics permits the study of fluids in situations far from isotropic equilibrium by taking the anisotropic character of the system into consideration. Also, it extends the regime of hydrodynamic treatments, allowing for a more precise description of fluid behavior under extreme conditions with significant momentum distribution imbalances, such as those encountered in heavy-ion collisions. Traditional viscous hydrodynamics dynamical equations are derived using a linearization approach that assumes an isotropic equilibrium distribution function as the first or leading-order approximation [63–96]. This method considers small departures from equilibrium and derives the equations of motion by linearizing the hydrodynamic equations around equilibrium. Linear response theory may now describe viscous effects like shear viscosity. This linearized

technique is limited in systems with severe deviations from isotropic equilibrium, such as ultrarelativistic heavy-ion collisions. Because of that hydrodynamics is a better framework for non-linear dynamics and large momentum-space anisotropies [95, 97–112].

In ultrarelativistic heavy-ion collisions (URHICs), the longitudinal pressure is significantly lower than the transverse pressure in the center of the fireball. The ratio is less than or equal to 0.3. This value shows substantial pressure anisotropies in URHIC quark-gluon plasma (QGP) shortly after the initial nuclear impact. Therefore, the momentum-space distribution of particles in the QGP is extremely anisotropic, with more pressure along transverse directions than longitudinal directions. In addition, the momentum-space anisotropy increases as one advances away from the center toward colder plasma areas. Such significant pressure anisotropy is indicative of significant viscous corrections to the presumed starting point of ideal hydrodynamics. Furthermore, when traditional linearized viscous hydrodynamic treatments are applied to QGP in heavy-ion collisions, certain regions of phase space can arise in which the one-particle distribution function becomes negative. Existence of negative values in the distribution function is problematic because it violates the distribution function's probabilistic interpretation and, therefore, physical consistency. In hydrodynamic modeling, physically valid distribution functions are essential for accurately describing the behavior of the system.

In order to study relativistic hydrodynamics in heavy-ion collisions, it is crucial to resolve this issue and discover new methods. *Anisotropic hydrodynamics* (aHydro) [95, 97–112], among other related methods, offers a promising approach to overcome this challenge and maintain a physically valid distribution function in the analysis of heavy-ion collisions. In this framework, the particles of the system can have significantly different momenta in different directions. This anisotropy can be described mathematically using a tensor called $\Xi_{\mu\nu}$, which quantifies how much momentum space is distorted from isotropy (where the momentum

distribution is the same in all directions). Therefore, the central idea is the distribution function, which describes the statistical distribution of particles in a system in terms of their position (x) and momentum (p), can be separated into a distorted isotropic part ($f_{\rm iso}$) and a non-elliptical anisotropic correction part ($\delta\tilde{f}$). The distorted isotropic part accounts for elliptical non-uniformity and anisotropy in momentum space. Mathematically, one can express the one-particle distribution function in the form

$$f(x,p) = \underbrace{f_{\rm iso}\left(\frac{\sqrt{p^\mu \Xi_{\mu\nu}(x) p^\nu}}{\Lambda(x)}, \frac{\mu(x)}{\Lambda(x)}\right)}_{f_{\rm aniso}(x,p)} + \delta\tilde{f}(x,p)\,, \tag{2.25}$$

where Λ is a temperature-like scale that can be related to the system's true temperature in the isotropic equilibrium limit, and $\mu(x)$ is the chemical potential. To gauge the degree of momentum-space anisotropy one uses $\Xi_{\mu\nu}$ which is a second-rank tensor

$$\Xi^{\mu\nu} = u^\mu u^\nu + \xi^{\mu\nu} - \Delta^{\mu\nu}\Phi\,, \tag{2.26}$$

where u^μ is the four-velocity associated with the local rest frame, $\xi^{\mu\nu}$ is a symmetric and traceless tensor, and Φ is the bulk degree of freedom. In this version, it is assumed that the momentum-space anisotropy in the system can be described using an ellipsoidal deformation shape. In the case that there is a rotational symmetry the ellipsoidal deformation becomes spheroidal. In this latter case the momentum distribution has a different width in the x and y directions different from that in the z direction ($T^{xx} = T^{yy} \neq T^{zz}$) and this is characterized by a single parameter, denoted as $\xi(x)$. This parameter varies in the range $-1 < \xi < \infty$, with the cases $\xi < 0$, $\xi = 0$, and $0 < \xi$ corresponding to the prolate, isotropic, and oblate momentum distribution, respectively, (see Fig. 2). In the more general case where the momentum-space anisotropy is ellipsoidal, meaning that all three components of

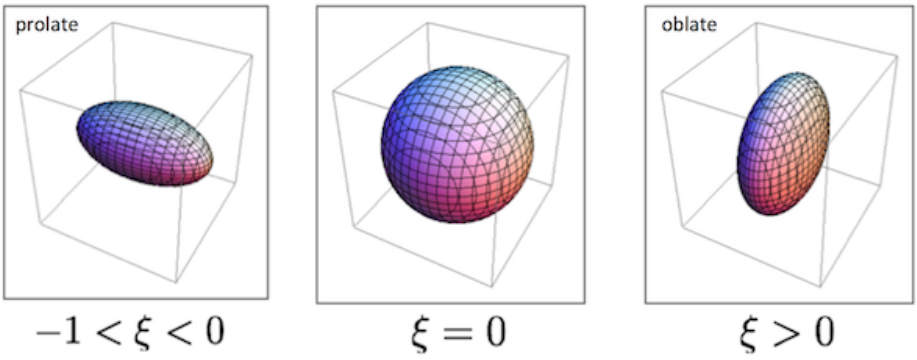

Figure 2: The different range of ξ for the spheroidal anisotropic distribution function [6].

the momentum tensor ($T^{xx} \neq T^{yy} \neq T^{zz}$) are different in the LRF. This is a more complex form of anisotropy compared to the simpler spheroidal form.

As mentioned, the results of microscopic calculations indicate that the transverse pressure of the systems produced initially in heavy-ion collisions is significantly greater than the longitudinal pressure [113–119], one can conclude that the initial distributions are most likely oblate.

Overall, anisotropic hydrodynamics seeks to develop a theoretical framework capable of accurately describing the behavior of this QGP in its initial phases following the collision. This period is essential for comprehending the formation and properties of the QGP and understanding the behavior of matter near the region's edges because it can differ significantly from the behavior of matter in the region's center particularly in the transverse (side-to-side) direction. Moreover, it aims to handle situations in which shear viscosity varies with temperature and may be relatively high. In certain extreme conditions, such as those encountered in heavy-ion collisions, traditional hydrodynamics assumptions (such as low shear viscosity and near equilibrium evolution) may not hold.

2.7 Exploring kinetic and hydrodynamic attractors in extreme matter dynamics

An attractor in a dynamical system is a specific solution that the system approaches as time passes, beginning from a variety of initial conditions within its basin of attraction [1]. In other words, the system will eventually resolve on this particular solution regardless of the initial conditions within a certain range. The behavior of the attractor is determined by the interplay between two factors:

- Expansion rate: This causes the system to become locally anisotropic, favoring the elongation or stretching of the system in particular directions in the momentum space.
- Isotropizing interaction rate: This counteracts the expansion and tends to make the system isotropic, which means that its properties tend to be the same in all directions in the momentum space.

Attractors have recently gained attention in the context of ultra-relativistic heavy-ion collisions. These attractor solutions are essential for comprehending the transition to fluid-dynamic behavior and showing non-thermal fixed-point behavior in systems that are far from equilibrium. They help scientists in determining the extent to which various collisional observations provide information about initial conditions or material properties.

In the field of heavy-ion collisions and the study of quark-gluon plasma (QGP), two significant concepts, namely the kinetic attractor and the hydrodynamic attractor, provide insights into the behavior of matter under extreme conditions. The kinetic attractor addresses the evolution of the particle distribution function over time. Due to extreme and non-equilibrium conditions, the distribution function of particles deviates from equilibrium during the initial phases of a collision. Nevertheless, as the system develops, the distribution function tends to relax and approach an attractor solution. This attractor represents a state

[1] The region of state space from which a dynamic system tends to approach a particular attractor is known as the "basin of attraction." Depending on the behavior of the system, various initial conditions may result in distinct or no attractors.

in which the distribution function is almost completely independent of the initial conditions, ultimately reflecting a universal behavior characteristic of the QGP. The kinetic attractor sheds light on the transition of the distribution function to a state of local thermal equilibrium, thereby providing essential insights into the mechanisms driving thermalization and equilibration within the QGP.

Concurrently, in the contexts of fluid dynamics and heavy-ion collisions, the hydrodynamic attractor retains an important role. It refers to a particular set of equations or conditions to which the macroscopic properties of a fluid system tend to converge as it approaches local thermal equilibrium. At the beginning of a heavy-ion collision, the matter is far from equilibrium and does not behave like a fluid. As the system evolves, it undergoes a transition to fluid-like behavior, with well-defined properties such as temperature, pressure, and energy density that are governed by fluid equations. The hydrodynamic attractor explains how these macroscopic properties conform to hydrodynamic equations as the system approaches thermal equilibrium. This concept is essential for understanding the emergence of fluid-like behavior and the rapid thermalization of quark-gluon plasma.

2.8 Relativistic Kinetic Theory

The study of kinetic theory is an important building block for understanding how complex systems behave in a wide range of scientific fields. From gases and plasma to condensed matter and particle physics, kinetic theory is a powerful way to figure out the microscopic dynamics behind macroscopic events. It helps us understand the traits and behaviors of systems as a whole by looking at the statistical behavior of moving particles and how they interact with each other. Relativistic kinetic theory is a theoretical framework that aims to explain the behavior of particles and systems of particles moving at speeds close to the speed of light using the principles of relativity, where the principles of classical mechanics begin to break down. The significance of this theory is contingent on its capacity to represent the

non-equilibrium relativistic (classical) dynamics of many-body systems, e.g. in Relativistic Heavy Ion Collisions (RHIC). It provides the foundation for numerous models of nuclear processes in various energy regimes. In addition, it serves as the basis for less microscopic approaches, such as relativistic hydrodynamics.

The essential assumption in this theory is that the relevant particles' mean free path is large in comparison to their De Broglie wavelength, allowing one to disregard obvious quantum mechanical effects. Moreover, this theory is dependent on the Boltzmann kinetic equation, which can be difficult to manipulate due to its complex collision term. This term is represented by a multidimensional integral and accounting for the interactions between particles. In the past, solving the Boltzmann equation required intricate numerical simulations that described the unconstrained motion and collisions of particles. To overcome these technical obstacles, a simplified variant of the kinetic equation employing a simplified form of the collision term is frequently employed. This approximation form is referred to as the relaxation-time approximation (RTA) [120–123]. The following sections will provide a comprehensive explanation of this strategy.

The main goal of this section is to explain in detail the theoretical structure and how it can be used in real life. We will look at the basic ideas behind kinetic theory, such as the Boltzmann equation and how it was made, as well as the statistical ideas that it is based on. We will also look at transport processes, where kinetic theory is a key part of understanding how heat, and momentum move through different materials. Also, presenting at how kinetic theory uses approximations and simplifications, such as the relaxation time approximation and the idea of effective kinetic theory. Even when direct microscopic models are not possible, these tools let us work with complicated systems and get useful information about how they work. In addition, we will introduce some of the fundamental macroscopic quantities and their definitions within the kinetic theory.

It is essential to note that later chapters in this dissertation rely on the RTA, as it permits exact solutions to the kinetic equation. In addition, the dynamics under consideration are restricted to boost-invariant systems [124, 125], which is another important assumption that facilitates the precise treatment of the system's behavior.

2.9 Basic definitions of macroscopic quantities

Here, some of the fundamental macroscopic quantities and their definitions within the kinetic theory are introduced.

2.9.1 Distribution function

In the kinetic theory, the fundamental quantity is the *one-particle distribution function* $f(x,p) = f(t,\mathbf{x},\mathbf{p})$ which is a mathematical function that describes the phase space density of the particles by providing the number of particles ΔN in the phase-space volume $\Delta V = \Delta^3 x\, \Delta^3 p$ located at a certain momentum and in a particular region of space and time t

$$f(t,\mathbf{x},\mathbf{p}) \propto \frac{\Delta N}{\Delta^3 x \Delta^3 p}\,, \tag{2.27}$$

where the distribution function depends on the temperature, density, and velocity of the gas as well as the mass and charge of the particles that make up the gas. Using a one-particle distribution function $f(x,p)$ in the kinetic theory is an important concept to study the thermodynamic properties of gases and establishes a relationship between macroscopic (flow, velocity, density, temperature, etc.) and microscopic (particle mass, momentum, energy, position) properties and used to describe the transport properties of gases, such as the viscosity. Therefore, the primary objective of transport equation is to derive the time evolution equation for the one-particle distribution function $f(t,\mathbf{x},\mathbf{p})$, which can be associated with

the number of on-shell particles[2] per unit phase space.

2.9.2 Boltzmann equation

The Boltzmann equation is a fundamental equation in kinetic theory that describes the statistical behavior of particles within a gas or a fluid, including the Quark-Gluon Plasma (QGP) in the context of heavy ion collisions. Mathematically, it is expressed as:

$$\frac{\partial f}{\partial t} + \vec{v} \cdot \nabla_x f + \vec{F} \cdot \nabla_p f = \mathcal{C}[f] \tag{2.28}$$

Here, $f(\vec{x}, \vec{p}, t)$ represents the one-particle distribution function, which depends on position ($\vec{x}$), momentum ($\vec{p}$), and time (t). The left-hand side of the equation describes how the distribution function changes the phase space. The first term, $\frac{\partial f}{\partial t}$, accounts for the change in f with respect to time. The second term, $\vec{v} \cdot \nabla_x f$, represents advection, where $\vec{v}$ is the particle's velocity, and ∇_x is the gradient operator with respect to position. The third term, $\vec{F} \cdot \nabla_p f$, accounts for the effect of external forces ($\vec{F}$) on the distribution function, where ∇_p is the gradient operator with respect to momentum. Finally, the right-hand side ($\mathcal{C}[f]$) represents the collision term, which encodes interactions among particles, including scattering processes. The Boltzmann equation is a powerful tool for describing the evolution of particle distributions in various physical systems, from classical gases to quantum fluids like the QGP, providing insights into equilibration, transport phenomena, and the emergence of macroscopic properties from microscopic interactions.

[2]The mass-shell condition, represented by $E^2 = p^2c^2 + m^2c^4$, links a particle's energy, momentum, and mass in accordance with classical physics. On-shell particles satisfy this condition precisely and behave as expected in experiments. However, virtual particles, briefly borrowing energy from the quantum vacuum, and the uncertainty principle, affecting precise measurements, introduce deviations from this ideal. These deviations are essential aspects of particle physics, enriching our understanding of the quantum world.

2.9.3 Particle current

Having knowledge of $f(x,p)$ permits the calculation of numerous crucial macroscopic quantities. In particular, the particle density that is a measure of the number of particles in a particular region of space and is usually expressed in units of particles per unit volume and their three-current which is a vector field that describes the flow of particles in space. They can be expressed in terms of the distribution function:

$$n(x) = \int dP\, p^0\, f(x,p) = \int \frac{d^3p}{(2\pi)^3}\, f(x,p)\,, \tag{2.29}$$

$$\vec{j}(x) = \int dP\, \vec{p}\, f(x,p) = \int \frac{d^3p}{(2\pi)^3}\, \frac{\vec{p}}{p^0}\, f(x,p)\,. \tag{2.30}$$

The two equations above can be combined in the covariant form as the four-vector field

$$N^\mu(x) = (n(x), \vec{j}(x)) = \int dP\, p^\mu\, f(x,p)\,. \tag{2.31}$$

The term "particle current" refers to the flow or flux of particles across a surface with unit area that is perpendicular to the flux. In this context, the symbol N^μ represents the density of the particle current. If particles possess conserved charges such as the baryon number b or the electric charge e, then the four-currents $B^\mu = bN^\mu$ and $J^\mu = eN^\mu$ represent the baryon and electric current densities, respectively. The four-current is a vector field that describes the flow of particles in space and is given by the equation $J^\mu = (\rho, j^1, j^2, j^3)$, where ρ is the particle density and j^1, j^2, and j^3 are the components of the current density, which is a vector that describes the flow of particles in space.

2.9.4 Energy-momentum tensor

Another macroscopic quantity describing matter is the energy-momentum tensor, which is the second moment of $f(x,p)$,

$$T^{\mu\nu} = \int dP\, p^\mu\, p^\nu\, f(x,p)\,. \tag{2.32}$$

There are only two components: rest mass and kinetic energy. The physical interpretation of the components of $T^{\mu\nu}$ is as follows:

$$\text{Energy density} \longrightarrow T^{00} = \int dP\, (p^0)^2\, f(x,p)\,, \tag{2.33}$$

$$\text{Energy flow} \longrightarrow T^{0i} = \int dP\, p^0 p^i\, f(x,p)\,, \tag{2.34}$$

$$\text{Momentum density} \longrightarrow T^{i0} = \int dP\, p^i p^0\, f(x,p)\,, \tag{2.35}$$

$$\text{Pressure tensor (momentum flow)} \longrightarrow T^{ij} = \int dP\, p^i\, p^j\, f(x,p)\,. \tag{2.36}$$

Integration measure

Due to the on-shell condition, $p^2 = p^\mu p_\mu = m^2$, only three momentum variables, say, p_x, p_y and p_z are treated as independent which for the momentum covariant integration measure implies

$$\begin{aligned}
\int dP(\dots) &= \int \frac{d^4p}{(2\pi)^4}\, 2\pi\delta\left(p^\mu p_\mu - m^2\right)\, 2\Theta(p_0)(\dots) \\
&= \frac{1}{(2\pi)^3}\int_{-\infty}^{\infty} dp^3 \int_{-\infty}^{\infty} dp^2 \int_{-\infty}^{\infty} dp^1 \int_{-\infty}^{\infty} dp^0\, 2\delta\left(p^\mu p_\mu - m^2\right)\Theta(p_0)(\dots) \\
&= \frac{1}{(2\pi)^3}\int_{-\infty}^{\infty} d^3\vec{p} \int_{-\infty}^{\infty} dp_0\, 2\frac{1}{2|E|}\left[\delta\left(p_0 - E\right) + \delta\left(p_0 + E\right)\right]\Theta(p_0)(\dots) \\
&= \int \frac{d^3\vec{p}}{(2\pi)^3}\frac{1}{E}(\dots)\,.
\end{aligned} \tag{2.37}$$

Using $\delta[g(x)] = \sum_i \frac{\delta(x-x_i)}{|g'(x_i)|}$ where x_i is the root of $g(x)$ in the second line, one can cast the δ-function in the form

$$\delta\left(p^\mu p_\mu - m^2\right) = \delta\left(p_0^2 - \vec{p}^{\,2} - m^2\right) = \delta\left(p_0^2 - E^2\right) = \frac{1}{2|E|}\left[\delta\left(p_0 - E\right) + \delta\left(p_0 + E\right)\right],$$

where $p^\mu p_\mu = p_0^2 - \vec{p}^{\,2}$, and $E = \sqrt{\vec{p}^{\,2} + m^2}$. Then to obtain the last result, we use the property $\int_{-\infty}^{\infty} f(x)\delta(x - x_i)dx = f(x_i)$ and Θ which is the Heaviside step function

$$\Theta(p^0) = \begin{cases} 1, & \text{for } p^0 \geq 0 \\ 0, & \text{for } p^0 < 0. \end{cases}$$

Here, the δ-function imposing the condition of only counting on-shell particles and the step-function restricts the sum to positive energy states. Finally, we note that the integration measure $\int dP$ is manifestly Lorentz invariant as can be seen from Eq. (2.37).

2.9.5 Relativistic equilibrium distributions

The Maxwell-Boltzmann distribution is a fundamental concept in statistical physics that describes the distribution of particles in thermal equilibrium. It describes the probability of finding a particle with a specific momentum and energy in a thermal system. The distribution depends on the temperature and chemical potential of the system. In addition to this classical distribution, heavy-ion collisions may involve particles that obey quantum statistics, such as fermions (e.g., protons and neutrons) and bosons (e.g., pions and kaons). In these cases, the Fermi-Dirac and Bose-Einstein distributions are used to characterize the momentum distributions of fermions and bosons, respectively, in these instances. These distributions reflect the Pauli exclusion principle for fermions and Bose-Einstein statistics for bosons.

$$f_{\text{eq}}(x,p) = \frac{1}{\exp(\frac{u\cdot p}{T} - \frac{\mu}{T}) + a}\,, \tag{2.38}$$

where the equilibrium distribution function with $a = 0, 1$, and -1 corresponding to classical, Fermi-Dirac, and Bose-Einstein statistics, respectively,

2.10 Relaxation time approximation

In this dissertation, we analyze the relativistic Boltzmann kinetic equations for conformal and non-conformal system with phase-space distribution functions $f(x,p)$ [105,106,111,126],

$$p_\mu \, \partial^\mu \, f(x,p) = \mathcal{C}[f(x,p)] \, . \tag{2.39}$$

The left-hand side of Eq. (2.39) describes free motion of particles often referred to as "free-streaming terms." This part represents how particles move without interactions, while the right-hand side contains the collision terms $\mathcal{C}[f(x,p)]$, which accounts for interactions among particles in the system. In this work, the latter are included in the relaxation time approximation (RTA), which is a common simpification in kinetic theory [120–122], namely, we use the form

$$\mathcal{C}[f(x,p)] = \frac{p \cdot u}{\tau_{\rm eq}} \left(f_{\rm eq} - f \right) , \tag{2.40}$$

where we introduce the notation with "dot" for scalar product, $p \cdot u = p_\mu u^\mu = g_{\mu\nu} p^\mu u^\nu$ that essentially measures how much of the particle momentum is aligned with the fluid four velocity. Here τ_{eq} is the relaxation time and the four-vector $u^\mu(x)$ is the hydrodynamic flow of matter. The form of the collision term in Eq. (2.40) has simple physical interpretation: it is assumed that the effect of the collisions on the actual distribution function $f(x,p)$ is to restore the distribution function to its local equilibrium $f_{\rm eq}(x,p)$ value and the rate at which this process occurs is governed by the value of the relaxation time [127].

Part II

Initial conditions

Chapter 3

Glauber Model and Bjorken Model

3.1 Glauber Model

In an ultra-relativistic collision, the result of colliding two heavy nuclei, such as lead and gold, produces the highest multiplicities of outgoing particles of all subatomic systems known in the laboratory. Even when two nuclei hit directly, tens or hundreds of thousands of particles are produced. This creates extremely complicated event compared to simple proton-proton collisions. Because of the complexity of those collisions, it is reasonable to ask how many incident nucleons are involved in a particular interaction and how the nuclei overlap. Despite the fact that this problem appears insurmountable due to the femtoscopic length scales involved, which preclude direct observation of the impact parameter (b) or the number of participating nucleons (N_{part}) or binary nucleon-nucleon collisions (N_{coll}), theoretical techniques have been developed to allow these quantities to be estimated from experimental data. These methods are commonly known as "Glauber Models" which take into account the multiple scattering of nucleons in nuclear targets [128–132].

Glauber models are phenomenological approaches designed to determine these values for femtosecond many-body systems. The Glauber model was developed by Roy Glauber (2005 Nobel Laureate in Physics) to solve the problem of high energy scattering with composite particles. It gives a quantitative representation of the geometrical configuration of nuclei during collisions. Its concept depends on the mean free path with some assumption that the cross-section of the baryon-baryon interaction remains constant throughout the passage of a baryon from one nucleus to another and that the nuclei travel in a straight line trajectories

along the collision direction. Given the Glauber model, one can simulate the initial conditions of a heavy-ion collision by tracing back each collision. One can then extract results that determine the number of participants N_{part}, and the number of binary nucleon-nucleon collisions N_{coll}, which have to be extracted approximately from experimental data using theoretical approaches that assume a given nuclear density distribution with fixed energy for a given impact parameter. This is because the femtometer scales on which these collisions occur prevent direct observation. Moreover, both N_{part} and N_{coll}, along with the impact parameter b, can describe the "centrality" of the collision.

Two basic approaches to studying the Glauber model exist: the optical technique and the Monte Carlo approach. In the Glauber Model, to calculate the geometric parameters and to be able to compare the geometric results of this semi-classical model with the actual experimental data, one must use experimental data given as model inputs. The two most important inputs are the nuclear density profile of the colliding nuclei extracted from low-energy electron scattering experiments, which provides information about how the nucleon density varies as a function of radial distance from the nucleus center and the energy dependence of the inelastic nucleon-nucleon cross-section, which characterizes the probability of nucleon-nucleon interactions as a function of collision energy.

3.1.1 Nuclear charge density

A nucleus is composed of protons and neutrons whose density distributions are $n_p(r)$ and $n_n(r)$, respectively. By integration over space, one can obtain the nucleus's atomic number (Z) and neutron number (N). The two density configurations are not equal when the neutron number is greater than the atomic number, especially for large-mass nuclei. Generally, because the protons and neutrons cannot be distinguished in high-energy collisions, one can integrate the nuclear one-body density function $n(r)d^3r$ to obtain the average number of

nucleons within a small volume d^3r as the following

$$\int n(r)d^3r = A\,, \tag{3.1}$$

where A is the number of nucleons (mass number) of the nucleus. Inside the nucleus, the nuclear charge density is similar to a hard-sphere, but not quite. The hard-sphere model is considered a step function characterized by constant density within the nuclear radius but everywhere outside the nuclear radius range, the density goes to zero, which means that no nucleons exist outside its radius.

$$n_{sphere}(r) = \begin{cases} n_0 & r < R \\ \\ 0 & r \geq R \end{cases}, \tag{3.2}$$

where n_{sphere} indicates the distribution given by the hard sphere model. However, the nucleus is more accurately treated as a diffuse object instead of a sphere-shaped object with well-defined boundaries. In the Glauber Model, the density is no longer fixed at a specific value; that is, the radius of the nucleus is no longer represented as distinct or defined. Also, an indefinitely long thin tail extends beyond the mean radius rather than a densely packed nucleus in the middle. This kind of density distribution inside the nucleus is commonly described with the Wood-Saxon nucleon density, allowing us to understand the model better. A Fermi distribution which describes the gradual change from a high density at the center to a lower density as one moves away from the center (radially outward), usually parameterizes this distribution with two parameters, and it governs the density of nucleons as a function of distance from the center of the nucleus.

$$n_{\rm ws}(r) = \frac{n_0}{1 + \exp[\frac{r-R}{d}]}\,, \tag{3.3}$$

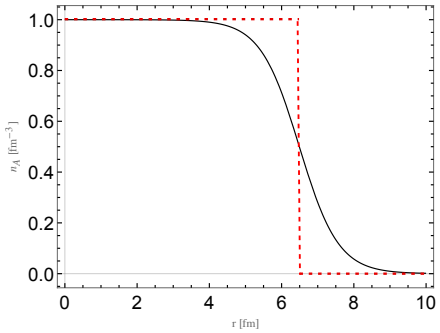

Figure 1: The density distribution for Pb^{208} where the black solid line represents the density distribution given by the Wood-Saxon nucleon density, and the red-dashed line is representing the distribution given by the hard sphere model.

where $n_{\rm ws}$ indicates the distribution given by the Wood-Saxon nucleon density, n_0 is the nuclear density at the center that is determined by using Eq. (3.1) and is fixed by this normalization condition, d is the skin depth "thickness", which identifies how sharp the edge of the nucleus is, and R is the nuclear radius. For spherical nuclei, such as Pb, the distribution is taken to be uniform in azimuthal and polar angles. Moreover, for a large number of nuclei the parameters can be approximated as

$$R = 1.12\, A^{1/3} - 0.86\, A^{-1/3} \;\text{ and }\; d = 0.54 \text{ fm}\,. \tag{3.4}$$

In Figure 1, the density distribution of Pb^{208} is plotted by assuming a Woods-Saxon distribution and using the values $R = 6.49$ fm and, $d = 0.54$ fm where the black solid line represents the density distribution given by the Wood-Saxon nucleon density, and the red-dashed line is representing the distribution given by the hard sphere model. The main feature of Fermi distribution is the density decreases rapidly near the surface.

3.1.2 Inelastic nucleons-nucleons cross section

The Glauber model assumes that nucleon collisions are inelastic and the colliding particles (nucleons) undergo significant interactions, leading to changes in their internal states, and that each collision's average number of charged particles is constant. In addition, because

each collision results in a slight energy loss and change in momentum, the same cross-section (a measure of the effective area for interactions) may be used for many collisions. When considering a single proton-proton collision, this cross-section is considered the same and is not affected by the nuclear environment. The model also includes the option to use protons and neutrons interchangeably. In reality, protons and neutrons have slightly different properties, but for simplicity, the Glauber model treats them as equivalent when calculating cross-sections. Moreover, because the cross section is dominated by low-momentum processes, perturbative quantum chromodynamics (valid for transverse momentum $p_T \geq 1$ GeV/c) cannot be used to compute it [131, 133]. As a result, the observed inelastic nucleon-nucleon cross-section σ_{inel}^{NN} is utilized as an input for Glauber computations.

3.2 Optical Glauber Model

In the Optical Glauber model limit, the interaction of two colliding nuclei is treated as a wave phenomenon. The overall phase shift of the incoming wave is taken as a sum over all possible two nucleon phase shifts and the imaginary part of the phase shifts is related to the nucleon – nucleon scattering cross–section through a principle known as the optical theorem. This optical approximation assumes that when the energies are high enough, the nucleons have enough momentum to flow through each other without being deflected. This is a simplification that becomes more accurate at higher collision energies. In addition, to simplify the description of the collision dynamics it is assumed the nucleons move in the nucleus independently. Moreover, the size of the nucleus is much larger than the extent of the nucleon–nucleon force. In the calculation regarding this model, one has to assume that the nucleus consists of a smooth matter density that follows the Fermi distribution in the radial direction (instead of thinking about individual protons and neutrons scattered around in a chaotic manner, they imagine the nucleus as a smoothly spread-out cloud of matter) and this distribution is taken to be uniform in azimuthal and polar angles. Because of the

possibility for considering the independent linear trajectories of the constituent nucleons, one can develop simple analytic expressions for the nucleus-nucleus interaction cross-section and for the number of interacting nucleons and the number of nucleon-nucleon collisions in terms of the basic nucleon-nucleon cross section [128].

A collision between two nuclei is referred to as an event and the line connecting centers of colliding nuclei in a plane parallel to beam direction gives an impact vector ($\vec{b}$). Therefore, the impact parameter (b) refers to the length of the impact vector. According to the magnitude of the impact parameter, one can determine the degree of centrality for the event. The two primary types of events are central, in which the nucleons collide directly (small impact parameters), and peripheral, in which the actual collision between the two objects does not involve their central regions but occurs when the outer parts of the objects come into contact (large impact parameters). As shown in Figure 2, two heavy ions, target A and projectile B, collide at relativistic speeds with impact parameters as indicated diagrammatically in the setup of the analytical equations. As present in the figure, two flux tubes placed at a distance $\vec{s}$ from the center of target nucleus and a displacement $\vec{s} - \vec{b}$ from the center of projectile. When the two objects collide, the tubes overlap, and that is what scientists are looking for to identify the particles produced during the collision [134].

3.3 Monte Carlo Glauber Model

The Glauber model randomly distributes nucleons within the nucleus on an event-by-event basis[1] and determines collision characteristics by averaging over many events resulting in the optical (smooth) limit [135–138]. In a Monte Carlo simulation, one can imagine a system of the collision of two nuclei and define rules or models for how different components of the system interact. Instead of solving complex mathematical equations analytically, one

[1]The term "event" in this context refers to a single instance of a nuclear collision. In each event, a specific configuration of nucleons is generated based on the random distribution.

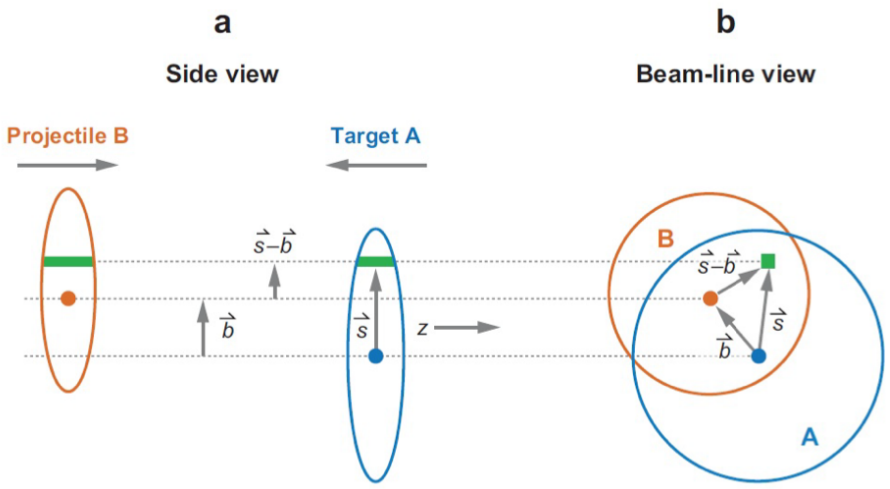

Figure 2: Schematic representation of the Optical Glauber model geometry, with transverse (a) and longitudinal (b) views [7].

can use random sampling to explore a wide range of possible scenarios. The simulation performs these random samplings or experiments repeatedly. Each time, it generates a set of random conditions (e.g., the initial positions and velocities of nucleons in the nuclei) based on probability distributions and rules that are defined. By repeating these simulations many times, one can collect data on how the system behaves under various conditions. Then by using statistical methods, one can estimate the average behavior or properties of the system based on the results of these simulated experiments. Therefore, there are two steps to perform the Monte Carlo Glauber model calculation. First, determine the position of the nucleon in each nucleus stochastically. Second, one assumes that when the two nuclei collide, the nucleons travel in a straight line along the beam axis.

3.3.1 Position of Nuclei

According to a probability density function, the position of each nucleon in the nucleus is determined where the probability distribution is typically taken to be uniform in azimuthal and polar angles. Therefore, by multiplying the Woods-Saxon function by the distance from the center of the nucleus squared (r^2), one can obtain the radial probability function $n_{\mathrm{ws}}(r)r^2$

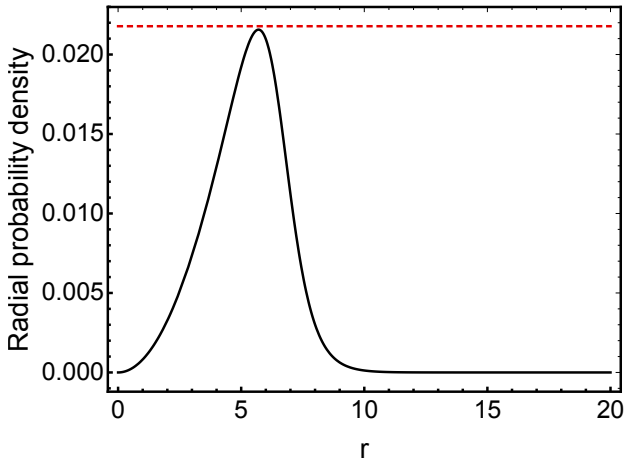

Figure 3: Radial probability function for a Pb nucleus (R=6.49 fm and d = 0.54 fm by assuming Woods-Saxon distribution.

as represented in Figure 3. The resulting equation is then used to randomly distribute the nucleons in a three-dimensional spherical coordinate system that will be accelerated towards each other in any given run of the model. Then, one need to convert the coordinates for each of the 416 nucleons in Pb + Pb from spherical to Cartesian to plot them on x-y coordinates as shown in Figure 4.

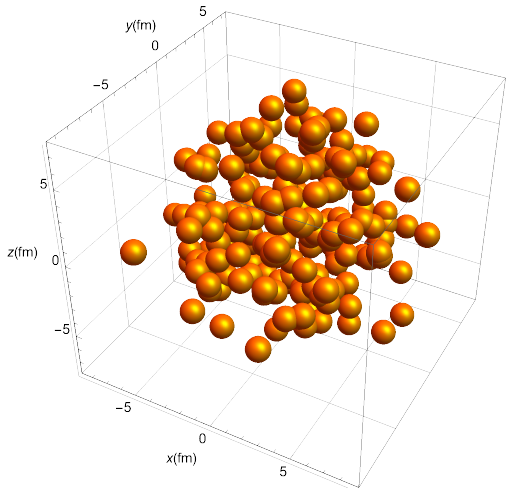

Figure 4: Positions of nucleons in a lead (Pb) nucleus, sampled at random from the Woods-Saxon distribution as part of a Monte Carlo Glauber procedure.

3.3.2 Collision Process

In this step, all of the constituents of one nucleus are shifted by the impact parameter that selected randomly from the following distribution up to $b_{max} \simeq 20$ fm $> 2R$ [7]

$$\frac{dN}{db} \propto b\,, \tag{3.5}$$

where N is the number of events and b is the impact parameter. The probability of a specific impact parameter following a linear trend where hitting the center of the target area is proportional to

$$\frac{d\sigma}{db} = 2\pi b\,. \tag{3.6}$$

The probability of approaching a peripheral collision (large b) is much higher than a central collision ($b = 0$). This model assumes that the offset is in the positive x-direction for simplicity; however, the impact parameter vector might point in any direction due to spherical system symmetry [139]. Moreover, to have a binary collision between two nucleons, the distance D between them (nucleons) must satisfy the following condition

$$D \leq \sqrt{\frac{\sigma_{inel}^{NN}}{\pi}}\,, \tag{3.7}$$

where σ_{inel}^{NN} is the total inelastic nucleon-nucleon cross-section. Every nucleon that experiences at least one binary collision is called a participant nucleons N_{part}. Each nucleon that does not satisfy this condition will pass through the interaction region without colliding or interacting and are subsequently labeled as spectator nucleons. For each event, the total number of binary collisions N_{coll} is defined as the number of nucleons that interact only once and it is calculated by the sum of individual number of collisions and the total number of participating nucleons N_{part}. Also, it is assumed that the nucleons follow a straight path along

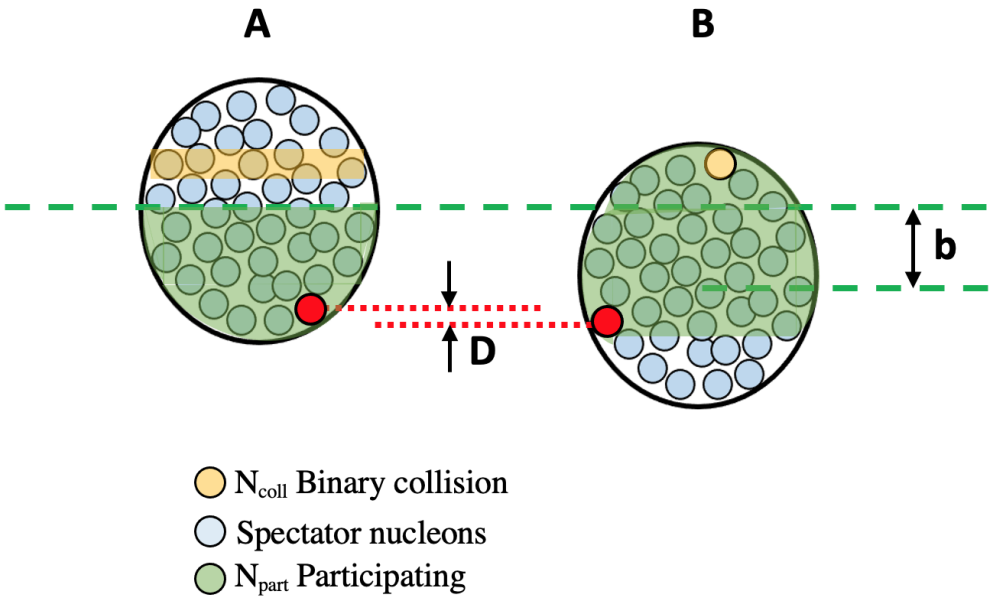

Figure 5: A simplistic picture of two nucleus (A and B) that shown the impact parameter (b) that separating the two nuclei, binary collisions N_{coll}, participating nucleons, N_{part}, spectator nucleons, and the transverse distance $D \leq \sqrt{\frac{\sigma_{inel}^{NN}}{\pi}}$.

the beam axis where the longitudinal coordinate does not play a role in the calculation.[2] Figure 5 illustrates these geometric quantities.

3.4 Results and Discussion

A simple Glauber multi-scattering eikonal model assumes that the colliding nucleus constituents have straight-line trajectories, which is the standard procedure for determining the transverse overlap area and other derived quantities in a generic nucleus-nucleus collision (A-B) separated by impact parameter b. Here, we will present the main formulas of the model that are used in our calculations.

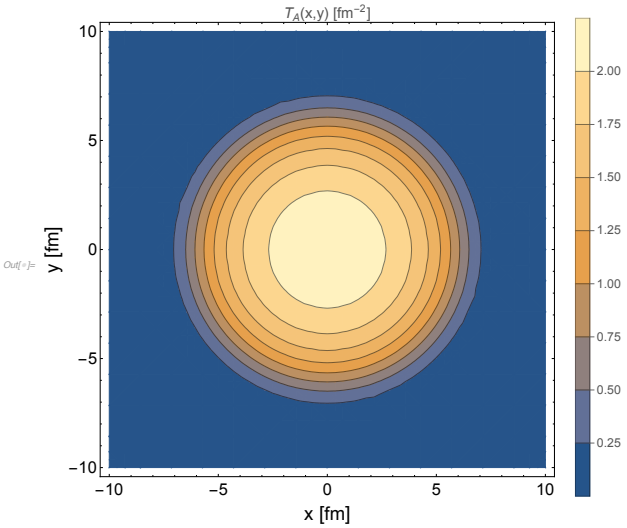

Figure 6: The nuclear thickness function, $T_A(\mathbf{b})$, for a Lead nucleus by using the Woods-Saxon parameterization.

3.4.1 Thickness and overlap functions

The primary quantity of a Glauber approach is the nuclear thickness function of the nucleus A . This function gives the number in the nucleus A per unit area along the direction z separated from the center of the nucleus A by an impact parameter b and is defined as

$$T_A(\mathbf{b}) = \int n_A(\mathbf{b}, z) dz \,, \tag{3.8}$$

where n_A is the nucleus A density. Note that $T_A(\mathbf{b})$ has units of inverse area and depends only on b. Thus, the maximum thickness at the center of the nucleus is $2\, n_0\, R_A$ while at the edge, $b \sim R_A$, the nucleus has zero thickness. We normalize by integrating over the transverse spatial coordinate $d^2\, b = 2\pi\, b\, db$ giving

$$\int d^2 b\, T_A(\mathbf{b}) = A \,, \tag{3.9}$$

[2]The x- and z-axes are used throughout this section to represent the reaction plane, which is determined by the impact parameter and the beam direction, and the x- and y-axes are used to represent the transverse plane.

independent of the parameterization of the nuclear density distribution since n_0 can be fixed from the normalization condition.

Figure 6 shows contour plot of the nuclear thickness function, $T_A(\mathbf{b})$ calculated with the 2-parameter Woods-Saxon density distribution for Pb^{208} with $\sqrt{s_{NN}} = 5023$ GeV, d=0.54 and $\sigma_{NN} = 67$ mb. Here, the highest thickness level is in the middle of the nucleus and decreases with increasing the radius of the nucleus. The most important result about the density for peripheral collisions where, although the impact parameter is large, the tails of the two distributions still overlap. As we will see, the tails are important for accounting for fluctuations in the number of participant nucleons and the number of nucleon-nucleon collisions.

When two nuclei collide, the nucleons in nucleus A's transverse distance $\mathbf{s}$ collide with the nucleons in nucleus B's transverse distance $\mathbf{b}-\mathbf{s}$, as seen in Fig. 2. When nucleus A is at location $(\mathbf{b}_A, z_A)$ and nucleus B is at position $(\mathbf{b}_B, z_B)$, we may compute the probability of a nucleon-nucleon collision at impact parameter $\mathbf{b}$. There are three components to find the probability $P_{AB}(b)$. First, the probability of finding a nucleon from nucleus A in the volume element $d^2b_A\, dz_A$ where this probability is $\propto \frac{n_A(\mathbf{b}_A,z_A)}{A} d^2b_A\, dz_A$. Because of $\int n(r)d^3r = A$, the probability is normalized and the integration over the nuclear volume gives unity. The second component is the probability of finding a nucleon from nucleus B in the volume element $d^2b_B\, dz_B$ and is given by a similar expression but follows for the projectile nucleon. The last is the probability of an inelastic nucleon-nucleon collision at impact parameter $\mathbf{b}$. The simplest inelastic nucleon-nucleon collision probability is a delta function times the NN inelastic cross section, $\sigma_{inel}\, \delta(\mathbf{b} - \mathbf{b}_A - \mathbf{b}_B)$. Therefore,

$$dP_{AB}(b) = \frac{n_A(\mathbf{b}_A, z_A)}{A} d^2b_A\, dz_A \frac{n_B(\mathbf{b}_B, z_B)}{B} d^2b_B\, dz_B \sigma_{inel}\, \delta(\mathbf{b} - \mathbf{b}_A - \mathbf{b}_B)\,. \tag{3.10}$$

The total probability as a function of b is the integral over the volume elements of both

nuclei, normalized per AB,

$$
\begin{aligned}
P_{AB}(b) &= \frac{\sigma_{inel} T_{AB}(b)}{AB} && (3.11)\\
&= \frac{\sigma_{inel}}{AB} \int d^2b_A \, dz_A d^2b_B \, dz_B \, n_A(\mathbf{b}_A, z_A) \, n_B(\mathbf{b}_B, z_B) \, \delta(\mathbf{b} - \mathbf{b}_A - \mathbf{b}_B) && (3.12)\\
&= \frac{\sigma_{inel}}{AB} \int d^2s \, dz_A \, dz_B \, n_A(\mathbf{s}, z_A) \, n_B(|\mathbf{b} - \mathbf{s}|, z_B) \, , && (3.13)
\end{aligned}
$$

where we have integrated over b_B using the delta function and identified b_A with s. By replacing $\int n_A(\mathbf{s}, z_A) dz_A$ with $T_A(s)$ and $\int n_B(|\mathbf{b}-\mathbf{s}|, z_B) dz_B$ with $T_B(|\mathbf{b}-\mathbf{s}|)$, then dropping the common factors of AB, we have the nuclear overlap function of nuclei A and B colliding at impact parameter b, $T_{AB}(b)$,

$$
T_{AB}(\mathbf{b}) = \int T_A(\mathbf{s}) T_B(|\mathbf{b} - \mathbf{s}|) d^2s \, , \tag{3.14}
$$

where the product $T_A(\mathbf{s}) \, T_B(\mathbf{b} - \mathbf{s}) \, d^2s$ gives the joint probability per unit area of nucleons being located in the respective overlapping target and projectile flux tubes of differential area d^2s. Note that $T_{AB}(\mathbf{b})$, like the nuclear profile function, $T_A(b)$, has dimensions of inverse area, fm^{-2}. The integral of $T_{AB}(\mathbf{b})$ over all impact parameters is a number equal to the product of the nuclear mass numbers

$$
\int d^2b \, T_{AB}(b) = AB \, . \tag{3.15}
$$

As shown in Fig. 7, where Lead nuclei are used to test the predictions of model. Greater impact parameter collisions have a smaller overlap zone and are referred to as peripheral collisions when the impact parameter is larger in a geometrical image. As the impact parameter values decrease, so does the number of nucleons involved and the number of binary collisions and as the result of the bigger overlap zone. Note that $T_{AB}(b)$ is purely a function

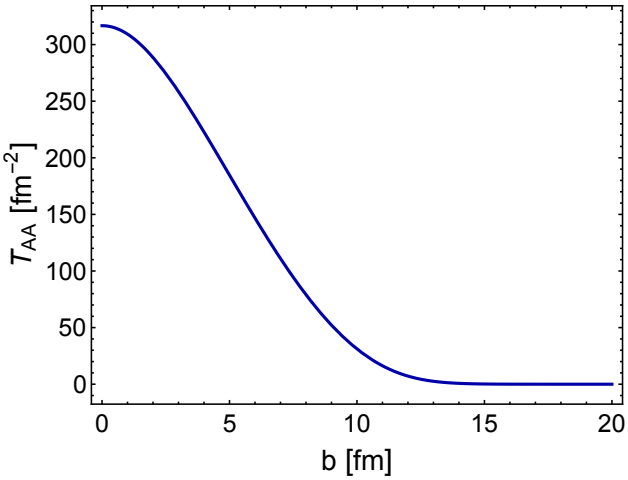

Figure 7: The nuclear overlap integral as a function of impact parameter b for Pb+Pb collisions.

of geometry, it is independent of the collision energy.

3.4.2 Number of binary nucleon-nucleon collisions

For a given nucleon-nucleon cross section σ_{inel}, one can define the number of binary collisions or the number of inelastic nucleon-nucleon collisions in a A+B collision at impact parameter b by the product $\sigma_{inel}\, T_{AB}(\mathbf{b})$ with

$$N_{coll}(b) = A\, B\, \sigma_{inel}\, T_{AB}(\mathbf{b})\,, \tag{3.16}$$

where the number of collisions is dimensionless because the units of $T_{AB}(b)$ is fm^{-2} and σ_{NN} is fm^2. From this last expression one can see that the nuclear overlap function, $T_{AB}(b) = \frac{N_{coll}(b)}{\sigma_{NN}}$. Note that $N_{coll}(b)$ does depend on energy since the inelastic cross section grows with $\sqrt{s_{NN}}$.

3.4.3 Number of participating nucleons

The number of nucleons in the target and projectile nuclei that interact in a collision at impact parameter b is called the number of participants is given by

$$N_{part}(\mathbf{b}) = A\int T_A(\mathbf{s})(1-[1-T_B(\mathbf{s}-\mathbf{b})\sigma_{inel}]^B)d^2s + B\int T_B(\mathbf{s}-\mathbf{b})(1-[1-T_A(\mathbf{s})\sigma_{inel}]^A)d^2s\,. \tag{3.17}$$

3.4.4 Eccentricity

Because heavy ions are extended objects and the impact parameter vector $\mathbf{b}$ is one of the most critical parameters that dictates the overall shape of the collision region, the system generated in a head-on collision differs from that created in a peripheral impact. In the collision, it will create a pressure differential from the dense core to the border of the system. For central heavy-ion collisions, this pressure gradient is radially symmetric and all particles produced in the system will give a radially outward boost that affects the transverse momentum spectra of particles. The impact parameter of the collision greatly influences the geometry of the interaction zone in non-central collisions. Just after the collision of the two nuclei in a heavy-ion reaction with non-zero impact parameter, the initial high-density volume has the shape of their overlap region. The overlap zone has an almond-like shape in the transverse plane. This region is elongated along an axis perpendicular to the reaction plane—that is, the plane defined by the beam direction and the line between the centers of the two nuclei as they collide. The momentum anisotropy of the generated particles results from the spatial anisotropy about the xy plane (the reaction plane).

The deviation of that shape from a circular shape can be described by the eccentricity ε under the assumption that the position of all participating nucleons is known. In other words, the eccentricity quantifies the initial spatial anisotropy (i.e. the shape and orientation) that ultimately results in the anisotropic final momentum distribution for emitted particles that

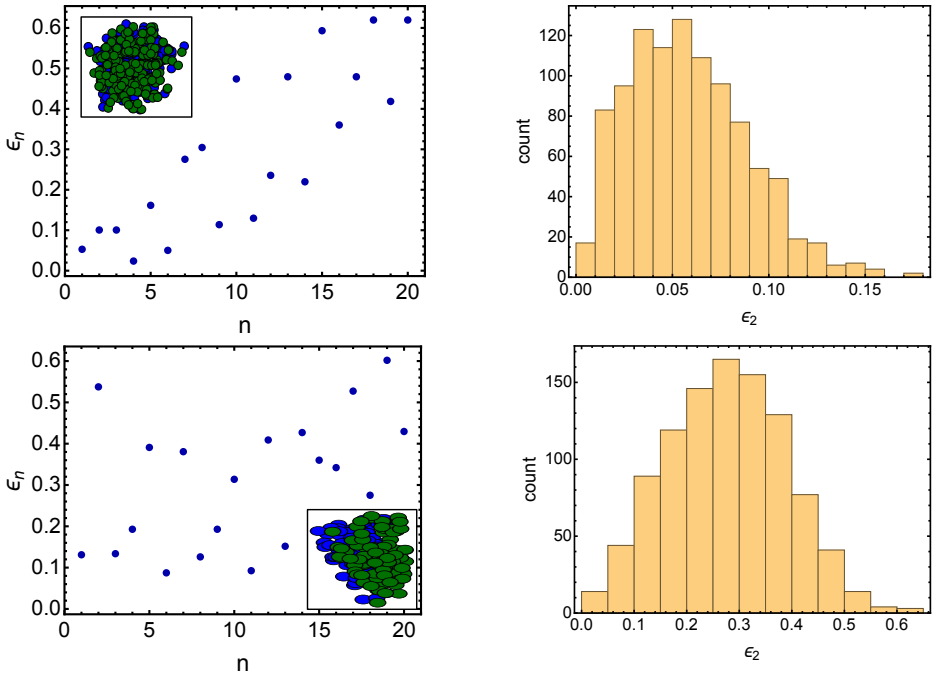

Figure 8: Top: the eccentricity of a A-B collision at impact parameter $b = 0$. Bottom: the eccentricity of a A-B collision at impact parameter $b = 8$ fm.

is observed in elliptic flow. The eccentricity of a A-B collision at impact parameter b can be obtained from the asymmetry ratio between the x and y "semi-axis" dimensions of the overlap zone, weighted by the number of nucleon-nucleon collisions at b. If the quarks and gluons occupying the initial asymmetric volume are indeed interacting collectively, pressure gradients during the subsequent expansion will result in an anisotropic distribution of the final particles with respect to the reaction plane. The eccentricity is defined as

$$\varepsilon_n = \frac{\sqrt{\langle r^n \cos n\phi \rangle^2 + \langle r^n \sin n\phi \rangle^2}}{\langle r^n \rangle} . \tag{3.18}$$

This may be calculated in two ways. In the optical limit, the averages are calculated with a fixed impact parameter and weighted by the local participant or binary collision density. The Monte Carlo method basically involves calculating the moments of the participants themselves.

In Fig. 8, one can see very different limiting behavior at very large and small impact parameter. For a central collision as $b = 0$ in the optical limit, ε_n also goes to zero as the system becomes radially symmetric. In the event-by-event MC Glauber model, one can see that there is very small eccentricity but non zero in all of n due to fluctuations. In addition, one can find the relation between the average eccentricity that is averaged over an ensemble of sampled collisions N=1000, by calculating ε_2 for each of these events and collecting them to get a probability distribution function for ε_2. As a result, one can see that it is peaked around 0.05 but it is non zero so on average a central heavy ion collision has a very small ε_2 which will seed even elliptic flow in a head on collision. By looking instead to non-central collision $b = 8$ fm, there is a very large second order eccentricity coefficient with peak at 0.3. Although there are fluctuations, they have on average a quantifiably larger spatially eccentricity in this centrality class than in the central collision.

Centrality Class

After defining these quantities, one can show that the "centrality class" in the Glauber model can be used for categorizing collision occurrences into different degrees of centrality. Knowing the distribution of inelastic cross-sections as a function of the impact parameter $\frac{d\sigma_{NN}}{d^2b}$, the portion of centrality (c_i) in the optical Glauber model is

$$c_i = \frac{1}{\sigma_{tot}^{AA}} \int_{b_i,min}^{b_i,max} d^2b[1 - \exp(-T_{AB}(b)\sigma^{nn})] \,. \tag{3.19}$$

This means, for each centrality class, the impact parameter intervals [0,b(c_i)] are fixed. Therefore, the average impact parameter in each class is

$$\bar{b_i} = \frac{1}{\sigma_{c_i}^{AA}} \int_{b_i,min}^{b_i,max} d^2b\, b[1 - \exp(-T_{AB}(b)\sigma^{nn})] \,. \tag{3.20}$$

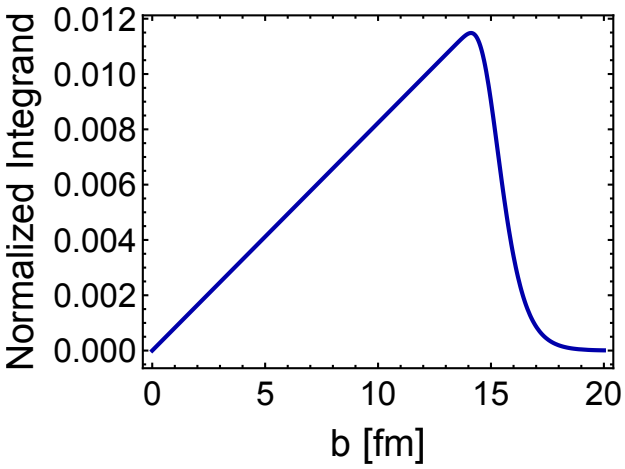

Figure 9: The impact parameter ($b = 4.5$) for Pb-Pb collisions at $\sqrt{s_{NN}} = 5023$ GeV.

Also, the average number of participants in each class is

$$\bar{N}_i^{part} = \frac{1}{\sigma_{c_i}^{AA}} \int_{b_i,min}^{b_i,max} d^2b \; n_{part}^{AA}[1 - \exp(-T_{AB}(b)\sigma^{nn})] \,. \tag{3.21}$$

The approach is similar for the Monte Carlo Glauber, except that the number of participants or binary collisions is utilized instead of the impact parameter.

Fig. 9 illustrates how the Woods-Saxon parameterization affects the result. The cross-section grows linearly with the value of the impact parameter (b) up to roughly twice the nuclear radius (R), at which point any nucleon-nucleon collisions start to decrease. When $b \approx 2R$, the cross-section slowly tails off to zero instead of sharply dropping off to zero. However, because the nuclei are not hard spheres but rather a bit more diffuse, as seen by the nucleon distribution map in Fig. 1, it is not a dramatic drop-off.

The optical limit of the Glauber Model has one problem related to the accurate results. Within optical approach, one treats the nucleons as a continuous fluid. In other words, the nucleons are fixed in space for every nucleus and eliminates all randomness. As a result, this model presents a slightly inaccurate portrayal of the nucleus. Because of this, one needs to a Monte Carlo Glauber Model that resolves this problem. An illustration of a Glauber Monte

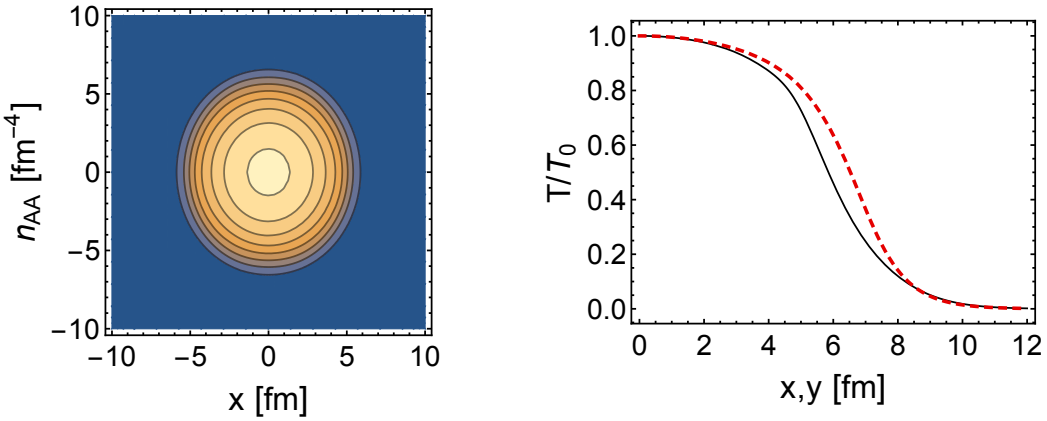

Figure 10: The impact parameter ($b = 4.5$) for Pb-Pb collisions at $\sqrt{s_{NN}} = 5023$ GeV.

Carlo event for a Pb+Pb collision at $\sqrt{s_{NN}} = 5023$ GeV is shown in Figure 11 with impact parameter of $b = 0$ fm (right) and $b = 8$ fm (left) viewed in the transverse plane. The darker green and darker blue circles are the participating nucleons, the lighter colored circles are spectator nucleons. This simulation is considered at the first moments of the collision. The average number of participating nucleons and binary nucleon-nucleon collisions and other quantities are then determined by simulating many nucleus-nucleus collisions as shown in Figure 12.

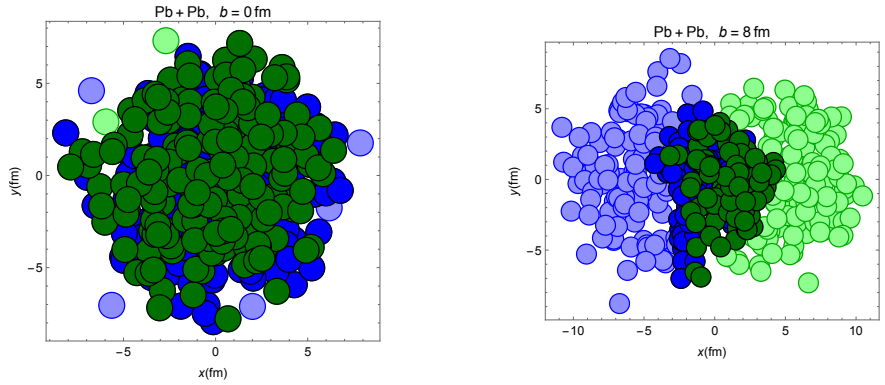

Figure 11: Typical Monte Carlo Event for Pb+Pb collisions at $\sqrt{s_{NN}} = 5023$ GeV with impact parameter of $b = 0$ fm (right) and $b = 8$ fm (left). Darker circles represent participating nucleons, and lighter circles show spectator nucleons.

In this histogram, the probability distribution for the number of participants where in

the head on collision that almost all of the nucleons are going to collide. Therefore, the number of participants will be basically two times in this case 416 for Pb^{208}. However, that is not very probable what is more probable is that roughly 408 of them collided. So even for a fixed impact parameter the number of participants fluctuate and change from event to event and hence even the multiplicity will fluctuate. Whereas if one consider an off central collision, it is between 120 and 200. By averaging over this distribution function, one get the average number of participants $\langle N_{part} \rangle$.

Centrality Class		Impact parameter		$\langle b \rangle$	N_{part}
c_{min}	c_{max}	b_{min}	b_{max}		
0	0	0	0	0	406.923
0	0.05	1.499×10^{-8}	3.48489	2.32326	376.44
0.05	0.1	3.48489	4.92838	4.24791	317.635
0.1	0.2	4.92838	6.96978	6.00746	245.143
0.2	0.3	6.96978	8.5362	7.77937	169.72
0.3	0.4	8.5362	9.85676	9.21228	113.231
0.4	0.5	9.85676	11.0202	10.4493	71.3126
0.5	0.6	11.0202	12.072	11.5541	41.3331
0.6	0.7	12.072	13.0393	12.5619	21.4075
0.7	0.8	13.0393	13.94	13.4945	9.69161
0.8	0.9	13.94	14.8437	14.3815	3.8046
0.9	1	14.8437	20.	15.6555	0.967611

Table 1: The relation between centrality class and impact parameter ,the average impact parameter, and N_{part} corresponding to each class.

In Table 1 in Pb-Pb collisions at $\sqrt{s_{NN}} = 5023$ GeV, we list the minimum centrality (c_{min}), and the maximum centrality (c_{max}) for each centrality class. We also show the corresponding minimum and maximum impact parameter in that class (b_{min}, b_{max}). In simulations, usually one takes the average impact parameter $\langle b \rangle$ corresponding to each class. In order to compare the result of the distribution between the optical limit and Monte Carlo simulations, we performed for Pb–Pb collision within the center of mass energy equal to 5023 GeV and $\sigma_{inel}^{NN} = 67$ mb.

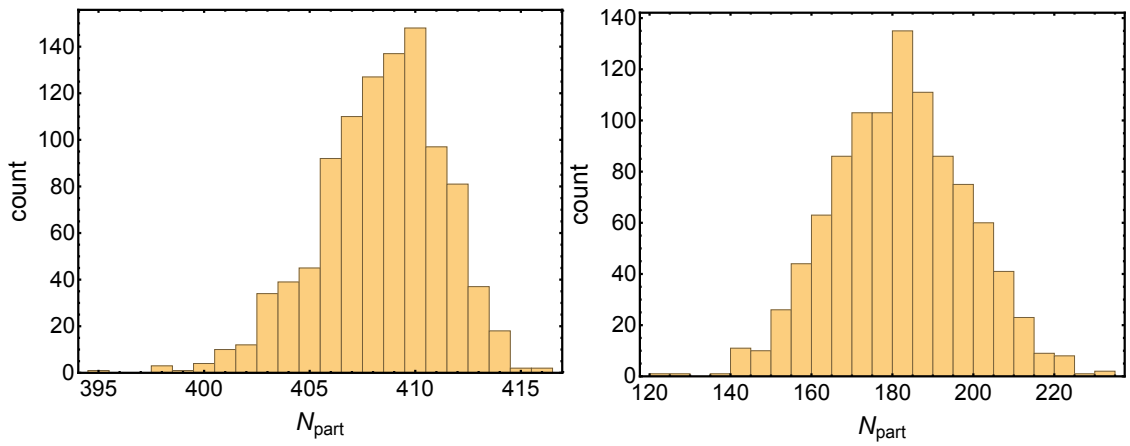

(a) $b = 0$ fm and mean=408.39

(b) $b = 8$ fm and mean=180.98

Figure 12: Probability distribution for the number of participants nucleons with number of sample = 1000 for Pb-Pb collisions at $\sqrt{s_{NN}} = 5023$ GeV and impact parameter $b = 0$ fm (right) and $b = 8$ fm (left).

3.5 Conclusion

In summary, although the Glauber model is somewhat straightforward, it is able to explain a wide range of effects observed in high-energy heavy-ion collisions by strictly considering geometric factors. The Glauber model provides a numerical account of the geometrical arrangement of the nuclei during a collision. It models the collision between two atomic nuclei as a sequence of individual collisions between the nucleons that make up each nucleus. Both the nuclear density profile and the inelastic nucleon-nucleon cross-section are provided as inputs to the model, allowing for a direct comparison of the geometric findings to actual experimental data. We assume that the static cross-section is independent of nuclear environment and is the same as for nucleon-nucleon collision. There is only this one non-trivial reliance of the model on the beam energy. By using the impact parameter and center-of-mass energy from the Glauber model, we can calculate the total number of nucleons involved and the total number of binary collisions. Both an optical and a Monte Carlo version of the Glauber model are available. The optical Glauber model treats the nucleus like a uniform distribution of matter, while the Monte Carlo variant randomly inserts nucleons into the

nucleus in accordance with the density profile of the nucleus. The number of binary collisions and involved nucleons is derived analytically for the Optical Glauber model and tallied for the Monte Carlo version. We define centrality classes and then map the Glauber model to them in order to better grasp its relevance with respect to the generation of charged particles. The reaction volume immediately following a non-central collision has an elliptical profile. The short side of the ellipse has a higher pressure gradient than the long side. Particles that are created as a result of this initial spatial anisotropy will have momentum anisotropy, which is defined by eccentricity. We discover that the experimentally observed value of the momentum anisotropy, v_2, increases with increasing eccentricity. Anisotropy in momentum space is established as a result of the anisotropy of the collision geometry, and eccentricity may be calculated using this straightforward geometric model. Overall, although the Glauber model is somewhat straightforward, it is able to explain a wide range of effects observed in high energy heavy ion collisions by strictly considering geometric factors.

3.6 Bjorken model

In this model, it is assumed that the collision axis is the longitudinal z-axis, and the nuclei are assumed to be homogeneous and have an infinite transverse extent. This indicates that the properties of colliding nuclei are independent of the orthogonal coordinates x and y. It is considered that collision-produced matter is invariant with respect to z-axis boosts. Boosts in this context refer to Lorentz transformations that account for relative z-axis motion. In heavy ion collisions with high energy, the two nuclei pass through each other and the partons are barely stopped. This assumption is the basis for much of the interpretation of high-energy events, and a vast quantity of evidence supports it. For a period of time that is short in comparison to the nucleus' transverse dimension, the transverse expansion can be disregarded. Because the nuclear constituents pass through one another, the longitudinal momentum is significantly greater than the transverse momentum. The space-time coordinates and the typical z momentum have a strong identity due to this scale gap. For example a particle with typical momentum p_z and energy E one can relate its position in space-time to its longitudinal momentum and find the velocity of matter along the z-axis as follows

$$v^z = \frac{p_z}{E} \simeq \frac{z}{t}\,, \tag{3.22}$$

where v^z represents the velocity of the particle in the z direction, p_z is its longitudinal momentum, z is the spatial coordinate in the z direction, and t is time. To analyze this kinematics effectively, one should deal with proper time τ and space-time rapidity[3] η_s that define as

$$\tau \equiv \sqrt{t^2 - z^2}, \qquad \eta_s \equiv \frac{1}{2}\log\left(\frac{t+z}{t-z}\right)\,.$$

Particles with rapidity y are predominately located at space-time rapidity under specific

[3]Here η_s denotes the space time rapidity, $\eta_{\rm pseudo}$ denotes the pseudo-rapidity, and η denotes the shear viscosity.

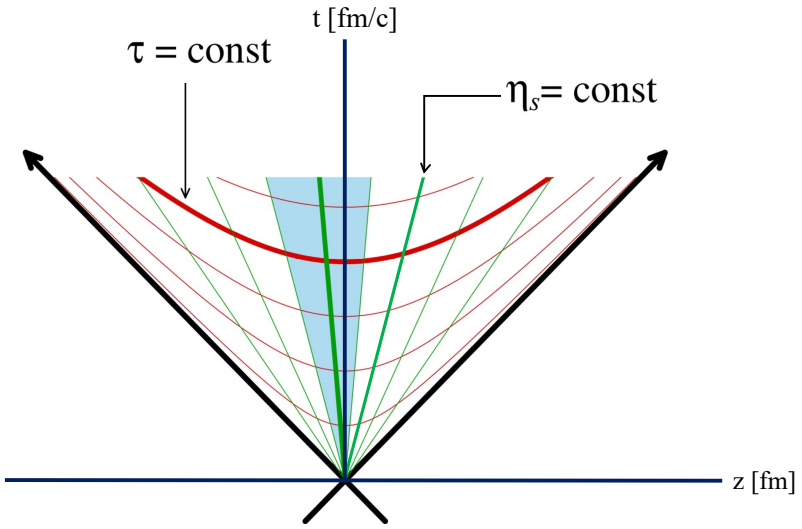

Figure 13: The green solid line represent the constant of rapidity η_s and the red solid curves indicate the constant of the proper time τ.

conditions specifically at the proper time τ (see fig. 13). Mathematically, to relate how fast a particle is moving y to where it is located in space and time η_s one can use this equation

$$y \equiv \frac{1}{2} \log \frac{p_z + E}{E - p_z} \simeq \frac{1}{2} \log \frac{t + z}{t - z} \equiv \eta_s \,. \tag{3.23}$$

In addition, Bjorken's simplifying assumption is that the energy density is uniform in space-time rapidity at a specific proper time. This assumption facilitates the analysis of particle behavior in high-energy nuclear collisions by implying that the relationship between space-time rapidity and positions remains constant as matter evolves over time, i.e.

$$\epsilon(\tau_0, \eta_s) \simeq \epsilon(\tau_0) \,. \tag{3.24}$$

With this simplification, the relationship between the properties of particles and their rapidities remains independent of η_s as the fluid evolves over time. This makes it much easier to study the behavior of particles at various rapidities without reanalyzing everything for

each value of rapidity. Therefore, this model has

$$\epsilon(t,x) = \epsilon(\tau), \qquad u^\mu(t,x) = (u^0, u^x, u^y, u^z) = (\cosh(\eta_s), 0, 0, \sinh(\eta_s)). \tag{3.25}$$

In addition to u^μ we introduce three additional four-vectors (x^μ, y^μ and z^μ) defined by the equations

$$x^\mu = (0,1,0,0), \tag{3.26}$$

$$y^\mu = (0,0,1,0), \tag{3.27}$$

$$z^\mu = (z/\tau, 0, 0, t/\tau) = (\sinh(\eta_s), 0, 0, \cosh(\eta_s)). \tag{3.28}$$

The four-vectors x^μ, y^μ and z^μ are space-like and orthogonal to u^μ

$$x \cdot x = y \cdot y = z \cdot z = -1, \tag{3.29}$$

$$x \cdot u = y \cdot u = z \cdot u = 0, \tag{3.30}$$

$$x \cdot y = y \cdot z = z \cdot x = 0. \tag{3.31}$$

We note that at each spacetime point x the four-vectors u^μ, x^μ, y^μ, and z^μ form a vector basis.

Although the matter is described in a four-dimensional Minkowski spacetime, to conveniently describe this system, the coordinates are modified from the four-dimensional Minkowski spacetime to Milne coordinates. This choice of a mathematical coordinate system makes the matter appears as if it is not moving at all (static), but the space-time itself is expanding in one particular direction (longitudinally along the z-axis). Moreover, this transformation is non-linear. It has a new metric described by $g_{\mu\nu}$ that describes how spacetime is structured in Milne coordinates. Specifically, it indicates that time (the τ component) is treated

differently from space (the spatial components), and the space-time is expanding but flat [4]. Therefore, instead of t and z, the analysis employs proper time (τ) and space-time rapidity (η_s) one obtains

$$x^\mu = (\tau, x_\perp, \eta_s), \qquad g_{\mu\nu} = \mathrm{diag}(1, -1, -1, -\tau^2), \qquad (u^\tau, u^x, u^y, u^{\eta_s}) = (1, 0, 0, 0)\,. \quad (3.32)$$

Substituting the boost invariant ansatz Eq. (3.25) into the conservation laws yields the following equation that describes the evolution of energy density in the ideal hydrodynamic limit

$$\partial_\tau \epsilon = -\frac{\epsilon + P}{\tau}\,, \tag{3.33}$$

and one can find the solution for energy density by using an equation of state that relates the pressure (P) to the energy density (ϵ). For a relativistic gas in three spatial dimensions, $P = c_s^2 \epsilon$, where c_s^2 represents the squared speed of sound, one finds

$$\frac{\epsilon(\tau)}{\epsilon(\tau_0)} = \left(\frac{\tau_0}{\tau}\right)^{1+c_s^2}\,, \tag{3.34}$$

where this equation has solution in the equilibrium case for massless ideal of gas equation of state with $c_s^2 = \frac{1}{3} (\epsilon = 3P \propto T^4)$

$$T(\tau) = T(\tau_0) \left(\frac{\tau_0}{\tau}\right)^{\frac{1}{3}}\,, \tag{3.35}$$

where τ_0 is an integration constant.

[4] In special relativity, spacetime is considered "flat" when it follows the rules of Euclidean geometry, where straight lines remain straight, and the shortest distance between two points is a straight line. In contrast, in general relativity, spacetime is curved by the presence of mass and energy. This curvature leads to the bending of paths that objects follow, which we perceive as gravity.

Chapter 4

An improved anisotropic hydrodynamics ansatz

4.1 Introduction

In the very early universe (a few microseconds after the Big Bang), the quark-gluon plasma (QGP) is believed to have existed where the energy density can reach values over ten times higher than those of ordinary nuclei. It was speculated theoretically that one can reach these extreme conditions by colliding two heavy nuclei with ultrarelativistic energies. In this collision, the temperatures can be over a million times hotter than the core of the sun, and a fraction of the kinetic energies of the two colliding nuclei is transformed to heating the QCD vacuum within an extremely small volume. Because of the appearance of modern accelerator facilities, ultrarelativistic heavy-ion collisions (URHICs) are able to provide an opportunity to systematically create and study different phases of the bulk nuclear matter. In heavy-ion collision experiments at Relativistic Heavy-Ion Collider (RHIC) located at Brookhaven National Laboratory, USA, and Large Hadron Collider (LHC) at European Organization for Nuclear Research (CERN), Geneva, the new state of matter (the QGP) is widely believed created. Results obtained at RHIC energies and recently at LHC energies strongly suggested the formation of a quark-gluon plasma (QGP) which may be close to (local) thermodynamic equilibrium, albeit in a tiny volume ($\sim 100 - 1000$ fm^3). After the QGP is generated, it is expected to expand, cool, and then hadronize in the final stage of its evolution, with a QGP lifetime on the order of 10 fm/c in central collisions [140–142].

Heavy-ion collisions such as those at RHIC and LHC provide a primary tool to study the thermodynamic and transport properties of the QGP. Of remarkable importance is knowledge of time evolution of the rapidly expanding QGP that is produced in these URHICs.

For this purpose, one can use a basic theoretical approach called relativistic hydrodynamics to describe the QGP. The reader can see chapter (2) for more details. The resulting models describe the collective behavior of the soft hadrons with $p_T \lesssim 2$ GeV quite well. In early studies, it was found that the QGP created at RHIC energies was well described by models which assume ideal hydrodynamic behavior from very early times $\tau \lesssim 1$ fm/c [64, 65, 143]. Strictly speaking, one can apply ideal hydrodynamics if the system is in perfect isotropic local thermal equilibrium. Based on these early studies, it was expected that the QGP would isotropize on a timescale $\tau \sim 0.5$ fm/c. In practice, however, when one includes viscous corrections to the hydrodynamical models [66–80, 82–96, 144] one observes that at times $\tau \lesssim 2$ fm/c there can still be sizable differences between the transverse pressure, $\mathcal{P}_T$, and longitudinal pressure, $\mathcal{P}_L$ which is associated with the existence of a non-equilibrium hydrodynamic attractor [145–182]. In addition, as one moves closer to the transverse/longitudinal edges of the QGP, the size of the pressure anisotropies increases at all times [6, 183, 184]. Faced with this, researchers suggested to find another method to formulate hydrodynamics in a momentum-space anisotropic QGP. Recently, there have been theoretical and phenomenological studies that try to better account for large deviations from isotropy by relaxing the assumption that the QGP is close to local isotropic thermal equilibrium. To address this issue, they introduced a framework called anisotropic hydrodynamics (aHydro) in order to describe the non-equilibrium dynamics of relativistic systems, without breaking important physics constraints such as the positivity of the one-particle distribution function [97, 98, 109, 185–187].

In a prior paper [165], comparisons between three hydrodynamic models and exact solutions of the RTA Boltzmann equation [188–190] were presented. It was found that linearized viscous hydrodynamics performed more poorly than the canonical formulation of aHydro in reproducing the exact attractor for all moments. However, although the canonical aHydro formulation [97, 98] did a reasonable job in describing moments with $l > 0$, Ref. [165] found

that it did not provide a good approximation for moments with $l = 0$. The failure of the canonical formulation was postulated to be due to the fact that the exact solutions to the RTA Boltzmann equation have an explicit two-component nature and cannot be accurately described by a single ellipsoidal form. As a result, it would be interesting to implement aHydro with a two-component ansatz for the distribution function to see if a better description of moments with $l = 0$ can be achieved. Additionally, it would be interesting to see if this also results in a quantitative improvement for higher-order moments.

In this chapter, we report on our progress in obtaining improved dynamical equations for anisotropic hydrodynamics through the use of an improved ansatz for the form of the underlying aHydro distribution function which explicitly includes a free streaming contribution. We demonstrate that with this improvement one can better reproduce exact results available in the literature for the evolution of moments of the distribution function, in particular, for moments which contain no powers of the longitudinal momentum in their definition ($l = 0$ moments). Using the resulting dynamical equations, we extract the non-equilibrium attractor associated with our improved aHydro ansatz and demonstrate that the improvement also allows one to better reproduce the exact dynamical attractor obtained using kinetic theory in the relaxation time approximation, particularly at early rescaled times and for $l = 0$ moments. We will focus our attention in this first work on a conformal system undergoing boost-invariant and transversally homogeneous Bjorken expansion, however, the method introduced herein is easily extended to full 3+1d.

The chapter is organized as follows. In Sec. (4.2) we present the basic setup and assumptions used for the system and introduce the original aHydro distribution function and our improved aHydro distribution function ansatz. We then use the first and second moments of the Boltzmann equation to obtain equations of motion for the dynamical parameters appearing in both versions. We do this explicitly for a system undergoing boost-invariant 0+1d

Bjorken expansion. Using the resulting dynamical equations we obtain the time evolution of all moments of these distribution functions. In Sec. (4.3), we present our numerical results and discuss. In Sec. (4.4) we present our conclusions and an outlook for the future.

4.2 Setup

For the original and modified anisotropic hydrodynamics work, we assume a system of massless particles that is undergoing boost invariant longitudinal expansion ($v_z = z/t$) and expands only along the beam-line axis. We ignore the effects of transverse dynamics. Accordingly, one can assume a homogeneous distribution in the transverse directions and set $v_{x,y} = 0$. By taking these assumptions into account, only proper-time derivatives remain, and the dynamics reduces to 0+1d dimensional evolution [124].

4.2.1 The distribution function

$$f_{\rm RS}(x,p) = f_{\rm eq}\left(\frac{\sqrt{\mathbf{p}^2 + \xi(x)p_z^2}}{\Lambda(x)}, \frac{\mu(x)}{\Lambda(x)}\right) \qquad \textbf{(Old aHydro)} \tag{4.1}$$

$$f(\mathbf{p},\tau) = f_0(\xi_{\rm FS},\Lambda_0)D(\tau,\tau_0) + f_{\rm RS}(\xi,\Lambda)[1 - D(\tau,\tau_0)] \qquad \textbf{(New aHydro)} \tag{4.2}$$

The old anisotropic hydrodynamics approach (old aHydro) allows for an intrinsic momentum-space anisotropy, which is characterized by a single parameter ξ. It is used to model the distribution of particles in the system in the local rest frame (LRF) as shown in Eq. (4.1). This distribution function is characterized by two parameters, the local anisotropy parameter ξ, and the local scale parameter Λ, which is related to the temperature of the system. Whereas it reduces to the temperature in the isotropic limit when $\xi(x) \to 0$. The symbol $\mu(x)$ indicates the local chemical potential. In what follows, we will additionally assume zero chemical potential, $\mu = 0$.

In the new anisotropic hydrodynamics approach (new aHydro), the particles are described by an improved distribution function that takes into account both the free-streaming and equilibrating contributions. The free-streaming term accounts for the motion of particles without any interactions or collisions between them since the interactions between particles will modify the initial conditions. Therefore, it represents the initial conditions of the system and contributes to the distribution function. This term is important for understanding how the system evolves over time, as it provides information about the behavior of particles before interactions occur. In contrast, the other term characterizes the particle interactions that lead to the establishment of thermal equilibrium. This term represents the effects of collisions and interactions that modify the free-streaming term's initial conditions. By incorporating the equilibrating term, the distribution function incorporates system changes caused by interactions and provides a more precise description of particle dynamics. This formulation permits a complete description of the system, taking into consideration both the initial free-streaming and the subsequent evolution caused by particle interactions. In this ansatz, f_0 is the initial particle distribution with $\xi_{\rm FS}$ obtains from $\partial_\tau \xi = \frac{2}{\tau}(1+\xi)$ with the initial condtion $\tau = \tau_0 \to \xi = \xi_0$

$$\xi_{\rm FS} = (1+\xi_0)\frac{\tau^2}{\tau_0^2} - 1\,, \tag{4.3}$$

where $\xi_{\rm FS}$ is the momentum-space anisotropy in the free-streaming term, and ξ_0 is the initial momentum-space anisotropy, τ_0 is the initial proper time, and Λ_0 is the initial momentum scale. The new aHydro approach is more accurate than the old aHydro approach, especially at early times when the system is far from equilibrium. In the new aHydro, taking the limit $D \to 0$ will reduces this ansatz to the original ansatz "old aHydro" used in aHydro [97, 98]. In the results section, we will compare to this limit and refer to it as "old aHydro" and refer to the new ansatz Eq. (4.2) as "new aHydro". We note that the form of the new ansatz is

similar in spirit to an approach advocated recently by McNelis and Heinz, with the second term being related to way they termed the hydrodynamic generator [191].

In both forms, the $f_{\rm RS}$ indicates the anisotropic Romatschke-Strickland form [192, 193]

$$f_{\rm RS}(\xi,\Lambda) = f_{\rm eq}\left(\frac{\sqrt{\mathbf{p}^2+\xi p_z^2}}{\Lambda}\right). \tag{4.4}$$

The thermal equilibrium distribution function has functional form

$$f_{\rm eq} = \left[\exp\left(\frac{p^\mu u_\mu(x)-\mu(x)}{T}\right)+a\right]^{-1} \tag{4.5}$$

with $a = 0, 1$, and -1 corresponding to Maxwell-Boltzmann, Fermi-Dirac, and Bose-Einstein statistics, respectively. Here we will assume that $f_{\rm eq}$ is given by a Boltzmann distribution. Note that, the free-streaming distribution function f_0 is also of RS form but with $\xi = \xi_{\rm FS}$ and $\Lambda = \Lambda_0$, i.e.

$$f_0(\xi_{\rm FS},\Lambda_0) = f_{\rm RS}(\xi_{\rm FS},\Lambda_0)\,. \tag{4.6}$$

Here we use the label '0' to emphasize that this contribution is constrained by the initial condition for the distribution function. Additionally, $-1 < \xi < \infty$ is a parameter that indicates the strength and type of momentum-space anisotropy. By stretching ($-1 < \xi < 0$) or squeezing ($\xi > 0$) the underlying isotropic distribution function $f_{\rm eq}$ along one direction in momentum-space, one can obtain an anisotropic distribution function.

4.2.2 The damping function

In Eq. (4.2) we have also introduced the damping function $D(\tau,\tau_0)$

$$D(\tau,\tau_0) = \exp\left[-\int_{\tau_0}^{\tau}\frac{d\tau''}{\tau_{\rm eq}(\tau'')}\right], \tag{4.7}$$

that quantifies the balance between the initial conditions (free-streaming term) and the interactions that lead to thermal equilibrium (equilibrating term) as a function of proper time τ. It allows the distribution function f to smoothly transition from its initial state to an equilibrium state over time, making the new aHydro formulation more suitable for capturing the time evolution of the system from its non-equilibrium state to a state of thermal equilibrium. For finite $\tau_{\rm eq}$, the damping function $D(\tau, \tau_0)$ satisfies $\lim_{\tau\to\tau_0} D(\tau, \tau_0) = 1$. This suggests that at early times, the distribution function f is dominated by the free-streaming term f_0, which represents the initial conditions of the system prior to the occurrence of significant interactions and the distribution function Eq. (4.2) reduces to the initial distribution function f_0. This indicates that the distribution function initially stores information regarding the initial momentum-space anisotropy. In contrast, as τ approaches infinity ($\lim_{\tau\to\infty} D(\tau, \tau_0) = 0$), the dynamical Romatschke-Strickland (RS) term dominates the distribution function f. This is because the system experiences significant interactions and approaches thermal equilibrium at late times. The equilibrating term dominates the distribution function because it represents the effects of collisions and interactions that modify the initial free-streaming conditions, resulting in an approach to thermal equilibrium. We note for future use that the damping function satisfies

$$\frac{\partial D(\tau, \tau_0)}{\partial \tau} = -\frac{D(\tau, \tau_0)}{\tau_{\rm eq}(\tau)}\,. \tag{4.8}$$

4.2.3 General moments of the distribution functions

In general, one can compute a large set of moments of the one-particle distribution function by using the form

$$\mathcal{M}^{nl}[f] = \int dP\,(p\cdot u)^n (p\cdot z)^{2l} f(\mathbf{p})\,, \tag{4.9}$$

with the Lorentz-invariant integration measure as we calculate in Eq. (2.37)

$$\int dP = \int \frac{d^3\mathbf{p}}{(2\pi)^3}\frac{1}{E}\,. \tag{4.10}$$

where p^μ is the particle four-momentum, u^μ is the time-like fluid four-velocity and z^μ is a space-like vector orthogonal to u^μ. In the LRF of the system, one has $u^\mu_{\rm LRF} = (1,0,0,0)$ and $z^\mu_{\rm LRF} = (0,0,0,1)$.

General moments of the old distribution function form

Using the old form, the necessary moments of the distribution function can be calculated analytically. Moreover, the moment in the LRF can be decomposed into a function that depends only on ξ and another function that depends only on the scale Λ as follow,

$$\begin{aligned}
\mathcal{M}^{nl}_{\rm old}[f] &= \int dP\,(p\cdot u)^n (p\cdot z)^{2l} f_{\rm eq}\left(\frac{\sqrt{\mathbf{p}^2+\xi p_z^2}}{\Lambda}\right), \\
&= \int \frac{d^3p}{(2\pi)^3}\,(p_T^2+p_z^2)^{\frac{n-1}{2}} p_z^{2l} f_{\rm eq}\left(\frac{\sqrt{p_T^2+(1+\xi)\,p_z^2}}{\Lambda}\right) \\
&= \frac{\Lambda^{n+2l+2}}{(2\pi)^3(1+\xi)^{l+\frac{1}{2}}}\int d^3\hat{p}\,\left(\hat{p}_T^2+\frac{1}{1+\xi}\,\hat{p}_z^2\right)^{\frac{n-1}{2}}\,\hat{p}_z^{2l}\;f_{\rm eq}(|\mathbf{p}|) \\
&= \frac{\Lambda^{n+2l+2}}{(2\pi)^2}\underbrace{\int_0^\infty dp\;p^{2l+n+1} f_{\rm eq}(|\mathbf{p}|)}_{\Gamma(2l+n+2)}\;\underbrace{\alpha^{2l+1}\int_0^\pi \sin\theta\,\cos^{2l}\theta\,(\alpha^2\cos^2\theta+\sin^2\theta)^{\frac{n-1}{2}}d\theta}_{\mathcal{H}_{nl}(\alpha)}\,.
\end{aligned} \tag{4.11}$$

Here, in the second line in order to evaluate the integral, we use $p\cdot u = E$, $p\cdot z = -p_z$, $E=\sqrt{p_T^2+p_z^2}$, and using the old aHydro distribution function Eq. (4.1). In third line, we have made a change of variables to $\hat{p}_T \equiv p_T/\Lambda$, and $\hat{p}_z \equiv \sqrt{1+\xi}\,p_z/\Lambda$. In the fourth line, we transform the variable to spherical coordinates by using: $\hat{p}_x = p\sin\theta\cos\phi$, $\hat{p}_y = p\sin\theta\sin\phi$, $\hat{p}_z = p\cos\theta$, and $\alpha = \frac{1}{\sqrt{1+\xi}}$. Now, working in $\mathcal{H}_{nl}\left(\alpha=\frac{1}{\sqrt{1+\xi}}\right)$ by using the identity $\sin^2\theta =$

$1-\cos^2\theta$, changing the variable to $u=\cos\theta$ with $du=\sin\theta d\theta$ and using the symmetry of the integral $2\int_0^1 du\,u$ one obtains the final expression for the integral in terms of a function of u. In practice, one finds

$$\begin{aligned}\mathcal{H}_{nl}\left(\alpha=\frac{1}{\sqrt{1+\xi}}\right) &= \alpha^{2l+1}\int_0^{\pi}\sin\theta\,\cos^{2l}\theta\,(\alpha^2\cos^2\theta+\sin^2\theta)^{\frac{n-1}{2}}d\theta \\ &= 2\,\alpha^{2l+1}\int_0^1 u^{2l}\left[1+(\alpha^2-1)u^2\right]^{\frac{n-1}{2}}\,du \\ &= \frac{2\,\alpha^{2l+1}}{2l+1}\,{}_2F_1\left(l+\frac{1}{2},\frac{1-n}{2};\frac{3}{2}+l;1-\alpha^2\right) \end{aligned} \tag{4.12}$$

where ${}_2F_1$ is a hypergeometric function, so the final result for the general moment for the old ansatz is

$$\begin{aligned}\mathcal{M}^{nl}_{\rm old}(\tau) &= \frac{\Lambda^{2l+n+2}\,\Gamma(2l+n+2)}{(2\pi)^2}\,\mathcal{H}_{nl}\left(\frac{1}{\sqrt{1+\xi}}\right) \\ &= \frac{2\Lambda^{2l+n+2}\,\Gamma(2l+n+2)}{(2\pi)^2\,(2l+1)\,(\sqrt{1+\xi})^{2l+1}}\,{}_2F_1\left(l+\frac{1}{2},\frac{1-n}{2};\frac{3}{2}+l;\frac{\xi}{1+\xi}\right)\end{aligned} \tag{4.13}$$

For the case $n=2$ and $l=0$ the function $\mathcal{H}_{20}$ appearing in Eq. (4.13) may be expressed in terms of the function $\mathcal{R}_{20}$ defined in Refs. [97, 100, 103], namely

$$\mathcal{H}_{20}\,(\alpha) \;=\; 2\,\mathcal{R}_{20}\left(\frac{1}{\alpha^2}-1\right), \tag{4.14}$$

where $\mathcal{R}_{20}(\xi)=\frac{1}{2}\left[(1+\xi)^{-1}+\arctan\left(\sqrt{\xi}\right)/\sqrt{\xi}\right]$. We provide additional information regarding the $\mathcal{H}$ and $\mathcal{R}$ functions in the appendix (D).

Bulk variables for the old form

Here, in this case the bulk variables, i.e the number density, the energy density, and the components of the pressure, are:

$$\mathit{n} = \mathcal{M}^{10}_{\rm old} = \int dP\,(p\cdot u) f(\mathbf{p}) = \frac{1}{\sqrt{1+\xi}} n_{\rm eq}(\Lambda) = \frac{1}{\pi^2\sqrt{1+\xi}}\Lambda^3 \tag{4.15}$$

$$\epsilon = \mathcal{M}^{20}_{\rm old} = \int dP\,(p\cdot u)^2 f(\mathbf{p}) = \mathcal{R}_\epsilon(\xi)\epsilon_{\rm eq}(\Lambda) = \frac{3}{\pi^2}\,\Lambda^4\,\mathcal{R}_\epsilon(\xi) \tag{4.16}$$

$$P_L = \mathcal{M}^{01}_{\rm old} = \int dP\,(p\cdot z)^2 f(\mathbf{p}) = \mathcal{R}_L(\xi) P_{\rm eq}(\Lambda) = \frac{1}{\pi^2}\,\Lambda^4\,\mathcal{R}_L(\xi) \tag{4.17}$$

$$P_T = \mathcal{R}_T(\xi) P_{\rm eq}(\Lambda) = \frac{1}{\pi^2}\,\Lambda^4\,\mathcal{R}_T(\xi) \tag{4.18}$$

with

$$\begin{aligned}
\mathcal{R}_\epsilon(\xi) &= \frac{1}{2}\left[\frac{1}{1+\xi} + \frac{\arctan\sqrt{\xi}}{\sqrt{\xi}}\right], \\
\mathcal{R}_T(\xi) &= \frac{3}{2\xi}\left[\frac{1+(\xi^2-1)\mathcal{R}_\epsilon(\xi)}{\xi+1}\right], \\
\mathcal{R}_L(\xi) &= \frac{3}{\xi}\left[\frac{(\xi+1)\mathcal{R}_\epsilon(\xi)-1}{\xi+1}\right],
\end{aligned} \tag{4.19}$$

which satisfy $3\mathcal{R}_\epsilon = 2\mathcal{R}_T + \mathcal{R}_L$ due to the conformality of the system. Note that certain moments map to familiar hydrodynamics variables, e.g. taking $n = 1$ and $l = 0$, one obtains the number density n, taking $n = 2$ and $l = 0$, one can evaluate the energy density ϵ, and taking $n = 0$ and $l = 1$, one obtains the longitudinal pressure P_L. Moreover, for a conformal system, one can use $\epsilon = 2P_T + P_L$ to determine the transverse pressure and by using the mass shell condition one obtains $p_T^{2l} = [(p\cdot u)^2 - (p\cdot z)^2]^l$.

General moments of the new distribution function form

Using the new form, one finds that all moments of the distribution function can be decomposed into two terms by following the same steps as in old aHydro:

- **First term (Free streaming term) in Eq.** (4.2)**:**

$$\begin{aligned}
\mathcal{M}_0^{nl} &= \int dP\,(p.u)^n (p.z)^{2l}\, f_0 \\
&= \int \frac{d^3p}{(2\pi)^3 E}\, E^n\, p_z^{2l}\, f_{\rm eq}\left(\frac{\sqrt{p_T^2+(1+\xi_{\rm FS})p_z^2}}{\Lambda_0}\right) \\
&= \frac{1}{(2\pi)^3}\int d^3p\,(p_T^2+p_z^2)^{\frac{n-1}{2}}\, p_z^{2l}\, f_{\rm eq}\left(\sqrt{\underbrace{\frac{p_T^2}{\Lambda_0^2}}_{\hat{p}_T}+\underbrace{\frac{p_z^2}{\alpha_0^2\Lambda_0^2}}_{\hat{p}_z}}\right), \quad \text{with } \alpha_0=\frac{1}{\sqrt{1+\xi_{\rm FS}}} \\
&= \frac{\Lambda_0^{2l+n+2}}{(2\pi)^2}\underbrace{\int_0^\infty d\hat{p}\;\hat{p}^{2l+n+1}\, f_{\rm eq}(\hat{p})}_{=\Gamma(2l+n+2)}\;\underbrace{\alpha_0^{2l+1}\int_0^\pi d\theta\sin\theta\,\cos^{2l}\theta\left(\alpha_0^2\cos^2\theta+\sin^2\theta\right)^{\frac{n-1}{2}}}_{\mathcal{H}_{nl}(\alpha_0)}
\end{aligned}$$

so the final result is

$$\begin{aligned}
\mathcal{M}_0^{nl} &= \frac{\Lambda_0^{2l+n+2}}{(2\pi)^2}\,\Gamma(2l+n+2)\,\mathcal{H}_{nl}(\alpha_0) \\
&= \frac{2\Lambda_0^{2l+n+2}}{(2\pi)^2(2l+1)}\,\Gamma(2l+n+2)\,\alpha_0^{2l+1}\,{}_2F_1\left(l+\frac{1}{2},\frac{1-n}{2};\frac{3}{2}+l;1-\alpha_0^2\right). \quad (4.20)
\end{aligned}$$

- **Second term (Evolution term)in Eq.** (4.2)**:**

We can obtain the result from the free streaming result, by noting that f_0 becomes $f_{\rm RS}$ under the subsutituions:

$$\begin{aligned}
\mathcal{M}_0^{nl} &\to \mathcal{M}_{\rm RS}^{nl} \\
\Lambda_0 &\to \Lambda \\
\xi_{\rm FS} &\to \xi \\
\alpha_0=\frac{1}{\sqrt{1+\xi_{\rm FS}}} &\to \alpha=\frac{1}{\sqrt{1+\xi}}
\end{aligned}$$

therefore, the general moment for this term will be

$$\begin{aligned}\mathcal{M}^{nl}_{\rm RS} &= \frac{\Lambda^{2l+n+2}}{(2\pi)^2}\,\Gamma(2l+n+2)\,\mathcal{H}_{nl}(\alpha)\\ &= \frac{2\Lambda^{2l+n+2}}{(2\pi)^2(2l+1)}\,\Gamma(2l+n+2)\,\alpha^{2l+1}\,{}_2F_1\left(l+\frac{1}{2},\frac{1-n}{2};\frac{3}{2}+l;1-\alpha^2\right). \quad (4.21)\end{aligned}$$

- **Putting the pieces of Eqs.** (4.20) **and** (4.21) **together:**

  By taking a general moment of Eq. (4.2), one finds

$$\mathcal{M}^{nl}_{\rm new}(\tau) = \mathcal{M}^{nl}_0[f_0(\xi_{\rm FS},\Lambda_0)]D(\tau,\tau_0) + \mathcal{M}^{nl}_{\rm RS}[f_{\rm RS}(\xi,\Lambda)][1-D(\tau,\tau_0)]. \quad (4.22)$$

  Using the result obtained above Eqs. (4.20) and (4.21), one can write the general moment for the new anstaz as

$$\mathcal{M}^{nl}_{\rm new}(\tau) = \frac{\Gamma(2l+n+2)}{(2\pi)^2}\,\left\{\Lambda_0^{2l+n+2}\,\mathcal{H}_{nl}(\alpha_0)D(\tau,\tau_0) + \Lambda^{2l+n+2}\,\mathcal{H}_{nl}(\alpha)[1-D(\tau,\tau_0)]\right\} \quad (4.23)$$

Bulk variables for the new form

Here, one finds that all moments of the distribution function can be decomposed into two terms, and the bulk variables; e.g. the number density

$$\begin{aligned}n = \mathcal{M}^{10}_{\rm new} &= \int dP\,(p\cdot u) f(\mathbf{p}) = \mathcal{M}^{10}[f_0]D(\tau,\tau_0) + \mathcal{M}^{10}[f_{\rm RS}][1-D(\tau,\tau_0)]\\ &= \frac{1}{\pi^2}\,\left[\alpha_0\,\Lambda_0^3\,D(\tau,\tau_0) + \alpha\,\Lambda^3\,[1-D(\tau,\tau_0)]\right], \quad (4.24)\end{aligned}$$

the energy density

$$\epsilon = \mathcal{M}^{20}_{\rm new} = \int dP\,(p\cdot u)^2 f(\mathbf{p}) = \mathcal{M}^{20}[f_0]D(\tau,\tau_0) + \mathcal{M}^{20}[f_{\rm RS}][1-D(\tau,\tau_0)]$$
$$= \frac{3}{2\pi^2}\left[\Lambda_0^4\,\mathcal{H}_\epsilon(\alpha_0)D(\tau,\tau_0) + \Lambda^4\,\mathcal{H}_\epsilon(\alpha)[1-D(\tau,\tau_0)]\right], \tag{4.25}$$

the longitudinal pressure

$$P_L = \mathcal{M}^{01}_{\rm new} = \int dP\,(p\cdot z)^2 f(\mathbf{p}) = \mathcal{M}^{01}[f_0]D(\tau,\tau_0) + \mathcal{M}^{01}[f_{\rm RS}][1-D(\tau,\tau_0)]$$
$$= \frac{3}{2\pi^2}\left[\Lambda_0^4\,\mathcal{H}_L((\alpha_0)D(\tau,\tau_0) + \Lambda^4\,\mathcal{H}_L(\alpha)[1-D(\tau,\tau_0)]\right], \tag{4.26}$$

the transverse pressure because the system is conformal, one can use $\epsilon = 2P_T + P_L$

$$P_T = P_{T,0}(\xi_{\rm FS},\Lambda_0)D(\tau,\tau_0) + P_{T,\rm RS}(\xi,\Lambda)[1-D(\tau,\tau_0)]$$
$$= \frac{3}{(2\pi)^2}\left\{\Lambda_0^4\,\left[\mathcal{H}_\epsilon(\alpha_0)-\mathcal{H}_L(\alpha_0)\right]D(\tau,\tau_0) + \Lambda^4\,\left[\mathcal{H}_\epsilon(\alpha)-\mathcal{H}_L(\alpha)\right][1-D(\tau,\tau_0)]\right\} \tag{4.27}$$

where the left hand sides in Eqs. (4.25), (4.26), and (4.27) are the non-equilibrium energy density, longitudinal pressure, and transverse pressure, respectively.

Since both the free-streaming and equilibrating contributions are of RS form, we can compute the moments for both of these contributions using [165]

$$\mathcal{M}^{nl}_{\rm aHydro}(\tau) = \frac{\Lambda^{2l+n+2}\Gamma(2l+n+2)}{(2\pi)^2}\mathcal{H}^{nl}\left(\frac{1}{\sqrt{1+\xi}}\right), \tag{4.28}$$

with

$$\mathcal{H}^{nl}(y) = \frac{2y^{2l+1}}{2l+1}\,{}_2F_1(\frac{1}{2}+l,\frac{1-n}{2};\frac{3}{2}+l;1-y^2)\,. \tag{4.29}$$

where $y = 1/\sqrt{1+\xi}$.

In practice, we will scale these moments by their equilibrium limit $\mathcal{M}^{nl}_{\rm eq}(T(\tau))$, which one

can follow the same steps as $\mathcal{M}^{nl}[f]$ by assuming that the underlying isotropic distribution function is a Boltzmann distribution function, and the moment in this limit is

$$\mathcal{M}^{nl}_{\rm eq}(T(\tau)) = \frac{2T^{2l+n+2}\Gamma(2l+n+2)}{(2\pi)^2(2l+1)}\,. \tag{4.30}$$

and for more details about the steps the reader can see the appendix (E). Using the improved aHydro ansatz Eq. (4.2) one obtains

$$\overline{\mathcal{M}}^{nl}[f] = \frac{\mathcal{M}^{nl}[f_0]D(\tau,\tau_0) + \mathcal{M}^{nl}[f_{\rm RS}][1-D(\tau,\tau_0)]}{\mathcal{M}^{nl}_{\rm eq}(\tau)}\,, \tag{4.31}$$

where we have introduce the scaled moments

$$\overline{\mathcal{M}}^{nl}(\tau) = \frac{\mathcal{M}^{nl}(\tau)}{\mathcal{M}^{nl}_{\rm eq}(\tau)}\,. \tag{4.32}$$

Note that one has $\overline{\mathcal{M}}^{nl}_{\rm aHydro}(\tau)$=1 if the system is in equilibrium.

4.2.4 Moments of Boltzmann equation

Low-order moments of the Boltzmann equation can be used to study the evolution of a system's bulk characteristics. The evolution equations for tensors of various ranks can be obtained by computing the moments of the Boltzmann equation; the first moment provides the evolution equation for the energy-momentum tensor, while the second moment describes the evolution of a rank three tensor.

Our starting point is the Boltzmann equation for massless particles

$$p^\mu \partial_\mu f = C[f]\,, \tag{4.33}$$

where the collisional kernel is taken to be the relaxation-time approximation (RTA) collisional

kernel

$$C[f] = -\frac{p \cdot u}{\tau_{\rm eq}(T)}[f - f_{\rm eq}(T)]\,, \tag{4.34}$$

and u^μ is the four-velocity associated with the local rest frame. The form of the collisional kernel has a simple physical interpretation: when the particles collide and interact with one another, their momenta and energies tend to be redistributed. The actual distribution function tends to approximate the equilibrium distribution function as a result of this redistribution process. Herein we will focus our attention on a system that is transversally homogenous and subject to boost-invariant Bjoken flow (0+1d). The equilibrium time ($\tau_{\rm eq}$) in RTA that determines the rate at which this process of approaching equilibrium takes place must be proportional to the inverse of the local temperature to maintain conformal invariance and is expressed as [194, 195]

$$\tau_{\rm eq}(T) = \frac{5\bar{\eta}}{T}\,, \tag{4.35}$$

where $\bar{\eta} = \eta/s$ is the ratio of shear viscosity η to entropy density s. The $1/T$ factor ensures the system equilibrates faster at higher temperatures and slower at lower temperatures, preserving the physics of the system during expansion and consistent with changes in temperature and system expansion.

First moment

The first moment of the left-hand side of the Boltzmann equation defines the divergence of the energy-momentum tensor that reduces to $\partial_\mu T^{\mu\nu}$; however, in the relaxation time approximation the first moment of the collisional kernel the right hand side results in a constraint that must be satisfied in order to conserve energy and momentum, i.e. $\int dP\, p^\mu C[f] = 0$. This constraint is referred to as the *matching condition* which we will talk about it later and allows one to compute the local effective temperature of the system. In RTA, it results

in the following constraint equation

$$\epsilon_{\rm eq}(T(\tau)) = \epsilon(\xi(\tau), \Lambda(\tau))\,, \tag{4.36}$$

where the equilibrium energy density $\epsilon_{\rm eq}$ only depends on the effective temperature T. As a result of this constraint, computing the first moment gives

$$\partial_\mu T^{\mu\nu} = 0\,. \tag{4.37}$$

Expanding this equation out in terms of the non-vanishing components of the energy-momentum tensor, for a 0+1d system, one obtains an evolution equation that can be written compactly as

$$\partial_\tau \epsilon = -\frac{\epsilon + P_L}{\tau}\,. \tag{4.38}$$

See the appendix (E.1.1) for more details about obtaining the last equation.

The 0+1d equation of motion for old aHydro case

The derivative of the energy density for the old case is given by

$$\partial_\tau \epsilon = \frac{3}{\pi^2}[\ \mathcal{R}'_\epsilon(\xi)\ \dot{\xi}\ \Lambda^4 + 4\ \Lambda^3\ \partial_\tau \Lambda\ \mathcal{R}_\epsilon(\xi)] \tag{4.39}$$

Here, the prime in $\mathcal{R}'_\epsilon$ denote the partial derivative with respect to the argument ξ. Plugging Eqs. (4.16), (4.17), and (4.39) into (4.38) one finds:

$$\frac{\mathcal{R}'_\epsilon(\xi)}{\mathcal{R}_\epsilon(\xi)}\partial_\tau \xi + \frac{4}{\Lambda}\partial_\tau \Lambda = -\frac{1}{\tau} - \frac{\mathcal{R}_L(\xi)}{3\,\tau \mathcal{R}_\epsilon(\xi)}. \tag{4.40}$$

The 0+1d equation of motion for new aHydro case

The derivative of the energy density for the new case is given by

$$\partial_\tau \epsilon = \frac{3}{\pi^2}\left\{\left[4\,\Lambda^3\,\partial_\tau\Lambda\,\mathcal{R}_\epsilon(\xi) + \Lambda^4\,\mathcal{R}'_\epsilon(\xi)\,\dot{\xi}\right]\,[1 - D(\tau,\tau_0)]\right\} + \frac{3}{\pi^2}\left\{\left[\Lambda_0^4\,\mathcal{R}'_\epsilon(\xi_{\rm FS})\,\dot{\xi_{\rm FS}} - \frac{1}{\tau_{\rm eq}}\Lambda_0^4\,\mathcal{R}_\epsilon(\xi_{\rm FS}) + \frac{1}{\tau_{\rm eq}}\Lambda^4\,\mathcal{R}_\epsilon(\xi)\right]\,D(\tau,\tau_0)\right\} \tag{4.41}$$

One can obtain the equation of motion for new aHydro by plugging Eqs. (4.25), (4.26) and (4.41) into (4.38):

$$[1 - D(\tau,\tau_0)]\left[\hat{\Lambda}^4\mathcal{R}'(\xi)\dot{\xi} + 4\hat{\Lambda}^3\mathcal{R}(\xi)\dot{\hat{\Lambda}} + \frac{\mathcal{R}(\xi)\hat{\Lambda}^4}{\tau}\left(1 + \frac{1}{3}\frac{\mathcal{R}_L(\xi)}{\mathcal{R}(\xi)}\right)\right] + D(\tau,\tau_0)\left[\mathcal{R}'(\xi_{\rm FS})\dot{\xi}_{\rm FS} - \left(\frac{1}{\tau_{\rm eq}} - \frac{1}{\tau}\right)\mathcal{R}(\xi_{\rm FS}) + \frac{1}{3\tau}\mathcal{R}_L(\xi_{\rm FS}) + \frac{\hat{\Lambda}^4\mathcal{R}(\xi)}{\tau_{\rm eq}}\right] = 0\,, \tag{4.42}$$

with $\hat{\Lambda} = \Lambda/\Lambda_0$.

Matching condition

The temperature $T(\tau)$ is determined by the Landau matching condition, which requires that the energy density calculated from the distribution function f is equal to the energy density obtained from the equilibrium distribution $f_{\rm eq}$. If the system is close to thermal equilibrium, T can be considered the true temperature of the system, but in non-equilibrium systems, T should be considered an effective temperature related to the non-equilibrium energy density of the system. At any time, we define the local effective temperature T of the fluid using the canonical matching condition which results from the vanishing of the right-hand-side of the first moment of the Boltzmann equation as following

$$T = \mathcal{R}_{\rm eff}^{1/4}\Lambda_0 \tag{4.43}$$

where $\mathcal{R}_{\rm eff}$ for both cases is

$$\mathcal{R}_{\rm eff} \equiv \mathcal{R}_\epsilon(\xi)\hat{\Lambda}^4 \qquad \textbf{(Old aHydro)} \tag{4.44}$$

$$\mathcal{R}_{\rm eff} \equiv D(\tau,\tau_0)\mathcal{R}_\epsilon(\xi_{\rm FS}) + [1-D(\tau,\tau_0)]\mathcal{R}_\epsilon(\xi)\hat{\Lambda}^4 \qquad \textbf{(New aHydro)} \tag{4.45}$$

Second moment

To close the system of equations, we use the zz projection of the second-moment of the Boltzmann equation minus 1/3 of the sum of xx, yy, and zz projections.[1] Therefore, the isotropic pressure contribution is effectively removed, leaving only the anisotropic pressure term, and this procedure will give us the second moment equations. For the second moment equation of motion, we will perform a similar manipulation by starting from the relaxation-time approximation (RTA) Boltzmann equation

$$p^\mu \partial_\mu f = -\frac{p\cdot u}{\tau_{\rm eq}(T)}[f - f_{\rm eq}(T)]\,. \tag{4.46}$$

We then encounter a rank three tensor which is defined as $I^{\mu\nu\lambda}[f] \equiv N_{\rm dof}\int dP\, p^\mu p^\nu p^\lambda\, f$, where $N_{\rm dof}$ is the number of degrees of freedom. One obtains the following equation of motion from the second moment of the RTA Boltzmann equation [196]

$$\partial_\mu I^{\mu\nu\lambda} = \frac{1}{\tau_{\rm eq}}(u_\mu I^{\mu\nu\lambda}_{\rm eq} - u_\mu I^{\mu\nu\lambda})\,, \tag{4.47}$$

with $I^{\mu\nu\lambda}_{\rm eq} \equiv I^{\mu\nu\lambda}[f_{\rm eq}] = \frac{4N_{\rm dof}}{\pi^2}T^5$. Note that $I^{\mu\nu\lambda}$ is symmetric with respect to interchanges of μ, ν, and λ and traceless in any pair of indices (massless particles/conformal invariance).

Defining $I_i = u^\mu X_i^\nu X_i^\lambda I_{\mu\nu\lambda}$ and $I_0 = u^\mu u^\nu u^\lambda I_{\mu\nu\lambda}$ where u^μ is the rest frame four-velocity and X_i^μ with $i \in \{1,2,3\}$ are space-like basis vectors that are orthogonal to u^μ,[2] in an

[1] For example, for a rank-two tensor $M^{\nu\lambda}$ the zz projection corresponds to $z_\nu z_\lambda M^{\nu\lambda}$.

[2] The three spacelike basis vectors can also be written as $X_1^\mu = x^\mu$, $X_2^\mu = y^\mu$, and $X_3^\mu = z^\mu$, for compactness.

isotropic system one finds $I_x = I_y = I_z = I_0$ with

$$I_0(\Lambda) = \frac{4N_{\rm dof}}{\pi^2}\Lambda^5 \,. \tag{4.48}$$

Using the old aHydro form (Eq. (4.1) with $D \to 0$) one finds

$$\begin{aligned} I_u &= \mathcal{S}_u(\xi) I_0(\Lambda) \,, \\ I_x &= I_y = \mathcal{S}_T(\xi) I_0(\Lambda) \,, \\ I_z &= \mathcal{S}_L(\xi) I_0(\Lambda) \,, \end{aligned} \tag{4.49}$$

However, using the new aHydro form Eq. (4.2) one finds

$$\begin{aligned} I_u &= \mathcal{S}_u(\xi_{\rm FS})\, I_0(\Lambda_0) D(\tau,\tau_0) + \mathcal{S}_u(\xi) I_0(\Lambda)[1 - D(\tau,\tau_0)] \,, \\ I_x &= I_y = \mathcal{S}_T(\xi_{\rm FS}) I_0(\Lambda_0)\, D(\tau,\tau_0) + \mathcal{S}_T(\xi) I_0(\Lambda)[1 - D(\tau,\tau_0)] \,, \\ I_z &= \mathcal{S}_L(\xi_{\rm FS}) I_0(\Lambda_0)\, D(\tau,\tau_0) + \mathcal{S}_L(\xi) I_0(\Lambda)[1 - D(\tau,\tau_0)] \,, \end{aligned} \tag{4.50}$$

with

$$\begin{aligned} \mathcal{S}_u(\xi) &= \frac{3+2\xi}{(1+\xi)^{3/2}} \,, \\ \mathcal{S}_T(\xi) &= \frac{1}{\sqrt{1+\xi}} \,, \\ \mathcal{S}_L(\xi) &= \frac{1}{(1+\xi)^{3/2}} \,, \end{aligned} \tag{4.51}$$

which satisfy $2\mathcal{S}_T + \mathcal{S}_L = \mathcal{S}_u$ due to the conformality of the system.

The $i = \{x, y, z\}$ equations result from

$$D I_i + I_i(\theta - 2\theta_i) = \frac{1}{\tau_{\rm eq}}(I_{\rm eq} - I_i) \,, \tag{4.52}$$

with the co-moving derivative $D = u^\mu \partial_\mu$, the expansion scalar $\theta = \partial_\mu u^\mu$, and $\theta_i \equiv -u_\mu D_i X_i^\mu$, where X_i^μ are space-like basis vectors that are orthogonal to u^μ. For the case of 0+1d Bjorken expansion one has $D = \partial_\tau$, $\theta = \partial_\mu u^\mu = 1/\tau$, $\theta_x = \theta_y = 0$ and $\theta_z = -1/\tau$. For more details concerning the basis vectors used see appendix (E.1.2). Based on this, one has

$$\partial_\tau I_i + \frac{3}{\tau} I_i \;\; = \;\; \frac{1}{\tau_{\rm eq}} (I_{\rm eq} - I_i) \, . \tag{4.53}$$

with

$$\begin{aligned} \partial_\tau I_{x,y} = & \left[\Lambda_0^5 \; \mathcal{S}_T'(\xi_{\rm FS}) \, \dot{\xi_{\rm FS}} \; - \frac{\Lambda_0^5}{\tau_{\rm eq}} \, \mathcal{S}_T(\xi_{\rm FS}) + \frac{\Lambda^5}{\tau_{\rm eq}} \, \mathcal{S}_T(\xi) \right] \; D(\tau, \tau_0) + \\ & \left[5 \Lambda^4 \; \partial_\tau \Lambda \, \mathcal{S}_T(\xi) \; + \Lambda^5 \; \mathcal{S}_T'(\xi) \, \dot{\xi} \right] \; [1 - D(\tau, \tau_0)] \end{aligned} \tag{4.54}$$

$$\begin{aligned} \partial_\tau I_z = & \left[\Lambda_0^5 \; \mathcal{S}_L'(\xi_{\rm FS}) \, \dot{\xi_{\rm FS}} \; - \frac{\Lambda_0^5}{\tau_{\rm eq}} \, \mathcal{S}_L(\xi_{\rm FS}) + \frac{\Lambda^5}{\tau_{\rm eq}} \, \mathcal{S}_L(\xi) \right] \; D(\tau, \tau_0) + \\ & \left[5 \Lambda^4 \; \partial_\tau \Lambda \, \mathcal{S}_L(\xi) \; + \Lambda^5 \; \mathcal{S}_L'(\xi) \, \dot{\xi} \right] \; [1 - D(\tau, \tau_0)] \end{aligned} \tag{4.55}$$

New aHydro:

The first two equations (xx and yy projections) both give

$$\begin{aligned} & [1 - D(\tau, \tau_0)] \left[\frac{1}{\tau} + \frac{\mathcal{S}_T'(\xi)}{\mathcal{S}_T(\xi)} \dot{\xi} + \frac{5 \dot{\hat{\Lambda}}}{\hat{\Lambda}} \right] + D(\tau, \tau_0) \left[\frac{1}{\tau_{\rm eq}} + \frac{\mathcal{S}_T'(\xi_{\rm FS})}{\hat{\Lambda}^5 \mathcal{S}_T(\xi)} \dot{\xi}_{\rm FS} + \left(\frac{1}{\tau} - \frac{1}{\tau_{\rm eq}} \right) \frac{\mathcal{S}_T(\xi_{\rm FS})}{\hat{\Lambda}^5 \mathcal{S}_T(\xi)} \right] \\ & = \frac{1}{\tau_{\rm eq}} \left[\frac{T^5}{\Lambda_0^5 \hat{\Lambda}^5 \mathcal{S}_T(\xi)} - D(\tau, \tau_0) \frac{\mathcal{S}_T(\xi_{\rm FS})}{\hat{\Lambda}^5 \mathcal{S}_T(\xi)} - [1 - D(\tau, \tau_0)] \right] . \end{aligned} \tag{4.56}$$

The third equation (zz projection) gives

$$[1-D(\tau,\tau_0)]\left[\frac{3}{\tau}+\frac{\mathcal{S}_L'(\xi)}{\mathcal{S}_L(\xi)}\dot{\xi}+\frac{5\dot{\hat{\Lambda}}}{\hat{\Lambda}}\right]+D(\tau,\tau_0)\left[\frac{1}{\tau_{\rm eq}}+\frac{\mathcal{S}_L'(\xi_{\rm FS})}{\hat{\Lambda}^5\mathcal{S}_L(\xi)}\dot{\xi}_{\rm FS}+\left(\frac{3}{\tau}-\frac{1}{\tau_{\rm eq}}\right)\frac{\mathcal{S}_L(\xi_{\rm FS})}{\hat{\Lambda}^5\mathcal{S}_L(\xi)}\right]$$
$$=\frac{1}{\tau_{\rm eq}}\left[\frac{T^5}{\Lambda_0^5\hat{\Lambda}^5\mathcal{S}_L(\xi)}-D(\tau,\tau_0)\frac{\mathcal{S}_L(\xi_{\rm FS})}{\hat{\Lambda}^5\mathcal{S}_L(\xi)}-[1-D(\tau,\tau_0)]\right]. \tag{4.57}$$

Taking the zz projection minus one-third of the sum of the xx, yy, and zz projections gives

$$[1-D(\tau,\tau_0)]\left(\frac{1}{1+\xi}\dot{\xi}-\frac{2}{\tau}\right)+\frac{\xi\sqrt{1+\xi}}{\tau_{\rm eq}}\frac{\hat{T}^5}{\hat{\Lambda}^5}=0\,, \tag{4.58}$$

with $\hat{T}=T/\Lambda_0$. We note that all of the free streaming contributions vanish. Solving for $\dot{\xi}$ using Eq. (4.58) we obtain

$$\dot{\xi}=(1+\xi)\left(\frac{2}{\tau}-\frac{\xi\sqrt{1+\xi}}{\tau_{\rm eq}}\frac{\hat{T}^5}{\hat{\Lambda}^5}\frac{1}{1-D(\tau,\tau_0)}\right). \tag{4.59}$$

As mentioned previously, in the limit $\tau\to\tau_0$, one has $D=1$ and hence the second term on the right-hand-side of Eq. (4.59) will diverge at $\tau=\tau_0$ unless either $\xi=0$ or $\xi=-1$. The latter condition makes the entire right hand side vanish and hence does not allow for dynamical evolution of ξ. For this reason we will use $\lim_{\tau\to\tau_0}\xi(\tau)=0$.

Old aHydro ($D=0$)

One can recompute the second-moment equation with $D=0$ to see if it agrees with results available in the literature. In this case on finds that the zz projection gives

$$(\log\mathcal{S}_L)'\dot{\xi}+5\partial_\tau\log\Lambda+\frac{3}{\tau}=\frac{1}{\tau_{\rm eq}}\left[\frac{\mathcal{R}^{5/4}}{\mathcal{S}_L}-1\right], \tag{4.60}$$

and the xx and yy projections both give

$$(\log \mathcal{S}_T)'\dot{\xi} + 5\partial_\tau \log\Lambda + \frac{1}{\tau} = \frac{1}{\tau_{\rm eq}}\left[\frac{\mathcal{R}^{5/4}}{\mathcal{S}_T} - 1\right], \tag{4.61}$$

where, in both cases, we used $T = \mathcal{R}^{1/4}(\xi)\Lambda$.

Finally, with $D = 0$, taking the zz projection minus one-third of the sum of the xx, yy, and zz projections gives in the relaxation time approximation, the second evolution equation

$$\frac{1}{1+\xi}\dot{\xi} - \frac{2}{\tau} + \frac{\mathcal{R}^{5/4}(\xi)}{\tau_{\rm eq}}\xi\sqrt{1+\xi} = 0\,. \tag{4.62}$$

One can verify explicitly that Eq. (4.58) reduces to this in the limit $D \to 0$.

4.3 Numerical solution of the dynamical equations and the anisotropic attractor

In this section we present some representative numerical solutions using different initial conditions along with the attractor solution to which they flow. For this purpose, we solve the first and second differential equations corresponding to Eq. (4.42) and (4.58) for the evolution of $\xi(\tau)$ and $\Lambda(\tau)$. However to evolve these equations we need to know the damping function. Herein, we solve the integral equation by using an iterative method. In the first iteration, we assume that the temperature evolution contained within the integral defining $D(\tau, \tau_0)$ is given by ideal hydrodynamics, i.e. $T_{\rm guess}(\tau) = T_0(\tau_0/\tau)^{1/3}$. We then solve the dynamical equations (4.42) and (4.58). From this we obtain the approximate dependence of the effective temperature T on proper time using Eq. (4.43). The resulting effective temperature $T(\tau)$ is then used to load the damping function for the next iteration. We repeat this process until the effective temperature and longitudinal pressure converge to a part in 10^8. In practice, this can be achieved with only five iterations. Once converged, the solutions for $\xi(\tau)$ and $\Lambda(\tau)$ can be used to compute the full distribution function using

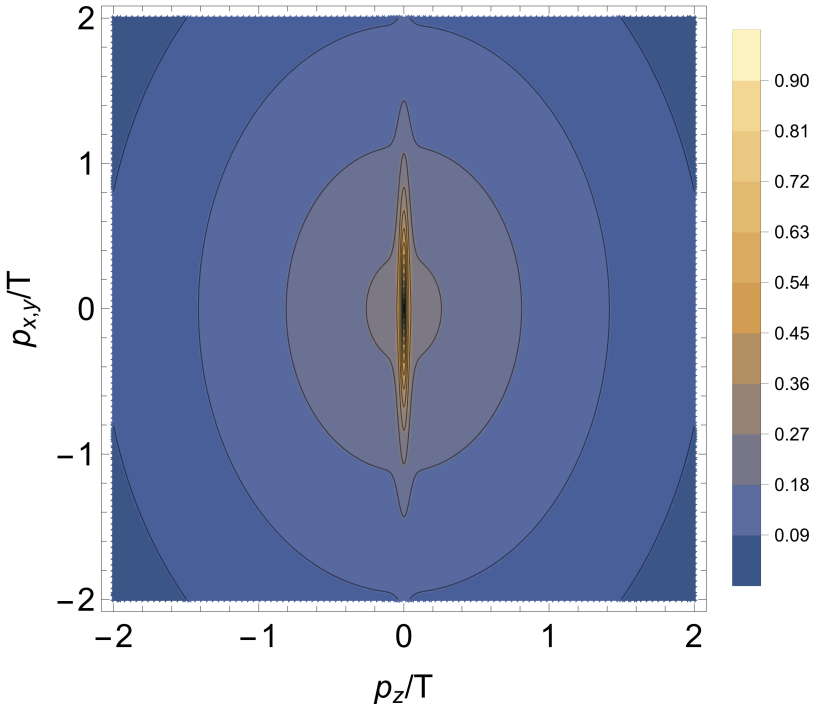

Figure 1: Visualization of the one-particle distribution function at a given moment in proper time. A bimodal structure can be seen, with the two contributions corresponding to a highly squeezed free-streaming component (inner ellipsoid) and a less anisotropic equilibrating contribution (outer ellipsoid).

Eq. (4.2) and all moments of the distribution function using Eq. (4.31).[3]

In Fig. 1 we present a contour plot of the one-particle distribution function at the proper time at which the contribution from the free streaming part and equilibrating part contribute equally.[4] Generically, the exact solution for the one-particle distribution function contains two independent components [165, 188–190]. The first component is an anisotropic part which has been squeezed in the longitudinal direction and is exponentially damped at late times. This contribution represents the subset particles that never had any interaction at all. Statistically, there is always such a population of particles. As a function of time, this contribution becomes compressed along the longitudinal direction in momentum space resulting in $P_L^{\rm FS} \to 0$ as the system evolves. This contribution comes from the first term in

[3]One can substantially reduce the number of iterations required by initializing instead with the canonical aHydro evolution equations.

[4]This occurs when $D(\tau, \tau_0) = 1/2$.

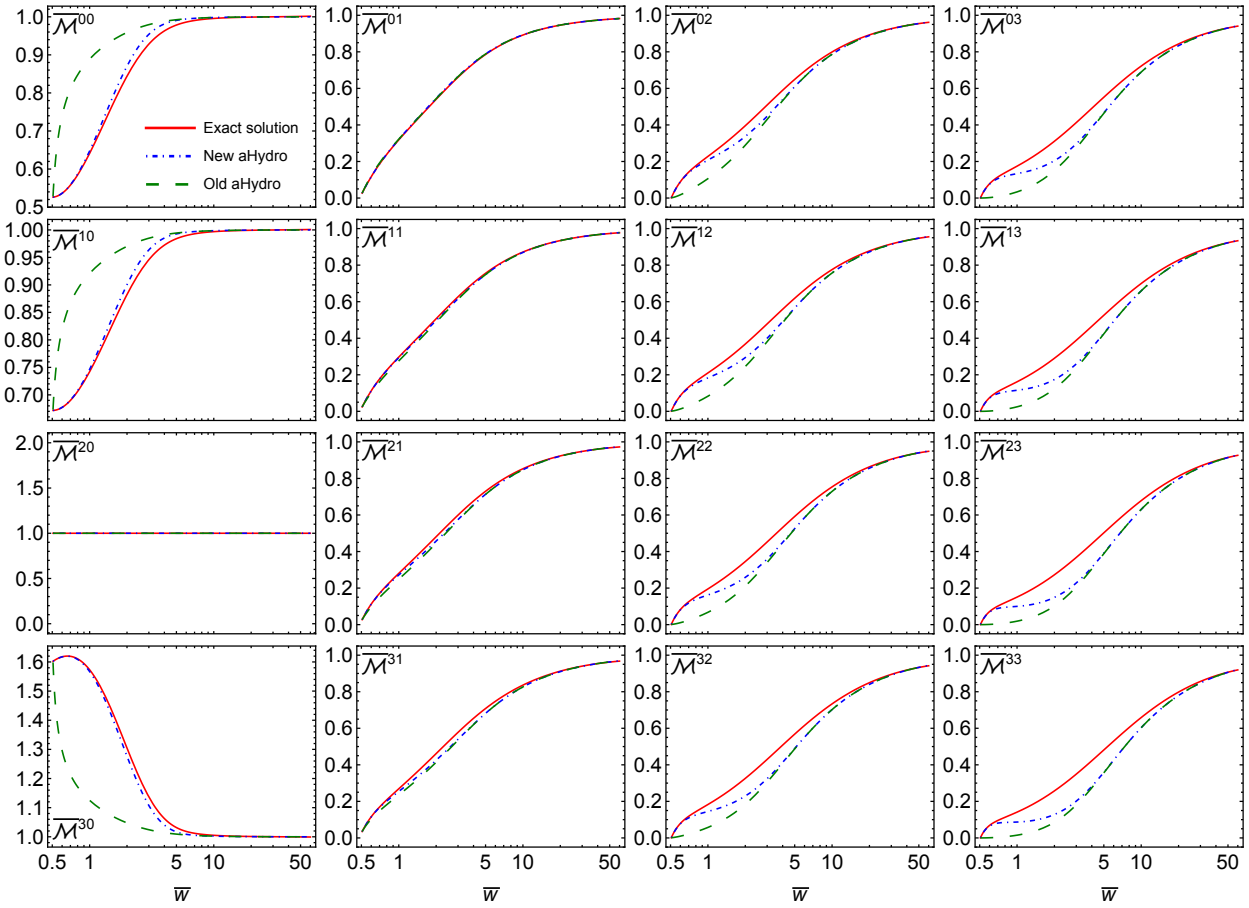

Figure 2: Scaled moments $\overline{\mathcal{M}}^{nl}$ obtained from the exact solution (solid red line) compared with the new aHydro (blue dashed lines), and the old aHydro (green long dashed lines). Horizontal axis is $\overline{w} = \tau T/5\overline{\eta}$. Panels show a grid in n and l.

Eq. (4.2), which corresponds to the free streaming contribution. Note that, because of the damping function $D(\tau, \tau_0)$ in the first term in Eq. (4.2), the amplitude of this very narrow ridge will decrease in time exponentially. The second visible component in Fig. 1 is an isotropizing part which dominates at late times. This contribution comes from the second term in Eq. (4.2).

In Fig. 2, we present the evolution of the scaled moments of the distribution function as a function the scaled time

$$\overline{w} = \frac{\tau}{\tau_{\rm eq}} = \frac{\tau T}{5\overline{\eta}}\,, \tag{4.63}$$

and we compare to the exact RTA solution (red solid line) obtained in Refs. [165, 188, 189].

Results from the new aHydro and old aHydro ansatze are shown as blue dashed and green long dashed lines, respectively. In all cases shown, the new aHydro ansatz provides a better approximation to the exact solution than the old aHydro ansatz. In addition, one observes that both aHydro ansatze result in positive definite results for all moments despite having large non-equilibrium deviations. Comparing the old and new ansatze, we see that the new ansatz is able to reproduce the dynamics of low-order moments much better than the old ansatz. This is particularly striking for moments with $l = 0$ for which we see that the new aHydro ansatz is very close to the exact results for all n shown.[5] We note, however, for higher moments, e.g. $\overline{\mathcal{M}}^{33}$, we see that the new aHydro ansatz interpolates between the exact solution at early times and the old aHydro result at lates times. As a result, one sees larger deviations from the exact solution in these moments.

In order to provide more quantitative comparison of the two methods, in Fig. 3 we present the relative errors of the old and new aHydro ansatze computed as the ratio of a given approximation to the the exact result minus one. The relative errors for the new and old schemes are shown as blue solid and red dashed lines, respectively. As one can see from Fig. 3, the new aHydro has a smaller error in all moments and at virtually all times. The one exception is $\overline{\mathcal{M}}^{01}$ for which one observes a slight smaller error with the old ansatze in a small time window. Returning to the general case, we see that, since the new scheme merges onto the old scheme at late times, they have similar relative errors, however at early time we see a dramatic reduction in the relative error using the new aHydro ansatz.

In Fig. 4, the new aHydro (blue dashed lines), and the old aHydro (green long dashed lines) attractors are compared to the attractor obtained via exact solution of the RTA Boltzmann equation(red solid line). In all cases shown, the new aHydro ansatz agrees best with the exact solution for the 0+1d conformal RTA attractor. Additionally, for all values of $\overline{w}$, we note that both aHydro attractors possess positive values for all moments. In the case

[5] We have checked that this holds true for larger n than shown in Fig. 2.

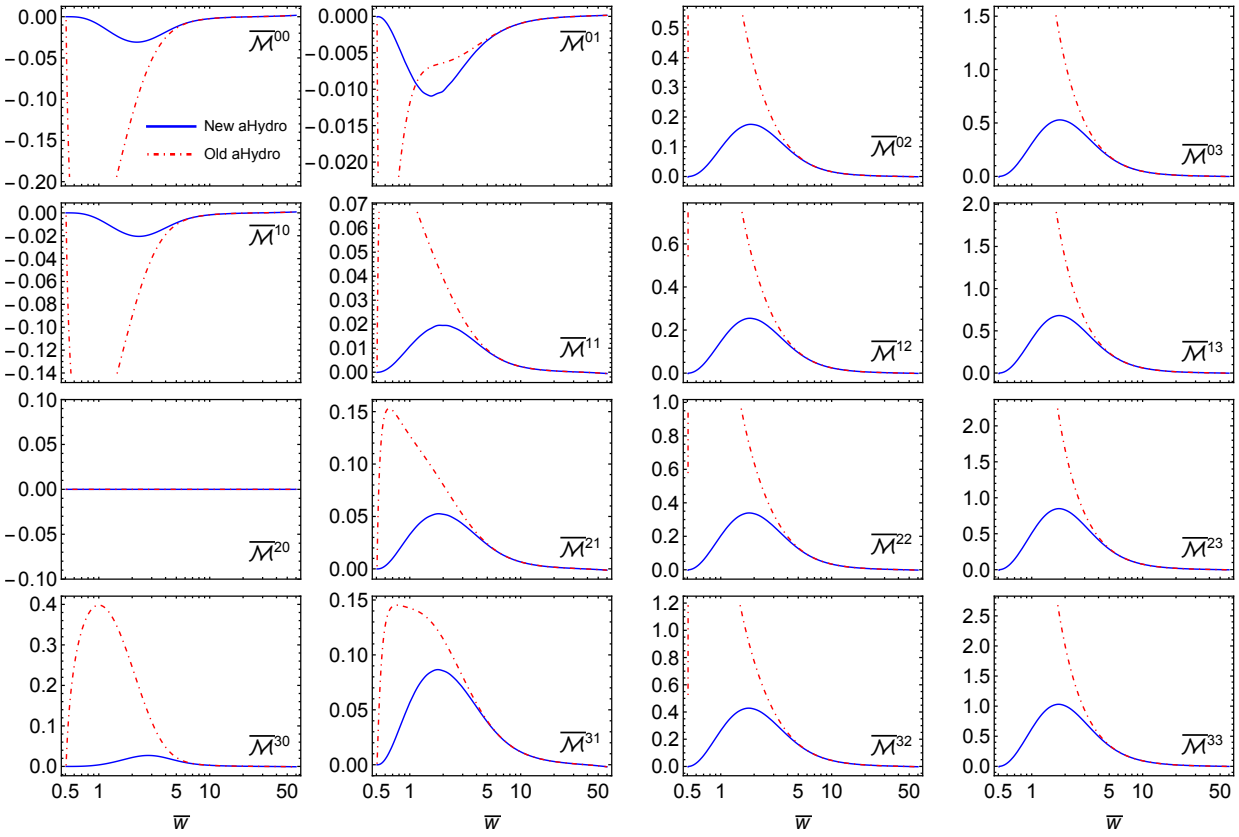

Figure 3: Plots of the relative error between the new (solid blue line) and old (red dashed lines) aHydro ansatz compared to the exact solution. Error is computed as approximation/exact -1.

of the new aHydro ansatz, firstly one sees that for $l = 0$ and $l = 1$ (first and second left column, respectively of Fig. 4) this scheme has the best agreement at all times. As a result, the new aHydro accurately describes the evolution of the modes with $l = 0$, and 1, which are sensitive to the free-streaming part of the evolution. For $l > 1$ one sees that, as l and n are increased, the new aHydro results differ more from the exact solutions in the region $\overline{w} \sim [10^{-5}, 1]$. The worst agreement is for the $l = 3$ moments (rightmost column of Fig. 4). One finds that the new aHydro ansatz fails to accurately describe the evolution of the scaled moments with $l = 3$ which are dominated by isotropizing contribution at late times. As a consequence, the new aHydro does not provide reliable approximations for these moments and the problem becomes more severe as one increases for $l > 1$. Turning to the old aHydro

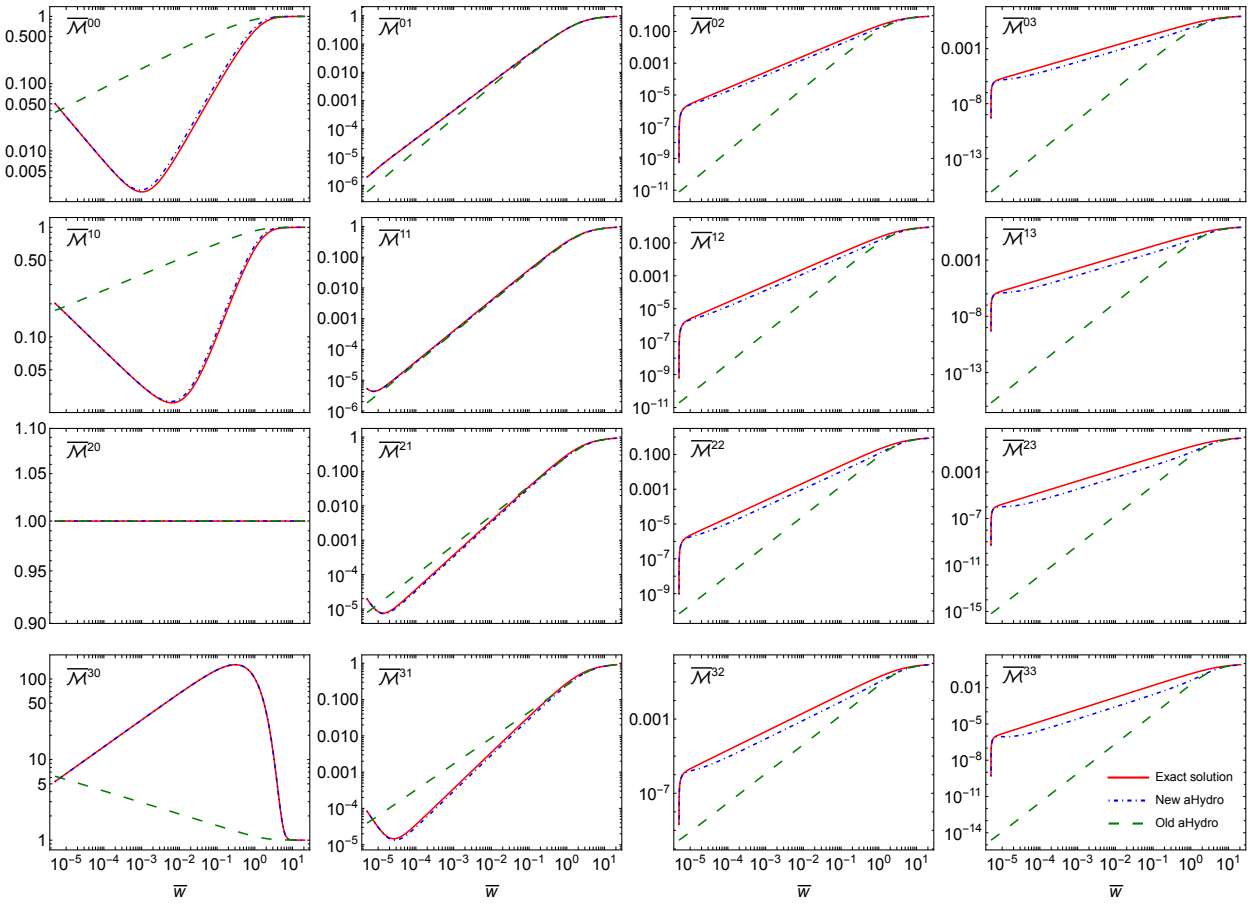

Figure 4: Scaled moments $\overline{\mathcal{M}}^{nl}$ obtained from the exact solution attractor (solid red line) compared with the new aHydro (blue dashed lines), and the old aHydro (green long dashed lines). Horizontal axis is $\overline{w}=\tau T/5\overline{\eta}$. Panels show a grid in n and l.

ansatz, for $l = 1$, one sees that, although the old aHydro ansatz does a reasonable job in describing the $l = 1$ moments, as n and l are increased or decreased, the results become significantly worse. Note that, even given the caveats mentioned above, comparing the old and new aHydro ansatze, we see that the new approach dramatically improves agreement with the exact RTA attractor and, in particular, can be used to fix the problem encountered with moments with $l = 0$.

4.4 Conclusions

In this chapter, our goal was to find an improved set of anisotropic hydrodynamic evolution equations that can more faithfully describe the non-equilibrium dynamics of the quark-gluon plasma created in relativistic heavy ion collisions at RHIC and LHC. We introduced a new version of anisotropic hydrodynamics that includes separate free-streaming and equilibrating contributions which allows for a better description of exact solutions to the Boltzmann equation available in the literature. We computed explicit expressions for the first and second moments of the one-particle distribution function in the new aHydro approach and used these to obtain the new 0+1d conformal equations of motion given by Eqs. (4.42) and (4.58). We presented comparisons of the numerical solution of the conformal 0+1d equations of motion for both the old and new aHydro schemes with the exact RTA solution. Our results demonstrated that the new aHydro form allows one to have a bimodal distribution function similar to what is seen in the exact RTA solution for the one-particle distribution function. We then computed the evolution of the scaled moments as a function of the scaled time, $\overline{w}$, and demonstrated that the new aHydro ansatz provides a better approximation to the exact solution than the original aHydro ansatz. Finally, we determined the non-equilibrium attractor associated with the new aHydro scheme and demonstrated that it provides much better agreement with the exact RTA attractor than the original aHydro scheme, in particular for moments with $l = 0$. In the future, it would be interesting to apply the ansatz obtained here to full 3+1d anisotropic hydrodynamics, including temperature-dependent masses for the particles similar to 'canonical' quasiparticle aHydro [8, 185].

Chapter 5

Far-from-equilibrium attractors for massive kinetic theory in the relaxation time approximation

5.1 Introduction

One of the most important questions that has emerged in the last twenty years in the area of far-from-equilibrium relativistic dynamics is to what extent can such dynamics be described by relativistic viscous hydrodynamics. In this context, the construction of a set of exact solutions to the relativistic Boltzmann equation in relaxation time approximation (RTA), despite its relative simplicity, has proven to be very useful in assessing the quantitative reliability of different dissipative hydrodynamical frameworks [156, 188–190, 199, 200]. In addition, these exact solutions have helped to understand the emergence of a far-from-equilibrium attractor in relativistic transport theory that matches smoothly onto viscous hydrodynamics at late times but which extends to earlier times when conventional linearized viscous hydrodynamics treatments break down [146, 148–151, 153–155, 157, 158, 162–165, 167, 168, 172, 175, 181, 201–213].

Although the majority of these references focused on conformal systems, some of these works have considered whether or not attractors exist in non-conformal systems since in this case more than one dimensionful scale appears in the problem [154, 156, 208–210, 214]. In this work we consider exact solutions of the RTA Boltzmann equation for a massive gas using the exact solution obtained originally in Ref. [190]. We extend this solution to allow computation of all moments, $\mathcal{M}^{nl}$, of the one-particle distribution using the moments introduced in Ref. [165]. We also extend prior works by making use of the self-consistently determined temperature and mass dependent relaxation time, $\tau_{\rm eq}(T, m)$, and considering

fixed specific shear viscosity. In Refs. [154,156,208–210,214] either a constant relaxation time or conformal relaxation time proportional to the inverse temperature was used. Finally, we systematically study both the forward and pull-back (early-time) attractors by varying both the initial anisotropy and initialization time and computing a large set of integral moments of the distribution function.

We will demonstrate that kinetic theory with an RTA collisional kernel possesses both forward and pull-back attractor for moments containing greater than one integral power of the longitudinal momentum squared ($l \geq 1$). The existence of a forward attractor for such moments is established by holding the initialization time and energy density fixed while varying the initial momentum-space anisotropy using a spheroidal form for the initial one-particle distribution function. Secondly, we establish the existence of an early-time (pull-back) attractor for such moments by holding the initial anisotropy and energy density fixed while varying the initialization time. As we will demonstrate, this implies that there does not exist an early time attractor for the pressure-scaled shear and bulk viscous corrections independently, however, the difference of the two does possess an attractor, which is consistent with there being an attractor in the scaled longitudinal pressure. Our findings are fully compatible with and extend those reported in Refs. [208, 214].

The structure of this chapter is as follows. In Sec. 5.2, we review basic thermodynamic and dynamic relations for non-conformal massive gases and extend the exact solution of the RTA Boltzmann equation obtained in Ref. [190] to all moments of the distribution function. In Sec. 5.3 we collect analytic formula for the viscosity corrected distribution functions and moments that are accurate to first order in hydrodynamic gradients using both the 14-moment and Chapman-Enskog approximations. In Sec. 5.4, we present our numerical results obtained from the exact solution of the RTA Boltzmann equation. In Sec. 5.6, we present our conclusions and an outlook for the future.

5.2 Setup

In this chapter we will make use of a previously obtained exact solution to the 0+1d RTA Boltzmann equation for a massive gas with Boltzmann statistics. The non-conformal exact solution was first presented in Ref. [190] and extended earlier conformal exact solutions in a Bjorken expansion scenario [188, 189]. We will extend the original work of Ref. [190] to include a relaxation time that self-consistently depends on both the temperature and mass of the particle, whereas the original work considered a constant relaxation time or the limit of low temperatures. Our solution also goes beyond the considerations of the recent work of Refs. [154, 208, 210] where a conformal relaxation time was used.

5.2.1 Basis vectors

Herein, we will assume Bjorken flow, where the medium expands longitudinally and has a boost-invariant velocity profile. The values of the four-velocity components u^μ in Milne coordinates for this flow are $u^\tau = 1$ and $u^{x,y,\varsigma} = 0$. When the system is boost invariant one can identify the longitudinal boost by using the quantities τ and ς which are the longitudinal proper-time and spatial rapidity, respectively. Here, the longitudinal proper-time is defined as $\tau = \sqrt{t^2 - z^2}$, which is a measure of the elapsed proper time for a particle that is moving with a constant velocity and longitudinal spatial rapidity as $\varsigma = \tanh^{-1}(z/t)$ with

$$\begin{aligned} t &= \tau \cosh\varsigma\,, \\ z &= \tau \sinh\varsigma\,. \end{aligned} \tag{5.1}$$

To obtain the derivatives of Eq. (5.1) with respect to the variables t and z, as well as the spatial rapidity ς, we can take the following partial derivatives

$$\begin{aligned} \frac{\partial\tau}{\partial t} = \frac{t}{\tau} &= \cosh\varsigma\,, \\ \frac{\partial\tau}{\partial z} = -\frac{z}{\tau} &= -\sinh\varsigma\,, \end{aligned}$$

$$\begin{aligned} \frac{\partial\varsigma}{\partial\tau} = -\frac{\sinh\varsigma}{\tau} &= -\frac{z}{\tau^2}\,, \\ \frac{\partial\varsigma}{\partial z} = \frac{\cosh\varsigma}{\tau} &= \frac{t}{\tau^2}\,. \end{aligned} \tag{5.2}$$

Therefore,

$$\frac{\partial}{\partial t} = \frac{\partial\tau}{\partial t}\frac{\partial}{\partial\tau} + \frac{\partial\varsigma}{\partial t}\frac{\partial}{\partial\varsigma} = \frac{t}{\tau}\frac{\partial}{\partial\tau} - \frac{z}{\tau^2}\frac{\partial}{\varsigma} = \cosh\varsigma\frac{\partial}{\partial\tau} - \frac{\sinh\varsigma}{\tau}\frac{\partial}{\partial\varsigma}\partial\varsigma, \tag{5.3}$$

and

$$\frac{\partial}{\partial z} = \frac{\partial\tau}{\partial z}\frac{\partial}{\partial\tau} + \frac{\partial\varsigma}{\partial z}\frac{\partial}{\partial\varsigma} = -\frac{z}{\tau}\frac{\partial}{\partial\tau} + \frac{\cosh\varsigma}{\tau}\frac{\partial}{\partial\varsigma} = -\sinh\varsigma\frac{\partial}{\partial\tau} + \frac{t}{\tau^2}\frac{\partial}{\partial\varsigma}. \tag{5.4}$$

Moreover, the basis vectors in the Lab Frame (LF) in the boost-invariant for a transversally homogenous system, where the transverse flow is absent, is summarized as

$$\begin{aligned} U^\mu &= (\cosh\varsigma, 0, 0, \sinh\varsigma) = (\frac{t}{\tau}, 0, 0, \frac{z}{\tau})\,, \\ X^\mu &= (0, \cos\phi, \sin\phi, 0)\,, \\ Y^\mu &= (0, -\sin\phi, \cos\phi, 0)\,, \\ Z^\mu &= (\sinh\varsigma, 0, 0, \cosh\varsigma) = (\frac{z}{\tau}, 0, 0, \frac{t}{\tau}). \end{aligned} \tag{5.5}$$

In the case of one-dimensional boost-invariant expansion (0+1d), all scalar quantities depend only on the longitudinal proper time τ. To describe boost-invariant 0+1d dynamics, one can

introduce a spacelike vector z^μ, which is orthogonal to the fluid four-velocity u^μ in all frames and corresponds to the z-direction in the local rest frame of the matter [103, 215]. The requirement of boost invariance implies that the one-particle distribution function $f(x,p)$ may depend only on three variables, τ, w, and $\vec{p}_T$ [216,217], with the boost-invariant variable w obtained as the following [1]

$$p \cdot z = \frac{Ez - tp_L}{\tau} = -\frac{w}{\tau} \quad \Rightarrow \quad w = tp_L - zE. \tag{5.6}$$

Using w and $\vec{p}_T$ one can define

$$\tau \; p \cdot u = Et - p_L z = \sqrt{w^2 + (m^2 + \vec{p}_T^{\,2})\,\tau^2} \equiv v\,. \tag{5.7}$$

Also, by using these variables, one can derive the longitudinal momentum p_L using equations Eq. (5.6) and Eq. (5.7), which yields $E = \frac{tp_L - w}{z}$ and $E = \frac{v + p_L z}{t}$, respectively. Substituting these equations, one can solve for p_L and write it in terms of w, v, t, and z. This yields

$$p_L = \frac{vz + wt}{\tau^2}. \tag{5.8}$$

Similarly, one can express the energy E in terms of w and v by substituting p_L into the equation $E = \frac{tp_L - w}{z}$. After some algebraic manipulation and substitution, this gives

$$E = \frac{tv + wz}{\tau^2}. \tag{5.9}$$

In the next section, we will rewrite the RTA Boltzmann equation in relaxation time approximation and the equilibrium distribution by using these boost-invariant variables.

[1] In Eq. (5.6), z is the spatial coordinate, which is not to be confused with the basis vector z^μ.

5.2.2 RTA Boltzmann equation

The relaxation time approximation (RTA) Boltzmann equation has been successfully used to describe the dynamics of many physical systems, including the quark-gluon plasma (QGP) produced in heavy-ion collisions, where the relaxation time can be related to the transport coefficients of the medium. The numerical solution of the RTA Boltzmann equation is a challenging task, and various techniques, such as the Monte Carlo methods and the parton cascade model, have been developed to simulate its evolution in realistic systems. In this chapter, all results presented herein follow from the RTA Boltzmann equation in relaxation time approximation. We start from the general Boltzmann equation

$$p^\mu \partial_\mu f(x,p) = C[f(x,p)]\,, \tag{5.10}$$

where f is the one-particle distribution function, $p^\mu = (E, p_T, p_L)$ is the particle four-momentum. Here by using the boost-invariant variable the left-hand-side will be

$$p^\mu \partial_\mu f = \left(E\frac{\partial}{\partial t} - p_L \frac{\partial}{\partial z} \right) f,$$

and by applying the result for $\frac{\partial}{\partial t}$ Eq. (5.3) and $\frac{\partial}{\partial z}$ Eq. (5.4) with $\frac{\partial f}{\partial \varsigma} = 0$, we obtain:

$$p^\mu \partial_\mu f = \left(E\cosh\varsigma \frac{\partial}{\partial \tau} - p_L \sinh\varsigma \frac{\partial}{\partial \tau} \right) f = \frac{1}{\tau}(Et - p_L z)\frac{\partial}{\partial \tau} f = \frac{v}{\tau}\partial_\tau f \tag{5.11}$$

Now, the right-hand-side is the collision kernel $C[f]$ that represents the effect of collisions on the distribution function and in RTA includes the difference between the non-equilibrium distribution function f and the equilibrium distribution function $f_{\rm eq}$, which is a function of the local temperature T and flow velocity u^μ or the four-velocity of the local rest frame

(LRF).

$$C[f] = \frac{p \cdot u}{\tau_{\rm eq}} \left(f_{\rm eq} - f\right) = \frac{1}{\tau_{\rm eq}} \left(E\frac{t}{\tau} - p_L \frac{z}{\tau}\right) \left(f_{\rm eq} - f\right) = \frac{v}{\tau \tau_{\rm eq}} \left(f_{\rm eq} - f\right), \tag{5.12}$$

with $p \cdot u \equiv p^\mu u_\mu = \frac{Et - p_L z}{\tau} = \frac{v}{\tau}$. Substituting the result of the left-hand-side and right-hand-side in Eq. (5.10), we find

$$\partial_\tau f = \frac{1}{\tau_{\rm eq}} \left(f_{\rm eq} - f\right). \tag{5.13}$$

The quantity $\tau_{\rm eq}$ appearing above is the relaxation time, which will be precisely specified below. For the equilibrium distribution, we will follow Ref. [190] and assume a Boltzmann equilibrium distribution function

$$f_{\rm eq} = \exp\left(-\frac{p \cdot u}{T}\right). \tag{5.14}$$

One can rewrite Eq. (5.14) by using the boost-invariant variables introduced in the previous section to get

$$f_{\rm eq} = \exp\left(-\frac{v}{T\tau}\right) = \exp\left(\frac{\sqrt{w^2 + \left(m^2 + p_T^2\right)\tau^2}}{T\tau}\right). \tag{5.15}$$

5.2.3 Thermodynamic variables

For a single-component massive gas obeying Boltzmann statistics, the equilibrium thermodynamic quantities are as follows where the general moment equations for $f_{\rm eq} = \exp\left(-\frac{\sqrt{\mathbf{p}^2 + m^2}}{T(\tau)}\right)$

are presented in the Appendix E.2.1 for readers who are interested in understanding the details.

$$\begin{aligned}
\mathcal{N}_{\rm eq} &= \frac{T^3}{2\pi^2}\,\hat{m}^2 K_2\left(\hat{m}\right), \\
\mathcal{S}_{\rm eq} &= \frac{T^3}{2\pi^2}\,\hat{m}^2\Big[4K_2\left(\hat{m}\right)+\hat{m}K_1\left(\hat{m}\right)\Big], \\
\mathcal{E}_{\rm eq} &= \frac{T^4}{2\pi^2}\,\hat{m}^2\Big[3K_2\left(\hat{m}\right)+\hat{m}K_1\left(\hat{m}\right)\Big], \\
\mathcal{P}_{\rm eq} &= nT = \frac{T^4}{2\pi^2}\,\hat{m}^2 K_2\left(\hat{m}\right), \qquad (5.16)
\end{aligned}$$

with $\hat{m} \equiv m/T$ and K_n being modified Bessel functions of the second kind. Above $\mathcal{N}_{\rm eq}$ is the number density, $\mathcal{S}_{\rm eq}$ is the entropy density, $\mathcal{E}_{\rm eq}$ is the energy density, and $\mathcal{P}_{\rm eq}$ is the pressure. These satisfy $\varepsilon + P = Ts$ and, from the above relations, one can determine the speed of sound squared, which has a direct connection to the QGP's equation of state. It explains how the pressure of the medium is affected by changes in energy density and how quickly these changes spread across the medium. If the speed of sound squared is high, the medium is rigid and modest pressure changes will not have a significant impact on its density. If it is low, the medium is soft, and changes in pressure cause noticeable changes in density.

$$c_s^2 = \frac{dP}{d\varepsilon} = \frac{\varepsilon + P}{3\varepsilon + (3+\hat{m}^2)P}\,. \qquad (5.17)$$

5.2.4 Relaxation time for a massive gas

The relaxation time is a measure of how quickly a system returns to equilibrium after being disturbed. In this section, the relaxation time of a gas with massive particles is discussed, and we show that the relaxation time depends on the particle mass and temperature through a function $\gamma(\hat{m})$, where $\hat{m}$ is the ratio of the particle mass to the temperature. For

a massive system, the shear viscosity η can be expressed as [8, 123, 218]

$$\eta = \frac{\tau_{\rm eq} P}{15} \kappa(\hat{m}) \,, \tag{5.18}$$

with

$$\kappa(x) \equiv x^3 \left[\frac{3}{x^2} \frac{K_3(x)}{K_2(x)} - \frac{1}{x} + \frac{K_1(x)}{K_2(x)} - \frac{\pi}{2} \frac{1 - x K_0(x) L_{-1}(x) - x K_1(x) L_0(x)}{K_2(x)} \right] , \tag{5.19}$$

and $L_n(x)$ being modified Struve functions.

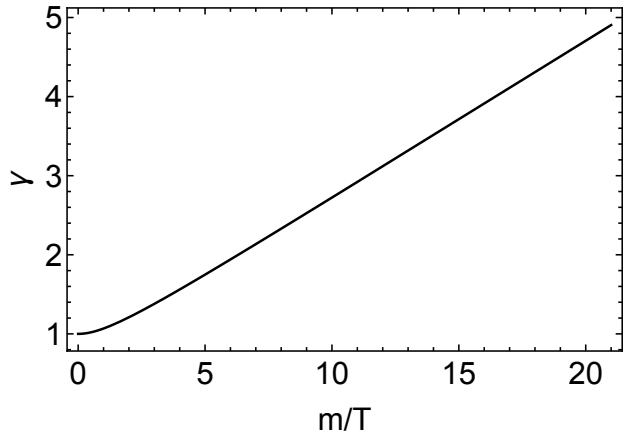

Figure 1: The non-conformal relaxation time modification factor γ Eq. (5.21) as a function of m/T.

For fixed specific shear viscosity, $\bar{\eta} \equiv \eta/s$, which is a measure of the efficiency of the QGP in transporting momentum and serves as a gauge of the QGP's resistance to deformation under shear force. The QGP would act like a thick fluid if the particular shear viscosity was too high, and the system would take a very long time to reach thermal equilibrium. Using $\varepsilon + P = Ts$ with Eq. (5.18) one obtains

$$\tau_{\rm eq}(T, m) = \frac{5\bar{\eta}}{T} \gamma(\hat{m}) \,, \tag{5.20}$$

with

$$\gamma(\hat{m}) \equiv \frac{3}{\kappa(\hat{m})}\left(1+\frac{\varepsilon}{P}\right). \tag{5.21}$$

Note that, in the massless limit, $m \to 0$, one has $\kappa(\hat{m}) \to 12$, $\varepsilon \to 3P$, and $\gamma \to 1$, giving the usual conformal RTA relaxation time that is well understood and follows a simple formula as following

$$\tau_{\rm eq}(T,0) = \frac{5\bar{\eta}}{T}\,. \tag{5.22}$$

For small $\hat{m}$, one has

$$\gamma(\hat{m}) = 1 + \frac{\hat{m}^2}{12} - \frac{13\hat{m}^4}{288} + \mathcal{O}\big(\hat{m}^5\big)\,, \tag{5.23}$$

and in the large $\hat{m}$ limit, one has

$$\gamma(\hat{m}) = \frac{\hat{m}}{5} + \frac{7}{10} + \mathcal{O}\left(\frac{1}{\hat{m}}\right). \tag{5.24}$$

In Fig. 1, we plot $\gamma(\hat{m})$. As can be seen from this figure, $\gamma(\hat{m})$ goes to unity in the massless limit and grows linearly at large m/T, which shows that the relaxation time gets longer as the particles get more massive. Consequently, the value of $\gamma(\hat{m})$ increases in proportion to the value of $\hat{m}$, which corresponds either to fixed temperature and large mass or fixed mass and small temperature. The fact that $\gamma(\hat{m}) \geq 1$ implies that a massive gas always relaxes more slowly to equilibrium than a massless one in physical units, however, it is unclear a priori how things will change as a function of the rescaled time $\overline{\tau} \equiv \tau/\tau_{\rm eq}$. We note that the strong enhancement of the relaxation time at low temperatures modifies the asymptotic approach to equilibrium.

5.2.5 Exact solution for the distribution function and its solution

In this section, we discuss the exact solution to the RTA Boltzmann equation for the distribution function of a fluid undergoing a 0+1D boost-invariant expansion. We will start

by reviewing the derivation of this solution and then present the integral equation obeyed by all moments of the distribution function. We will also generalize the results to the full set of integral moments. These integral moments can be used to determine the bulk properties of the expanding system, such as the energy density, pressure, and velocity fields. The distribution function $f(\tau, w, p_T)$ and the initial distribution function $f_0(w, p_T)$ can be determined by solving the forthcoming integral equation Eq. (5.26). The moment equations provide a test of the numerical solution of the Boltzmann equation, since they can be used to calculate the time evolution of the bulk properties of the system.

We will assume that the initial distribution function f_0 can be expressed in spheroidally-deformed form [192, 193]

$$\begin{aligned} f_0(w, p_T) &= \exp\left[-\frac{\sqrt{(p\cdot u)^2 + \xi_0 (p\cdot z)^2}}{\Lambda_0}\right] \\ &= \exp\left[-\frac{\sqrt{(1+\xi_0)w^2 + (m^2+p_T^2)\tau_0^2}}{\Lambda_0 \tau_0}\right], \end{aligned} \tag{5.25}$$

where ξ_0 is the initial anisotropy parameter and Λ_0 is the initial transverse momentum scale. The reason why the initial distribution function is called spheroidally-deformed is because it describes an ellipsoidal shape of the momentum distribution in the local rest frame of the fluid. The distribution of momentum is not spherical; instead, it is anisotropic, and the axis of the ellipsoid is in the same direction as the flow (the fluid velocity). To change the deformation of the momentum distribution, one uses the anisotropy parameter ξ_0 that measures how much the momentum distribution is stretched or flattened, and it determines the initial shape of the momentum distribution function. Varying this parameter can change the initial deformation of the momentum distribution function, which in turn affects the behavior of the QGP during its evolution. We consider a slight generalization of this initial condition in Sec. (5.5).

For $-1 < \xi_0 < 0$, this corresponds to an initially prolate distribution in the local rest frame and, conversely, for $\xi_0 > 0$ this corresponds to an initially oblate distribution function. For $\xi_0 = 0$, one obtains an isotropic Boltzmann distribution function as the initial condition. Moreover, the initial distribution function is chosen in its spheroidally-deformed version because it is a straightforward and adaptable model that can be used to explain a wide range of various initial conditions. Particularly, it can be used to analyze how the initial anisotropies affect how the fluid changes over time as well as the function of different physical factors, such as viscosity in the relaxation of the anisotropy. By adjusting the value of the anisotropy parameter, you can study the change from an anisotropic to an isotropic distribution and see how the final state depends on the conditions at the beginning.

The exact solution to Eq. (5.13) is given by [188–190, 219–222]

$$f(\tau, w, p_T) = D(\tau, \tau_0) f_0(w, p_T) + \int_{\tau_0}^{\tau} \frac{d\tau'}{\tau_{\rm eq}(\tau')} D(\tau, \tau')\, f_{\rm eq}(\tau', w, p_T)\,, \tag{5.26}$$

where $f_0(w, p_T)$ is the initial distribution function specified at $\tau = \tau_0$ and the damping function D is defined as

$$D(\tau_2, \tau_1) = \exp\left[-\int_{\tau_1}^{\tau_2} \frac{d\tau''}{\tau_{\rm eq}(\tau'')}\right]. \tag{5.27}$$

Note that taking the derivative Eq. (5.26), one can find the same result as Eq. (5.13) as function of τ, w, and p_T

$$\frac{\partial f(\tau, w, p_T)}{\partial \tau} = \underbrace{-\frac{1}{\tau_{\rm eq}} D(\tau, \tau_0) f_0(w, p_T) - \frac{1}{\tau_{\rm eq}} \int_{\tau_0}^{\tau} \frac{d\tau'}{\tau_{\rm eq}(\tau')} D(\tau, \tau') f_{\rm eq}(\tau', w, p_T)}_{=-\tau_{\rm eq} f(\tau, w, p_T)} + \frac{1}{\tau_{\rm eq}} \underbrace{D(0,0)}_{=1} f_{\rm eq}(\tau')$$

$$\frac{\partial f(\tau, w, p_T)}{\partial \tau} = \frac{f_{\rm eq} - f}{\tau_{\rm eq}} \tag{5.28}$$

5.2.6 The integral equation obeyed by all moments

We will work with the following moments of the one-particle distribution function [165, 168]

$$\mathcal{M}^{nl}[f] \equiv \int dP\,(p\cdot u)^n\,(p\cdot z)^{2l}\,f(\tau,w,p_T)\,. \tag{5.29}$$

with $\int dP$ is the Lorentz-invariant momentum integration measure. To write $\int dP$ by using w, v, and p_T variables, we need to take the derivative for Eq. (5.7) and Eq. (5.8)

$$\frac{dv}{dw} = \frac{1}{2}(w^2 + \left(m^2 + \vec{p}_T^{\,2}\right)\tau^2)^{-\frac{1}{2}}(2w) = \frac{w}{\sqrt{w^2 + (m^2+\vec{p}_T^{\,2})\,\tau^2}} = \frac{w}{v} \quad \Rightarrow \quad dv = \frac{w}{v}dw\,,$$

and

$$\tau^2 dp_L = tdw + zdv = tdw + \frac{zw}{v}dw = \underbrace{(tv+zw)}_{E\tau^2}\frac{dw}{v} \qquad \Rightarrow \qquad dp_L = \frac{E}{v}dw\,,$$

applying this result in

$$dP = \frac{d^4p}{(2\pi)^4}\,2\pi\delta\left(p^2-m^2\right)2\theta(p^0) = \frac{dp_L}{(2\pi)^3 p^0}d^2p_T\,,$$

we obtain

$$dP = \frac{dw\,d^2p_T}{(2\pi)^3 v}\,, \tag{5.30}$$

where $p^0 = E$. In principle, powers of p_T^2 could also appear in a general moment, however, such moments can be expressed as a linear combination of the two-index moment appearing above using $p^2 = m^2$ to write $p_T^2 = (p\cdot u)^2 - (p\cdot z)^2 - m^2$. Some specific cases of $\mathcal{M}^{nl}$ map to familiar quantities, e.g., $n = 1$ and $l = 0$ maps to the number density $\mathfrak{n} = \mathcal{M}^{10}$, $n = 2$ and $l = 0$ maps to the energy density, and $n = 0$ and $l = 1$ maps to the longitudinal pressure, P_L. The transverse pressure, P_T, can be obtained by using $p_T^2 = (p\cdot u)^2 - (p\cdot z)^2 - m^2$

to obtain $P_T = \mathcal{M}^{20} - \mathcal{M}^{01} - m^2\mathcal{M}^{00}$. For a Boltzmann equilibrium distribution function, these moments reduce to [2]

$$\mathcal{M}^{nl}_{\rm eq}(T,m) \equiv \mathcal{M}^{nl}[f_{\rm eq}] = \frac{2T^{n+2l+2}}{(2\pi)^2(2l+1)} \int_0^\infty d\hat{p}\, \hat{p}^{n+2l+1} \left(1+\frac{\hat{m}^2}{\hat{p}^2}\right)^{(n-1)/2} e^{-\sqrt{\hat{p}^2+\hat{m}^2}}\,. \quad (5.31)$$

We note that by changing variables to $x \equiv \sqrt{\hat{p}^2+\hat{m}^2}$ it is possible to perform this integral analytically in terms of generalized hypergeometric functions, however, the resulting expression is not straightforward to evaluate for integer-valued n and l. For this reason, it is typically easier to simply evaluate it numerically.

In what follows, we will present results for these general moments scaled by their equilibrium values, i.e.,

$$\overline{\mathcal{M}}^{nl} \equiv \frac{\mathcal{M}^{nl}}{\mathcal{M}^{nl}_{\rm eq}}\,. \quad (5.32)$$

which gives a measure of how far the system is from equilibrium. In the late-time limit (the limit of non-interacting particles $\tau \to \infty$), if the system approaches equilibrium, then $\overline{\mathcal{M}}^{nl} \to 1$. In the general case, using the boost-invariant variables introduced earlier, one finds that the general moments can be expressed as

$$\begin{aligned} \mathcal{M}^{nl}[f] &= \int \frac{dw\, d^2p_T}{(2\pi)^3 v} \left(\frac{v}{\tau}\right)^n \left(\frac{w}{\tau}\right)^{2l} f(\tau,w,p_T)\,, \\ &= \frac{1}{(2\pi)^3\,\tau^{n+2l}} \int dw\, d^2p_T\, v^{n-1} w^{2l}\, f(\tau,w,p_T)\,. \end{aligned} \quad (5.33)$$

Taking a general moment of Eq. (5.26) one obtains

$$\mathcal{M}^{nl}(\tau) = D(\tau,\tau_0)\mathcal{M}^{nl}_0(\tau) + \int_{\tau_0}^{\tau} \frac{d\tau'}{\tau_{\rm eq}(\tau')}\, D(\tau,\tau')\, \mathcal{M}^{nl}_{\rm eq}(\tau').$$

[2] For more details see the appendix (E.2).

Evaluating the integrals necessary results in

$$\begin{aligned}\mathcal{M}^{nl} &= \frac{D(\tau,\tau_0)\Lambda_0^{n+2l+2}}{(2\pi)^2}\tilde{H}^{nl}\left(\frac{\tau_0}{\tau\sqrt{1+\xi_0}},\frac{m}{\Lambda_0}\right) \\ &\quad + \frac{1}{(2\pi)^2}\int_{\tau_0}^{\tau}\frac{d\tau'}{\tau_{\rm eq}(\tau')}\,D(\tau,\tau')\,T^{n+2l+2}(\tau')\,\tilde{H}^{nl}\left(\frac{\tau'}{\tau},\frac{m}{T(\tau')}\right)\,, \quad (5.34)\end{aligned}$$

where

$$\tilde{H}^{nl}(y,z) = \int_0^\infty du\,u^{n+2l+1}e^{-\sqrt{u^2+z^2}}\,H^{nl}\Big(y,\frac{z}{u}\Big)\,, \quad (5.35)$$

with

$$H^{nl}(y,x) = \frac{2\,y^{2l+1}(1+x^2)^{\frac{n-1}{2}}}{2l+1}\,{}_2F_1\left(l+\frac{1}{2},\frac{1-n}{2};l+\frac{3}{2};\frac{1-y^2}{1+x^2}\right), \quad (5.36)$$

and ${}_2F_1$ being a hypergeometric function. Finally, specializing to the case $n=2$ and $l=0$ and requiring conservation of energy $\varepsilon(\tau)=\varepsilon_{\rm eq}(T)$, also known as Landau matching, we obtain the following integral equation

$$\begin{aligned}&2T^4(\tau)\,\hat{m}^2\left[3K_2\left(\frac{m}{T(\tau)}\right)+\hat{m}K_1\left(\frac{m}{T(\tau)}\right)\right] \\ &\quad = D(\tau,\tau_0)\Lambda_0^4\tilde{H}^{20}\left(\frac{\tau_0}{\tau\sqrt{1+\xi_0}},\frac{m}{\Lambda_0}\right)+\int_{\tau_0}^{\tau}\frac{d\tau'}{\tau_{\rm eq}(\tau')}\,D(\tau,\tau')\,T^4(\tau')\tilde{H}^{20}\left(\frac{\tau'}{\tau},\frac{m}{T(\tau')}\right). \quad (5.37)\end{aligned}$$

This is the integral equation obtained originally in Ref. [190] with the understanding that $\tilde{H}^{20}=\tilde{\mathcal{H}}_2$ defined therein. The integral equation for the temperature of the system at a particular time $T(\tau)$ can not be solved analytically. Therefore, an iterative method is used to numerically approximate the solution. The iterative method involves starting with an initial guess for $T(\tau)$, plugging it into the right hand side of the integral equation, and using the resulting solution as the next guess. This process is repeated until the solution converges to a desired level of accuracy. After that the solution can be used in Eq. (5.34) to compute all moments.

5.2.7 Viscous corrections expressed in terms of moments

For comparisons to come, here we collect expressions for the viscous corrections written in terms of the moments computed herein. We start by noting that the equilibrium pressure can be expressed as

$$P = -\frac{1}{3}\Delta_{\mu\nu}\int dP\, p^\mu p^\nu\, f_{\rm eq} = \frac{1}{3}\left[\mathcal{M}^{20}_{\rm eq} - m^2\mathcal{M}^{00}_{\rm eq}\right] . \tag{5.38}$$

Next, we note that the bulk viscous correction can be expressed as

$$\begin{aligned}
\Pi &= -\frac{1}{3}\Delta_{\mu\nu}\int dP\, p^\mu p^\nu\, (f - f_{\rm eq}) \\
&= \frac{1}{3}\left[\mathcal{M}^{20} - m^2\mathcal{M}^{00}\right] - \frac{1}{3}\left[\mathcal{M}^{20}_{\rm eq} - m^2\mathcal{M}^{00}_{\rm eq}\right] \\
&= -\frac{1}{3}m^2\left[\mathcal{M}^{00} - \mathcal{M}^{00}_{\rm eq}\right] ,
\end{aligned} \tag{5.39}$$

where we have used $\Delta^{\mu\nu} = g^{\mu\nu} - u^\mu u^\nu$ and in going from the second the third lines we have used Landau matching, which implies that $\mathcal{M}^{20} = \mathcal{M}^{20}_{\rm eq}$. To characterize the size of the bulk viscous correction relative to the equilibrium pressure, one can scale it by the equilibrium pressure to obtain a dimensionless measure of the bulk viscous pressure, $\tilde{\Pi}$. The resulting quantity is

$$\tilde{\Pi} \equiv \frac{\Pi}{P} = -\frac{m^2\left(\mathcal{M}^{00} - \mathcal{M}^{00}_{\rm eq}\right)}{\mathcal{M}^{20}_{\rm eq} - m^2\mathcal{M}^{00}_{\rm eq}} . \tag{5.40}$$

From this we see that $\tilde{\Pi}$ is proportional to the difference of the $n = 0$ and $l = 0$ moment from its equilibrium value. We note that for the behavior of these quantities under time evolution, if $\mathcal{M}^{00}$ does not possess an attractor, meaning that its time evolution is sensitive to the initial conditions, then this would imply that $\tilde{\Pi}$ does not possess an attractor. This implies that the behavior (the time evolution) of the bulk viscous pressure would be highly dependent on the specific conditions at the start of the evolution, and may not exhibit a well-defined

long-term behavior. Next, to compute the shear correction, it is most straightforward to start from

$$\mathcal{M}^{01} = P_L = P - \pi + \Pi\,, \tag{5.41}$$

which results in

$$\tilde{\pi} \equiv \frac{\pi}{P} = 1 - \overline{\mathcal{M}}^{01} + \tilde{\Pi}\,. \tag{5.42}$$

or one can be expressed the shear stress tensor $\pi^{\mu\nu}$ as

$$\pi^{\mu\nu} = \Delta^{\mu\nu}_{\alpha\beta} \int dP\, p^\alpha p^\beta\, (f - f_{\rm eq}), \tag{5.43}$$

where $\Delta^{\mu\nu}_{\alpha\beta} \equiv \frac{1}{2}(\Delta^\mu_\alpha \Delta^\nu_\beta + \Delta^\mu_\beta \Delta^\nu_\alpha) - \frac{1}{3}\Delta^{\mu\nu}\Delta_{\alpha\beta}$ is a traceless symmetric projection operator orthogonal to u^μ. We note that this implies that, if there exists an attractor for $\overline{\mathcal{M}}^{01}$, but not for $\tilde{\Pi}$, then $\tilde{\pi}$ will also not possess an attractor.[3] This means that the long-term behavior of the system might be sensitive to the initial conditions, and does not approach a unique attractor state.

5.3 Evaluation of the moments to first order in hydrodynamic gradients

In the context of hydrodynamics, the Grad's 14-moment approximation [223] and the Chapman-Enskog method [224] are two commonly used methods to determine the form of the distribution function close to local thermodynamic equilibrium. Both methods involve expanding $f(x,p)$ around an equilibrium distribution function $f_0(x,p)$. The relativistic version of **Grad's 14-moment approximation** is a method to describe the behavior of a fluid near equilibrium in a relativistic setting. The approximation assumes that the fluid is not in exact thermal equilibrium but is slightly out of equilibrium due to small deviations from the equilibrium state. To account for these small deviations, the approximation uses a

[3] This point was originally emphasized in refs. [208, 214].

Taylor-like series expansion in momenta truncated at quadratic order. This means that the deviation from equilibrium is expressed as a sum of terms that are quadratic in the fluid's momenta, with coefficients that depend on the dissipative fluxes of the fluid. The question of whether this series expansion is convergent is a valid one, as a power series without a small expansion parameter may not necessarily converge. However, the justification for using such an ansatz lies in the assumption that the deviations from equilibrium are small, so the higher-order terms in the series expansion are negligible. Additionally, the assumption that the coefficients in the expansion are linear in the dissipative fluxes is based on the idea that these fluxes are proportional to the deviation from equilibrium. This assumption is motivated by the fact that in many physical systems, dissipative effects are proportional to the deviation from equilibrium, so a linear relationship between the dissipative fluxes and the deviation from equilibrium is reasonable.

However, **the Chapman-Enskog method** is a perturbative approach to solving the Boltzmann transport equation, which describes the behavior of a dilute gas in terms of the evolution of its distribution function. The method involves expanding the distribution function as a power series in the Knudsen number, which is a dimensionless parameter that characterizes the ratio of the mean free path of the gas molecules to a typical macroscopic length scale of the system. The expansion is equivalent to making a gradient expansion about the local equilibrium distribution function. The expansion involves assuming that the distribution function can be written as a sum of terms that are each multiplied by a power of the Knudsen number. The first term in this expansion corresponds to the local equilibrium distribution function, while the higher-order terms correspond to deviations from equilibrium due to the presence of gradients in the fluid variables.

The main differences between the relativistic version of Grad's 14-moment approximation and the Chapman-Enskog method are:

- Expansion parameter: The 14-moment approximation expands the distribution function in terms of moments of the Boltzmann equation, while the Chapman-Enskog method expands the distribution function in a power series in the Knudsen number. The moments in the 14-moment approximation are not necessarily small, whereas the Knudsen number is assumed to be small in the Chapman-Enskog method.

- Order of expansion: The 14-moment approximation expands the distribution function up to 14th order in moments, while the Chapman-Enskog method expands the distribution function up to a desired order in the Knudsen number. The order of the expansion in the 14-moment approximation is fixed, while in the Chapman-Enskog method, the order of the expansion can be chosen based on the desired level of accuracy.

In this section we will present expressions for the shear and bulk viscosity corrected distribution functions and resulting integral moments obtained using both the 14-moment [81, 225, 226] and Chapman-Enskog [96, 224] approximations. In both cases, one can decompose the linearly-corrected one-particle distribution function as

$$f = f_{\rm eq} + \delta f_{\rm shear} + \delta f_{\rm bulk}\,. \tag{5.44}$$

Therefore, to understand the relationship between kinetic theory out of equilibrium and viscous hydrodynamics, one can consider small departures from equilibrium. In this case, the distribution function can be expressed as a sum of an equilibrium part and a small correction term, denoted by δf represents the deviation of the distribution function from equilibrium.

$$f(p^\mu, x^\mu) = f_{\rm eq}\left(\frac{p^\mu u_\mu}{T}\right)\left[1 + \delta f(p^\mu, x^\mu)\right]\,, \tag{5.45}$$

The equilibrium part is a function of the momentum p^μ and the four-velocity u^μ, given by $f_{\rm eq}\left(\frac{p^\mu u_\mu}{T}\right)$, where T is the temperature, and the out-of-equilibrium correction to the

distribution function $\delta f(p^\mu, x^\mu) \ll 1$. In the next two subsections we specify the 14-moment and Chapman-Enskog forms for $\delta f_{\rm shear}$ and $\delta f_{\rm bulk}$ and evaluate the moments of each in order to obtain the corresponding approximations at first order in gradients.

5.3.1 14-moment approximation

In the 14-moment approximation, the viscous corrections to the distribution function for a single component massive gas obeying classical statistics can be written as [227–230]

$$\delta f_{\rm shear} = f_{\rm eq} \frac{p_\mu p_\nu \pi^{\mu\nu}}{2(\varepsilon + P)T^2}\,, \tag{5.46}$$

$$\delta f_{\rm bulk} = -f_{\rm eq} \frac{\beta}{\beta_\Pi} \left[\frac{m^2}{3\,p\cdot u} - \Big(\frac{1}{3} - c_s^2\Big) p\cdot u \right] \Pi\,, \tag{5.47}$$

with $\beta = 1/T$ and

$$\beta_\Pi = \frac{5}{3}\beta\, I_{42}^{(1)} - (\varepsilon + P) c_s^2\,. \tag{5.48}$$

The thermodynamic integral $I_{42}^{(1)}$ can be expressed as [96]

$$I_{42}^{(1)} = \frac{T^5 \hat{m}^5}{30\pi^2} \left[\frac{1}{16}\Big(K_5(\hat{m}) - 7K_3(\hat{m}) + 22K_1(\hat{m}) \Big) - K_{i,1}(\hat{m}) \right], \tag{5.49}$$

with

$$K_{i,1}(\hat{m}) = \int_0^\infty \frac{d\theta}{\cosh\theta}\, \exp(-\hat{m}\cosh\theta)\,. \tag{5.50}$$

For 0+1d boost-invariant Bjorken expansion as considered in this chapter, one can write the shear tensor in terms of one independent component $\pi \equiv -\pi^{zz}$, with the other two diagonal components determined by symmetry and the tracelessness of $\pi^{\mu\nu}$, giving $\pi^{xx} = \pi^{yy} = \pi/2$. Note that in this case, all dynamical variables only depend on the longitudinal proper time τ.

Navier-Stokes shear-viscous correction

For the case of 0+1d boost-invariant Bjorken expansion one has

$$\delta f_{\rm shear} = f_{\rm eq} \frac{p_\mu p_\nu \pi^{\mu\nu}}{2(\varepsilon + P)T^2} \,, \tag{5.51}$$

$$p_\mu p_\nu \pi^{\mu\nu} = p_x p_x \pi^{xx} + p_y p_y \pi^{yy} + p_z p_z \pi^{zz} = p_x^2 \frac{\pi}{2} + p_y^2 \frac{\pi}{2} - p_z^2 \pi = \frac{\pi}{2}(p_x^2 + p_y^2 - 2p_z^2) \,,$$

using

$$E^2 = p_x^2 + p_y^2 + p_z^2 + m^2 \,,$$

then

$$p_x^2 + p_y^2 = E^2 - p_z^2 - m^2 \,,$$

therefore,

$$p_\mu p_\nu \pi^{\mu\nu} = \frac{\pi}{2}(E^2 - p_z^2 - m^2 - 2p_z^2) = \frac{\pi}{2}(E^2 - 3p_z^2 - m^2) = \frac{\pi}{2}[(p\cdot u)^2 - 3(p\cdot z)^2 - m^2] \,.$$

This gives

$$\delta f_{\rm shear} = f_{\rm eq} \frac{\pi[(p\cdot u)^2 - 3(p\cdot z)^2 - m^2]}{4(\varepsilon + P)T^2} = f_{\rm eq} \frac{\pi[(p\cdot u)^2 - 3(p\cdot z)^2 - m^2]}{4\varepsilon(1 + \frac{P}{\varepsilon})T^2} \,,$$

$$\delta f_{\rm shear,14-moment} = \frac{\bar{\pi}}{4(1+\frac{P}{\varepsilon})T^2} \left[(p\cdot u)^2 - 3(p\cdot z)^2 - m^2\right] f_{\rm eq} \,, \tag{5.52}$$

where $\bar{\pi} = \pi/\varepsilon$. Computing the moments of $\delta f_{\rm shear}^{\rm 14\text{-}moment}$ one obtains

$$\mathcal{M}^{nl}_{\rm shear,14-moment} = \frac{\bar{\pi}}{4(1+\frac{P}{\varepsilon})T^2} \left[\mathcal{M}^{n+2,l}_{\rm eq} - 3\mathcal{M}^{n,l+1}_{\rm eq} - m^2 \mathcal{M}^{n,l}_{\rm eq}\right] . \tag{5.53}$$

The Navier-Stokes shear-viscous correction term in the equation for the energy-momentum tensor is given by

$$\pi^{\mu\nu} = \eta\sigma^{\mu\nu}\,,$$

with

$$\sigma^{\mu\nu} = 2\nabla^{(\mu}u^{\nu)} - \frac{2}{3}\Delta^{\mu\nu}\nabla_\gamma u^\gamma\,.$$

Using

$$\nabla^{(\mu}u^{\nu)} = \frac{1}{2}(\nabla^\mu u^\nu + \nabla^\nu u^\mu)\,,$$

one obtains

$$\theta = \nabla_\gamma u^\gamma = \frac{1}{\tau}\,,$$

$$\pi^{\mu\nu} = 2\,\frac{1}{2}\,\eta\,(\nabla^\mu u^\nu + \nabla^\nu u^\mu) - \frac{2}{3\tau}\eta\Delta^{\mu\nu}\,,$$

$$\pi^{xx} = 2\,\frac{1}{2}\,\eta\,(\nabla^x u^x + \nabla^x u^x) - \frac{2}{3\tau}\eta\Delta^{xx} = \frac{2}{3\tau}\eta = \pi^{yy}\,,$$

with $\Delta^{xx} = \Delta^{yy} = -1$, and $\nabla^x u^x = \nabla^x u^x$. From the tracelessness, one has we find that

$$\pi^{xx} + \pi^{yy} + \pi^{zz} = 0\,,$$

then

$$\pi^{zz} = -\pi^{xx} - \pi^{yy} = -\frac{4}{3\tau}\eta\,.$$

As a result

$$\pi^{zz} = -\pi = -\frac{4}{3\tau}\eta\,.$$

Therefore, at first order in the gradient expansion, which corresponds to the Navier-Stokes (NS) limit, one has

$$\pi^{\rm NS}(\tau) = \frac{4\eta}{3\tau}\,. \tag{5.54}$$

Using $\bar{\eta} \equiv \eta/s$, and $\varepsilon + P = Ts$, one obtains

$$\pi^{\rm NS}(\tau) = \frac{4\eta}{3\tau} = \frac{4\bar{\eta}s}{3\tau} = \frac{4\bar{\eta}(\varepsilon + P)}{3\tau T}\,,$$

which, when written in terms of $\overline{\tau} = \tau/\tau_{\rm eq}$ becomes

$$\pi^{\rm NS} = \frac{4\bar{\eta}(\varepsilon + P)}{3\overline{\tau}\tau_{\rm eq} T}\,,$$

or

$$\bar{\pi}^{\rm NS} = \frac{4\bar{\eta}}{3\overline{\tau}\tau_{\rm eq} T}(1 + \frac{P}{\varepsilon})\,.$$

Using $\eta = \frac{\tau_{\rm eq} P}{15}\kappa(\hat{m})$, $\bar{\eta} \equiv \eta/s$, and $\varepsilon + P = Ts$

$$\bar{\pi}^{\rm NS} = \frac{4\eta}{3\overline{\tau}\tau_{\rm eq} Ts}\left(1 + \frac{P}{\varepsilon}\right) = \frac{4}{3\overline{\tau}\tau_{\rm eq}(P+\varepsilon)}\left(1 + \frac{P}{\varepsilon}\right)\cdot\frac{\tau_{\rm eq}P}{15}\kappa(\hat{m}) = \frac{4}{45\bar{\tau}(P+\varepsilon)}(1+\frac{P}{\varepsilon})\cdot P\kappa(\hat{m})\,.$$

Using $\gamma(\hat{m}) \equiv \frac{3}{\kappa(\hat{m})}\left(1 + \frac{P}{\varepsilon}\right)$ one finds

$$\bar{\pi}^{\rm NS} = \frac{4}{45\bar{\tau}(P+\varepsilon)}\left(1 + \frac{P}{\varepsilon}\right)\cdot P\cdot\frac{3}{\gamma(\hat{m})}\left(1 + \frac{\varepsilon}{P}\right) = \frac{12}{45\bar{\tau}}\frac{P}{\varepsilon}\cdot\frac{1}{\gamma(\hat{m})}\left(1 + \frac{\varepsilon}{P}\right).$$

Therefore,

$$\bar{\pi}^{\rm NS} = \frac{4}{15\gamma(\hat{m})\overline{\tau}}\left(1 + \frac{P}{\varepsilon}\right)\,, \tag{5.55}$$

applying this result into Eq. (5.53), the general moment for the 14-moment approximation in shear-viscous correction in the Navier-Stokes limit is

$$\mathcal{M}^{nl,{\rm NS}}_{\rm shear,14-moment} = \frac{1}{15\,\overline{\tau}\,T^2\,\gamma(\hat{m})}\left[\mathcal{M}^{n+2,l}_{\rm eq} - 3\mathcal{M}^{n,l+1}_{\rm eq} - m^2\mathcal{M}^{n,l}_{\rm eq}\right]. \tag{5.56}$$

Navier-Stokes bulk-viscous correction

Taking the moments of Eq. (5.47), one obtains

$$\mathcal{M}^{nl}_{\text{bulk,14-moment}} = -\frac{\beta}{3\beta_\Pi}\left[m^2\mathcal{M}^{n-1,l}_{\text{eq}} - \left(1-3c_s^2\right)\mathcal{M}^{n+1,l}_{\text{eq}}\right]\Pi\,. \tag{5.57}$$

To proceed, one can use the fact that $\Pi = -\tau_{\text{eq}}\,\beta_\Pi\,\partial_\mu u^\mu$ [96]. At first order, for boost-invariant Bjorken flow, since $\partial_\mu u^\mu = 1/\tau$, this reduces to

$$\Pi^{\text{NS}} = -\beta_\Pi/\overline{\tau}\,, \tag{5.58}$$

giving

$$\mathcal{M}^{nl,\text{NS}}_{\text{bulk,14-moment}} = \frac{1}{3\,\overline{\tau}\,T}\left[m^2\mathcal{M}^{n-1,l}_{\text{eq}} - \left(1-3c_s^2\right)\mathcal{M}^{n+1,l}_{\text{eq}}\right]. \tag{5.59}$$

Total Navier-Stokes viscous correction

Finally, by adding the shear and bulk corrections to the equilibrium result and scaling by the equilibrium moments, we obtain the following expression for the scaled moments in the Navier-Stokes limit within the 14-moment approximation

$$\begin{aligned}\overline{\mathcal{M}}^{nl,\text{NS}}_{\text{14-moment}} \;=\; & 1 + \frac{1}{15\,\overline{\tau}\,T^2\,\gamma(\hat{m})}\left[\mathcal{M}^{n+2,l}_{\text{eq}} - 3\mathcal{M}^{n,l+1}_{\text{eq}} - m^2\mathcal{M}^{n,l}_{\text{eq}}\right] \\ & + \frac{1}{3\,\overline{\tau}\,T}\,\frac{\left[m^2\mathcal{M}^{n-1,l}_{\text{eq}} - \left(1-3c_s^2\right)\mathcal{M}^{n+1,l}_{\text{eq}}\right]}{\mathcal{M}^{n,l}_{\text{eq}}}\,. \end{aligned} \tag{5.60}$$

5.3.2 Chapman-Enskog approximation

Navier-Stokes shear-viscous correction

In the Chapman-Enskog approximation one has the following shear viscous correction [96]

$$\delta f_{\text{shear,CE}} = \frac{\beta f_{\text{eq}}}{2(u\cdot p)\beta_\pi}\,p^\mu p^\nu \pi_{\mu\nu}\,. \tag{5.61}$$

Using

$$p_\mu p_\nu \pi^{\mu\nu} = \frac{\pi}{2}[(p\cdot u)^2 - 3(p\cdot z)^2 - m^2]\,,$$

and

$$\bar{\pi}^{\rm NS} = \frac{4}{15\gamma(\hat{m})\overline{\tau}}\left(1+\frac{P}{\varepsilon}\right)\,,$$

one obtains

$$\delta f_{\rm shear,CE} = \frac{\beta f_{\rm eq}}{2(u\cdot p)\beta\, I_{42}^{(1)}}\,\frac{\pi}{2}[(p\cdot u)^2 - 3(p\cdot z)^2 - m^2] = \frac{\bar{\pi}}{4\, I_{42}^{(1)}}[(p\cdot u)^2 - 3(p\cdot z)^2 - m^2]f_{\rm eq}\,.$$

In the Navier-Stokes limit Eq. (5.54) one obtains,

$$\delta f_{\rm shear,CE} = \frac{4}{15\gamma(\hat{m})\overline{\tau}\cdot 4\, I_{42}^{(1)}}\left(1+\frac{P}{\varepsilon}\right)[(p\cdot u)^2 - 3(p\cdot z)^2 - m^2]f_{\rm eq}\,,$$

giving

$$\delta f_{\rm shear,CE} = \frac{(\varepsilon+P)}{15\gamma(\hat{m})\overline{\tau}\, I_{42}^{(1)}}[(p\cdot u) - 3(p\cdot u)^{-1}(p\cdot z)^2 - m^2(p\cdot u)^{-1}]f_{\rm eq}\,,$$

where $\beta_\pi = \beta\, I_{42}^{(1)}$. Following a similar procedure as was used for the 14-moment approximation, ones find that, in the Navier-Stokes limit, the moments of the shear viscous correction become

$$\mathcal{M}^{nl,\rm NS}_{\rm shear,CE} = \frac{\varepsilon+P}{15\,\overline{\tau}\,\gamma(\hat{m})\, I_{42}^{(1)}}\left[\mathcal{M}^{n+1,l}_{\rm eq} - 3\mathcal{M}^{n-1,l+1}_{\rm eq} - m^2\mathcal{M}^{n-1,l}_{\rm eq}\right]\,, \tag{5.62}$$

with $I_{42}^{(1)}$ given in Eq. (5.49) and $\gamma(\hat{m})$ given in Eq. (5.21).

Navier-Stokes bulk-viscous correction

The bulk viscous correction in the Chapman-Enskog approximation can be written as [96]

$$\delta f_{\rm bulk,CE} = -\frac{\beta f_{\rm eq}}{3(u\cdot p)\beta_\Pi}\left[m^2 - \left(1-3c_s^2\right)(u\cdot p)^2\right]\Pi\,, \tag{5.63}$$

which is precisely the same form as the 14-moment approximation and hence the moments reduce to Eq. (5.59).

Total Navier-Stokes viscous correction

Adding the shear and bulk corrections to the equilibrium result and scaling by the equilibrium moments, we obtain the following expression for the scaled moments in the Navier-Stokes limit within the Chapman-Enskog approximation

$$\begin{aligned}\overline{\mathcal{M}}^{nl,\mathrm{NS}}_{\mathrm{CE}} &= 1+\frac{\varepsilon+P}{15\,\overline{\tau}\,\gamma(\hat{m})\,I^{(1)}_{42}}\frac{\left[\mathcal{M}^{n+1,l}_{\mathrm{eq}}-3\mathcal{M}^{n-1,l+1}_{\mathrm{eq}}-m^2\mathcal{M}^{n-1,l}_{\mathrm{eq}}\right]}{\mathcal{M}^{n,l}_{\mathrm{eq}}} \\ &\quad +\frac{1}{3\,\overline{\tau}\,T}\frac{\left[m^2\mathcal{M}^{n-1,l}_{\mathrm{eq}}-(1-3c_s^2)\,\mathcal{M}^{n+1,l}_{\mathrm{eq}}\right]}{\mathcal{M}^{n,l}_{\mathrm{eq}}}\,. \qquad (5.64)\end{aligned}$$

5.4 Results

The integral equation (5.37) can be solved iteratively for $T(\tau)$ and, once converged to the desired accuracy, this solution can be used in Eq. (5.34) to compute all moments. For the iterative solution, we discretized $T(\tau)$ on a logarithmic grid in time with 4096 points. We consider two cases: (a) holding the initial energy density, ε_0, and initialization time, τ_0, fixed, while varying the initial momentum anisotropy, ξ_0; and (b) holding the initial energy density, ε_0, and the initial momentum anisotropy, ξ_0 fixed, while varying the initialization time, τ_0. These two scenarios allow us to assess whether or not forward and early-time (or pull-back) attractors exist, respectively. In both cases, we hold the specific shear viscosity $\bar{\eta} = \eta/s$ fixed during the entire evolution. In both cases, the initial energy density used corresponds to a massive gas at a temperature of $T_0 = 1$ GeV and the final evolution time was held fixed at $\tau_f = 100$ fm/c. Additionally, in both cases we iterated the integral equation for 200 iterations, which allowed for convergence of the result to 8 digits at all proper times. For case (a), we used $\tau_0 = 0.1$ fm/c and, for case (b), we used $\xi_0 = 0$. We consider three constant masses of $m = 0.2$ GeV, $m = 1$ GeV, and $m = 5$ GeV. We note that we have explicitly

checked that the small mass limit our results converge to the conformal limit presented in Ref. [165]. The `RTA-MASSIVE-CUDA` code used to generate all results can be obtained using Ref. [231].

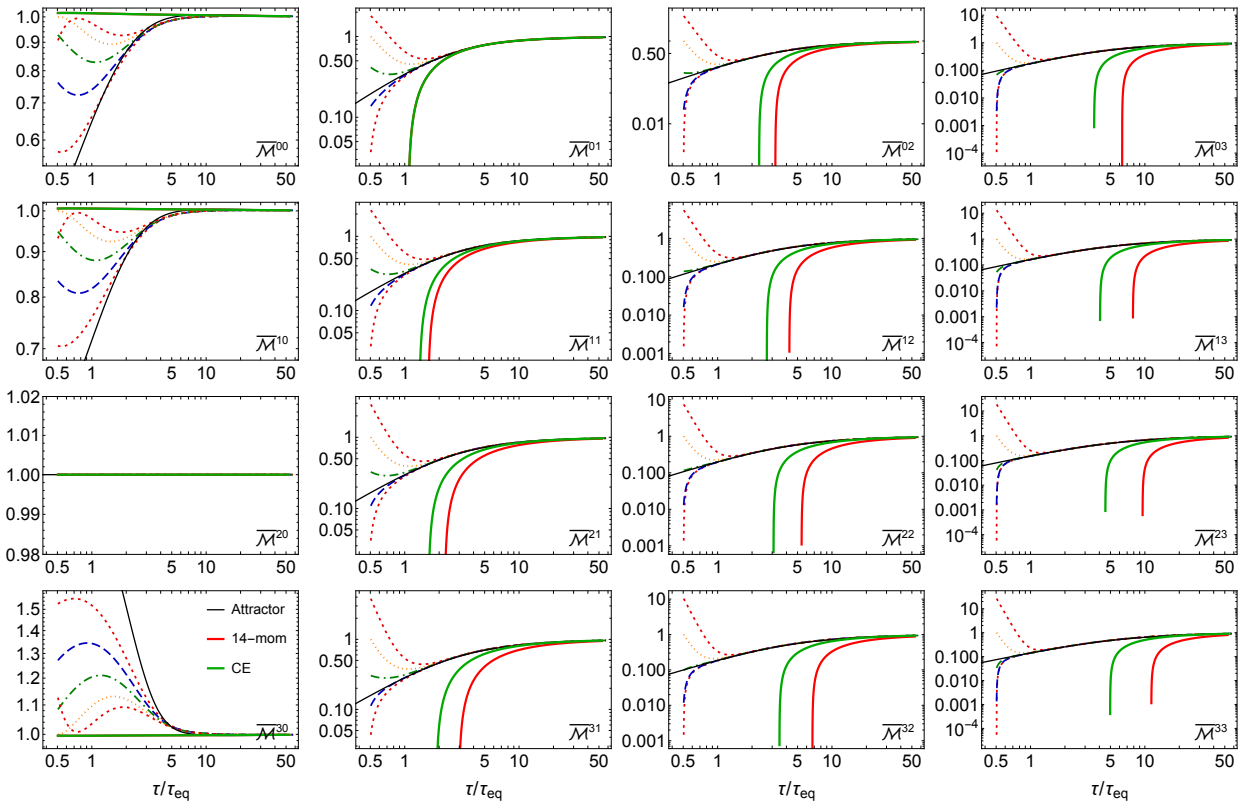

Figure 2: Scaled moments $\overline{\mathcal{M}}^{nl}$ as a function of rescaled time for the case $m = 0.2$ GeV. The non-solid lines are specific initial conditions initialized at $\tau_0 = 0.1$ fm/c with $T_0 = 1$ GeV and $\alpha_0 = 1/\sqrt{1+\xi_0} \in \{0.12, 0.25, 0.5, 1, 2\}$. The solid black lines correspond to the attractor solution, the solid red lines are the first-order 14-moment predictions in Eq. (5.60), and the solid green lines are the first-order Chapman-Enskog predictions in Eq. (5.64).

5.4.1 General moments

In Fig. 2 we present our first results for the scaled moments as a function of rescaled time $\overline{\tau} = \tau/\tau_{\text{eq}}$, which correspond to varying the initial anisotropy while holding the initialization time and initial temperature fixed using a constant mass of $m = 0.2$ GeV. The relaxation time used depends on both the mass and temperature as detailed in Eq. (5.20). The non-solid lines are specific initial conditions initialized at $\tau_0 = 0.1$ fm/c with $T_0 = 1$ GeV and

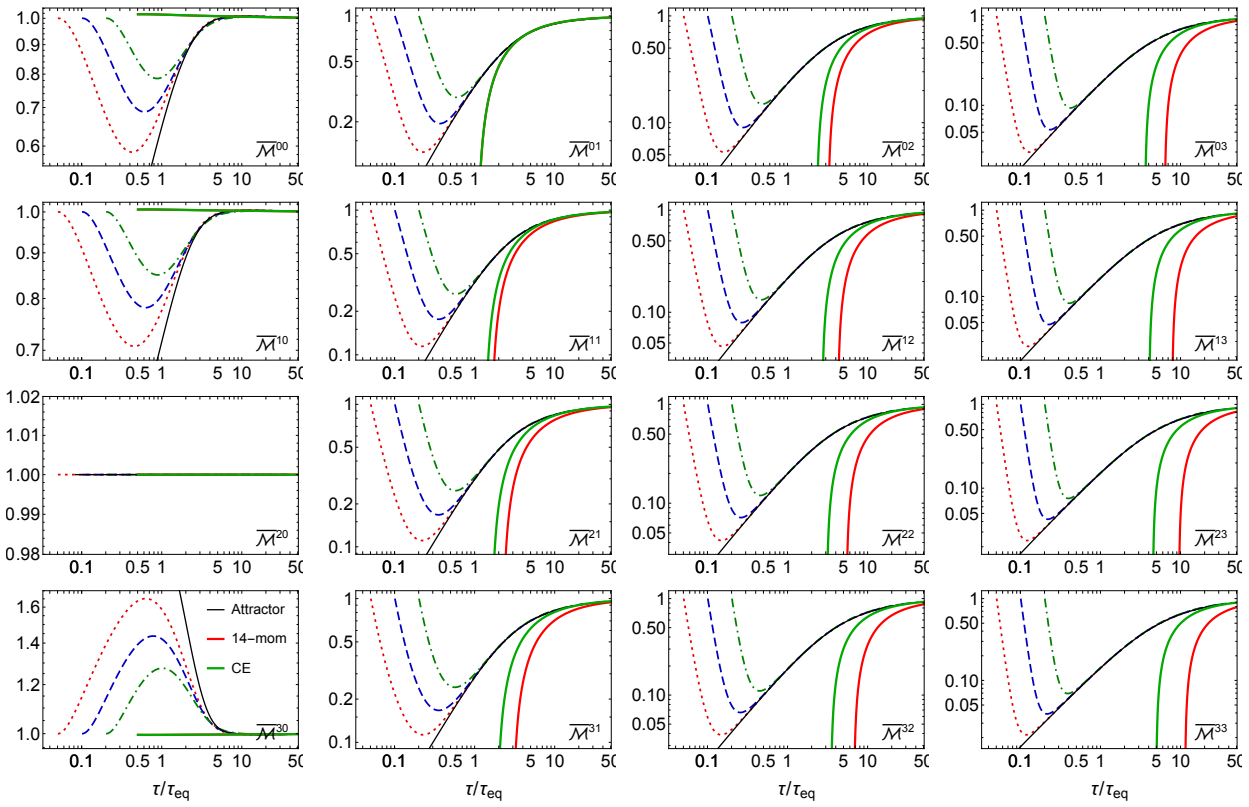

Figure 3: Scaled moments $\overline{\mathcal{M}}^{nl}$ as a function of rescaled time for the case $m = 0.2$ GeV. The non-solid lines are specific initial conditions initialized with $T_0 = 1$ GeV and $\xi_0 = 0$ at $\tau_0 \in \{0.01, 0.02, 0.04\}$ fm/c. Line styles are the same as in Fig. 2.

$\alpha_0 = 1/\sqrt{1+\xi_0} \in \{0.12, 0.25, 0.5, 1, 2\}$. The solid black lines correspond to the attractor solution, the solid red lines are the first-order 14-moment predictions in Eq. (5.60), and the solid green lines are the first-order Chapman-Enskog predictions in Eq. (5.64). To obtain the two first-order curves, we evaluated Eqs. (5.60) and (5.64) using the temperature evolution obtained from the exact solution. The attractor lines (black solid line) were obtained by initializing the system at $\tau_0 = 0.01$ fm/c with a high-degree of momentum anisotropy of $\alpha_0 = 1/\sqrt{1+\xi_0} = 0.1$, corresponding to $\xi_0 = 99$. We note that in this figure and similar panel figures that follow, the fact that the scaled moment $\overline{\mathcal{M}}^{20}$ is equal to one at all times is due to energy conservation and any deviations from one allow us to gauge the suitability of the discretization used and the convergence of the iterative solution.

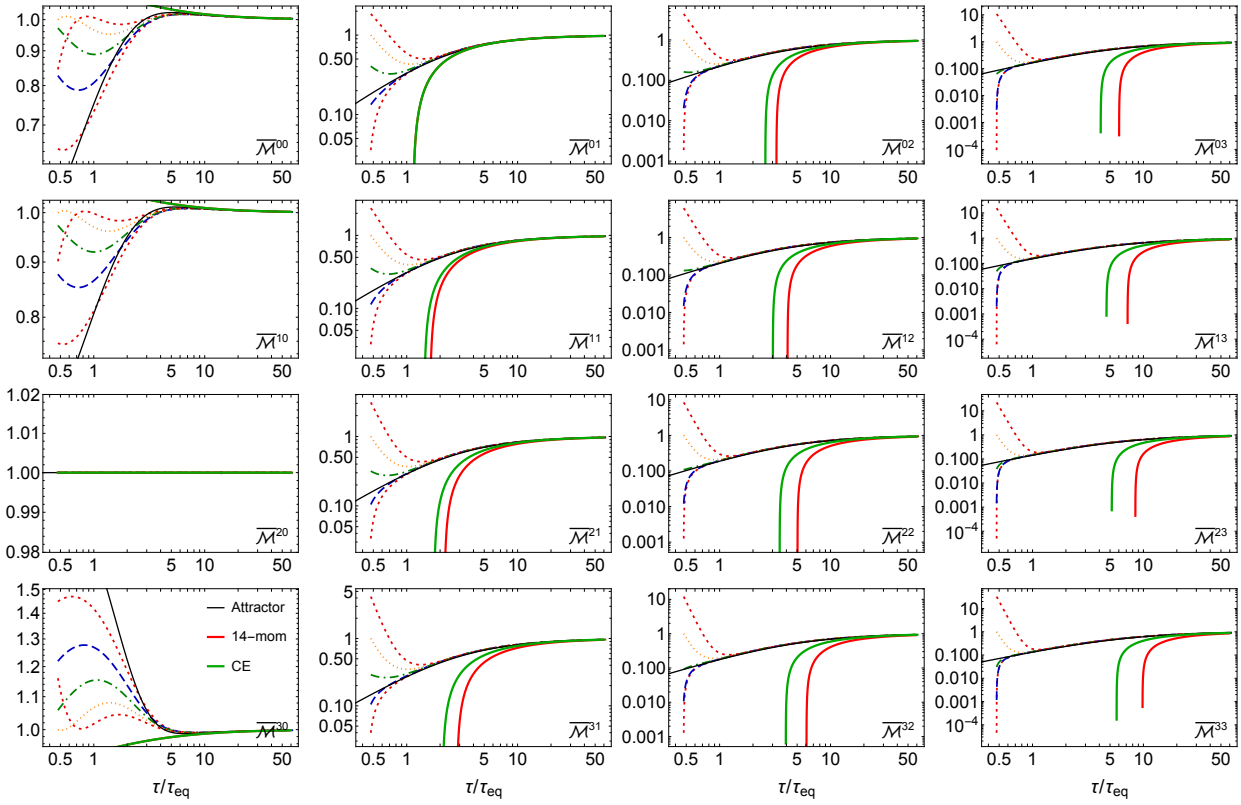

Figure 4: Scaled moments $\overline{\mathcal{M}}^{nl}$ as a function of rescaled time for the case $m = 1$ GeV. Initial conditions and line styles are the same as in Fig. 2.

As can be seen from Fig. 2, all moments collapse towards the first-order viscous hydrodynamics predictions at late times, with lower-order moments typically converging more quickly than higher-order moments. For the case of moments with $l = 0$, the two first-order schemes Chapman-Enskog and 14-moment coincide identically. For moments with $l \geq 1$, we find that, for $m = 0.2$ GeV, the first-order Chapman-Enskog approximation form for the one-particle distribution function performs better than the 14-moment approximation, particularly for high-order moments. That said, it is important to emphasize that both fail at early times, with the time scale for breakdown of each scheme becoming larger for higher-order moments. As demonstrated in Ref. [165], this continues to be the case if one includes second-order viscous corrections, with only resummed dissipative schemes such as anisotropic hydrodynamics [97, 98, 109, 185, 232, 233] being able to more reliably describe the

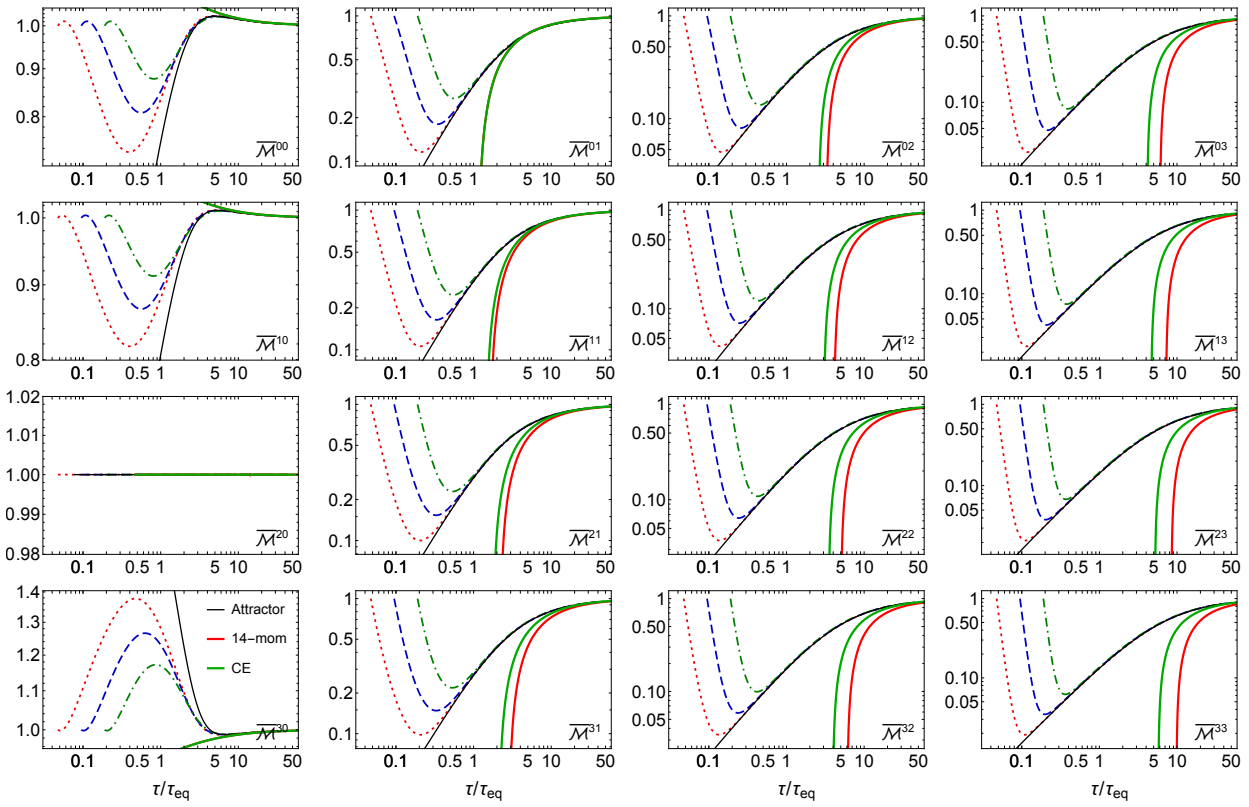

Figure 5: Scaled moments $\overline{\mathcal{M}}^{nl}$ as a function of rescaled time for the case $m = 1$ GeV. Initial conditions and line styles are the same as in Fig. 3.

early-time features of all scaled moments (see in particular the improved schemes introduced in Refs. [214, 232]).

Considering earlier times, in Fig. 2 we see that for all moments with $l \geq 1$ there are indications of a non-equilibrium attractor that extends to very early times. For the moments with $l = 0$, however, we observe that, although the solutions tend towards the attractor, the approach appears to be slower and there doesn't seem to be a complete collapse of the solutions as seen for $l \geq 1$. Finally, we note that for higher-order moments, we see a very rapid collapse to their respective attractors, indicating that the high-momentum region of the one-particle distribution function quickly approaches a universal form. This is very similar to what occurred in the conformal case [165, 232]. In those works it was noted

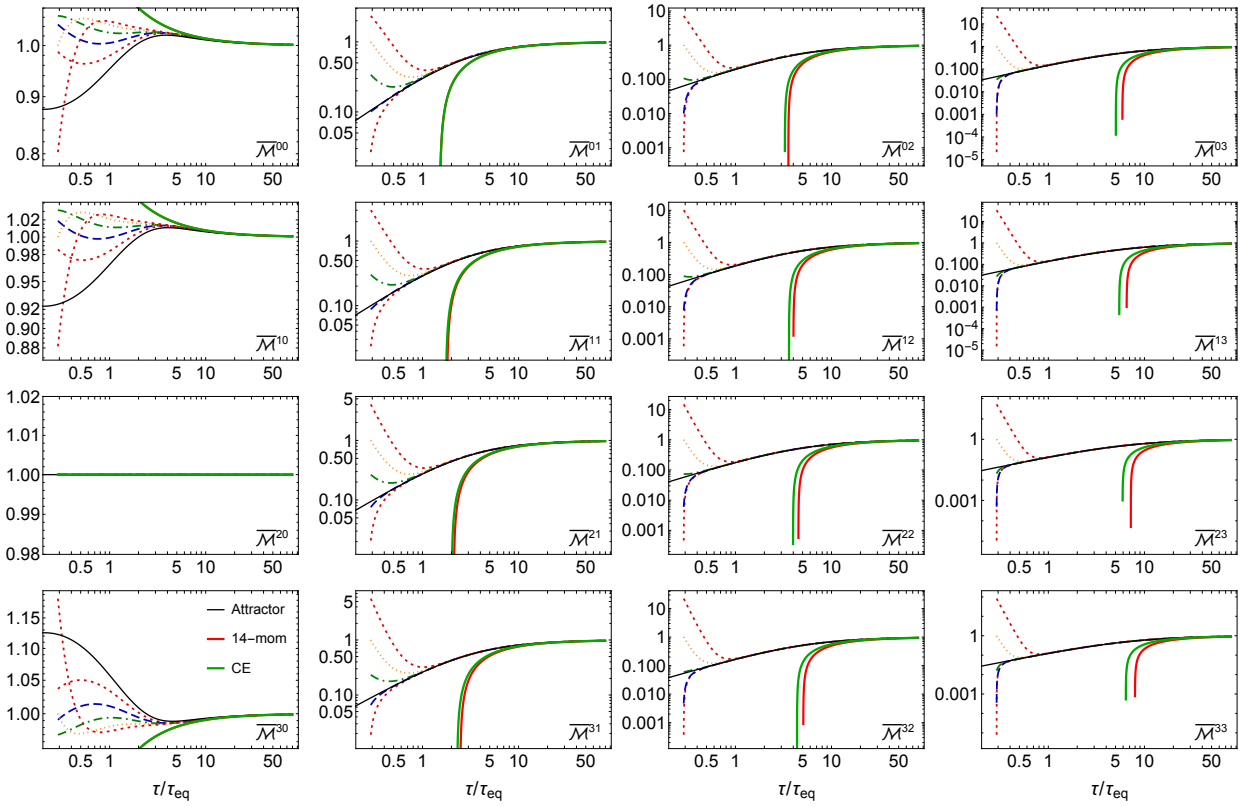

Figure 6: Scaled moments $\overline{\mathcal{M}}^{nl}$ as a function of rescaled time for the case $m = 5$ GeV. Initial conditions and line styles are the same as in Fig. 2.

that the reason for the slow hydrodynamization of the $l = 0$ moments was due to a two-component form of the exact one-particle distribution function, which includes free-streaming and thermalizing components, with the former being highly squeezed along the p_z axis but eventually decreasing in amplitude to a point that it becomes negligible.

In order to better understand whether an early-time attractor exists in this case, in Fig. 3 we present the case of holding the initial anisotropy and temperature fixed while varying the initialization time for, again, $m = 0.2$ GeV. In this figure, the non-solid lines are specific initial conditions initialized with $T_0 = 1$ GeV and $\xi_0 = 0$ at $\tau_0 \in \{0.01, 0.02, 0.04\}$ fm/c. The other line styles are the same as in Fig. 2. As can be see from figure, there clearly exists an early-time attractor for all moments with $l \geq 1$. In the moments with $l = 0$ we see a slower approach to the attractor solution, however, the three specific solutions shown

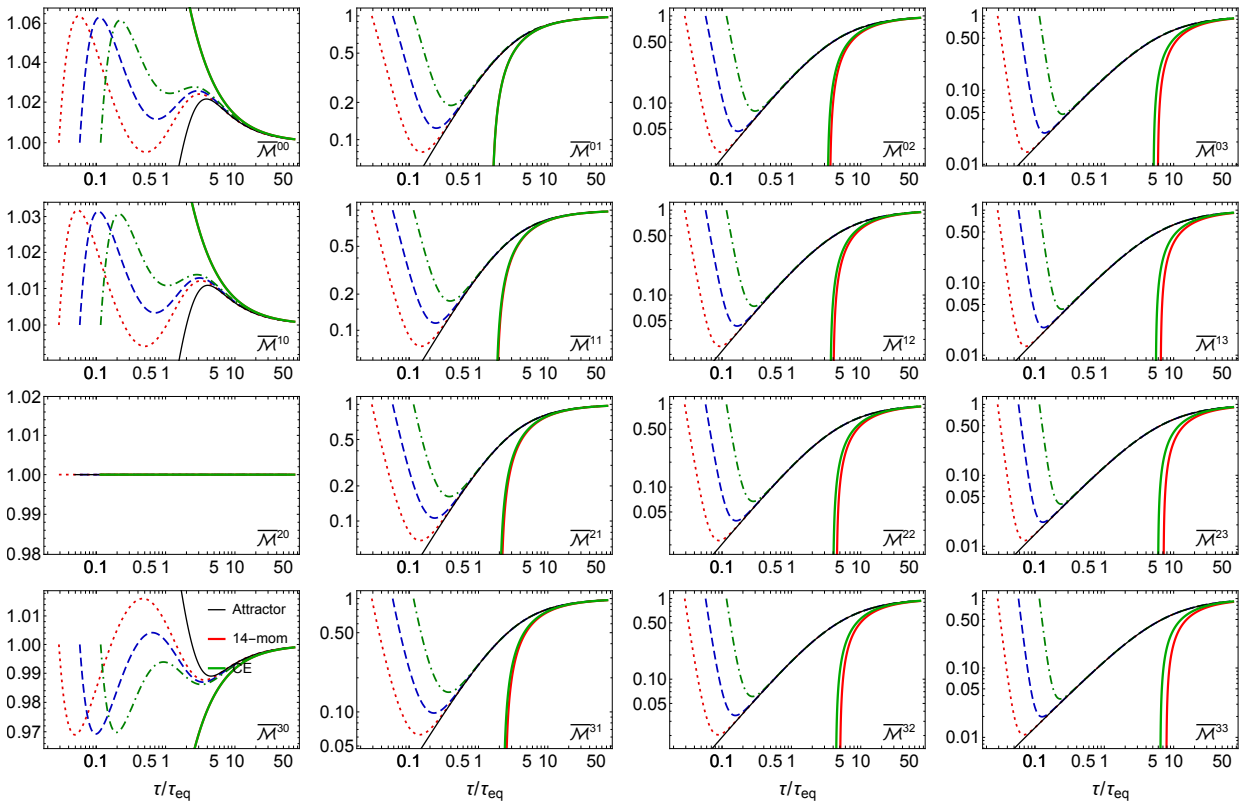

Figure 7: Scaled moments $\overline{\mathcal{M}}^{nl}$ as a function of rescaled time for the case $m = 5$ GeV. Initial conditions and line styles are the same as in Fig. 3.

approach a semi-universal result at fairly early times in the evolution. For moments with $l \geq 1$ we observe that the rate of approach of all specific solutions to the attractor are the same, being associated with the free-streaming period of the evolution.

Turning next to Figs. 4 and 5, we present the result of varying the initial anisotropy and initialization times in the case that $m = 1$ GeV. As before, the initial temperature is held fixed at $T_0 = 1$ GeV meaning that, in this case, the temperature is always less than or equal to the mass at all times. From these figures, we see again that there exists both a forward attractor and a pull-back attractor for moments with $l \geq 1$ and that moments with $l = 0$ have a slower approach to their respective attractors. Despite this, the results are still semi-universal after a short time. With respect to the first-order hydrodynamical forms, we once again see that for higher-order moments, the Chapman-Enskog form provides

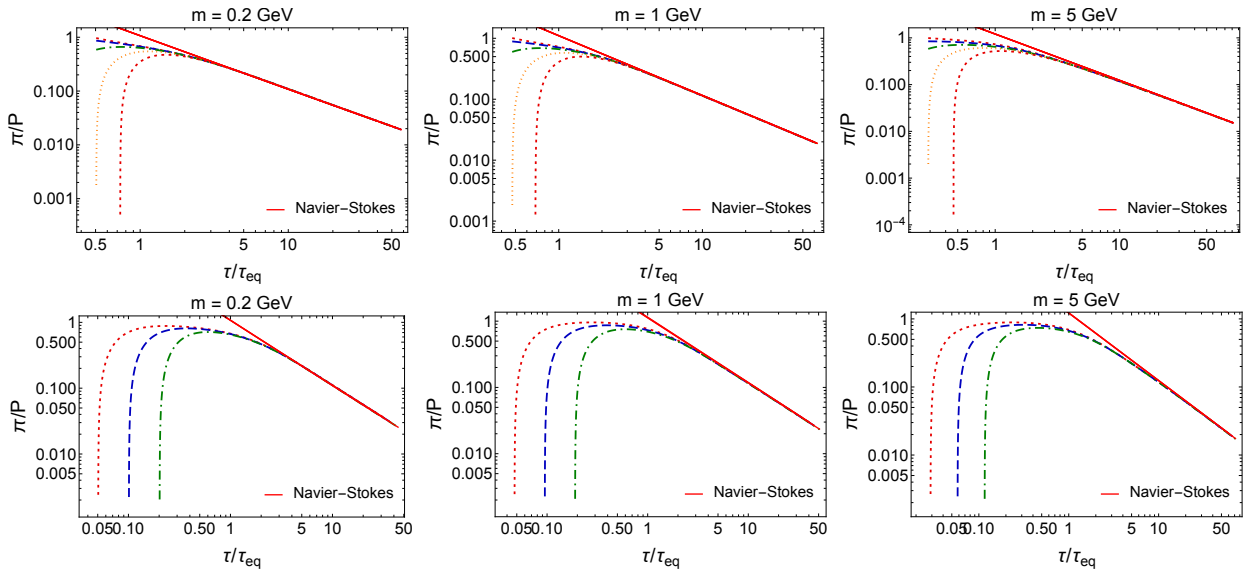

Figure 8: Scaled shear viscous correction π/P from Eq. (5.42) as a function of rescaled time $\tau/\tau_{\rm eq}$. The top row shows the result of varying the initial anisotropy and the bottom row shows the result of varying the initialization time. These correspond to the same initializations shown in Figs. 2 - 7. Columns from left to right show the cases of $m = 0.2$, 1, and 5 GeV, respectively. The non-solid curves are specific runs and the solid curve shows the first-order Navier-Stokes prediction given in Eq. (5.54).

a more quantitatively reliable asymptotic result than the 14-moment approximation for the higher-order moments, however, both first-order results break down at early times as was seen previously.

Finally, in Figs. 6 and 7 we present the result of varying the initial anisotropy and initialization times in the case that $m = 5$ GeV. Once again, the initial temperature is held fixed at $T_0 = 1$ GeV. For this case the temperature is always small compared to the mass scale. From these figures, we see again that there exists both a forward attractor and a pull-back attractor for $l \geq 1$. Similar to the other cases, we find that moments with $l = 0$ do not seem to possess early-time attractors and, based on Fig. 7, we see that not even a partial collapse of the different initialization times occurs until around $\tau/\tau_{\rm eq} \sim 3$. However, we still see a rapid collapse to an attractor for all moments with $l \geq 1$. In particular, we call attention to the panel showing $\overline{\mathcal{M}}^{01}$, which is equal to the ratio of the longitudinal pressure, P_L, divided by the equilibrium longitudinal pressure, $P_{{\rm eq},L} = P$. A similar collapse

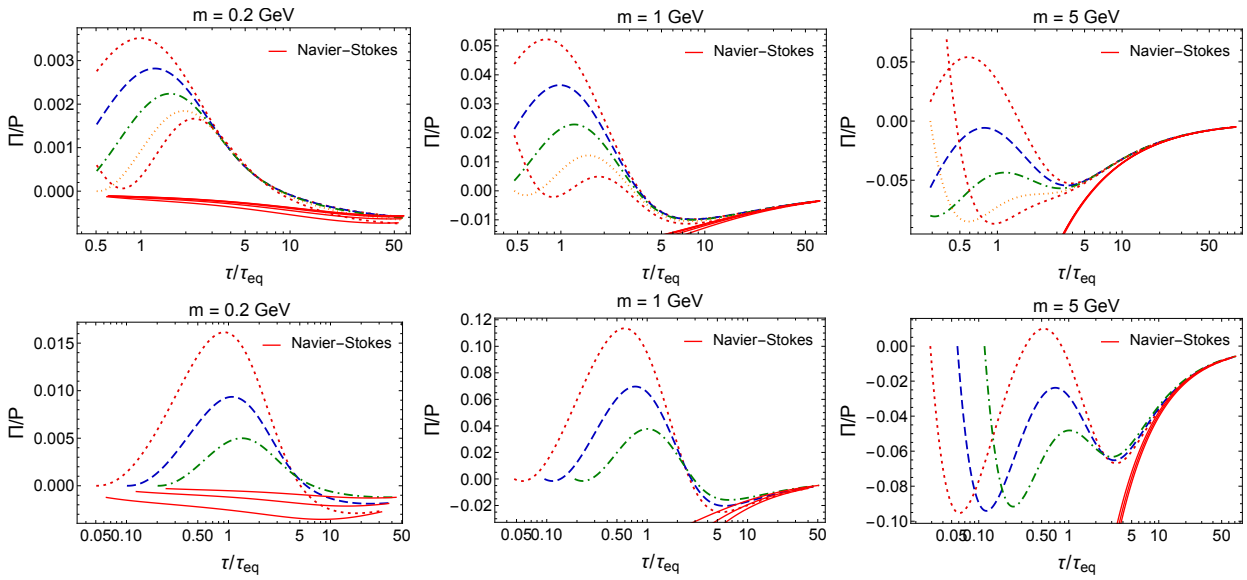

Figure 9: Scaled bulk viscous correction Π/P from Eq. (5.40) as a function of rescaled time $\tau/\tau_{\rm eq}$. The rows and columns are the same as in Fig. 8. The non-solid curves are specific runs and the solid curve shows the first-order Navier-Stokes prediction given in Eq. (5.58).

of P_L/P was reported in Refs. [208, 214], where a conformal relaxation time was employed and a smaller mass of $m = 0.2$ GeV was considered. Here we have considered even larger masses of 1 and 5 GeV and reached the same conclusion, namely that there is an attractor for P_L/P and we have extended this conclusion to include all moments with $l \geq 1$.

5.4.2 Bulk and shear viscous corrections

We now turn to extractions of the shear and bulk viscous corrections from the general moments using Eqs. (5.42) and (5.40), respectively. In Fig. 8, we present the scaled shear viscous correction π/P as a function of rescaled time $\tau/\tau_{\rm eq}$. The top row shows the result of varying the initial anisotropy and the bottom row shows the result of varying the initialization time. These correspond to the same initializations shown in Figs. 2 - 7. Columns from left to right show the cases of $m = 0.2$, 1, and 5 GeV, respectively. The non-solid curves are specific runs and the solid curve shows the first-order Navier-Stokes prediction given in Eq. (5.54). As these figures demonstrate, as the mass is increased, there no longer exists an early time collapse of the solutions to a unique attractor curve and the solutions only fully collapse

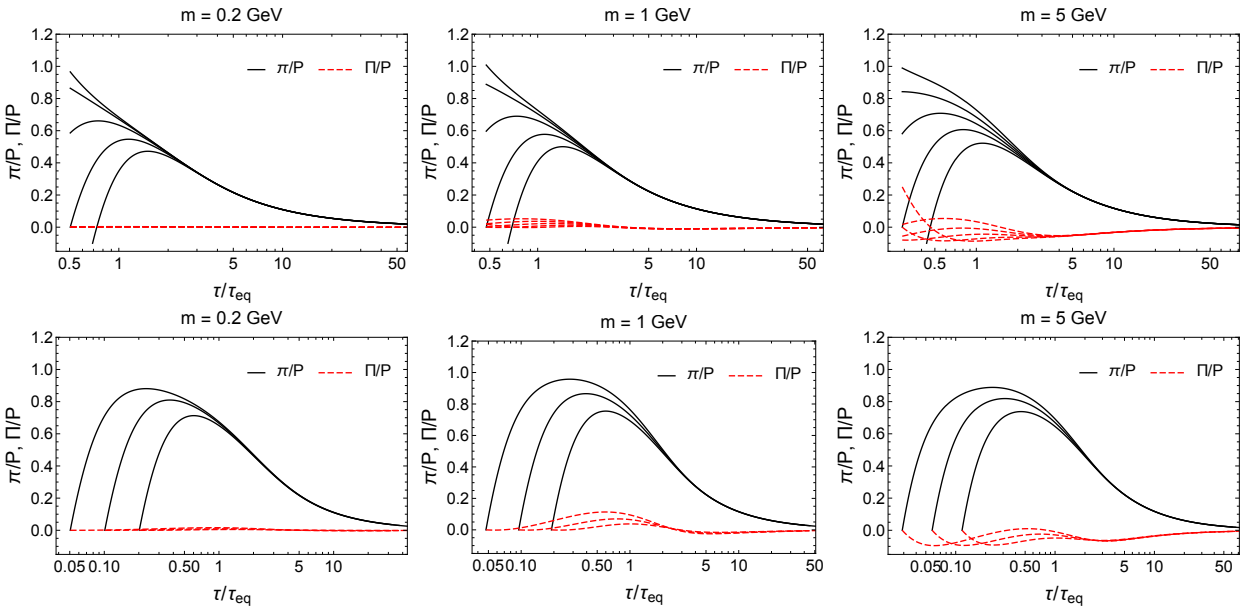

Figure 10: Scaled shear and bulk viscous corrections from Eqs. (5.42) and (5.40), respectively, as a function of rescaled time $\tau/\tau_{\rm eq}$. The black solid lines are the scaled shear correction. and the red dashed lines are the scaled bulk correction. The rows and columns are the same as in Fig. 8.

once one enters the region describable by first-order viscous hydrodynamics.

We turn next to Fig. 9 where we present the scaled bulk viscous correction Π/P Eq. (5.40) as a function of rescaled time $\tau/\tau_{\rm eq}$. The rows and columns are the same as in Fig. 8. The non-solid curves are specific runs and the solid curve shows the first-order Navier-Stokes prediction given in Eq. (5.58). As can be seen from the top row of this figure, only for the smallest mass shown of 0.2 GeV do we see a semi-universal result at early times in the top row and, for the largest mass of 5 GeV, we only see signs of a collapse to a semi-universal curve just prior to the onset of the applicability of first-order hydrodynamics. The bottom row of this figure shows that if one reduces the initialization time while holding the initial temperature fixed, there is no early-time attractor and, on top of that, even the late time Navier-Stokes result is not unique. This should be contrasted with Fig. 8 where one sees that the late-time Navier-Stokes results for the non-conformal shear collapse to a single line. Interestingly, as can be seen from the bottom row of Fig. 9, as the mass is increased, the

late-time Navier-Stokes curves begin to collapse to a unique curve, however, there is no indication of a unique early-time attractor.

In order to put the results for the scaled shear and scaled bulk corrections in a more easily comparable form, in Fig. 10 we present both in the same panels so that the magnitude of the non-universal behavior can be visualized. In this figure, the black solid lines are the scaled shear correction. and the red dashed lines are the scaled bulk correction. The rows and columns are the same as in Fig. 8. As the bottom right panel, in particular, demonstrates, there is a non-trivial cancellation between the shear and the bulk corrections even when the magnitude of the bulk correction is relatively large.

Finally, as was observed in Refs. [208, 214], a cancellation of the non-universal features of the scaled shear and bulk corrections occurs, resulting in a universal attractor for the scaled longitudinal pressure, $P_L/P = \overline{\mathcal{M}}^{01}$ which can be clearly see in Figs. 2 - 7. Such a cancellation occurs in all moments with $l \geq 1$ as these figures demonstrate implying that the high-momentum part of the distribution quickly approaches a universal form. This observation is once again in accordance with the finding of Refs. [208, 214], where they presented plots of the scaled-time evolution of the full one-particle distribution function.

5.5 Generalized initial condition

Starting from the general quantum statistical distribution function

$$f = \frac{1}{\exp\left(\frac{E-\mu}{T}\right) \pm 1},$$

in the limit of low densities and high temperatures $\exp\left(\frac{E-\mu}{T}\right) \gg 1$, the distribution reduces to the Maxwell-Boltzmann distribution. This is because at high temperatures, the thermal energy of the particles is much greater than the energy spacing between the quantum states, and the particles behave like classical particles. One can expand the exponential term in the

denominator using the Taylor series expansion for small values of $x = \frac{E-\mu}{T}$, so we can write:

$$f \simeq \frac{1}{\exp\left(\frac{E-\mu}{T}\right)} = \exp\left[-\frac{(E-\mu)}{T}\right] = \gamma_0 \exp\left(-\frac{E}{T}\right),$$

which is the Maxwell-Boltzmann distribution where $\gamma_0 = \exp\left(\frac{\mu}{T}\right)$. We present results obtained using the generalized spheroidal initial condition introduced in Ref. [214]

$$f_0(w, p_T) = \frac{1}{\gamma_0} \exp\left[-\frac{\sqrt{(p\cdot u)^2 + \xi_0 (p\cdot z)^2}}{\Lambda_0}\right], \tag{5.65}$$

where γ_0 allows us to independently vary the initial shear and bulk corrections. Since there are now three independent parameters to vary, we consider here varying all of them simultaneously, while holding the initial energy density fixed to that of an isotropic equilibrium gas with $m = 1$ GeV and $T_0 = 1$ GeV. In Figs. 11 and 12 we present the evolution of the scaled moments and viscous corrections resulting from such a scan. As these figures demonstrate, as with the spheroidal initial conditions used in the main body of the text, there does not seem to be a pull-back attractor for moments with $l = 0$ nor the viscous corrections π and Π, while both forward and pull-back attractors are still evident for all moments with $l \neq 0$.

5.6 Conclusions

In this paper we have confirmed and extended prior works that studied whether or not attractors exist in non-conformal kinetic theory. We did this by making use of an exact solution of the boost-invariant Boltzmann equation in relaxation time approximation. This exact solution is expressed in terms of an integral equation that can be solved numerically by the method of iteration and we derived an integral expression for general moments that allowed us to obtain their time evolution after having solved for the time evolution of the system's temperature. Associated with this paper we have released the code used for our

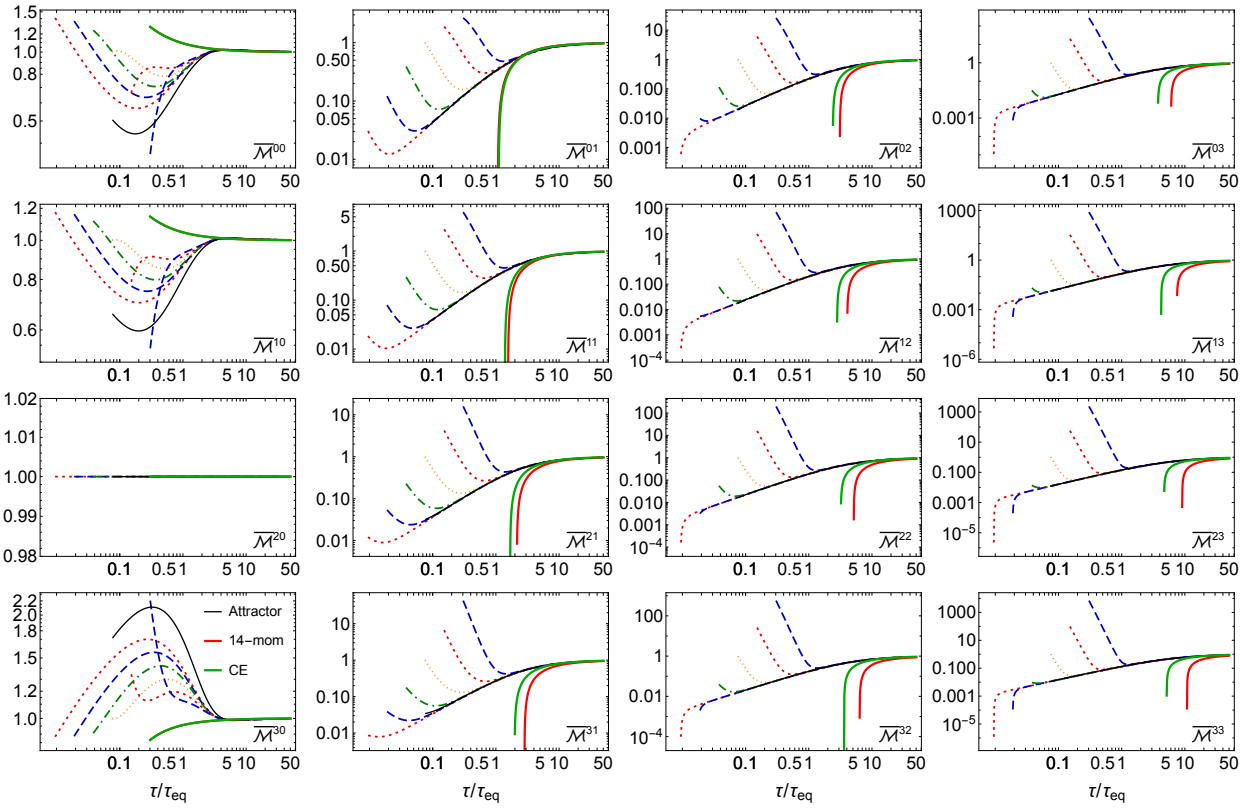

Figure 11: Scaled moments $\overline{\mathcal{M}}^{nl}$ as a function of rescaled time for the case $m = 1$ GeV obtained using the generalized spheroidal initial condition specified in Eq. (5.65) and varying all parameters appearing therein, ξ_0, γ_0, and τ_0.

studies as a publicly available package [231]. Using this method, we studied the time evolution of a large set of integral moments of the one-particle distribution function, varying both the initial momentum-space anisotropy and initialization time, while holding the initial energy density fixed. We considered three different values of the mass and our main results are presented in Figs. 2 - 7. From the time evolution of the general moments, we were able to compute the exact time evolution of both the shear and bulk viscous corrections to the one-particle distribution function and we presented these in Figs. 8 - 10, where we compared them to their corresponding expressions at leading-order in the gradient expansion.

Our conclusions from this study are consistent with those found by the authors of Refs. [208, 214], namely that there exists both late- and early-time attractors for the scaled longitudinal pressure P_L/P, while these do not exist separately for the shear and bulk viscous

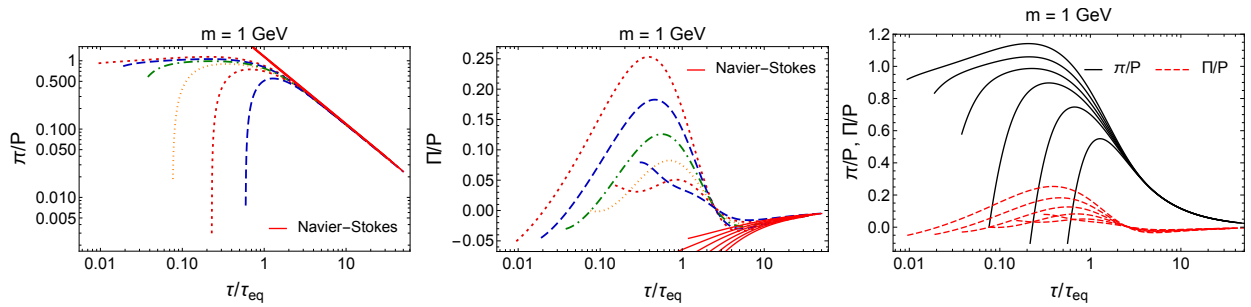

Figure 12: Scaled shear viscous correction π/P (left), bulk viscous correction Π/P (middle), and both combined (right) as a function of rescaled time $\tau/\tau_{\rm eq}$ for $m = 1$ GeV and varying all parameters appearing in Eq. (5.65), ξ_0, γ_0, and τ_0, while holding the initial energy density fixed to that of an isotropic equilibrium gas with $T_0 = 1$ GeV.

corrections. In terms of the moments, this is manifested in the fact that moments with $l = 0$ for the n values considered herein ($n \leq 3$), do not seem to possess an early-time attractor. In order to assess the approach to the late-time hydrodynamic attractor, we derived expressions for the viscosity-corrected one-particle distribution function to leading order in the gradient expansion (Navier-Stokes limit) within both the 14-moment and Chapman-Enskog approximations. We found that, for small masses, the first-order Chapman-Enskog form was quantitatively more reliable at late times than the 14-moment approximation, particularly for higher-order moments; however, for larger masses, the two approximations resulted in quantitatively similar results when compared to the exact solutions. Finally, in order to connect to standard viscous hydrodynamics corrections, we extracted the time evolution of both the shear and bulk viscous corrections from the exact solution. One new observation on this front is contained in Fig. 9, where it can be seen that the bulk viscous correction at first-order in gradients does not collapse in the late-time, Navier-Stokes, limit.

As to the practical implications of our results we note that, in the conformal case Ref. [158] demonstrated that even the $l = 0$ moments possessed a universal forward attractor and that this implied that there was an attractor for the full one-particle distribution function. In the non-conformal case, the authors of Ref. [214] presented results for the full

one-particle distribution function, finding that apart from slower convergence to the attractor at very low longitudinal momentum, it exhibited attractor behavior as well. Although their study was restricted to a conformal relaxation time, our work indicates that the same conclusion would be reached with a non-conformal relaxation time.

Finally, as to the implications for heavy-ion phenomenology, it has been shown that in the conformal case the existence of a longitudinal pressure attractor can be used, e.g. to constrain the initial energy density of the QGP [234] and electromagnetic emissions [235]. Since the arguments therein only rely on their being a longitudinal pressure attractor, it seems that they would go through unchanged. Our results, at worst, indicate that may be some additional uncertainty associated with such treatments if, in the future, they were to rely on attractors existing also in the case $l = 0$. Because of this, the overarching idea to use attractors in this manner would still be sound. This is due to the fact that, when considering the forward attractor with phenomenologically relevant initialization times, e.g. 0.1 fm/c, we still see a universal collapse to the forward attractor for all moments with $l \neq 0$ and a semi-universal collapse for the moments with $l = 0$ (see e.g. Figs. 2). This semi-universality would introduce a small degree of uncertainty in the conclusions compared to the conformal case, but would not make this a useless exercise.

Looking to the future, it would be very interesting to see if the conclusions contained herein can be extended to the case of a quasiparticle Boltzmann gas with temperature-dependent masses. Such a picture underpins quasiparticle anisotropic hydrodynamics and allows it to make use of a realistic non-conformal equation of state [8, 9, 11, 13, 186]. It will also be interesting to see if these findings are modified if one includes the effect of dynamical 2+1D and 3+1D expansion [154] and thermal noise [236]. We leave these considerations to future works.

Chapter 6

Resummed Relativistic Dissipative Hydrodynamics

6.1 Introduction

Experiments at the Relativistic Heavy Ion Collider (RHIC) at Brookhaven National Laboratory and the Large Hadron Collider (LHC) at CERN are probing the nature of hot and dense matter by colliding heavy-ions at ultrarelativistic center of mass energies of up to 5 TeV per nucleon [141, 237]. The goal of these experiments is to generate conditions similar to those present in the early universe and during mergers of compact astrophysical objects such as neutron stars [238]. These conditions correspond to high temperature ($T \gtrsim 150$ MeV) and net baryon density ($\rho \gtrsim 2 - 3\,\rho_{\rm sat}$), respectively. In both cases it is expected that nuclear matter undergoes a phase transition from a state in which quarks and gluons are confined inside hadrons to a deconfined state, called the quark-gluon plasma (QGP), in which quarks and gluons are not bound inside of hadrons. At finite temperatures and zero net baryon density it is possible to make use of lattice quantum chromodynamics (LQCD) to determine the temperature at which the deconfinement transition occurs and the nature of the transition. For realistic quark masses, continuum extrapolated lattice QCD calculations find that the transition is a smooth crossover with a pseudocritical temperature $T_{\rm pc} \simeq 155$ MeV [239, 240]. Due to the fermionic sign problem it is not possible to perform calculations at finite baryochemical potential μ_B, however, it is possible to make use of Taylor expansions around $\mu_B = 0$ or analytic continuations of imaginary chemical potential calculations to determine quantities of interest such as various quark susceptibilities and the curvature of the QCD phase transition line itself [133, 241–250]. These measurements provide constraints on the equation of state of QCD which can then be used in dynamical simulations of QGP

evolution.

For modeling the spatiotemporal dynamics of the QGP created in ultrarelativistic heavy-ion collisions, one of the main tools used is relativistic viscous hydrodynamics [142, 251, 252]. Early studies using relativistic hydrodynamics used the ideal limit [64, 65, 143] in which all dissipative transport coefficients, such as the shear viscosity were assumed to be zero, however, this was known to be an idealization because one expects, both on quantum uncertainty and causality bounds, that the ratio of the shear viscosity to entropy density ratio should have a lower bound. In order to incorporate such dissipative transport coefficients in the dynamics it was necessary to develop a causal version of viscous hydrodynamics called *second-order viscous hydrodynamics* [66–72, 88, 89, 91–96]. Application of second-order viscous hydrodynamics to QGP phenomenology quickly followed, with practitioners able to extract estimates of the shear viscosity to entropy density ratio that were consistent with the generation of a strongly-coupled QGP. Progress since then has included the development of consistent second-order truncations of the relativistic dissipative hydrodynamics from relativistic kinetic theory [88, 89] and recently formulations of casual first-order formulations which make use of different hydrodynamic frames [253, 254].

One of the major issues faced by second-order formulations of dissipative relativistic hydrodynamics is that, at very early times after the nuclear pass through, the system is quite far from equilibrium, with the largest non-equilibrium deviations reflected in the fact that, in the local rest frame (LRF), the system possesses a much smaller pressure along the beam-line direction (longitudinal direction) than transverse to it, i.e. $P_L \ll P_T$. This LRF pressure anisotropy emerges due to the rapid longitudinal expansion of the QGP and has been shown to exist in both the weak- and strong-coupling limits, with the anisotropy becoming more pronounced as the coupling is decreased. The implication of this is that the viscous corrections, in particular the shear correction, are large at early times, calling

into doubt the reliability of fixed-order truncations in the magnitude of the inverse Reynolds number [255].

Another issue faced by fixed order truncations of viscous hydrodynamics is that, due to the assumed polynomial from of the corrections to the one-particle distribution function, there is the possibility that the viscous-corrected one-particle distribution function can become negative, which violates the positivity of probabilities. In order to address both of these issues, in *anisotropic hydrodynamics* (aHydro) one makes use of a form for the one-particle distribution function that is, by construction, non-negative while also having kinetic pressures which are non-negative. The original papers on aHydro focused on application to systems undergoing boost-invariant conformal Bjorken expansion [97,98]. In Ref. [97] it was demonstrated that one could obtain both the ideal hydrodynamics and free-streaming limits in the aHydro framework and numerical solutions to the resulting coupled evolution equations demonstrated that both the one-particle distribution function and the kinetic pressures remained positive at all times. Since then many works have extended these initial studies to include more realistic features associated with heavy-ion collisions, ultimately allowing practitioners to simulate the full three-dimensional non-conformal evolution of the QGP with a lattice-based equation of state [8,13,102–104,108,109,112,162,186,197,198,215,230,256–264].

In this chapter we will summarize the progress made in recent years including phenomenological applications. We will begin with a demonstration that the aHydro dynamical equations resum an infinite series of terms when expanded as a power series in the inverse Reynolds number. We will then present a review of the underpinnings of the 3+1D quasiparticle aHydro (aHydroQP) framework, which goes beyond traditional approaches by resumming viscous contributions to all orders in the shear and bulk inverse Reynolds numbers. In this second part, we will focus on recent phenomenological applications of 3+1D aHydroQP to AA collisions at RHIC and LHC energies.

The structure of this chapter is as follows. In Sec. 6.2 we discuss the case of conformal Bjorken expansion in order to demonstrate how anisotropic hydrodynamics resums contributions to all orders in the inverse shear Reynolds number. In Sec. 6.3, we introduce quasiparticle anisotropic hydrodynamics. In Sec. 6.4, we outline the construction of the QCD equation in aHydroQP. In Sec. 6.5, evolution and freezeout are discussed in the 3+1D aHydroQP model. In Sec. 6.6, phenomenological comparisons to experimental data are presented at various collision energies. Sec. 6.7 contains our conclusions and a summary of ongoing projects.

6.2 Resummed dissipative hydrodynamics in the conformal Bjorken limit

Before presenting the full 3+1D formalism for non-conformal QCD plasmas, it is instructive to consider the 0+1D conformal limit in which the system undergoes Bjorken expansion. As mentioned in chapter (4), the conformal Bjorken limit describes the expansion of a system with conformal symmetry in 0+1 dimensions. The distribution function in this limit [192]

$$f(x,p) = f_{\rm eq}\left(\frac{\sqrt{\mathbf{p}^2+\xi p_z^2}}{\lambda}\right), \tag{6.1}$$

depends on a single anisotropy parameter ξ and a non-equilibrium momentum scale λ. The evolution equations for ξ and λ can be derived from energy-momentum conservation and the second moment of the Boltzmann equation. The evolution equation for ξ is given by [97]

$$\frac{\mathcal{R}'(\xi)}{\mathcal{R}(\xi)}\partial_\tau\xi + \frac{4}{\lambda}\partial_\tau\lambda = \frac{1}{\tau}\left[\frac{1}{\xi(1+\xi)\mathcal{R}(\xi)} - \frac{1}{\xi} - 1\right], \tag{6.2}$$

which involves the derivative of the function $\mathcal{R}(\xi) = \frac{1}{2}\left[\frac{1}{1+\xi} + \frac{\arctan\sqrt{\xi}}{\sqrt{\xi}}\right]$ and the proper time derivative of λ, and this equation describes the evolution of the scale λ with respect to proper time. The second evolution equation that is following the Florkowski-Tinti prescription [109]

is

$$\frac{1}{1+\xi}\partial_\tau \xi - \frac{2}{\tau} + \frac{\mathcal{R}^{5/4}(\xi)}{\tau_{\rm eq}}\xi\sqrt{1+\xi} = 0\,, \tag{6.3}$$

which relates the proper time derivative of ξ to τ, $\mathcal{R}(\xi)$, and the relaxation time $\tau_{\rm eq}$. Therefore, this equation accounts for dissipative effects in the system. These non-linear evolution equations can be solved numerically, and they capture the transition between the ideal hydrodynamic limit and the free streaming limit.

6.2.1 Relation to second-order viscous hydrodynamics in the small anisotropy limit

In order to make a connection to standard second-order viscous hydrodynamics, one can rewrite

$$\frac{\partial\epsilon(\tau)}{\partial\tau} = -\frac{\epsilon(\tau)+P_L(\tau)}{\tau}\,, \tag{6.4}$$

and (6.3) in terms of the single shear stress tensor component $\pi \equiv \pi^{\varsigma}{}_{\varsigma}$ required for conformal Bjorken flow. Start with the energy conservation equation (6.4) and multiply both sides of the equation by τ then divide both sides of the equation by ϵ. This manipulation allows us to transform the equation into a logarithmic derivative form, where the time derivative of the logarithm of energy density, $\partial_\tau \log\epsilon$, appears. Substitute $\pi = P_{\rm eq} - P_L$, where π is the shear stress tensor component required for conformal Bjorken flow, then simplifying further by using the relation $\epsilon = 3P_{\rm eq}$, which holds for conformal hydrodynamics. After that, we obtain the equation that serves as a connection to standard second-order viscous hydrodynamics by relating the time evolution of the logarithm of energy density to the shear stress tensor component π as following

$$\tau\partial_\tau \log\epsilon = -\frac{4}{3} + \frac{\pi}{\epsilon}\,. \tag{6.5}$$

To relate π and ξ one can start with this definition $\pi = P_{\rm eq} - P_L$ and divide by ϵ on both sides. Then by using these relations $\epsilon = 3P_{\rm eq}$, $\epsilon = \mathcal{R}(\xi)\epsilon_{\rm eq}$, and $P_L = \mathcal{R}_L(\xi)P_{\rm eq}$ to simplify

and one obtains $\overline{\pi}$, which is the ratio of shear stress to energy density.

$$\overline{\pi}(\xi) \equiv \frac{\pi}{\epsilon} = \frac{1}{3}\left[1 - \frac{\mathcal{R}_L(\xi)}{\mathcal{R}(\xi)}\right] \tag{6.6}$$

with

$$\mathcal{R}_L(\xi) = \frac{3}{\xi}\left[\frac{(\xi+1)\mathcal{R}(\xi) - 1}{\xi + 1}\right]. \tag{6.7}$$

For conformal Bjorken flow, $\overline{\pi}$ is related to the shear inverse Reynolds number[1] via

$$R_\pi^{-1} \equiv \frac{\sqrt{\pi^{\mu\nu}\pi_{\mu\nu}}}{P_{\text{eq}}} = 3\sqrt{\frac{3}{2}}|\overline{\pi}|\,. \tag{6.8}$$

where the factor of $3\sqrt{\frac{3}{2}}$ arises due to the specific scaling properties of conformal hydrodynamics. The shear inverse Reynolds number, R_π^{-1}, shows how important the effects of dissipation (shown by the shear stress tensor) are compared to the equilibrium pressure in the QGP. Therefore, the number of R_π^{-1} is used to describe the size of the shear stress and measure how far from ideal hydrodynamics the situation is. A small value of R_π^{-1} means that the fluid is almost perfect and has weak dissipative effects, while a large value means that the fluid is far from perfect and has strong dissipative effects. As a consequence of Eq. (6.8), it is true that an expansion in $\overline{\pi}$ would match an expansion in R_π^{-1}. Since R_π^{-1} is proportional to $|\overline{\pi}|$, every series expansion in $\overline{\pi}$ may be represented as a series expansion in R_π^{-1} by substituting $R_\pi^{-1}/(3\sqrt{\frac{3}{2}})$ for $\overline{\pi}$. The ability to convert findings or computations expressed in terms of $\overline{\pi}$ to their equivalent form in terms of R_π^{-1} and vice versa is made possible by this relationship.

[1]The Reynolds number is a dimensionless variable used in fluid dynamics to describe a fluid's flow characteristics and it measures the dissipative strength of the system

Changing variables to π in Eq. (6.3) and using Eq. (6.5), one obtains [158]

$$\frac{\partial_\tau \pi}{\epsilon} + \frac{\pi}{\epsilon\tau}\left(\frac{4}{3} - \frac{\pi}{\epsilon}\right) - \left[\frac{2(1+\xi)}{\tau} - \frac{\mathcal{H}(\xi)}{\tau_{\rm eq}}\right]\overline{\pi}'(\xi) = 0\,, \tag{6.9}$$

where $\xi = \xi(\overline{\pi})$ is the inverse function from $\overline{\pi}$ to ξ, $\overline{\pi}' \equiv d\overline{\pi}/d\xi$, and $\mathcal{H}(\xi) \equiv \xi(1+\xi)^{3/2}\mathcal{R}^{5/4}(\xi)$. When expressed in this form one sees that the aHydro second-moment equation resums an infinite series in the inverse Reynolds number Eq. (6.8). This is because the last term on the right hand side of Eq. (6.9) is a function that contains all orders in ξ and, hence, $\overline{\pi}$.[2]

Using small-anisotropy expansions one obtains [158]

$$\begin{aligned}
\overline{\pi}' &= \frac{8}{45} - \frac{26}{21}\overline{\pi} + \frac{1061}{392}\overline{\pi}^2 + \mathcal{O}(\overline{\pi}^3)\,,\\
(1+\xi)\overline{\pi}' &= \frac{8}{45} - \frac{5}{21}\overline{\pi} - \frac{38}{49}\overline{\pi}^2 + \mathcal{O}(\overline{\Pi}^3)\,,\\
\mathcal{H} &= \frac{45}{8}\overline{\pi}\left[1 + \frac{405}{56}\overline{\pi} + \mathcal{O}(\overline{\pi}^3)\right]\,,\\
\mathcal{H}\overline{\pi}' &= \overline{\pi} + \frac{15}{56}\overline{\pi}^2 + \mathcal{O}(\overline{\pi}^3).
\end{aligned} \tag{6.10}$$

Plugging these expansions into Eq. (6.9) and keeping terms through second order in π gives

$$\partial_\tau \pi - \frac{4\eta}{3\tau_\pi\tau} + \frac{38}{21}\frac{\pi}{\tau} - \frac{36\tau_\pi}{245\eta}\frac{\pi^2}{\tau} = -\frac{\pi}{\tau_\pi} - \frac{15}{56}\frac{\pi^2}{\tau_\pi\epsilon} + \mathcal{O}(\pi^3)\,.$$

When truncated at linear order π, this evolution equation agrees exactly with previously obtained second-order viscous hydrodynamics evolution equations in relaxation time approximation [81, 88, 91, 92, 266]. This demonstrates that, in the limit of small momentum-space anistropy, aHydro automatically reproduces the correct second-order viscous hydrodynamics equations. Note that it is possible to obtain higher-order terms such as those contributing at the order of the inverse Reynolds number squared as well, where these terms capture

[2] A similar construction can be made in the case of Gubser flow, see Sec. IIIC of Ref. [265].

dissipative effects beyond the linear regime and account for a wider range of deviations from ideal hydrodynamics. When applied to phenomenology, one does not expand Eqs. (6.3) or (6.9) in $\bar{\pi}$. However, when solving the aHydro dynamical equations, an infinite number of orders in the inverse Reynolds number are automatically included. This is why aHydro represents a *resummed dissipative hydrodynamic theory*. In practice, aHydro automatically regulates the magnitude of $\bar{\pi}$ such that unphysical behaviour of the kinetic pressures, e.g., $P_L < 0$, simply cannot occur. In other words, in traditional dissipative hydrodynamics, one approximates the behavior of a fluid system by expanding the equations of motion in terms of small parameters that represent deviations from equilibrium. However, this approach has limitations when the deviations from equilibrium are large. aHydro takes a different approach. Instead of relying on a perturbative expansion and truncating the equations at a certain order, aHydro solves the equations without explicit truncation. This means that it includes an infinite number of terms in the equations, which allows for a more accurate description of the system's dynamics. By including an infinite number of terms, aHydro effectively "resums" the contributions related to dissipative effects. This resummation takes into account higher-order effects and provides a more comprehensive understanding of the system's behavior, especially in cases where the deviations from equilibrium are significant.

6.3 Quasiparticle anisotropic hydrodynamics

In order to faithfully model heavy-ion collisions one must obtain the evolution equations for arbitrary 3+1D configurations and include the non-conformality of QCD consistent with a realistic lattice-based equation of state. In order to do this in *quasiparticle anisotropic hydrodynamics* we assume a system of massive relativistic quasiparticles with temperature-dependent masses $m(T)$. The system is assumed to obey a relativistic Boltzmann equation with $m(T)$ determined from lattice QCD (LQCD) computations of QCD thermodynamics. In quasiparticle anisotropic hydrodynamics (aHydroQP), the Boltzmann equation is modified

to take into account the temperature dependence of the mass of the quasiparticles. This is because the mass is no longer a constant, but varies with temperature which affects the behavior of the system. As a result, when the masses are temperature dependent, the Boltzmann equation contains an additional force term on the left-hand side related to gradients in the temperature, and hence gradients in m,

$$p^\mu \partial_\mu f + \frac{1}{2}\partial_i m^2 \partial^i_{(p)} f = \underbrace{-\frac{p\cdot u}{\tau_{\rm eq}(T)}[f - f_{\rm eq}(T)]}_{C[f]} \,. \tag{6.11}$$

Here, in the additional force term ∂_i denotes a derivative with respect to spatial coordinates, $\partial^i_{(p)} \equiv -\partial/\partial p^i$ denotes a derivative with respect to momentum coordinates, m is the mass of the quasiparticle, and f is the one-particle distribution function. Also, we note that this term $\frac{1}{2}\partial_i m^2 \partial^i_{(p)} f$ matches exactly the result obtained by deriving the Boltzmann equation using quantum field theoretical methods [133]. The right-hand side of the Boltzmann equation is the collisional kernel $C[f]$, which we take to be given by the relaxation time approximation (RTA), where u^μ is the four-velocity associated with the local rest frame (LRF) of the matter and Latin indices such as i indicate spatial indices. The collisional kernel is a functional of the one-particle distribution function $f(x,p)$ which depends on space-time coordinates x and momentum p. Moreover, this term represents the rate of change of the one-particle distribution function due to collisions. This rate of change is given by the difference between the actual distribution function f and the equilibrium distribution function $f_{\rm eq}$, multiplied by an inverse relaxation time $\tau_{\rm eq}$. The relaxation time is a measure of how fast the system approaches equilibrium, and it depends on the specific properties of the system, such as the temperature and the density. For a gas of massive quasiparticles, the relaxation time is given by [185]

$$\tau_{\rm eq}(T) = \bar{\eta}\,\frac{\epsilon + P}{I_{3,2}(\hat{m}_{\rm eq})} \,. \tag{6.12}$$

Here, $\bar{\eta} = \eta/s$ is the specfic shear viscosity that quantifies the resistance of the system to shear flow, where η is the shear viscosity and s is the entropy density, ϵ is the energy density, P is the pressure which is fixed by the equation of state, and the special functions appearing are given by

$$I_{3,2}(\hat{m}_{\rm eq}) = \frac{N_{\rm dof} T^5 \hat{m}_{\rm eq}^5}{30\pi^2}\left[\frac{1}{16}\Big(K_5(\hat{m}_{\rm eq}) - 7K_3(\hat{m}_{\rm eq}) + 22K_1(\hat{m}_{\rm eq})\Big) - K_{i,1}(\hat{m}_{\rm eq})\right], \quad (6.13)$$

$$K_{i,1}(\hat{m}_{\rm eq}) = \frac{\pi}{2}\Big[1 - \hat{m}_{\rm eq}K_0(\hat{m}_{\rm eq})s_{-1}(\hat{m}_{\rm eq}) - \hat{m}_{\rm eq}K_1(\hat{m}_{\rm eq})s_0(\hat{m}_{\rm eq})\Big], \quad (6.14)$$

with $\hat{m}_{\rm eq} = m/T$, $N_{\rm dof}$ is being the number of degrees of freedom (degeneracy), K_n are the modified Bessel functions of the second kind, and s_n are the modified Struve functions. The effective temperature $T(\tau)$ is computed by requiring the non-equilibrium kinetic energy densities calculated from f to be equal to the equilibrium kinetic energy density calculated from the equilibrium distribution, $f_{\rm eq}(T, m)$. One should notice that in a hydrodynamic model, it is usually assumed the temperature of the system is in equilibrium throughout its evolution. But in real life, the temperature can change because of non-equilibrium effects like the system's dissipation and expansion. In quasiparticle anisotropic hydrodynamics, the temperature is not thought to be in equilibrium. Instead, the temperature is allowed to change based on how the quasiparticles in the system interact with each other. Also, as the temperature changes, so does the mass of the quasiparticles. By taking into account both how the mass changes with temperature and how the system is not in equilibrium, a self-consistent solution for the temperature can be found that accurately describes how the system changes over time.

In this chapter, we assume the distribution function is given by the leading-order aHydro

form, parameterized by a diagonal anisotropy tensor as follows

$$f(x,p) = f_{\rm eq}\left(\frac{1}{\lambda}\sqrt{p_\mu \Xi^{\mu\nu} p_\nu}\right) \underset{\rm LRF}{\longrightarrow} f_{\rm eq}\left(\frac{1}{\lambda}\sqrt{\sum_i \frac{p_i^2}{\alpha_i^2} + m^2}\right) , \tag{6.15}$$

where $i \in \{x, y, z\}$, $\Xi^{\mu\nu}$ is the anisotropy tensor and the second equality holds in the local rest frame (LRF), which is a local Lorentz frame where the fluid is at rest. Here, the one-particle distribution function f is the local rest frame in momentum space. We start with the general form of f given by Equation (6.15). This equation states that f is a function of the square root of a symmetric tensor $\Xi^{\mu\nu}(t, \mathbf{x})$ multiplied by the momentum vector divided by a momentum scale $\lambda(t, \mathbf{x})$. We then assume that the tensor $\Xi^{\mu\nu}$ is diagonal in the local rest frame. As indicated, in the LRF the argument of the distribution function can be expressed in terms of three independent momentum-anisotropy parameters α_i. Here we will assume that $f_{\rm eq}$ is given by a Boltzmann distribution which depends on $p \cdot u$ and the isotropic temperature T. Therefore, one can calculate the energy density and pressures by integrating the distribution function Eq. (6.15) times $p^\mu p^\nu$ using the Lorentz-invariant integration measure $\int dP = \int \frac{d^3\mathbf{p}}{(2\pi)^3}\frac{1}{E}$. Performing the same operation allows one to extract all moments, and then one can create the requisite dynamical equations.

The first aHydroQP equation of motion is obtained from the first moment of the left-hand side of the quasiparticle Boltzmann equation (6.11), which reduces to $\partial_\mu T^{\mu\nu}$. In the relaxation time approximation, however, the first moment of the collisional kernel on the right hand side results in a constraint that must be satisfied in order to conserve energy and momentum, i.e.$\int dP\, p^\mu C[f] = 0$. This constraint can be enforced by expressing the effective temperature in terms of the microscopic parameters λ and $\vec{\alpha}$. As a consequence, computing the first moment of the Boltzmann equation gives the energy-momentum conservation law for the system

$$\partial_\mu T^{\mu\nu} = 0\,, \tag{6.16}$$

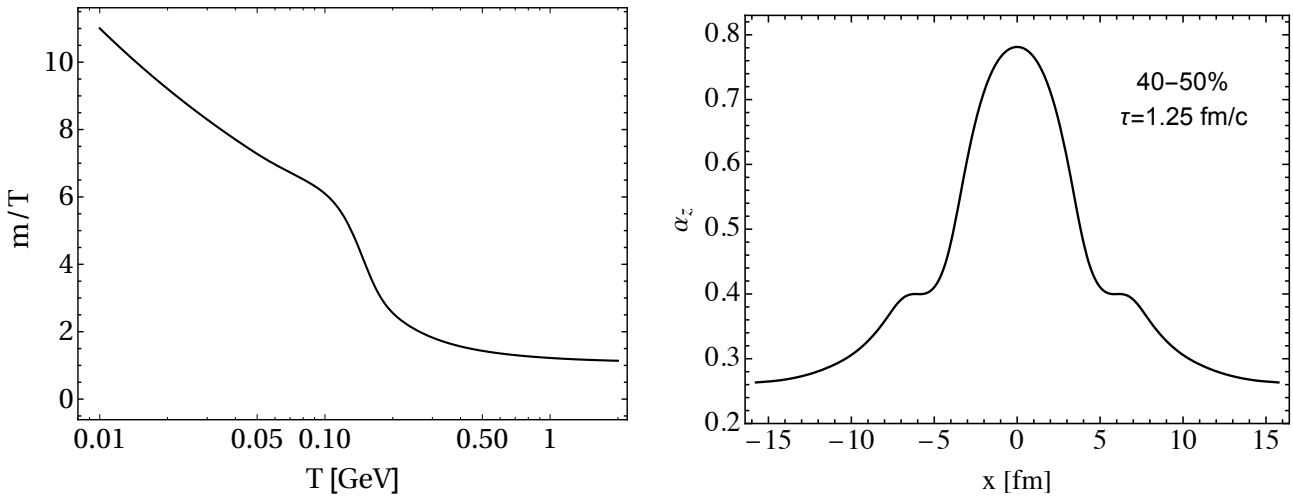

Figure 1: (a) The temperature dependence of the quasiparticle mass scaled by the temperature [8]. (b) Atypical spatial profile of the anisotropy parameter α_z as a function of x at $\tau = 1.25$ fm/c [9].

where

$$T^{\mu\nu} = \int \frac{d^3\mathbf{p}}{(2\pi)^3} \frac{1}{E} p^\mu p^\nu f + B g^{\mu\nu} \,. \tag{6.17}$$

Here, $B(T)$ represents the additional background contribution. For the second equation of motion, we will perform a similar procedure using the second moment of the quasiparticle Boltzmann equation

$$\partial_\alpha I^{\alpha\nu\lambda} - J^{(\nu}\partial^{\lambda)} m^2 = -\int \frac{d^3\mathbf{p}}{(2\pi)^3} \frac{1}{E} p^\nu p^\lambda \mathcal{C}[f] \,, \tag{6.18}$$

with $I^{\mu\nu\lambda} \equiv \int \frac{d^3\mathbf{p}}{(2\pi)^3} \frac{1}{E} p^\mu p^\nu p^\lambda f$ and the particle four-current $J^\mu = \int \frac{d^3\mathbf{p}}{(2\pi)^3} \frac{1}{E} p^\mu f$.

6.4 The equation of state for aHydroQP

For a system of massive particles obeying Boltzmann statistics, the equilibrium energy density, pressure, and entropy density are given by

$$\epsilon_{\rm eq}(T,m) = 4\pi\tilde{N}T^4\,\hat{m}_{\rm eq}^2\Big[3K_2\left(\hat{m}_{\rm eq}\right)+\hat{m}_{\rm eq}K_1\left(\hat{m}_{\rm eq}\right)\Big]\,, \tag{6.19}$$

$$P_{\rm eq}(T,m) = 4\pi\tilde{N}T^4\,\hat{m}_{\rm eq}^2K_2\left(\hat{m}_{\rm eq}\right)\,, \tag{6.20}$$

$$s_{\rm eq}(T,m) = 4\pi\tilde{N}T^3\,\hat{m}_{\rm eq}^2\Big[4K_2\left(\hat{m}_{\rm eq}\right)+\hat{m}_{\rm eq}K_1\left(\hat{m}_{\rm eq}\right)\Big]\,. \tag{6.21}$$

In the quasiparticle approach, one assumes the mass to be temperature dependent, i.e. $m(T)$. This results in a change in the bulk variables Eqs. (6.21). However, one can not simply insert $m(T)$ into the bulk variables since this will not be thermodynamically consistent. In the case of an equilibrium Boltzmann gas, the number and entropy densities remain unchanged. Therefore, the discrepancy arises because the entropy density can be obtained using two different approaches: $s_{\rm eq} = (\epsilon_{\rm eq} + P_{\rm eq})/T$ and $s_{\rm eq} = \partial P_{\rm eq}/\partial T$. Then, by basically inserting a temperature-dependent mass $m(T)$, the two identities will not give the same result. To address this inconsistency, an additional background contribution is introduced to the energy-momentum tensor. This background field corrects the thermodynamic inconsistency arising from the temperature dependence of the mass. The energy-momentum tensor is then defined as

$$T^{\mu\nu} = T^{\mu\nu}_{\rm kinetic} + g^{\mu\nu}B(T)\,. \tag{6.22}$$

By introducing the background field, thermodynamic consistency is restored, and the modified energy-momentum tensor accounts for the effects of the temperature-dependent mass. This background field plays a crucial role in ensuring the correct behavior of the system and maintaining the thermodynamic relationships between the energy density, pressure, and entropy density. Thus, in an equilibrium Boltzmann gas with quasiparticles, the bulk

thermodynamic variables for the gas become

$$\epsilon_{\rm eq}(T,m) = \epsilon_{\rm kinetic} + B_{\rm eq}\,, \tag{6.23}$$

$$P_{\rm eq}(T,m) = P_{\rm kinetic} - B_{\rm eq}\,, \tag{6.24}$$

$$s_{\rm eq}(T,m) = s_{\rm kinetic}\,. \tag{6.25}$$

As a result of introducing the background field, the energy density and the pressure are modified by $+B_{\rm eq}$ and $-B_{\rm eq}$ terms, respectively.

One can determine the value of the background contribution $B_{\rm eq}$ by imposing a thermodynamic identity. Specifically, by requiring the thermodynamic identity given by

$$Ts_{\rm eq} = \epsilon_{\rm eq} + P_{\rm eq} = T\frac{\partial P_{\rm eq}}{\partial T}\,. \tag{6.26}$$

However, we need to know in advance $m(T)$ to determine $B(T)$. The quasi mass $m(T)$ can be determined using the following thermodynamic identity

$$\epsilon_{\rm eq} + P_{\rm eq} = Ts_{\rm eq} = 4\pi\tilde{N}T^4\,\hat{m}_{\rm eq}^3 K_3\left(\hat{m}_{\rm eq}\right)\,. \tag{6.27}$$

As we can see, one can solve numerically for $m(T)$ once the equilibrium energy density and pressure are determined using the lattice QCD parameterization. The resulting effective mass scaled by T extracted from continuum extrapolated Wuppertal-Budapest lattice data [267] is shown in Fig. 1 (left panel) [8]. At high temperatures ($T \sim 0.6$ GeV) the scaled mass is $\sim T$ in agreement with the expected high-temperature behavior of QCD [268].

6.5 Evolution and freezeout in aHydroQP

The evolution equations for u^μ, λ, and α_i are obtained from moments of the quasiparticle Boltzmann equation. These can be expressed compactly by introducing a timelike vector u^μ which is normalized as $u^\mu u_\mu = 1$ and three spacelike vectors X_i^μ which are individually normalized as $X_i^\mu X_{\mu,i} = -1$. These vectors are mutually orthogonal and obey $u_\mu X_i^\mu = 0$ and $X_{\mu,i} X_j^\mu = 0$ for $i \neq j$ [103, 215]. The four equations resulting from the first moment are

$$D_u \epsilon + \epsilon \theta_u + \sum_j P_j u_\mu D_j X_j^\mu = 0\,, \tag{6.28}$$

$$D_i P_i + P_i \theta_i - \epsilon X_{\mu,i} D_u u^\mu + P_i X_{\mu,i} D_i X_i^\mu - \sum_j P_j X_{\mu,i} D_j X_j^\mu = 0\,, \tag{6.29}$$

where $i, j \in \{x, y, z\}$, $D_u \equiv u^\mu \partial_\mu$, and $D_i \equiv X_i^\mu \partial_\mu$. The expansion scalars are $\theta_u = \partial_\mu u^\mu$ and $\theta_i = \partial_\mu X_i^\mu$. Explicit expressions for the basis vectors, derivative operators and expansion scalars can be found in the appendix E.1.1 and Refs. [8, 13, 112, 230]. The quantities ϵ and P_i are the kinetic energy density and pressures obtained using the anisotropic hydrodynamics ansatz for the one-particle distributions function corrected by the background contribution $B(T)$ necessary to enforce thermodynamic consistency

$$\epsilon = \epsilon_{\text{kinetic}}(\lambda, \vec{\alpha}, m) + B(\lambda, \vec{\alpha})\,, \tag{6.30}$$

$$P_i = P_{i,\text{kinetic}}(\lambda, \vec{\alpha}, m) - B(\lambda, \vec{\alpha})\ , \tag{6.31}$$

The three equations resulting from the second moment of the Boltzmann equation are

$$D_u I_i + I_i(\theta_u + 2 u_\mu D_i X_i^\mu) = \frac{1}{\tau_{\text{eq}}} \Big[I_{\text{eq}}(T, m) - I_i \Big], \tag{6.32}$$

with [112]

$$
\begin{aligned}
I_i &= \alpha\, \alpha_i^2\, I_{\rm eq}(\lambda, m)\,, \\
I_{\rm eq}(\lambda, m) &= 4\pi \tilde{N} \lambda^5 \hat{m}^3 K_3(\hat{m})\,,
\end{aligned}
\tag{6.33}
$$

where $\hat{m} = m/\lambda$, $\alpha = \alpha_x \alpha_y \alpha_z$ and $\tilde{N} = N_{\rm dof}/(2\pi)^3$, with $N_{\rm dof}$ being the number of degrees of freedom present in the theory under consideration.

Equations (6.28), (6.29), and (6.32) provide seven partial differential equations for $\vec{u}$, $\vec{\alpha}$, and λ which we solve numerically. To determine the local effective temperature we make use of Landau matching; requiring the equilibrium and non-equilibrium energy densities in the LRF to be equal and solving for T. Herein, we assume the system to initially be isotropic in momentum space $\alpha_i(\tau_0) = 1$, with zero transverse flow. However, the system evolves quite fast away from isotropy $\tau_{\rm aniso} \lesssim 1$ fm. As an example, in Fig. 1-right panel we show the spatial profile of the longitudinal anisotropy parameter at 40-50% centrality class where this parameter characterizes the degree of anisotropy in the longitudinal direction of the evolving system. As can be seen from this figure, α_z differs from unity (with unity indicating isotropy) especially in the dilute regions $|x| > 5$ fm. In these dilute regions, the system is less dense compared to other regions. We note here that no regulation is required in aHydroQP to evolve in these dilute regions. This suggests that the framework can manage the system evolution in these low-density areas without the need for further modifications or special interventions. This system of partial differential equations are evolved until the effective temperature in the entire simulation volume falls below a given freeze-out temperature of $T_{\rm FO}$. From the results, we extract a three-dimensional freeze-out hypersurface with a fixed energy density (temperature). We assume in this step all hadronic species in a given cell on the freeze-out hypersurface share the same fluid anisotropy tensor and scale parameter. We also assume that all hadrons created are in chemical equilibrium. This means that it is assumed that the

particle abundances at freeze-out follow the equilibrium distribution for the given temperature and chemical potentials. This assumption simplifies the calculations by allowing the use of aHydro-modified equilibrium distribution functions for the hadrons. To convert the hydrodynamic quantities (velocity, anisotropy, and scale) into explicit 'primordial' hadronic distribution functions on the freeze-out hypersurface, an extended Cooper-Frye prescription is used. The Cooper-Frye prescription is a standard method to convert hydrodynamic quantities into particle distributions at freeze-out. The extended version takes into account the non-equilibrium effects and anisotropy of the fluid. By applying the extended Cooper-Frye prescription [185], the hydrodynamic information (such as velocity, anisotropy, and scale) is used to calculate the distribution functions of the produced hadrons on the freeze-out hypersurface. These distribution functions provide information about the momentum distributions and other properties of the hadrons at freeze-out, which can be compared with experimental measurements to study the dynamics of the system.

The values of the aHydroQP parameters on the freezeout hypersurface are passed to a modified version of THERMINATOR 2 [269], which generates hadronic configurations using Monte-Carlo sampling. After sampling the primordial hadrons, further hadronic decays are taken into account using the built-in routines in THERMINATOR 2. The source code for aHydroQP and our custom version of THERMINATOR 2 are both freely accessible [270]. The aHydroQP formalism was used at different collision energies, and it was found that the observed differential spectra of identified hadrons, charged particle multiplicity, elliptic flow, and Hanbury-Brown-Twiss radii could be reproduced. Finally, in Table 1 we list the fitting parameters that we extracted and used in the comparisons.

collision energy	T_0 [MeV]	η/s
200 GeV	455	0.179
2.76 TeV	600	0.159
5.02 TeV	630	0.159

Table 1: The key parameters used in the presented results.

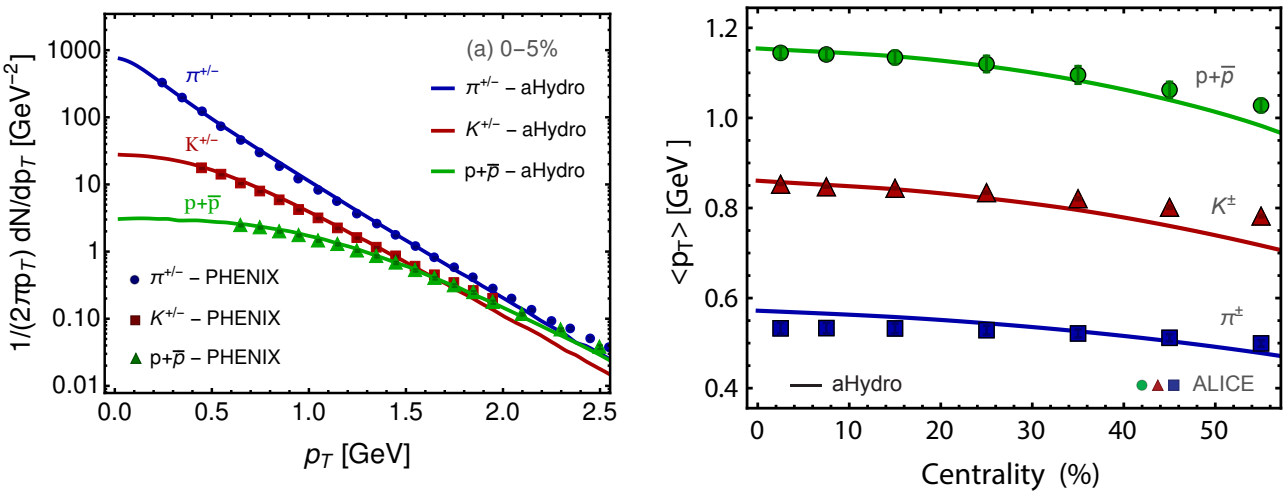

Figure 2: Left: Pion, kaon, and proton spectra compared to experimental data by the PHENIX collaboration at 200 GeV for Au-Au collisions [10, 11]. Right: Pion, kaon, and proton average transverse momentum as a function of centrality compared to data by the ALICE collaboration at 2.76 TeV for Pb-Pb collisions [12, 13]

6.6 Results and Discussion

In this section we present phenomenological comparisons of 3+1D aHydroQP model to experimental data. For the sake of brevity, we present comparisons of a small set of observables performed at various collision energies $\sqrt{s_{NN}} = 200$ GeV, 2.76, and 5.02 TeV for Au-Au and Pb-Pb collisions from the PHENIX, PHOBOS, STAR, and ALICE collaborations. We first present comparisons of bulk observables between our model and experimental results. In Fig. 2-left panel, we show the spectra of pions, kaons, and protons as a function of the transverse momentum p_T. The agreement shown between our model and the experimental results is good up to quite large $p_T \sim 2$ GeV. In this figure, we show only one centrality class 0-5%, however one can see Ref. [11] for more comparisons up to 30-40% centrality class. It suffices here to say that the agreement is quite good up to $p_T \sim 1.5$ GeV for high centrality classes. Next, we present the centrality dependence of the average transverse momentum of pions, kaons, and protons at 2.76 TeV for Pb-Pb collisions. Again, the agreement is very good up to high centrality classes $\sim 50\%$. The spectra at this energy is not presented here,

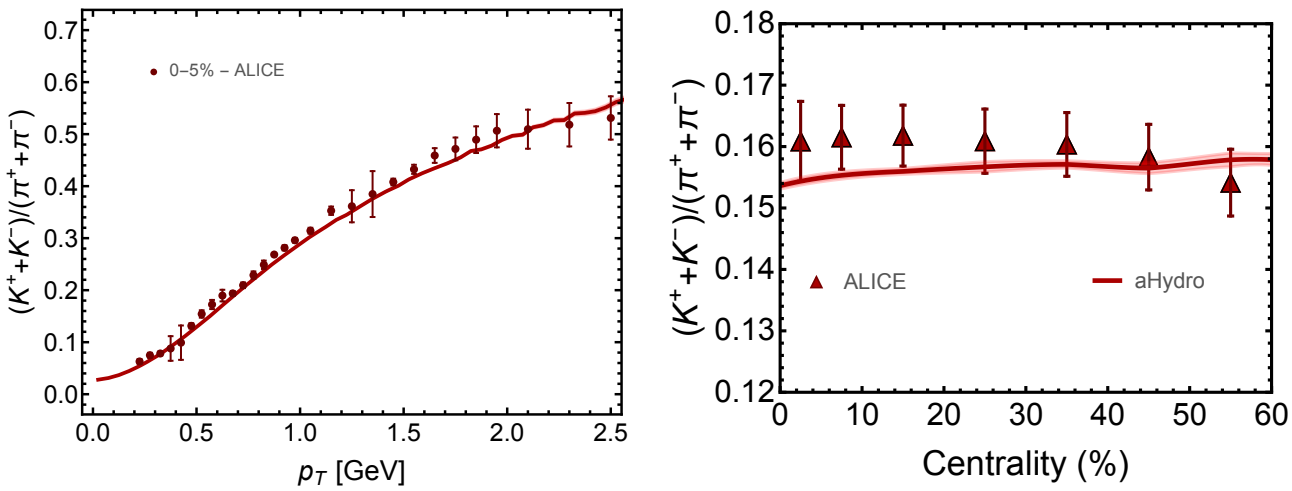

Figure 3: left: The kaon-to-pion ratio as a function of the transverse momentum. Right: The centrality dependence of the kaon-to-pion ratio. In both panels, the predictions of aHydroQP model are compared to experimental data from the ALICE collaboration in Pb-Pb collisions at $\sqrt{s_{NN}} = 5.02$ TeV. [9, 14].

however, it can be found in Ref. [13], where the agreement between aHydroQP model and the data for different centrality classes is good.

Next, in the left panel of Fig. 3, the kaon-to-pion ratio $(K^+ + K^-)/(\pi^+ + \pi^-)$ is presented as a function of p_T in the 0-5% centrality class. As can be seen from this figure, our model was able to reproduce the ratios well up to fairly large $p_T \sim 2.5$ GeV. We also show, in Fig. 3-right panel, the kaon-to-pion ratio as a function of centrality where our model again describes the data quite well over a wide range of centrality classes. In Ref. [9], we showed the kaon-to-pion ratio and also the proton-to-pion ratio for multiple different centrality classes with a reasonable agreement to the data at 5.023 TeV for Pb-Pb collisions from ALICE collaboration.

Next, we present comparisons of the anisotropic flow at 5.023 TeV for Pb-Pb collisions from the ALICE collaboration. In Fig. 4-left panel, the identified elliptic flow coefficient v_2 is shown in the 30-40% centrality class. A similar agreement between this model and experimental data is seen across different energies, see Refs. [9, 11, 13]. Moreover, the elliptic flow for charged hadrons as a function of p_T is shown in Fig. 4-right panel at 30-40% centrality

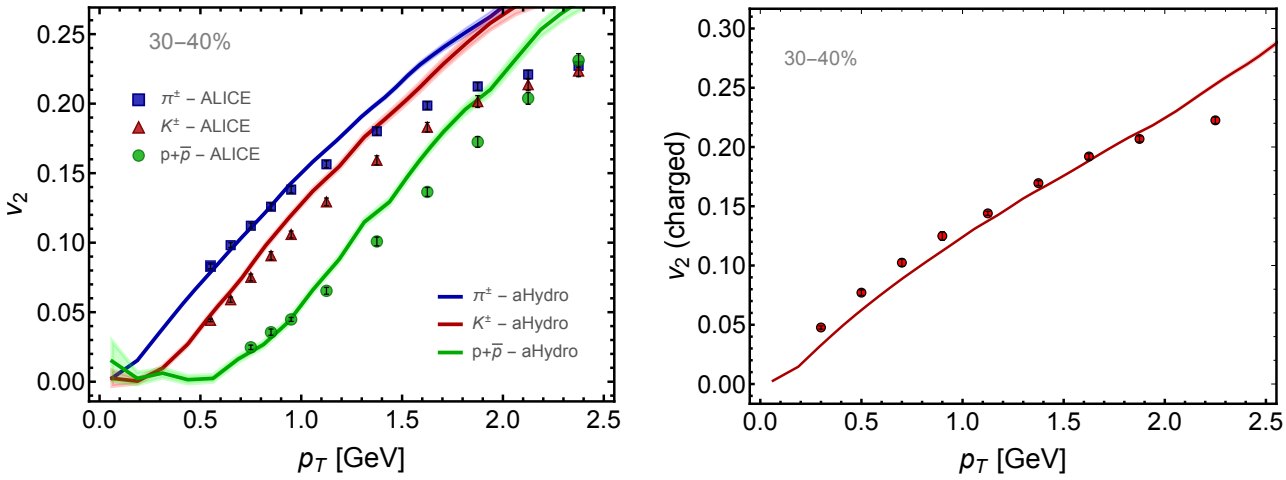

Figure 4: Left: The elliptic flow coefficient (v_2) as a function of the transverse momentum [15]. Right: The p_T dependence of v_2 of all charged particles [16]. In both panels, aHydroQP predictions are compared to experimental data from the ALICE collaboration in Pb-Pb collisions at $\sqrt{s_{NN}} = 5.02$ TeV in the 30-40% centrality class [9].

class. One can see that our model prediction agrees quite well with the data up to p_T GeV.

Furthermore, we present, in Fig. 5-left panel, the charged particle multiplicity as a function of the pseduorapidity where data are from the PHOBOS collaboration for Au+Au collisions at $\sqrt{s_{NN}}$=200 GeV. In this plot, the multiplicity is shown for different centrality classes: 0-3%, 3-6%, 6-10%, 10-15%, 15-20%, and 20-25%. We find that our model does a good job in reproducing the pseudorapidity dependence of the multiplicity in a wide range of centrality classes. A similar agreement to the data using aHydroQP model is observed for other systems at different energies [9, 13].

Finally, we present the aHydroQP predictions for HBT radii determined from pion correlations. As an example, in Fig. 5-right panel, we show the R_{out}/R_{side} ratio as a function of the mean transverse momentum of the pair $\pi^+\pi^+$ in the 5-10 % centrality class. As can be seen from this figure, our model was able to describe the experimental data from the STAR collaboration quite well especially for low k_T up to ~ 0.4 GeV. For more details, see Ref. [19]. We note here that a similar agreement of the HBT radii and their ratios with data is seen for 2.76 TeV Pb-Pb collisions [13].

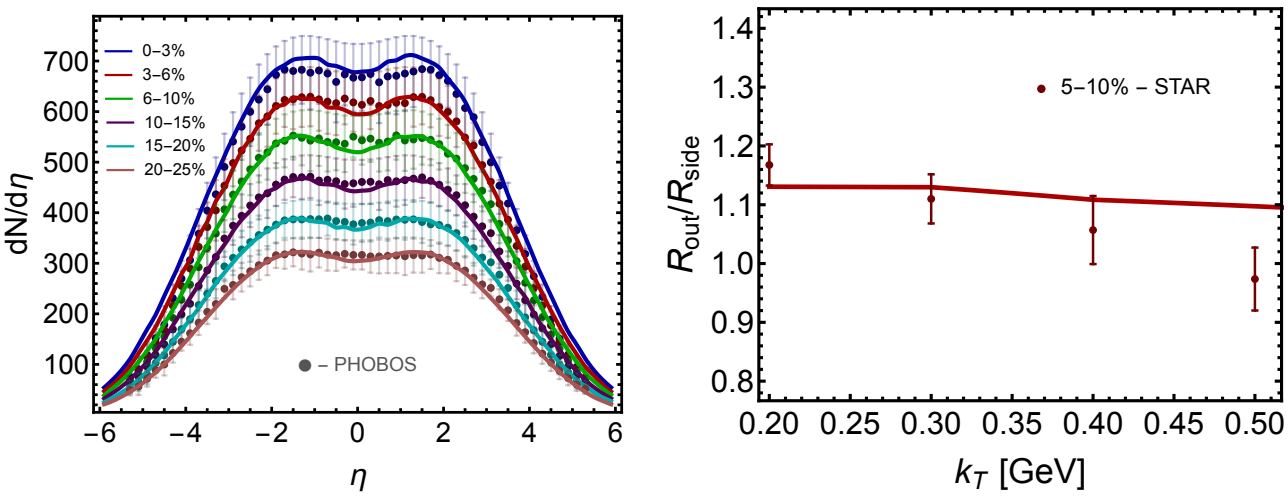

Figure 5: Left: Charged particle multiplicity as a function of pseudorapidity where data are from the PHOBOS collaboration [11, 17]. Right: The $R_{\rm out}/R_{\rm side}$ ratio as a function of the pair mean transverse momentum (k_T) for $\pi^+\pi^+$ in the 5-10% centrality class where data are from the STAR collaboration [18, 19]. In both panels, results are from Au-Au collisions at $\sqrt{s_{NN}}$=200 GeV.

6.7 Conclusions

In this chapter we presented a summary of recent progress in anisotropic hydrodynamics and its application to heavy-ion phenomenology. We began with a demonstration in the simple case of conformal Bjorken expansion that aHydro resums an infinite number of terms in the inverse Reynolds number. This feature allows aHydro to better describe systems that are far from equilibrium than traditional approaches. In AA collision large non-equilibrium corrections occur during the initial stages of the QGP ($\tau < 1$ fm/c) and at all times near the cold edges of the plasma where the relaxation time grows large. In collisions of small systems such as pA and pp one expects that, if a QGP is generated, it will be much more short-lived than in central AA collisions due to larger transverse gradients and, as a consequence, it will experience larger deviations from equilibrium during its evolution and freeze out.

Turning to AA phenomenology, we presented comparisons between the 3+1D aHydroQP model and heavy-ion experimental data collected at RHIC and LHC. We list the extracted initial central temperature and shear viscosity at 200 GeV, 2.76 TeV, and 5.02 TeV in Table

1. At all three collision energies with these parameters, we were able to describe the identified hadron spectra well, including the p_T-dependence of the kaon to pion ratio. In addition, the extracted integrated elliptic flow for charged particles and p_T-dependence of the pion, proton, and kaon elliptic flow were found to also be in good agreement with the data. Finally, we also presented comparisons between aHydroQP model predictions and STAR data from the ratio of 'out' and 'side' HBT radii, again finding good agreement with the data given current experimental uncertainties.

Looking to the future, final work is underway to release a new computational pipeline for 3+1D aHydroQP which includes fluctuating initial conditions of various types such as Trento [271, 272] or IP-Glasma [273–275], a custom anisotropic hadronic freeze-out sampler based on ISS [276], and full URQMD [277, 278] or SMASH [279] hadronic afterburners that include elastic as well as inelastic channels. Once complete, this will allow us to compute higher-order flow coefficients using aHydroQP in AA, pA, and pp collisions.

Chapter 7

Summary and outlook

This chapter provides a summary of the principal findings of the research, followed by discussions and prospective directions for relevant research projects. The primary objective of this research was to gain a deeper comprehension of the non-equilibrium dynamics of the Quark-Gluon Plasma (QGP) generated in ultra-relativistic heavy-ion collisions. The purpose of this study was to investigate the role of non-equilibrium effects at various phases of dynamical evolution. In order to accomplish this, we employed the Romatschke-Strickland anisotropic distribution function in both theoretical and phenomenological investigations. This distribution function allowed us to analyze and quantify the observed anisotropic flow phenomena in heavy-ion collisions. In order to provide an exhaustive and accurate evaluation of the results, we also compared them to other formulations of viscous hydrodynamics.

In Sections 4.4, 5.6, and 6.7, where each chapter concludes with more in-depth analyses, the findings are discussed in greater detail. These sections delve into the particular results of the research, highlighting the significance of non-equilibrium effects and casting light on the complex dynamics of the QGP system. It is suggested that the reader consult these sections for a fuller understanding of the research findings. The research initiatives discussed in this chapter provide avenues for future investigation. The non-equilibrium dynamics of the QGP system remain a subject of interest and significance in the field. Additional aspects of the system's behavior, the effects of various initial conditions, and the interplay between non-equilibrium dynamics and other phenomena could be the focus of future research.

7.1 Summary

The main purpose of the work presented in Chapter 4 was to develop a more accurate set of equations for the anisotropic hydrodynamic evolution in order to better characterize the non-equilibrium dynamics of the quark-gluon plasma produced in relativistic heavy ion collisions at RHIC and LHC. To improve the description of exact solutions to the Boltzmann equation found in the literature, a novel version of anisotropic hydrodynamics was developed, which incorporates free-streaming and equilibrating contributions. Using the new aHydro method, we computed explicit expressions for the first and second moments of the one-particle distribution function and used these to derive new 0+1d conformal equations of motion. The study also compared the exact RTA solution with the numerical solutions of the conformal 0+1d equations of motion for both the old and new aHydro schemes. According to the results, the new aHydro form can generate a bimodal distribution function comparable to the exact RTA solution for the one-particle distribution function. In addition, the study computed the evolution of the scaled moments as a function of the scaled time and we found that the new aHydro ansatz provides a more accurate approximation to the exact solution than the original aHydro ansatz. The study concluded by determining the non-equilibrium attractor associated with the new aHydro scheme and concluding that it provides significantly greater agreement with the exact RTA attractor than the original aHydro scheme, especially for moments with $l = 0$. In the future, the study suggests that it would be fascinating to apply the ansatz obtained here to full 3+1d anisotropic hydrodynamics, including temperature-dependent masses for the particles similar to 'canonical' quasiparticle aHydro.

In Chapters 5, by examining an explicit solution of the boost-invariant Boltzmann equation within the relaxation time approximation, we sought to determine whether attractors

exist in non-conformal kinetic theory. The time evolution of integral moments of the one-particle distribution function was studied by numerically solving the integral equation associated with the exact solution and taking into account a variety of initial momentum-space anisotropies and initialization times, while keeping the initial energy density constant. The occurrence of early and late attractors for the scaled longitudinal pressure, which indicates the convergence towards a universal behavior, was the study's key finding. These attractors provide important insights into the dynamics of non-conformal systems and suggested that the longitudinal pressure evolution may exhibit universal behavior that goes beyond the specifics of the initial conditions. Separate attractors did not, however, appear for the shear and bulk viscous corrections, suggesting that these variables have non-universal characteristics. For the values of n considered, moments with $l = 0$, in particular, did not show an early-time attractor.

Expressions for the first-order viscosity-corrected one-particle distribution function were generated inside the 14-moment and Chapman-Enskog approximations to evaluate the approach to the late-time hydrodynamic attractor. The findings showed that the first-order Chapman-Enskog form had greater quantitative agreement at late times, especially for higher-order moments and small masses relative to the initial temperature. However, when compared to the exact answers, the two approximation methods produced results that were equivalent for larger masses. Notably, it was found in chapters 5 Fig. 9 that the bulk viscous correction did not collapse to a single curve in the late-time, which corresponds to the Navier-Stokes limit accurate at first-order in gradients. This finding emphasizes how critical it is to take into account higher-order gradients in order to appropriately describe the behavior of the bulk viscous correction.

Finally, Chapter 6 provides a comprehensive overview of the most recent developments in anisotropic hydrodynamics and their application to heavy-ion phenomenology. We began

by demonstrating aHydro's resummation capability in the context of conformal Bjorken expansion, where it effectively includes an infinite number of terms in the inverse Reynolds number. This unique characteristic of aHydro enables it to describe systems that are far from equilibrium more accurately than conventional methods. Particularly, in heavy-ion collisions, significant non-equilibrium effects arise during the early phases of quark-gluon plasma (QGP) formation (at $\tau \lesssim 1$ fm/c) and close to the plasma's boundaries, where the relaxation time is extended. Moreover, in smaller systems, such as pA and pp collisions, the QGP's shorter lifetime owing to larger transverse gradients results in even more pronounced deviations from equilibrium during its evolution and freeze-out.

Shifting our attention to heavy-ion phenomenology, we provided extensive comparisons between the 3+1D aHydroQP model and experimental data from RHIC and LHC. The extracted initial central temperature and shear viscosity for collision energies of 200 GeV,2.76 TeV, and 5.02 TeV are shown in Table 1. Remarkably, the model reproduces the identified hadron spectra, including the p_T-dependence of the kaon-to-pion ratio, with these parameter values. In addition, the extracted integrated elliptic flow for charged particles and the p_T-dependence of elliptic flow for pions, protons, and kaons were in outstanding agreement with the experimental data. In addition, we presented comparisons between the aHydroQP model predictions and STAR data on the ratio of 'out' and 'side' HBT (Hanbury Brown-Twiss) radii, which showed good agreement within the experimental uncertainties.

7.2 Outlook

On the basis of these findings in Chapter 4, it would appear that the new version of anisotropic hydrodynamics (aHydro) improves the description of the non-equilibrium dynamics of the quark-gluon plasma in heavy-ion collisions. Here are some recommendations for future research in this area. Since the new aHydro method can reproduce a bimodal

distribution function similar to the exact RTA solution, it would be fascinating to investigate the physical implications and consequences of this bimodal structure. Understanding the fundamental mechanisms and their relationship to experimental observables could yield valuable insights. Extensive comparisons with experimental information: Validate the new aHydro method by comparing its predictions to heavy-ion collision experiments at RHIC and LHC. This would entail analyzing various observables, such as particle spectra, anisotropic flow coefficients, and correlations, as well as determining the accord between the new aHydro predictions and the experimental measurements. Addition of more physical principles such as examine the extension of the new aHydro framework to incorporate more realistic physics, including additional dissipative effects, finite-size effects, and quantum statistics. By investigating the effect of these additional factors on the system's evolution and the resulting observables, the dynamics of the quark-gluon plasma can be better understood. Application to various collision systems: Examine the applicability of the new aHydro method to systems besides heavy-ion collisions, such as proton-proton and proton-nucleus collisions. This would enable for a more extensive examination of the method's validity and its capacity to describe various collision system types. While the study focused on 0+1d conformal equations of motion, extending the new aHydro formalism to higher dimensions (such as 1+1d, 2+1d, or even 3+1d) would be advantageous. This would allow for the examination of more realistic scenarios and provide a deeper understanding of anisotropic hydrodynamics. The aforementioned recommendations are intended to enhance our comprehension of the non-equilibrium dynamics in heavy-ion collisions and further refine the new aHydro method. We can continue to improve our modeling of the quark-gluon plasma and obtain insight into the properties of the strongly interacting matter produced by these collisions by combining theoretical developments with experimental investigations.

Moreover, the discoveries obtained in Chapter 5 provide new opportunities for non-conformal kinetic theory studies in the future. By examining various initial conditions, system characteristics, and enhanced approximation techniques, the study of attractors in non-conformal systems can be refined and expanded. Another potential area, illustrated by the conformal instance, is to examine the implications of attractors for heavy-ion phenomenology. For instance, it has been demonstrated that the initial energy density of the quark-gluon plasma (QGP) and electromagnetic emissions can be constrained by the presence of a longitudinal pressure attractor. The general concept of using attractors in heavy-ion phenomenology is still relevant, even though the study's findings indicate that there may be some additional uncertainty related to how attractors are treated in the $l = 0$ scenario. The forward attractor nevertheless exhibits a collapse to a universal behavior when seen in moments with $l \neq 0$ for phenomenologically relevant starting times. Contrary to the conformal situation, the existence of a semi-universal collapse for moments with $l = 0$ introduces a small degree of uncertainty. Future research can focus on addressing these uncertanities and provide a more thorough explanation of the function of attractors in non-conformal kinetic theory.

Finally, depending on the result that we obtain in Chapter 6, in preparation for the future, we are currently developing a new computational infrastructure for 3+1D aHydroQP. This pipeline incorporates fluctuating initial conditions based on models such as Trento or IP-Glasma, a custom anisotropic hadronic freeze-out sampler inspired by the Integrated Surface Sampler (ISS), and full URQMD or SMASH hadronic afterburners that include both elastic and inelastic channels. This pipeline will allow us to compute higher-order flow coefficients using aHydroQP in a variety of collision systems, including AA, pA, and pp collisions, once it is completed. This effort represents a significant step toward a more complete comprehension of the collective behavior of strongly interacting matter in various collision scenarios.

Appendix A

Units

Natural units are a system of units used in physics, where physical quantities are expressed in terms of the fundamental constants of nature. The most common natural units in use today are based on the speed of light, c, and the reduced Planck constant, $\hbar$, with $c = 1$ and $\hbar = 1$. This means that instead of using standard units like meters and seconds, they use the speed of light (c) and the reduced Planck constant ($\hbar$) as the units for measuring velocities and actions. For example, energy, momentum, temperature, and mass are measured in units of GeV (or MeV) instead of Joules, while length and time are measured in units of GeV^{-1} instead of meters and seconds. In high-energy physics, scientists use the natural units to make their equations and calculations simpler. The advantage of using natural units is that many physical equations become much simpler and more transparent. For example, the expression for the energy of a particle with mass m and momentum p can be written as $E = \sqrt{p^2c^2 + m^2c^4} = \sqrt{p^2 + m^2}$ in natural units. This equation is much simpler and easier to understand than the equivalent equation in standard units, where c and $\hbar$ are explicit. To convert to SI units (stands for the International System of Units), we use

$$\begin{aligned} 1\,\mathrm{fm} &= 10^{-15}\,\mathrm{m}\,, \\ 1\,\mathrm{eV} &= 1.602 \times 10^{-19}\ \mathrm{J}\,, \end{aligned} \tag{A.1}$$

where in SI units we have

$$h = 6.626070150(81) \times 10^{-34}\,\mathrm{Js}\,, \tag{A.2}$$

$$c = 2.99792458 \times 10^{8}\ \mathrm{m/s}\,. \tag{A.3}$$

By setting $\hbar = c = 1$ in natural units, we obtain the conversion relations that allow us to easily convert from the energies and spatial/temporal lengths in natural units to SI units.

$$1\,\mathrm{GeV}^{-1} \equiv 0.197\,\mathrm{fm} \equiv 6.582 \times 10^{-25}\,\mathrm{s}\,. \tag{A.4}$$

Also, it is interesting to obtain an estimation of the temperature of the QGP in terms of Kelvin. For a typical temperature of QGP, i.e. $T_c \simeq 150$ MeV, and to convert from MeV to Kelvin (K), one needs to use the Boltzmann constant (k_B), which relates temperature to energy in the following way

$$E = k_B\, T$$

with E is the energy in joules, Boltzmann constant $k_B = 1.38 \times 10^{-23} J/K$, and T is the temperature in Kelvin. It yields

$$T_c \simeq 1.74 \times 10^{12}\,\mathrm{K}\,. \tag{A.5}$$

Throughout the text we use natural units with $c = \hbar = k_B = 1$.

Appendix B

Basic Notation

B.1 Coordinate system and local rest frame

It is practical to establish a unique coordinate system in particle and nuclear physics, where the spatial z-axis is parallel to the accelerator beam. The 3-vector connecting the centers of a beam particle and a target particle typically points in the opposite direction in collisions that are not quite central (not head on). The impact vector b, is a two-dimensional component of this vector that is orthogonal to the beam. The x direction is typically used to indicate this vector's direction. The so-called response plane of a specific collision $[x, z]$ is spanned by these two axes, x and z. Additionally, the local rest frame (LRF) of an object is the frame of reference in which the object is at rest, even if it is actually moving through spacetime. Therefore, in the LRF, we have

$$\begin{aligned} u^{\mu}_{LRF} &= (1,0,0,0), \\ x^{\mu}_{LRF} &= (0,1,0,0), \\ y^{\mu}_{LRF} &= (0,0,1,0), \\ z^{\mu}_{LRF} &= (0,0,0,1)\,. \end{aligned} \tag{B.1}$$

B.2 Spacetime parametrization

In special relativity, spacetime is treated as a four-dimensional continuum, and the spacetime coordinates are represented as x^μ, where μ takes on values from 0 to 3. These coordinates are used to describe events in spacetime,

$$x^\mu = (x^0, x^1, x^2, x^3) = (t, x, y, z)\,. \tag{B.2}$$

The invariant time that also called the longitudinal proper time τ is the invariant time (often called the longitudinal proper time) is defined as the proper time experienced by an observer moving along a trajectory in spacetime. It is calculated using the spacetime coordinates as

$$\tau = \sqrt{t^2 - z^2}, \tag{B.3}$$

The spacetime rapidity η is a parameter used in high-energy physics to describe the rapidity of particles. It is defined as

$$\eta = \frac{1}{2} \ln \frac{t+z}{t-z}. \tag{B.4}$$

Rapidity is a useful concept because it transforms linearly under Lorentz transformations and is additive in particle collisions.

We further define the distance in the transverse plane r, which refers to the plane perpendicular to the longitudinal direction (usually along the z-axis). Moreover, the transverse plane angle ϕ which defined as the angle between the vector from the origin to a point and the positive x-axis

$$r = \sqrt{x^2 + y^2}, \quad \phi = \tan^{-1}\left(\frac{y}{x}\right). \tag{B.5}$$

Moving to the scalar product of two four-vectors (or four-momenta) that is often used in

relativity to calculate quantities like energy, momentum, and invariant mass its notation is

$$a \cdot b = a_\mu b^\mu = g_{\mu\nu} a^\mu b^\nu \,, \tag{B.6}$$

where a_μ and b^μ are components of four-vectors, and $g_{\mu\nu}$ is the metric tensor. The metric tensor specifies the geometry of spacetime. In flat spacetime, such as in special relativity, the metric tensor has a diagonal form

$$g^{\mu\nu} = \begin{pmatrix} 1 & 0 & 0 & 0 \\ 0 & -1 & 0 & 0 \\ 0 & 0 & -1 & 0 \\ 0 & 0 & 0 & -1 \end{pmatrix}, \tag{B.7}$$

where the spacetime intervals have a signature of $g^{\mu\nu} = (1, -1, -1, -1)$, and $g^{\mu\nu} g_{\mu\nu} = 4$ is a property of this metric tensor.

B.3 Four-momentum parametrization

One of the key concepts in relativistic kinetic theory is the four-momentum of a particle p^μ, which is a vector quantity that combines the particle's energy, mass, and momentum into a single entity. The momentum of a particle depends on its energy as well as its mass and velocity, and the four-momentum incorporates all of these factors and it is typically parameterized as follows due to ultra-relativistic speeds along the z-axis in space-time: The four-momentum of a particle is a measure of the particle's mass and its motion. It is a four-vector in spacetime, which means that it has three spatial components (representing the particle's momentum) and one temporal component (representing the particle's energy).

In classical mechanics, the four-momentum of a particle is given by the following equation:

$$p^{\mu} = (p^0, p^1, p^2, p^3) = (E, p_x, p_y, p_z \equiv p_L)\,, \tag{B.8}$$

where E is the energy of the particle, p_x, p_y, and p_z are the components of the particle's momentum. In this case, the energy and momentum of the particle are related by the equation $E = \sqrt{\vec{p}^{\,2} + m^2}$, where m is the rest mass of the particle. Moreover, the transverse mass and the transverse momentum are

$$m_T = \sqrt{m^2 + p_T^2}\,,$$
$$p_T = \sqrt{p_x^2 + p_y^2}\,.$$

Additionally, the longitudinal rapidity, and the azimuthal angle in the transverse plane are

$$y = \frac{1}{2} \ln \frac{E_p + p_L}{E_p - p_L}\,,$$
$$\phi_p = \tan^{-1}\left(\frac{p_y}{p_x}\right)\,.$$

The pseudorapidity is defined as following

$$\eta = \frac{1}{2} \ln \left(\frac{|\mathbf{p}| + p_z}{|\mathbf{p}| - p_z} \right) = -\ln \Big[\tan(\theta/2) \Big]\,, \tag{B.9}$$

where θ is the angle that particle makes with the longitudinal direction (beamline direction). So, by measuring θ one can calculate η. Pseudorapidity ranges $(-\infty, \infty)$ for the particle along the beamline moving backward and forward, respectively. For the massless particles one has $\eta = y$.

B.4 Fluid velocity

In particle physics, the four-velocity of a particle u^μ describes how a particle moves through space-time and how is affected by external forces and it referred as a "time-like" unit vector parallel to the world-line of the particles (if there are particles in the matter, otherwise it is parallel to the energy flow). It is defined as $u^\mu = (u^0, u^1, u^2, u^3)$, where u^0 is the time component of the four-velocity and u^1, u^2, and u^3 are the space components. The four-velocity is normalized such that $u^\mu u_\mu = c^2 = 1$, where c is the speed of light and u_μ is the four-velocity in contravariant form (obtained by lowering the index with the metric tensor).

Appendix C

Tensor decomposition

We close this chapter with a section discussing algebraic structures of tensors used in our approach. Of special importance are the structures obtained for equilibrium and anisotropic RS distributions. The basis vectors are represented by the four-vectors denoted as A, B, C $\in [U, X, Y, Z]$. These vectors are used to form a basis for representing tensors and vectors in spacetime. Each vector corresponds to a specific direction in spacetime. These vectors are chosen to be orthogonal to each other, and they form a complete set, meaning any four-vector can be expressed as a linear combination of these basis vectors. The basis (B.1) is a orthonormal one in the sense that

$$A \cdot B = \begin{cases} 0 & \text{for } A \neq B, \\ 1 & \text{for } A = B = U, \\ -1 & \text{for } A = B \neq U. \end{cases} \tag{C.1}$$

In particular, one may express any four-vector by decomposing in the basis $\{A\}$. For example, the particle number flux can be written as

$$N^{\mu}(x) = \sum_{A} n_A \, A^{\mu}, \tag{C.2}$$

where the coefficients n_A, due to Eqs. (C.1), are given by the projections

$$n_A \;\; = \;\; A_{\mu} N^{\mu}(x) \, A^2, \tag{C.3}$$

with $A^2 = A \cdot A$ (note that $A^2 = -1$ for space-like four-vectors of the basis (B.1)).

The tensorial basis for the rank-two tensors is constructed using tensor products of the basis four-vectors $\{A \otimes B\}$. Using Eq. (B.1) one may express the metric tensor as [103]

$$g^{\mu\nu} = u^\mu u^\nu - \sum_{A \neq U} A^\mu A^\nu \,. \tag{C.4}$$

where this expression reflects the spacetime metric in a coordinate system aligned with the observer's four-velocity. The projector on the space orthogonal to the four-velocity, $\Delta^{\mu\nu} \equiv g^{\mu\nu} - U^\mu U^\nu$, then takes the form

$$\Delta^{\mu\nu} = - \sum_{A \neq U} A^\mu A^\nu \,, \tag{C.5}$$

and satisfies the conditions $U_\mu \Delta^{\mu\nu} = 0$, $\Delta^\mu{}_\alpha \Delta^{\alpha\nu} = \Delta^{\mu\nu}$, and $\Delta^\mu{}_\mu = 3$. In addition, the decomposition of the energy-momentum tensor takes the form

$$T^{\mu\nu}(x) \;\; = \;\; \sum_{A,B} t_{AB} A^\mu B^\nu, \tag{C.6}$$

with the components of $T^{\mu\nu}(x)$ defined as

$$t_{AB} = A_\mu B_\nu T^{\mu\nu}(x)\, A^2 B^2. \tag{C.7}$$

Similarly, one can construct the tensorial basis for the rank-three tensors allowing to decompose $I^{\mu\nu\lambda}$ tensor as follows

$$I^{\mu\nu\lambda}(x) = \sum_{A,B,C} c_{ABC} A^\mu B^\nu C^\lambda, \tag{C.8}$$

where the coefficients c_{ABC} are defined through the expression

$$c_{ABC} = A_\mu B_\nu C_\lambda I^{\mu\nu\lambda}(x)\, A^2 B^2 C^2. \tag{C.9}$$

Next, by using

$$\begin{aligned} N^\mu &= \int dP\, p^\mu f(x,p), & \text{(C.10)} \\ T^{\mu\nu}(x) &= \int dP\, p^\mu p^\nu f(x,p), & \text{(C.11)} \\ I^{\mu\nu\lambda}(x) &= \int dP\, p^\mu p^\nu p^\lambda f(x,p). & \text{(C.12)} \end{aligned}$$

in Eqs. (C.3), (C.7) and (C.9) one gets

$$\begin{aligned} n_A &= \int dP\, p^\mu A_\mu\, A^2 f(x,p), & \text{(C.13)} \\ t_{AB} &= \int dP\, p^\mu\, p^\nu\, A_\mu\, B_\nu\, A^2\, B^2\, f(x,p), & \text{(C.14)} \\ c_{ABC} &= \int dP\, p^\mu\, p^\nu\, p^\lambda A_\mu\, B_\nu\, C_\lambda\, A^2\, B^2\, C^2 f(x,p). & \text{(C.15)} \end{aligned}$$

In case of using equilibrium or anisotropic distribution function in Eqs. (C.13), (C.14) and (C.15) one has

$$\begin{aligned} n_A &= 0 \quad \text{if} \quad A \neq U, & \text{(C.16)} \\ t_{AB} &= 0 \quad \text{if} \quad A \neq B, & \text{(C.17)} \end{aligned}$$

where in the case of the equilibrium distribution function, the momentum-isotropic state

Eqs. (C.2) and (C.6) will be as the following

$$N^{\mu}_{\rm eq}(x) = n^{\rm eq}_{U} U^{\mu}, \tag{C.18}$$

$$T^{\mu\nu}_{\rm eq}(x) = t^{\rm eq}_{UU} U^{\mu}U^{\nu} - t^{\rm eq}_{XX} X^{\mu}X^{\nu} - t^{\rm eq}_{YY} Y^{\mu}Y^{\nu} - t^{\rm eq}_{ZZ}\, Z^{\mu}Z^{\nu} = \mathcal{E}^{\rm eq} U^{\mu}U^{\nu} - \mathcal{P}^{\rm eq}\Delta^{\mu\nu}, \tag{C.19}$$

$$I^{\mu\nu\lambda}(x) = c^{\rm eq}_{UUU} U^{\mu}U^{\nu}U^{\lambda} + \sum_{A} c^{\rm eq}_{UAA}(U^{\lambda}A^{\mu}A^{\nu} + A^{\lambda}U^{\mu}A^{\nu} + A^{\lambda}A^{\mu}U^{\nu}). \tag{C.20}$$

However, in the anisotropic distribution function, one obtains

$$N^{\mu}_{\rm a}(x) = n^{\rm a}_{U} U^{\mu}, \tag{C.21}$$

$$T^{\mu\nu}_{\rm a}(x) = t^{\rm a}_{UU} U^{\mu}U^{\nu} - t^{\rm a}_{XX} X^{\mu}X^{\nu} - t^{\rm a}_{YY} Y^{\mu}Y^{\nu} - t^{\rm a}_{ZZ}\, Z^{\mu}Z^{\nu}, \tag{C.22}$$

$$= \mathcal{E}^{\rm a} U^{\mu}U^{\nu} - \mathcal{P}^{\rm a}\Delta^{\mu\nu}_{T} + \mathcal{P}^{\rm a}_{L} Z^{\mu}Z^{\nu}, \tag{C.23}$$

$$\begin{aligned} I^{\lambda\mu\nu}_{\rm a} &= c^{\rm a}_{UUU}\, U^{\lambda}U^{\mu}U^{\nu} \\ &- c^{\rm a}_{UTT}\left(U^{\lambda}\Delta^{\mu\nu}_{T} + U^{\mu}\Delta^{\lambda\nu}_{T} + U^{\nu}\Delta^{\lambda\mu}_{T}\right) \\ &+ c^{\rm a}_{UZZ}\left(U^{\lambda}Z^{\mu}Z^{\nu} + U^{\mu}Z^{\lambda}Z^{\nu} + U^{\nu}Z^{\lambda}Z^{\mu}\right), \end{aligned} \tag{C.24}$$

with

$$\mathcal{E}^{\rm a} = t^{\rm a}_{UU}, \quad \mathcal{P}^{\rm a}_{T} = t^{\rm a}_{XX} = t^{\rm a}_{YY}, \quad \mathcal{P}^{\rm a}_{L} = t^{\rm a}_{ZZ}, \quad c^{\rm a}_{UXX} = c^{\rm a}_{UYY} = c^{\rm a}_{UTT}. \tag{C.25}$$

Here $\Delta^{\mu\nu}_{T} = -\left(X^{\mu}X^{\nu} + Y^{\mu}Y^{\nu}\right)$ is the projection operator on the direction orthogonal to U and Z.

Appendix D

The $\mathcal{H}$ and $\mathcal{R}$ functions

The functions $\mathcal{H}$, $\mathcal{H}_L$, and $\mathcal{H}_T$ are defined by the integrals

$$\begin{aligned}
\mathcal{H}(y) &= y\int_0^\pi d\theta\,\sin\theta\,\sqrt{y^2\cos^2\theta+\sin^2\theta}\,,\\
\mathcal{H}_L(y) &= y^3\int_0^\pi d\theta\,\frac{\sin\theta\cos^2\theta}{\sqrt{y^2\cos^2\theta+\sin^2\theta}}\,,\\
\mathcal{H}_T(y) &= y\int_0^\pi d\theta\,\frac{\sin^3\theta}{\sqrt{y^2\cos^2\theta+\sin^2\theta}}\,.
\end{aligned}\tag{D.1}$$

There are simple relations connecting $\mathcal{H}$, $\mathcal{H}_L$, and $\mathcal{H}_T$ with the functions $\mathcal{R}$, $\mathcal{R}_L$, and $\mathcal{R}_T$ defined in Ref. [97], namely

$$\begin{aligned}
\mathcal{H}\left(\frac{1}{\sqrt{1+\xi}}\right) &= 2\,\mathcal{R}(\xi)\,,\\
\mathcal{H}_L\left(\frac{1}{\sqrt{1+\xi}}\right) &= \frac{2}{3}\mathcal{R}_L(\xi)\,,\\
\mathcal{H}_T\left(\frac{1}{\sqrt{1+\xi}}\right) &= \frac{4}{3}\mathcal{R}_T(\xi)\,.
\end{aligned}\tag{D.2}$$

with

$$\begin{aligned}
\mathcal{R}_\epsilon(\xi) &= \frac{1}{2}\left[\frac{1}{1+\xi}+\frac{\arctan\sqrt{\xi}}{\sqrt{\xi}}\right],\\
\mathcal{R}_T(\xi) &= \frac{3}{2\xi}\left[\frac{1+(\xi^2-1)\mathcal{R}_\epsilon(\xi)}{\xi+1}\right],\\
\mathcal{R}_L(\xi) &= \frac{3}{\xi}\left[\frac{(\xi+1)\mathcal{R}_\epsilon(\xi)-1}{\xi+1}\right].
\end{aligned}\tag{D.3}$$

Appendix E

Finding a general moment for a Boltzmann equilibrium distribution function

E.1 For conformal system $m = 0$

$$\begin{aligned}
\mathcal{M}^{nl}_{\rm eq}(\tau) &= \int dP\,(p\cdot u)^n (p\cdot z)^{2l} f_{\rm eq}\left(-\frac{p.u}{T}\right), \\
&= \int \frac{d^3p}{(2\pi)^3}\, E^{\frac{n-1}{2}} p_z^{2l}\, f_{\rm eq}\left(-\frac{E}{T}\right), \\
&= \int \frac{d^3p}{(2\pi)^3}\, (p_T^2+p_z^2)^{\frac{n-1}{2}} p_z^{2l} f_{\rm eq}\left(-\sqrt{\frac{p_T^2}{T^2}+\frac{p_z^2}{T^2}}\right)
\end{aligned}$$

Changing variables to $\hat{p}_i \equiv \frac{p_i}{T}$ with $i \in (x, y, z)$

$$\mathcal{M}^{nl}_{\rm eq}(\tau) = \frac{T^{n+2l+2}}{(2\pi)^3}\int d^3\hat{p}\,(\hat{p}_T^2 + \hat{p}_z^2)^{\frac{n-1}{2}} \hat{p}_z^{2l} f_{\rm eq}\left(-|\hat{\mathbf{p}}|\right)$$

Next, transform to spherical coordinates:

$$\begin{aligned}
\hat{p}_x &= p\sin\theta\cos\phi\,, \\
\hat{p}_y &= p\sin\theta\sin\phi\,, \\
\hat{p}_z &= p\cos\theta\,,
\end{aligned}$$

one obtains

$$\mathcal{M}^{nl}_{\rm eq}(\tau) = \frac{T^{n+2l+2}}{(2\pi)^3}\underbrace{\int_0^\infty dp\; p^{n+2l+1}\; f_{\rm eq}\left(-|\hat{\mathbf{p}}|\right)}_{=\Gamma(2l+n+2)}\int_0^\pi \cos^{2l}\theta\,\sin\theta\,d\theta\int_0^{2\pi} d\phi$$

$$\mathcal{M}^{nl}_{\rm eq}(\tau) = \frac{2T^{2l+n+2}\Gamma(2l+n+2)}{(2\pi)^2(2l+1)}\,. \tag{E.1}$$

E.1.1 Computing the first moment for a 0+1d system

Computing the first moment gives

$$\partial_\mu T^{\mu\nu} = 0\,. \tag{E.2}$$

where

$$T^{\mu\nu} = \epsilon\; u^\mu u^\nu - P\;\Delta^{\mu\nu}\,, \tag{E.3}$$

and the standard transverse projection operator, which is orthogonal to u^μ, can be expressed as the following

$$\Delta^{\mu\nu} = g^{\mu\nu} - u^\mu u^\nu = -\sum_i X_i^\mu X_i^\nu\,. \tag{E.4}$$

Therefore

$$\begin{aligned}
T^{\mu\nu} &= \epsilon\; u^\mu u^\nu + \sum_i P_i X_i^\mu X_i^\nu\,,\\
\partial_\mu T^{\mu\nu} &= u^\nu \underbrace{u^\mu \partial_\mu}_{D}\epsilon + u^\nu \epsilon\, \underbrace{\partial_\mu u^\mu}_{\theta} + \epsilon\, \underbrace{u^\mu \partial_\mu}_{D} u^\nu + \sum_i [X_i^\nu \underbrace{X_i^\mu \partial_\mu}_{D_i} P_i + X_i^\nu P_i\, \underbrace{\partial_\mu X_i^\mu}_{\theta_i} + P_i\, \underbrace{X_i^\mu \partial_\mu}_{D_i} X_i^\nu]\,,\\
u_\nu \partial_\mu T^{\mu\nu} &= \underbrace{u_\nu u^\nu}_{1} D\epsilon + \underbrace{u_\nu u^\nu}_{1}\epsilon\,\theta + \underbrace{\epsilon\, D u^\nu u_\nu}_{0} + \sum_i [\underbrace{u_\nu X_i^\nu}_{0} D_i P_i + \underbrace{u_\nu X_i^\nu}_{0} P_i\,\theta_i + u_\nu P_i\, D_i X_i^\nu]\,,\\
u_\nu \partial_\mu T^{\mu\nu} &= D\epsilon + \epsilon\,\theta + \sum_i u_\nu P_i\, D_i X_i^\nu = D\epsilon + \epsilon\,\theta + \sum_i P_i\,\theta_i
\end{aligned} \tag{E.5}$$

with the co-moving derivative $D \equiv u^\mu \partial_\mu$, the expansion scalar $\theta \equiv \partial_\mu u^\mu$, and $\theta_i \equiv -u_\mu D_i X_i^\mu$, where X_i^μ are space-like basis vectors that are orthogonal to u^μ. Moreover, by taking into account the conservation of energy $\partial_\mu T^{\mu\nu} = 0$, one finds

$$D\epsilon + \epsilon\,\theta + \sum_i P_i\,\theta_i = 0. \tag{E.6}$$

For the case of 0+1d Bjorken expansion one has $D = \partial_\tau$, $\theta = \partial_\mu u^\mu = 1/\tau$, $\theta_x = \theta_y = 0$ and $\theta_z = -1/\tau$. Therefore, by expanding this equation out in terms of the non-vanishing components of the energy-momentum tensor, for a 0+1d system, one obtains the evolution equation that can be written compactly as

$$\partial_\tau \epsilon = -\frac{\epsilon + P_L}{\tau}\,. \tag{E.7}$$

E.1.2 Computing the second moment for a 0+1d system

$$I^{\mu\nu\lambda} = \int dP\; p^\mu p^\nu p^\lambda f\,. \tag{E.8}$$

Finding I_z

$$I_z = \int dP\; (p\cdot u)(p\cdot z)(p\cdot z) f\,. \tag{E.9}$$

By applying $f = \exp\left(-\frac{\sqrt{p_T^2+(1+\xi(\tau))p_z^2}}{\Lambda(\tau)}\right)$, $p\cdot u = E$, $p\cdot z = -p_z$, and $dP = \frac{d^3p}{(2\pi)^3 E}$, one finds

$$\begin{aligned} I_z &= \int \frac{d^3p}{(2\pi)^3 E}\; E\; p_z^2 \exp\left(-\frac{\sqrt{p_T^2 + (1+\xi(\tau))p_z^2}}{\Lambda(\tau)}\right), &\text{(E.10)}\\ &= \frac{1}{(2\pi)^3}\int d^3p\; p_z^2 \exp\left(-\sqrt{\frac{p_T^2}{\Lambda^2} + \frac{p_z^2}{\alpha^2\Lambda^2}}\right)\,, &\text{(E.11)} \end{aligned}$$

where $\alpha = \frac{1}{\sqrt{1+\xi}}$. Next, by changing variables to

$$\hat{p}_T = \frac{p_T}{\Lambda},$$
$$\hat{p}_z = \frac{p_z}{\alpha\Lambda},$$

one obtains

$$I_z = \frac{\alpha^3 \Lambda^5}{(2\pi)^3} \int d^2\hat{p}_T \; d\hat{p}_z \; \hat{p}_z^2 \exp\left(-\sqrt{\hat{p}_T^2 + \hat{p}_z^2}\right) , \tag{E.12}$$

then transforming to spherical coordinates

$$\hat{p}_x = p \sin\theta \cos\phi \,,$$

$$\hat{p}_y = p \sin\theta \sin\phi \,,$$

$$\hat{p}_z = p \cos\theta,$$

gives

$$\int d^2\hat{p}_T \; d\hat{p}_z = \int_0^\infty p^2 \; dp \int_0^\pi \sin\theta \; d\theta \int_0^{2\pi} d\phi = 2\pi \int_0^\infty p^2 \; dp \int_0^\pi \sin\theta \; d\theta \,,$$

$$I_z = \frac{\alpha^3 \Lambda^5}{(2\pi)^2} \underbrace{\int_0^\infty p^4 dp \exp(-|\mathbf{p}|)}_{\Gamma(z)=\int_0^\infty t^{(z-1)} e^{-t} dt = 24} \underbrace{\int_0^\pi \sin\theta \cos^2\theta d\theta}_{\frac{2}{3}} \,, \tag{E.13}$$

$$\boxed{I_z = \frac{\alpha^3}{(2\pi)^2}(24)(\frac{2}{3})\Lambda^5 = I_0 \; \mathcal{S}_L(\xi) \,,} \tag{E.14}$$

where $I_0 = \frac{4}{(2\pi)^2}\Lambda^5$.

Finding I_x :

Now to find I_x by doing the same steps:

$$I_x = \int dP \; (p \cdot u)(p \cdot x)(p \cdot x) f \,, \tag{E.15}$$

with $f = \exp\left(-\frac{\sqrt{p_T^2+(1+\xi(\tau))p_z^2}}{\Lambda(\tau)}\right)$, $p\cdot u = E$, $p\cdot z = -p_z$, and $dP = \frac{d^3p}{(2\pi)^3 E}$, one finds

$$I_x = \int \frac{d^3p}{(2\pi)^3 E}\; E\; p_x^2 \exp\left(-\frac{\sqrt{p_T^2+(1+\xi(\tau))p_z^2}}{\Lambda(\tau)}\right), \tag{E.16}$$

$$= \frac{1}{(2\pi)^3}\int d^3p\; p_x^2 \exp\left(-\sqrt{\frac{p_T^2}{\Lambda^2}+\frac{p_z^2}{\alpha^2\Lambda^2}}\right), \tag{E.17}$$

where $\alpha = \frac{1}{\sqrt{1+\xi}}$. Next, by changing variables to

$$\hat{p}_T = \frac{p_T}{\Lambda},$$
$$\hat{p}_z = \frac{p_z}{\alpha\Lambda},$$

one obtains

$$I_x = \frac{\alpha\Lambda^5}{(2\pi)^3}\int d^2\hat{p}_T\; d\hat{p}_z\; \hat{p}_x^2 \exp\left(-\sqrt{\hat{p}_T^2+\hat{p}_z^2}\right), \tag{E.18}$$

then transforming to spherical coordinates

$$\hat{p}_x = p\sin\theta\cos\phi\,,$$
$$\hat{p}_y = p\sin\theta\sin\phi\,,$$
$$\hat{p}_z = p\cos\theta,$$

gives

$$\int d^2\hat{p}_T\; d\hat{p}_z = \int_0^\infty p^2\; dp \int_0^\pi \sin\theta\; d\theta \int_0^{2\pi} d\phi = 2\pi\int_0^\infty p^2\; dp\int_0^\pi \sin\theta\; d\theta\,,$$

$$I_x = \frac{\alpha\Lambda^5}{(2\pi)^2} \underbrace{\int_0^\infty p^4 dp \exp(-|\mathbf{p}|)}_{\Gamma(z)=\int_0^\infty t^{(z-1)}e^{-t}dt=24} \underbrace{\int_0^\pi \sin\theta\cos^2\theta d\theta}_{\frac{2}{3}}, \tag{E.19}$$

$$\boxed{I_x = \frac{\alpha}{(2\pi)^2}(24)(\frac{2}{3})\Lambda^5 = I_0\ \mathcal{S}_T(\xi) = I_y} \tag{E.20}$$

E.2 For non conformal system $m \neq 0$

Start by using the classical Boltzmann statistics distribution function

$$f_{\rm eq} = \exp\left(-\frac{\sqrt{p_z^2+p_T^2+m^2}}{T(\tau)}\right). \tag{E.21}$$

Then, the general expression is

$$\mathcal{M}^{nl}_{\rm eq} \;=\; \int dP\,(p\cdot u)^n (p\cdot z)^{2l}\, f_{\rm eq}(w,p_T)\,, \tag{E.22}$$

and by using $p\cdot u = E$, $p\cdot z = -p_z$, $dP = \frac{d^3p}{(2\pi)^3E}$, and $E = \sqrt{p_T^2+p_z^2+m^2}$

$$\begin{aligned}
\mathcal{M}^{nl}_{\rm eq} &= \int \frac{d^3p}{(2\pi)^3E}\,E^n\,p_z^{2l}\,\exp\left(-\frac{\sqrt{p_T^2+p_z^2+m^2}}{T(\tau)}\right)\\
&= \frac{1}{(2\pi)^3}\int d^3p\,E^{n-1}\,p_z^{2l}\,\exp\left(-\sqrt{\frac{p_T^2}{T^2}+\frac{p_z^2}{T^2}+\frac{m^2}{T^2}}\right)\\
&= \frac{1}{(2\pi)^3}\int d^3p\,(p_T^2+p_z^2+m^2)^{\frac{n-1}{2}}\,p_z^{2l}\,\exp\left(-\sqrt{\frac{p_T^2}{T^2}+\frac{p_z^2}{T^2}+\frac{m^2}{T^2}}\right).
\end{aligned}$$

Changing variables to

$$\begin{aligned} \hat{p}_T &= \frac{p_T}{T}\,, & dp_T &= T\, d\hat{p}_T\,, \\ \hat{p}_z &= \frac{p_z}{T}\,, & dp_z &= T\, d\hat{p}_z\,, \\ \hat{m}_{\rm eq} &= \frac{m}{T}\,, \end{aligned}$$

one obtains

$$\mathcal{M}_{\rm eq}^{nl} \;=\; \frac{T^{2l+n+2}}{(2\pi)^3}\int d^2\hat{p}_T\; d\hat{p}_z\,(\hat{p}_T^2+\hat{p}_z^2+\hat{m}_{\rm eq}^2)^{\frac{n-1}{2}}\,\hat{p}_z^{2l}\,\exp\left(-\sqrt{\hat{p}_T^2+\hat{p}_z^2+\hat{m}_{\rm eq}^2}\right).$$

Transforming to spherical coordinates one finds

$$\begin{gathered} \sqrt{\hat{p}_T^2+\hat{p}_z^2+\hat{m}_{\rm eq}^2} = \sqrt{\hat{p}^2+\hat{m}_{\rm eq}^2}\,, \\ \int d^2\hat{p}_T d\hat{p}_z = \int_0^\infty \hat{p}^2 d\hat{p}\int_0^\pi \sin\theta d\theta\int_0^{2\pi} d\phi = 2\pi\int_0^\infty \hat{p}^2 d\hat{p}\int_0^\pi \sin\theta d\theta\,, \\ \hat{p}_T^2+\hat{p}_z^2+\hat{m}_{\rm eq}^2 = \hat{p}^2+\hat{m}_{\rm eq}^2\,. \end{gathered}$$

Therefore,

$$\mathcal{M}_{\rm eq}^{nl} = \frac{T^{2l+n+2}}{(2\pi)^2}\underbrace{\int_0^\infty d\hat{p}\,\hat{p}^{2l+2}\,\exp\left(-\sqrt{\hat{p}^2+\hat{m}_{\rm eq}^2}\right)\left(\hat{p}^2+\hat{m}_{\rm eq}^2\right)^{\frac{n-1}{2}}}_{F_1}\int_0^\pi d\theta\sin\theta\,\cos^{2l}\theta\,. \quad \text{(E.23)}$$

To find F_1, we change variables as following

$$
\begin{aligned}
x &\equiv \sqrt{\hat{p}^2 + \hat{m}_{\rm eq}^2}\,, & &\Rightarrow \hat{p} = \sqrt{x^2 - \hat{m}_{\rm eq}^2}\,,\\
dx &= \frac{\hat{p} d\hat{p}}{\sqrt{\hat{p}^2 + \hat{m}_{\rm eq}^2}} = \frac{\hat{p}\, d\hat{p}}{x}\,, & &\Rightarrow x dx = \hat{p} d\hat{p}\,,\\
\hat{p} &= 0 \Rightarrow x = \hat{m}_{\rm eq}\,,\\
\hat{p} &= \infty \Rightarrow x = \infty\,.
\end{aligned}
$$

giving

$$
\mathcal{M}_{\rm eq}^{nl} = \frac{T^{2l+n+2}}{(2\pi)^2} \underbrace{\int_{\hat{m}_{\rm eq}}^{\infty} x dx \,(x^2 - \hat{m}_{\rm eq}^2)^{\frac{2l+1}{2}}\, e^{-x}\,(x)^{n-1}}_{F_2} \int_0^{\pi} d\theta \sin\theta\, \cos^{2l}\theta\,.
$$

Now we compute the part F_2 using the following form, which is a Bessel function

$$
K_\nu(z) = \frac{\sqrt{\pi}}{\Gamma(\nu + \frac{1}{2})} \left(\frac{z}{2}\right)^\nu \int_1^\infty e^{-zx}\,(x^2-1)^{\nu-\frac{1}{2}} dx\,. \qquad \nu > -\frac{1}{2}\,. \tag{E.24}
$$

When $\nu = 1$

$$
K_1(z) = \underbrace{\frac{\sqrt{\pi}}{\Gamma(3/2)}}_{=\frac{\sqrt{\pi}}{2}} \left(\frac{z}{2}\right) \int_1^\infty e^{-zx}\,(x^2-1)^{\frac{1}{2}} dx = z \int_1^\infty e^{-zx}\,(x^2-1)^{\frac{1}{2}} dx\,,
$$

$$
\boxed{\frac{K_1(z)}{z} = \int_1^\infty e^{-zx}\,(x^2-1)^{\frac{1}{2}} dx} \tag{E.25}
$$

Taking the derivative in Eq. (E.25) one obtains

$$
\frac{dK_1(z)}{dz} = K_1'(z) = \underbrace{\int_1^\infty e^{-zx}\,(x^2-1)^{\frac{1}{2}} dx}_{=\frac{K_1(z)}{z}} - z \int_1^\infty x\, e^{-zx}\,(x^2-1)^{\frac{1}{2}} dx\,. \tag{E.26}
$$

By using the identity:

$$K'_\nu(z) = -\frac{1}{2}K_{\nu-1}(z) - \frac{1}{2}K_{\nu+1}(z)\,, \tag{E.27}$$

when $\nu = 1$

$$K'_1(z) = -\frac{1}{2}K_0(z) - \frac{1}{2}K_2(z)\,, \tag{E.28}$$

we then substitute the results of Eq. (E.26) in Eq. (E.28), one obtains

$$-\frac{1}{2}K_0(z) - \frac{1}{2}K_2(z) \;=\; \frac{K_1(z)}{z} - z\int_1^\infty x\, e^{-zx}\,(x^2-1)^{\frac{1}{2}}dx\,. \tag{E.29}$$

Then using the identity:

$$K_{\nu+1}(z) = K_{\nu-1}(z) + \frac{2\nu}{z}K_\nu(z)\,, \tag{E.30}$$

when $\nu = 1$ one obtains

$$\begin{aligned} K_2(z) &= K_0(z) + \frac{2}{z}K_1(z) \\ &\Rightarrow K_0(z) = K_2(z) - \frac{2}{z}K_1(z)\,. \end{aligned}$$

Applying this result in Eq. (E.29), gives

$$\begin{aligned} \frac{1}{z}K_1(z) - \frac{1}{2}K_2(z) - \frac{1}{2}K_2(z) &= \frac{K_1(z)}{z} - z\int_1^\infty x\, e^{-zx}\,(x^2-1)^{\frac{1}{2}}dx \\ K_2(z) &= z\int_1^\infty x\, e^{-zx}\,(x^2-1)^{\frac{1}{2}}dx\,. \end{aligned}$$

which results in

$$\boxed{\frac{K_2(z)}{z} = \int_1^\infty xe^{-zx}\,(x^2-1)^{\frac{1}{2}}dx\,.} \tag{E.31}$$

Using

$$x = \sqrt{\hat{p}^2 + \hat{m}_{\rm eq}^2} = \hat{m}_{\rm eq} \sqrt{\underbrace{\frac{\hat{p}^2}{\hat{m}_{\rm eq}^2}}_{\kappa^2} + 1} = \hat{m}_{\rm eq} \underbrace{\sqrt{\kappa^2 + 1}}_{y}, \qquad \Rightarrow x = \hat{m}_{\rm eq}\, y\,,$$

$$dx = \hat{m}_{\rm eq}\, dy\,, \qquad \Rightarrow x\, dx = \hat{m}_{\rm eq}^2 y\, dy\,,$$

$$x = \hat{m}_{\rm eq} \Rightarrow y = 1\,, \qquad x = \infty \Rightarrow y = \infty\,,$$

$$\mathcal{M}_{\rm eq}^{nl} = \frac{T^{2l+n+2}}{(2\pi)^2} \int_1^\infty \hat{m}_{\rm eq}^2 y\, dy\, (\hat{m}_{\rm eq}^2 y^2 - \hat{m}_{\rm eq}^2)^{\frac{2l+1}{2}}\, e^{-\hat{m}_{\rm eq}\, y}\, (\hat{m}_{\rm eq}\, y)^{n-1} \int_0^\pi d\theta \sin\theta\, \cos^{2l}\theta\,,$$

or

$$\boxed{\mathcal{M}_{\rm eq}^{nl} = \frac{(\hat{m}_{\rm eq}\, T)^{2l+n+2}}{(2\pi)^2} \int_1^\infty y^n\, (y^2-1)^{\frac{2l+1}{2}}\, e^{-\hat{m}_{\rm eq}\, y}\, dy \int_0^\pi d\theta \sin\theta\, \cos^{2l}\theta\,.} \tag{E.32}$$

E.2.1 Equilibrium thermodynamic functions

The general moment that I obtain in section 1.3 is:

$$\boxed{\mathcal{M}_{\rm eq}^{nl} = \frac{(\hat{m}_{\rm eq}\, T)^{2l+n+2}}{(2\pi)^2} \int_1^\infty y^n\, (y^2-1)^{\frac{2l+1}{2}}\, e^{-\hat{m}_{\rm eq}\, y}\, dy \int_0^\pi d\theta \sin\theta\, \cos^{2l}\theta\,.} \tag{E.33}$$

The equilibrium particle density

Using the general form Eq. (E.33) when $n = 1$ and $l = 0$ to find the equilibrium particle density:

$$\mathcal{M}_{\rm eq}^{10} = \frac{\hat{m}_{\rm eq}^3\, T^3}{2\pi^2} \int_1^\infty y \sqrt{y^2-1}\; e^{-\hat{m}_{\rm eq}\, y}\; dy\,. \tag{E.34}$$

By comparing the integral in Eq. (E.34) with Eq. (E.31)), one finds :

$$\mathcal{M}^{10}_{\rm eq} = \frac{\hat{m}^3_{\rm eq}\, T^3}{2\pi^2} \frac{K_2(\hat{m}_{\rm eq})}{\hat{m}_{\rm eq}}\,,$$

$$\boxed{\mathcal{N}_{\rm eq} = \frac{\hat{m}^2_{\rm eq}\, T^3}{2\pi^2} K_2(\hat{m}_{\rm eq})\,.} \tag{E.35}$$

The equilibrium energy density

Using the general form Eq. (E.33) when $n = 2$ and $l = 0$

$$\mathcal{M}^{20}_{\rm eq} = \frac{\hat{m}^4_{\rm eq}\, T^4}{2\pi^2} \int_1^\infty y^2 \sqrt{y^2-1}\ e^{-\hat{m}_{\rm eq}\, y}\ dy\,. \tag{E.36}$$

To solve the integral $\int_1^\infty y^2 \sqrt{y^2-1}\ e^{-\hat{m}_{\rm eq}\, y}\ dy$ we start by taking a derivative of Eq. (E.31)

$$\frac{dK_2(z)}{dz} = K_2'(z) = \underbrace{\int_1^\infty x\, e^{-zx}\, (x^2-1)^{\frac{1}{2}} dx}_{=\frac{K_2(z)}{z}} - z \int_1^\infty x^2\, e^{-zx}\, (x^2-1)^{\frac{1}{2}} dx\,. \tag{E.37}$$

Then using the identity in Eq. (E.28) one obtains

$$K_2'(z) = -\frac{1}{2} K_1(z) - \frac{1}{2} K_3(z)\,, \tag{E.38}$$

after that, combining Eq. (E.37) and Eq. (E.38), one finds

$$-\frac{1}{2} K_1(z) - \frac{1}{2} K_3(z) \ = \ \frac{K_2(z)}{z} - z \int_1^\infty x^2\, e^{-zx}\, (x^2-1)^{\frac{1}{2}} dx\,. \tag{E.39}$$

then using the identity Eq. (E.30) when $\nu = 2$ gives

$$K_3(z) = K_1(z) + \frac{4}{z} K_2(z)\,. \tag{E.40}$$

Applying this result in Eq. (E.39) gives

$$\begin{aligned} -\frac{1}{2}K_1(z) - \frac{1}{2}K_1(z) - \frac{2}{z}K_2(z) &= \frac{K_2(z)}{z} - z\int_1^\infty x^2\, e^{-zx}\,(x^2-1)^{\frac{1}{2}}\,dx \\ \frac{1}{z}K_1(z) + \frac{3}{z^2}K_2(z) &= \int_1^\infty x^2\, e^{-zx}\,(x^2-1)^{\frac{1}{2}}\,dx\,. \end{aligned} \tag{E.41}$$

The form of the integral in Eq. (E.41) is the same as in Eq. (E.36) by considering $z = \hat{m}_{\rm eq}$ and $x = \hat{m}_{\rm eq}\, y$, so

$$\mathcal{M}^{20}_{\rm eq} = \frac{\hat{m}^4_{\rm eq}\, T^4}{2\pi^2}\left[\frac{1}{\hat{m}_{\rm eq}} K_1(\hat{m}_{\rm eq}) + \frac{3}{\hat{m}^2_{\rm eq}} K_2(\hat{m}_{\rm eq})\right], \tag{E.42}$$

$$\boxed{\mathcal{E}_{\rm eq} = \frac{\hat{m}^2_{\rm eq}\, T^4}{2\pi^2}\left[3K_2(\hat{m}_{\rm eq}) + \hat{m}_{\rm eq} K_1(\hat{m}_{\rm eq})\right].} \tag{E.43}$$

The equilibrium pressure

Using the general form Eq. (E.33) when $n = 0$ and $l = 1$

$$\mathcal{P}_{\rm eq} = \frac{(\hat{m}_{\rm eq}\, T)^4}{(2\pi)^2}\int_1^\infty (y^2-1)^{\frac{3}{2}}\, e^{-\hat{m}_{\rm eq}\, y}\, dy \int_0^\pi d\theta \sin\theta\, \cos^2\theta\,, \tag{E.44}$$

$$\mathcal{P}_{\rm eq} = \frac{\hat{m}^4_{\rm eq}\, T^4}{6\pi^2}\int_1^\infty (y^2-1)^{\frac{3}{2}}\, e^{-\hat{m}_{\rm eq}\, y}\, dy\,. \tag{E.45}$$

To solve the integral in Eq. (E.45), we use Eq. (E.24) when $\nu = 2$ and $z = \hat{m}_{\rm eq}$, and $x = y$

$$K_2(\hat{m}_{\rm eq}) = \frac{\sqrt{\pi}}{\Gamma(\frac{5}{2})}\frac{\hat{m}^2_{\rm eq}}{4}\int_1^\infty e^{-\hat{m}_{\rm eq} y}\,(y^2-1)^{\frac{3}{2}}\,dy\,, \tag{E.46}$$

or, equivalently,

$$\int_1^\infty e^{-\hat{m}_{\rm eq} y}\,(y^2-1)^{\frac{3}{2}} dy = \frac{3}{\hat{m}_{\rm eq}^2} K_2(\hat{m}_{\rm eq})\,. \tag{E.47}$$

Therefore,

$$\mathcal{P}_{\rm eq} \;=\; \frac{\hat{m}_{\rm eq}^4\, T^4}{6\pi^2}\frac{3}{\hat{m}_{\rm eq}^2} K_2(\hat{m}_{\rm eq}) = \frac{\hat{m}_{\rm eq}^2\, T^4}{2\pi^2} K_2(\hat{m}_{\rm eq})\,. \tag{E.48}$$

$$\boxed{\mathcal{P}_{\rm eq} = T\mathcal{N}_{\rm eq}\,.} \tag{E.49}$$

The equilibrium entropy

The entropy can obtained as follows

$$\begin{aligned}\mathcal{S}_{\rm eq} &= \frac{\mathcal{E}_{\rm eq}+\mathcal{P}_{\rm eq}}{T} \\ &= \frac{1}{T}\frac{\hat{m}_{\rm eq}^2\, T^4}{2\pi^2}\left[3K_2(\hat{m}_{\rm eq}) + \hat{m}_{\rm eq} K_1(\hat{m}_{\rm eq})\right] + \frac{\hat{m}_{\rm eq}^2\, T^4}{2\pi^2} K_2(\hat{m}_{\rm eq})\,,\end{aligned} \tag{E.50}$$

which upon simplification gives

$$\boxed{\mathcal{S}_{\rm eq} = \frac{\hat{m}_{\rm eq}^2\, T^3}{2\pi^2}\left[4K_2(\hat{m}_{\rm eq}) + \hat{m}_{\rm eq} K_1(\hat{m}_{\rm eq})\right]\,.} \tag{E.51}$$

References

[1] M. Strickland, *Relativistic Quantum Field Theory, Volume 2*. 2053-2571. Morgan & Claypool Publishers, 2019. https://dx.doi.org/10.1088/2053-2571/ab3108.

[2] **Particle Data Group** Collaboration, R. L. Workman *et al.*, "Review of Particle Physics", *PTEP* **2022** (2022) 083C01.

[3] A. Deur, S. J. Brodsky, and G. F. de Teramond, "Connecting the Hadron Mass Scale to the Fundamental Mass Scale of Quantum Chromodynamics", *Phys. Lett. B* **750** (2015) 528–532, arXiv:1409.5488 [hep-ph].

[4] **NA60+** Collaboration, A. De Falco, "Prospects for the NA60+ experiment at the CERN SPS", *EPJ Web Conf.* **259** (2022) 09003, arXiv:2108.11300 [nucl-ex].

[5] F. Gelis, "The Early Stages of a High Energy Heavy Ion Collision", *J. Phys. Conf. Ser.* **381** (2012) 012021, arXiv:1110.1544 [hep-ph].

[6] M. Strickland, "Anisotropic hydrodynamics: Three lectures", *Acta Physica Polonica B* **45** no. 12, (2014) 2355. http://dx.doi.org/10.5506/APhysPolB.45.2355.

[7] M. L. Miller, K. Reygers, S. J. Sanders, and P. Steinberg, "Glauber modeling in high energy nuclear collisions", *Ann. Rev. Nucl. Part. Sci.* **57** (2007) 205–243, arXiv:nucl-ex/0701025.

[8] M. Alqahtani, M. Nopoush, and M. Strickland, "Quasiparticle equation of state for anisotropic hydrodynamics", *Phys. Rev. C* **92** no. 5, (2015) 054910, arXiv:1509.02913 [hep-ph].

[9] M. Alqahtani and M. Strickland, "Bulk observables at 5.02 TeV using quasiparticle anisotropic hydrodynamics", *Eur. Phys. J. C* **81** no. 11, (2021) 1022, arXiv:2008.07657 [nucl-th].

[10] **PHENIX** Collaboration, S. S. Adler *et al.*, "Identified charged particle spectra and yields in Au+Au collisions at S(NN)**1/2 = 200-GeV", *Phys. Rev. C* **69** (2004) 034909, arXiv:nucl-ex/0307022.

[11] D. Almaalol, M. Alqahtani, and M. Strickland, "Anisotropic hydrodynamic modeling of 200 GeV Au-Au collisions", *Phys. Rev. C* **99** no. 4, (2019) 044902, arXiv:1807.04337 [nucl-th].

[12] **ALICE** Collaboration, B. Abelev *et al.*, "Centrality dependence of π, K, p production in Pb-Pb collisions at $\sqrt{s_{NN}} = 2.76$ TeV", *Phys. Rev. C* **88** (2013) 044910, arXiv:1303.0737 [hep-ex].

[13] M. Alqahtani, M. Nopoush, R. Ryblewski, and M. Strickland, "Anisotropic hydrodynamic modeling of 2.76 TeV Pb-Pb collisions", *Phys. Rev. C* **96** no. 4, (2017) 044910, arXiv:1705.10191 [nucl-th].

[14] **ALICE** Collaboration, S. Acharya *et al.*, "Production of charged pions, kaons, and (anti-)protons in Pb-Pb and inelastic *pp* collisions at $\sqrt{s_{NN}} = 5.02$ TeV", *Phys. Rev. C* **101** no. 4, (2020) 044907, arXiv:1910.07678 [nucl-ex].

[15] **ALICE** Collaboration, S. Acharya *et al.*, "Anisotropic flow of identified particles in Pb-Pb collisions at $\sqrt{s}_{\rm NN} = 5.02$ TeV", *JHEP* **09** (2018) 006, arXiv:1805.04390 [nucl-ex].

[16] **ALICE** Collaboration, J. Adam *et al.*, "Anisotropic flow of charged particles in Pb-Pb collisions at $\sqrt{s_{\rm NN}} = 5.02$ TeV", *Phys. Rev. Lett.* **116** no. 13, (2016) 132302, arXiv:1602.01119 [nucl-ex].

[17] **PHOBOS** Collaboration, B. Alver *et al.*, "Phobos results on charged particle multiplicity and pseudorapidity distributions in Au+Au, Cu+Cu, d+Au, and p+p collisions at ultra-relativistic energies", *Phys. Rev. C* **83** (2011) 024913, arXiv:1011.1940 [nucl-ex].

[18] **STAR** Collaboration, J. Adams *et al.*, "Pion interferometry in Au+Au collisions at S(NN)**(1/2) = 200-GeV", *Phys. Rev. C* **71** (2005) 044906, arXiv:nucl-ex/0411036.

[19] M. Alqahtani and M. Strickland, "Pion interferometry at 200 GeV using anisotropic hydrodynamics", *Phys. Rev. C* **102** no. 6, (2020) 064902, arXiv:2007.04209 [nucl-th].

[20] S. Weinberg, "A model of leptons", *Phys. Rev. Lett.* **19** (1967) 1264–1266.

[21] A. Salam, "Weak and electromagnetic interactions", *Nuclear Physics* **22** (1968) 683–696.

[22] R. Brock, *The Higgs Boson*. CRC Press, 2015.

[23] S. L. Glashow, "Partial-symmetries of weak interactions", *Nuclear Physics* **22** (1961) 579–588.

[24] D. J. Griffiths, *Introduction to Quantum Mechanics*. Cambridge University Press, 3rd ed., 2020.

[25] J. L. Alonso, C. Bouthelier-Madre, J. Clemente-Gallardo, and D. Martínez-Crespo, "A sufficient condition for confinement in qcd", 2022.

[26] M. E. Peskin and D. V. Schroeder, *An Introduction to Quantum Field Theory*. CRC Press, frontiers in physics, volume 85 ed., 2018.

[27] M. D. Schwartz, *Quantum Field Theory and the Standard Model*. Cambridge University Press, 2014.

[28] C. P. Burgess, *The Standard Model: A Primer*. Cambridge University Press, 2007.

[29] D. J. Griffiths, *Introduction to Elementary Particles*. Wiley-VCH, 2008.

[30] P. W. Higgs, "Broken symmetries and the masses of gauge bosons", *Physical Review Letters* **13** no. 16, (1964) 508–509.

[31] M. E. Peskin and D. V. Schroeder, *An Introduction to Quantum Field Theory*. Westview Press, 1995.

[32] A. Einstein, "The foundation of the general theory of relativity", *Annalen der Physik* **354** no. 7, (1916) 769–822.

[33] S. Weinberg, *The Quantum Theory of Fields*, vol. 1. Cambridge University Press, 1995.

[34] D. J. Gross and F. Wilczek, "Ultraviolet behavior of non-abelian gauge theories", *Physical Review Letters* **30** no. 26, (1973) 1343–1346.

[35] H. D. Politzer, "Reliable perturbative results for strong interactions?", *Physical Review Letters* **30** no. 26, (1973) 1346–1349.

[36] F. Halzen and A. D. Martin, *Quarks and Leptons: An Introductory Course in Modern Particle Physics*. Wiley, 1984.

[37] P. Braun-Munzinger, K. Redlich, and J. Stachel, "Particle production in heavy ion collisions", *Quark-Gluon Plasma 3* (2003) 491–599.

[38] T.-P. Cheng and L.-F. Li, "Gauge theory of elementary particle physics", *Reviews of Modern Physics* **56** no. 3, (1984) 723–883.

[39] H. Fritzsch, "Color confinement in quantum chromodynamics", *Physical Review Letters* **31** no. 15, (1973) 1013–1016.

[40] G. Ecker, "Quantum chromodynamics", in *2005 European School of High-Energy Physics*. 4, 2006. `arXiv:hep-ph/0604165`.

[41] S. Mandelstam, "Vortices and quark confinement in non-abelian gauge theories", *Physical Review D* **10** no. 8, (1974) 3145–3155.

[42] J. Greensite, "An introduction to the confinement problem", *Lectures on Quark Confinement and the Hadron Spectrum* (2011) 1–78.

[43] J. C. Collins, A. Duncan, and S. Joglekar, "Trace and conformal anomalies in gauge theories", *Physical Review D* **16** no. 2, (1974) 438–449.

[44] D. J. Gross and A. Neveu, "Dynamical symmetry breaking in asymptotically free field theories", *Physical Review D* **10** no. 12, (1974) 3235–3253.

[45] T. Bhattacharya *et al.*, "QCD Phase Transition with Chiral Quarks and Physical Quark Masses", *Phys. Rev. Lett.* **113** no. 8, (2014) 082001, `arXiv:1402.5175 [hep-lat]`.

[46] M. A. Lisa, S. Pratt, R. Soltz, and U. Wiedemann, "Femtoscopy in relativistic heavy ion collisions: Two decades of progress", *Annual Review of Nuclear and Particle Science* **55** no. 1, (2005) 357–402, https://doi.org/10.1146/annurev.nucl.55.090704.151533. https://doi.org/10.1146/annurev.nucl.55.090704.151533.

[47] E. Shuryak, "Physics of Strongly coupled Quark-Gluon Plasma", *Prog. Part. Nucl. Phys.* **62** (2009) 48–101, arXiv:0807.3033 [hep-ph].

[48] F. Gelis, E. Iancu, J. Jalilian-Marian, and R. Venugopalan, "The Color Glass Condensate", *Ann. Rev. Nucl. Part. Sci.* **60** (2010) 463–489, arXiv:1002.0333 [hep-ph].

[49] R. Pasechnik and M. Šumbera, "Phenomenological Review on Quark–Gluon Plasma: Concepts vs. Observations", *Universe* **3** no. 1, (2017) 7, arXiv:1611.01533 [hep-ph].

[50] E. V. Shuryak, "What rhic experiments and theory tell us about properties of quark–gluon plasma?", *Nuclear Physics A* **750** (2005) 64–83.

[51] P. Arnold, G. D. Moore, and L. G. Yaffe, "Transport coefficients in high temperature gauge theories. ii: Beyond leading log", *Journal of High Energy Physics* **2003** no. 5, (2003) 051.

[52] J. Casalderrey-Solana and D. Teaney, "Transverse momentum broadening of a fast quark in a n=4 yang mills plasma", *Journal of High Energy Physics* **2007** no. 4, (2007) 039.

[53] S. Caron-Huot, "Asymptotics of thermal spectral functions", *Physical Review D* **79** no. 12, (2009) 125009.

[54] J. Adams and et al. (STAR Collaboration), "Experimental and theoretical challenges in the search for the quark-gluon plasma: The star collaboration's critical assessment of the evidence from rhic collisions", *Nuclear Physics A* **757** no. 1-2, (2005) 102–183.

[55] K. Adcox and et al. (PHENIX Collaboration), "Formation of dense partonic matter in relativistic nucleus-nucleus collisions at rhic: Experimental evaluation by the phenix collaboration", *Nuclear Physics A* **757** no. 1-2, (2005) 184–283.

[56] I. Arsene and et al. (BRAHMS Collaboration), "Quark gluon plasma and color glass condensate at rhic? the perspective from the brahms experiment", *Nuclear Physics A* **757** no. 1-2, (2005) 1–27.

[57] S. Acharya and et al. (ALICE Collaboration), "Anisotropic flow of charged particles in pb-pb collisions at $\sqrt{s_{\mathrm{NN}}} = 5.02$ tev", *Physical Review Letters* **123** no. 14, (2019) 142301.

[58] A. M. Sirunyan and et al. (CMS Collaboration), "Observation of long-range near-side angular correlations in proton-proton collisions at the lhc", *Physics Letters B* **789** (2019) 754–775.

[59] G. Aad and et al. (ATLAS Collaboration), "Observation of two-source interference in the pb+pb collision data at the lhc", *Nature Physics* **16** (2020) 736–740.

[60] H. R. Schmidt and J. Schukraft, "The Physics of ultrarelativistic heavy ion collisions", *J. Phys. G* **19** (1993) 1705–1796.

[61] L. D. Landau and E. M. Lifshitz, *Fluid Mechanics*, vol. 6 of *Course of Theoretical Physics*. Pergamon, second ed., 1987. http://www.worldcat.org/isbn/9781483161044.

[62] S. Weinberg, *Gravitation and Cosmology: Principles and Applications of the General Theory of Relativity*. John Wiley and Sons, New York, 1972.

[63] P. Huovinen, P. F. Kolb, U. W. Heinz, P. V. Ruuskanen, and S. A. Voloshin, "Radial and elliptic flow at RHIC: further predictions", *Phys. Lett.* **B503** (2001) 58–64, arXiv:hep-ph/0101136.

[64] T. Hirano and K. Tsuda, "Collective flow and two pion correlations from a relativistic hydrodynamic model with early chemical freezeout", *Phys. Rev. C* **66** (2002) 054905, arXiv:nucl-th/0205043.

[65] P. F. Kolb and U. W. Heinz, "Hydrodynamic description of ultrarelativistic heavy ion collisions", arXiv:nucl-th/0305084.

[66] A. Muronga, "Second order dissipative fluid dynamics for ultrarelativistic nuclear collisions", *Phys. Rev. Lett.* **88** (2002) 062302, arXiv:nucl-th/0104064. [Erratum: Phys.Rev.Lett. 89, 159901 (2002)].

[67] A. Muronga, "Causal theories of dissipative relativistic fluid dynamics for nuclear collisions", *Phys. Rev. C* **69** (2004) 034903, arXiv:nucl-th/0309055.

[68] A. Muronga and D. H. Rischke, "Evolution of hot, dissipative quark matter in relativistic nuclear collisions", arXiv:nucl-th/0407114.

[69] U. W. Heinz, H. Song, and A. K. Chaudhuri, "Dissipative hydrodynamics for viscous relativistic fluids", *Phys. Rev. C* **73** (2006) 034904, arXiv:nucl-th/0510014.

[70] R. Baier, P. Romatschke, and U. A. Wiedemann, "Dissipative hydrodynamics and heavy ion collisions", *Phys. Rev. C* **73** (2006) 064903, arXiv:hep-ph/0602249.

[71] P. Romatschke and U. Romatschke, "Viscosity Information from Relativistic Nuclear Collisions: How Perfect is the Fluid Observed at RHIC?", *Phys. Rev. Lett.* **99** (2007) 172301, arXiv:0706.1522 [nucl-th].

[72] R. Baier, P. Romatschke, D. T. Son, A. O. Starinets, and M. A. Stephanov, "Relativistic viscous hydrodynamics, conformal invariance, and holography", *JHEP* **04** (2008) 100, arXiv:0712.2451 [hep-th].

[73] K. Dusling and D. Teaney, "Simulating elliptic flow with viscous hydrodynamics", *Phys. Rev. C* **77** (2008) 034905, arXiv:0710.5932 [nucl-th].

[74] M. Luzum and P. Romatschke, "Conformal Relativistic Viscous Hydrodynamics: Applications to RHIC results at s(NN)**(1/2) = 200-GeV", *Phys. Rev. C* **78** (2008) 034915, arXiv:0804.4015 [nucl-th]. [Erratum: Phys.Rev.C 79, 039903 (2009)].

[75] H. Song and U. W. Heinz, "Extracting the QGP viscosity from RHIC data - A Status report from viscous hydrodynamics", *J. Phys. G* **36** (2009) 064033, arXiv:0812.4274 [nucl-th].

[76] U. W. Heinz, "Early collective expansion: Relativistic hydrodynamics and the transport properties of QCD matter", *Landolt-Bornstein* **23** (2010) 240, arXiv:0901.4355 [nucl-th].

[77] A. El, Z. Xu, and C. Greiner, "Third-order relativistic dissipative hydrodynamics", *Phys. Rev. C* **81** (2010) 041901, arXiv:0907.4500 [hep-ph].

[78] J. Peralta-Ramos and E. Calzetta, "Divergence-type nonlinear conformal hydrodynamics", *Phys. Rev. D* **80** (2009) 126002, arXiv:0908.2646 [hep-ph].

[79] J. Peralta-Ramos and E. Calzetta, "Divergence-type 2+1 dissipative hydrodynamics applied to heavy-ion collisions", *Phys. Rev. C* **82** (2010) 054905, arXiv:1003.1091 [hep-ph].

[80] G. S. Denicol, T. Kodama, and T. Koide, "The effect of shear and bulk viscosities on elliptic flow", *J. Phys. G* **37** (2010) 094040, arXiv:1002.2394 [nucl-th].

[81] G. S. Denicol, T. Koide, and D. H. Rischke, "Dissipative relativistic fluid dynamics: a new way to derive the equations of motion from kinetic theory", *Phys. Rev. Lett.* **105** (2010) 162501, arXiv:1004.5013 [nucl-th].

[82] B. Schenke, S. Jeon, and C. Gale, "Elliptic and triangular flow in event-by-event (3+1)D viscous hydrodynamics", *Phys. Rev. Lett.* **106** (2011) 042301, arXiv:1009.3244 [hep-ph].

[83] B. Schenke, S. Jeon, and C. Gale, "Anisotropic flow in $\sqrt{s} = 2.76$ TeV Pb+Pb collisions at the LHC", *Phys. Lett. B* **702** (2011) 59–63, arXiv:1102.0575 [hep-ph].

[84] P. Bozek, "Components of the elliptic flow in Pb-Pb collisions at s**(1/2) = 2.76-TeV", *Phys. Lett. B* **699** (2011) 283–286, arXiv:1101.1791 [nucl-th].

[85] H. Niemi, G. S. Denicol, P. Huovinen, E. Molnar, and D. H. Rischke, "Influence of the shear viscosity of the quark-gluon plasma on elliptic flow in ultrarelativistic heavy-ion collisions", *Phys. Rev. Lett.* **106** (2011) 212302, arXiv:1101.2442 [nucl-th].

[86] H. Niemi, G. S. Denicol, P. Huovinen, E. Molnar, and D. H. Rischke, "Influence of a temperature-dependent shear viscosity on the azimuthal asymmetries of transverse momentum spectra in ultrarelativistic heavy-ion collisions", *Phys. Rev. C* **86** (2012) 014909, arXiv:1203.2452 [nucl-th].

[87] P. Bozek and I. Wyskiel-Piekarska, "Particle spectra in Pb-Pb collisions at $\sqrt{S_{NN}} = 2.76$ TeV", *Phys. Rev. C* **85** (2012) 064915, arXiv:1203.6513 [nucl-th].

[88] G. S. Denicol, H. Niemi, E. Molnar, and D. H. Rischke, "Derivation of transient relativistic fluid dynamics from the Boltzmann equation", *Phys. Rev. D* **85** (2012) 114047, arXiv:1202.4551 [nucl-th]. [Erratum: Phys.Rev.D 91, 039902 (2015)].

[89] G. S. Denicol, E. Molnár, H. Niemi, and D. H. Rischke, "Derivation of fluid dynamics from kinetic theory with the 14-moment approximation", *Eur. Phys. J. A* **48** (2012) 170, arXiv:1206.1554 [nucl-th].

[90] J. Peralta-Ramos and E. Calzetta, "Macroscopic approximation to relativistic kinetic theory from a nonlinear closure", *Phys. Rev. D* **87** no. 3, (2013) 034003, arXiv:1212.0824 [nucl-th].

[91] A. Jaiswal, "Relativistic dissipative hydrodynamics from kinetic theory with relaxation time approximation", *Phys. Rev. C* **87** no. 5, (2013) 051901, arXiv:1302.6311 [nucl-th].

[92] A. Jaiswal, "Relativistic third-order dissipative fluid dynamics from kinetic theory", *Phys. Rev. C* **88** (2013) 021903, arXiv:1305.3480 [nucl-th].

[93] E. Calzetta, "Hydrodynamic approach to boost invariant free streaming", *Phys. Rev. D* **92** no. 4, (2015) 045035, arXiv:1402.5278 [hep-ph].

[94] G. S. Denicol, S. Jeon, and C. Gale, "Transport Coefficients of Bulk Viscous Pressure in the 14-moment approximation", *Phys. Rev. C* **90** no. 2, (2014) 024912, arXiv:1403.0962 [nucl-th].

[95] G. S. Denicol, W. Florkowski, R. Ryblewski, and M. Strickland, "Shear-bulk coupling in nonconformal hydrodynamics", *Phys. Rev. C* **90** no. 4, (2014) 044905, arXiv:1407.4767 [hep-ph].

[96] A. Jaiswal, R. Ryblewski, and M. Strickland, "Transport coefficients for bulk viscous evolution in the relaxation time approximation", *Phys. Rev. C* **90** no. 4, (2014) 044908, arXiv:1407.7231 [hep-ph].

[97] M. Martinez and M. Strickland, "Dissipative Dynamics of Highly Anisotropic Systems", *Nucl. Phys. A* **848** (2010) 183–197, arXiv:1007.0889 [nucl-th].

[98] W. Florkowski and R. Ryblewski, "Highly-anisotropic and strongly-dissipative hydrodynamics for early stages of relativistic heavy-ion collisions", *Phys. Rev. C* **83** (2011) 034907, arXiv:1007.0130 [nucl-th].

[99] R. Ryblewski and W. Florkowski, "Non-boost-invariant motion of dissipative and highly anisotropic fluid", *J.Phys.G* **G38** (2011) 015104, arXiv:1007.4662 [nucl-th].

[100] M. Martinez and M. Strickland, "Non-boost-invariant anisotropic dynamics", *Nucl. Phys. A* **856** (2011) 68–87, arXiv:1011.3056 [nucl-th].

[101] R. Ryblewski and W. Florkowski, "Highly-anisotropic and strongly-dissipative hydrodynamics with transverse expansion", *Eur.Phys.J.* **C71** (2011) 1761, arXiv:1103.1260 [nucl-th].

[102] W. Florkowski and R. Ryblewski, "Projection method for boost-invariant and cylindrically symmetric dissipative hydrodynamics", *Phys. Rev. C* **85** (2012) 044902, arXiv:1111.5997 [nucl-th].

[103] M. Martinez, R. Ryblewski, and M. Strickland, "Boost-Invariant (2+1)-dimensional Anisotropic Hydrodynamics", *Phys. Rev. C* **85** (2012) 064913, arXiv:1204.1473 [nucl-th].

[104] R. Ryblewski and W. Florkowski, "Highly-anisotropic hydrodynamics in 3+1 space-time dimensions", *Phys. Rev. C* **85** (2012) 064901, arXiv:1204.2624 [nucl-th].

[105] W. Florkowski, R. Maj, R. Ryblewski, and M. Strickland, "Hydrodynamics of anisotropic quark and gluon fluids", *Phys.Rev.* **C87** no. 3, (2013) 034914, arXiv:1209.3671 [nucl-th].

[106] W. Florkowski and R. Maj, "Mixture of anisotropic fluids", *Acta Phys.Polon.* **B44** no. 10, (2013) 2003–2017, arXiv:1309.2786 [nucl-th].

[107] R. Ryblewski, "Anisotropic hydrodynamics for ultra-relativistic heavy-ion collisions", *J.Phys.* **G40** (2013) 093101.

[108] D. Bazow, U. W. Heinz, and M. Strickland, "Second-order (2+1)-dimensional anisotropic hydrodynamics", *Phys. Rev. C* **90** no. 5, (2014) 054910, arXiv:1311.6720 [nucl-th].

[109] L. Tinti and W. Florkowski, "Projection method and new formulation of leading-order anisotropic hydrodynamics", *Phys. Rev. C* **89** no. 3, (2014) 034907, arXiv:1312.6614 [nucl-th].

[110] W. Florkowski, R. Ryblewski, M. Strickland, and L. Tinti, "Leading-order anisotropic hydrodynamics for systems with massive particles", *Phys.Rev.* **C89** (2014) 054909, arXiv:1403.1223 [hep-ph].

[111] W. Florkowski and O. Madetko, "Kinetic description of mixtures of anisotropic fluids", *Acta Phys.Polon.* **B45** (2014) 1103, arXiv:1402.2401 [nucl-th].

[112] M. Nopoush, R. Ryblewski, and M. Strickland, "Bulk viscous evolution within anisotropic hydrodynamics", *Phys. Rev. C* **90** no. 1, (2014) 014908, arXiv:1405.1355 [hep-ph].

[113] R. Baier, A. H. Mueller, D. Schiff, and D. T. Son, "'Bottom up' thermalization in heavy ion collisions", *Phys. Lett.* **B502** (2001) 51–58, arXiv:hep-ph/0009237 [hep-ph].

[114] M. P. Heller, R. A. Janik, and P. Witaszczyk, "The characteristics of thermalization of boost-invariant plasma from holography", *Phys. Rev. Lett.* **108** (2012) 201602, arXiv:1103.3452 [hep-th].

[115] W. van der Schee, P. Romatschke, and S. Pratt, "Fully Dynamical Simulation of Central Nuclear Collisions", *Phys. Rev. Lett.* **111** no. 22, (2013) 222302, arXiv:1307.2539 [nucl-th].

[116] S. Mrowczynski, "Instabilities driven equilibration of the quark-gluon plasma", *Acta Phys. Polon. B* **37** (2006) 427–454, arXiv:hep-ph/0511052.

[117] T. Lappi and L. McLerran, "Some features of the glasma", *Nucl. Phys. A* **772** (2006) 200–212, arXiv:hep-ph/0602189.

[118] T. Epelbaum and F. Gelis, "Pressure isotropization in high energy heavy ion collisions", *Phys. Rev. Lett.* **111** (2013) 232301, arXiv:1307.2214 [hep-ph].

[119] J. Berges, K. Boguslavski, S. Schlichting, and R. Venugopalan, "Turbulent thermalization process in heavy-ion collisions at ultrarelativistic energies", *Phys. Rev. D* **89** no. 7, (2014) 074011, arXiv:1303.5650 [hep-ph].

[120] P. L. Bhatnagar, E. P. Gross, and M. Krook, "A Model for Collision Processes in Gases. 1. Small Amplitude Processes in Charged and Neutral One-Component Systems", *Phys. Rev.* **94** (1954) 511–525.

[121] J. L. Anderson and H. R. Witting, "A relativistic relaxation-time model for the Boltzmann equation", *Physica* **74** (1974) 466.

[122] J. L. Anderson and H. R. Witting, "Relativistic quantum transport coefficients", *Physica* **74** (1974) 489.

[123] W. Czyz and W. Florkowski, "Kinetic Coefficients for Quark - Anti-quark Plasma", *Acta Phys. Polon. B* **17** (1986) 819–837.

[124] J. D. Bjorken, "Highly Relativistic Nucleus-Nucleus Collisions: The Central Rapidity Region", *Phys. Rev. D* **27** (1983) 140–151.

[125] G. Baym, B. L. Friman, J. P. Blaizot, M. Soyeur, and W. Czyz, "Hydrodynamics of Ultrarelativistic Heavy Ion Collisions", *Nucl. Phys. A* **407** (1983) 541–570.

[126] W. Florkowski, E. Maksymiuk, R. Ryblewski, and L. Tinti, "Anisotropic hydrodynamics for a mixture of quark and gluon fluids", *Phys. Rev.* **C92** no. 5, (2015) 054912, arXiv:1508.04534 [nucl-th].

[127] A. Jaiswal and V. Roy, "Relativistic hydrodynamics in heavy-ion collisions: general aspects and recent developments", *Adv. High Energy Phys.* **2016** (2016) 9623034, arXiv:1605.08694 [nucl-th].

[128] J. Mifsud and T. S. Kollegger, "Optical glauber modeling in high-energy nuclear collisions", 2013. https://api.semanticscholar.org/CorpusID:125870214.

[129] J. Wang, J.-Y. Tang, and C. Gong, "Monte carlo based glauber model in pb-pb collisions at lhc", *The Frontiers of Society, Science and Technology* (2021) . https://api.semanticscholar.org/CorpusID:233991909.

[130] B. H. Alver, M. D. Baker, C. Loizides, and P. Steinberg, "The phobos glauber monte carlo", *arXiv: Nuclear Experiment* (2008) . https://api.semanticscholar.org/CorpusID:117349254.

[131] B. H. Alver and G. Roland, "Collision-geometry fluctuations and triangular flow in heavy-ion collisions", 2010. https://api.semanticscholar.org/CorpusID:59403206.

[132] D. d'Enterria and C. Loizides, "Progress in the glauber model at collider energies", *arXiv: High Energy Physics - Phenomenology* (2020) . https://api.semanticscholar.org/CorpusID:227228055.

[133] J. Berges and S. Borsányi, "Range of validity of transport equations", *Physical Review D* **74** no. 4, (Aug, 2006) . http://dx.null_doi.org/10.1103/PhysRevD.74.045022.

[134] H.-S. Shao, "Probing impact-parameter dependent nuclear parton densities from double parton scatterings in heavy-ion collisions", *Phys. Rev. D* **101** no. 5, (2020) 054036, arXiv:2001.04256 [hep-ph].

[135] T. Drozhzhova, V. Kovalenko, A. Seryakov, and G. Feofilov, "Centrality and multiparticle production in ultrarelativistic nuclear collisions", *Physics of Atomic Nuclei* **79** (2016) 737–748. https://api.semanticscholar.org/CorpusID:126188631.

[136] M. Deliyergiyev and M. Rybczyński, "Multiplicity fluctuations in the glauber monte carlo approach", *Physical Review C* (2019) . https://api.semanticscholar.org/CorpusID:202540215.

[137] S. Bhattacharyya, "Investigation of centrality dependence of dynamical fluctuations in narrow pseudo-rapidity interval on event-by-event basis", *International Journal of Modern Physics E-nuclear Physics* (2020) 2050083. https://api.semanticscholar.org/CorpusID:229416427.

[138] R. L. Ray and M. Daugherity, "Applicability of monte carlo glauber models to relativistic heavy-ion collision data", *Journal of Physics G* **35** (2007) 125106. https://api.semanticscholar.org/CorpusID:15921355.

[139] K. Olive, "Review of particle physics", *Chinese Physics C* **38** no. 9, (Aug, 2014) 090001. https://dx.doi.org/10.1088/1674-1137/38/9/090001.

[140] T. Schörner-Sadenius, ed., *The Large Hadron Collider: Harvest of Run 1*. Springer, Berlin, 2015.

[141] X.-N. Wang, ed., *Quark-Gluon Plasma 5*. World Scientific, New Jersey, 2016.

[142] P. Romatschke and U. Romatschke, *Relativistic Fluid Dynamics In and Out of Equilibrium*. Cambridge Monographs on Mathematical Physics. Cambridge University Press, 5, 2019. arXiv:1712.05815 [nucl-th].

[143] P. Huovinen, P. Kolb, U. Heinz, P. Ruuskanen, and S. Voloshin, "Radial and elliptic flow at rhic: further predictions", *Physics Letters B* **503** no. 1-2, (Mar, 2001) 58–64. http://dx.doi.org/10.1016/S0370-2693(01)00219-2.

[144] H. Song and U. W. Heinz, "Suppression of elliptic flow in a minimally viscous quark-gluon plasma", *Phys. Lett. B* **658** (2008) 279–283, arXiv:0709.0742 [nucl-th].

[145] P. M. Chesler and L. G. Yaffe, "Boost invariant flow, black hole formation, and far-from-equilibrium dynamics in N = 4 supersymmetric Yang-Mills theory", *Phys. Rev. D* **82** (2010) 026006, arXiv:0906.4426 [hep-th].

[146] M. P. Heller and M. Spalinski, "Hydrodynamics Beyond the Gradient Expansion: Resurgence and Resummation", *Phys. Rev. Lett.* **115** no. 7, (2015) 072501, arXiv:1503.07514 [hep-th].

[147] P. M. Chesler, "How big are the smallest drops of quark-gluon plasma?", *JHEP* **03** (2016) 146, arXiv:1601.01583 [hep-th].

[148] L. Keegan, A. Kurkela, P. Romatschke, W. van der Schee, and Y. Zhu, "Weak and strong coupling equilibration in nonabelian gauge theories", *JHEP* **04** (2016) 031, arXiv:1512.05347 [hep-th].

[149] M. P. Heller, A. Kurkela, M. Spaliński, and V. Svensson, "Hydrodynamization in kinetic theory: Transient modes and the gradient expansion", *Phys. Rev. D* **97** no. 9, (2018) 091503, arXiv:1609.04803 [nucl-th].

[150] W. Florkowski, M. P. Heller, and M. Spalinski, "New theories of relativistic hydrodynamics in the LHC era", *Rept. Prog. Phys.* **81** no. 4, (2018) 046001, arXiv:1707.02282 [hep-ph].

[151] P. Romatschke, "Relativistic Fluid Dynamics Far From Local Equilibrium", *Phys. Rev. Lett.* **120** no. 1, (2018) 012301, arXiv:1704.08699 [hep-th].

[152] F. S. Bemfica, M. M. Disconzi, and J. Noronha, "Causality and existence of solutions of relativistic viscous fluid dynamics with gravity", *Phys. Rev. D* **98** no. 10, (2018) 104064, arXiv:1708.06255 [gr-qc].

[153] M. Spaliński, "On the hydrodynamic attractor of Yang–Mills plasma", *Phys. Lett. B* **776** (2018) 468–472, arXiv:1708.01921 [hep-th].

[154] P. Romatschke, "Relativistic Hydrodynamic Attractors with Broken Symmetries: Non-Conformal and Non-Homogeneous", *JHEP* **12** (2017) 079, arXiv:1710.03234 [hep-th].

[155] A. Behtash, C. N. Cruz-Camacho, and M. Martinez, "Far-from-equilibrium attractors and nonlinear dynamical systems approach to the Gubser flow", *Phys. Rev. D* **97** no. 4, (2018) 044041, arXiv:1711.01745 [hep-th].

[156] W. Florkowski, E. Maksymiuk, and R. Ryblewski, "Coupled kinetic equations for fermions and bosons in the relaxation-time approximation", *Phys. Rev. C* **97** no. 2, (2018) 024915, arXiv:1710.07095 [hep-ph].

[157] W. Florkowski, E. Maksymiuk, and R. Ryblewski, "Anisotropic-hydrodynamics approach to a quark-gluon fluid mixture", *Phys. Rev. C* **97** no. 1, (2018) 014904, arXiv:1711.03872 [nucl-th].

[158] M. Strickland, J. Noronha, and G. Denicol, "Anisotropic nonequilibrium hydrodynamic attractor", *Phys. Rev. D* **97** no. 3, (2018) 036020, arXiv:1709.06644 [nucl-th].

[159] A. Kurkela, A. Mazeliauskas, J.-F. Paquet, S. Schlichting, and D. Teaney, "Effective kinetic description of event-by-event pre-equilibrium dynamics in high-energy heavy-ion collisions", *Phys. Rev. C* **99** no. 3, (2019) 034910, arXiv:1805.00961 [hep-ph].

[160] A. Kurkela, U. A. Wiedemann, and B. Wu, "Opacity dependence of elliptic flow in kinetic theory", *Eur. Phys. J. C* **79** no. 9, (2019) 759, arXiv:1805.04081 [hep-ph].

[161] A. Kurkela, U. A. Wiedemann, and B. Wu, "Flow in AA and pA as an interplay of fluid-like and non-fluid like excitations", *Eur. Phys. J. C* **79** no. 11, (2019) 965, arXiv:1905.05139 [hep-ph].

[162] D. Almaalol and M. Strickland, "Anisotropic hydrodynamics with a scalar collisional kernel", *Phys. Rev. C* **97** no. 4, (2018) 044911, arXiv:1801.10173 [hep-ph].

[163] G. S. Denicol and J. Noronha, "Hydrodynamic attractor and the fate of perturbative expansions in Gubser flow", *Phys. Rev. D* **99** no. 11, (2019) 116004, arXiv:1804.04771 [nucl-th].

[164] A. Behtash, C. N. Cruz-Camacho, S. Kamata, and M. Martinez, "Non-perturbative rheological behavior of a far-from-equilibrium expanding plasma", *Phys. Lett. B* **797** (2019) 134914, arXiv:1805.07881 [hep-th].

[165] M. Strickland, "The non-equilibrium attractor for kinetic theory in relaxation time approximation", *JHEP* **12** (2018) 128, arXiv:1809.01200 [nucl-th].

[166] M. P. Heller and V. Svensson, "How does relativistic kinetic theory remember about initial conditions?", *Phys. Rev. D* **98** no. 5, (2018) 054016, arXiv:1802.08225 [nucl-th].

[167] A. Behtash, S. Kamata, M. Martinez, and H. Shi, "Global flow structure and exact formal transseries of the Gubser flow in kinetic theory", *JHEP* **07** (2020) 226, arXiv:1911.06406 [hep-th].

[168] M. Strickland and U. Tantary, "Exact solution for the non-equilibrium attractor in number-conserving relaxation time approximation", *JHEP* **10** (2019) 069, arXiv:1903.03145 [hep-ph].

[169] S. Jaiswal, C. Chattopadhyay, A. Jaiswal, S. Pal, and U. Heinz, "Exact solutions and attractors of higher-order viscous fluid dynamics for Bjorken flow", *Phys. Rev. C* **100** no. 3, (2019) 034901, arXiv:1907.07965 [nucl-th].

[170] A. Kurkela, W. van der Schee, U. A. Wiedemann, and B. Wu, "Early- and Late-Time Behavior of Attractors in Heavy-Ion Collisions", *Phys. Rev. Lett.* **124** no. 10, (2020) 102301, arXiv:1907.08101 [hep-ph].

[171] C. Chattopadhyay and U. W. Heinz, "Hydrodynamics from free-streaming to thermalization and back again", *Phys. Lett. B* **801** (2020) 135158, arXiv:1911.07765 [nucl-th].

[172] J. Brewer, L. Yan, and Y. Yin, "Adiabatic hydrodynamization in rapidly-expanding quark–gluon plasma", *Phys. Lett. B* **816** (2021) 136189, arXiv:1910.00021 [nucl-th].

[173] M. P. Heller, R. Jefferson, M. Spaliński, and V. Svensson, "Hydrodynamic Attractors in Phase Space", *Phys. Rev. Lett.* **125** no. 13, (2020) 132301, arXiv:2003.07368 [hep-th].

[174] D. Almaalol, A. Kurkela, and M. Strickland, "Nonequilibrium Attractor in High-Temperature QCD Plasmas", *Phys. Rev. Lett.* **125** no. 12, (2020) 122302, arXiv:2004.05195 [hep-ph].

[175] J.-P. Blaizot and L. Yan, "Analytical attractor for Bjorken flows", *Phys. Lett. B* **820** (2021) 136478, arXiv:2006.08815 [nucl-th].

[176] T. Mitra, S. Mondkar, A. Mukhopadhyay, A. Rebhan, and A. Soloviev, "Hydrodynamic attractor of a hybrid viscous fluid in Bjorken flow", *Phys. Rev. Res.* **2** no. 4, (2020) 043320, arXiv:2006.09383 [hep-ph].

[177] T. Dore, E. McLaughlin, and J. Noronha-Hostler, "Far From Equilibrium Hydrodynamics and the Beam Energy Scan", *J. Phys. Conf. Ser.* **1602** no. 1, (2020) 012017, arXiv:2006.04206 [nucl-th].

[178] A. Dash and V. Roy, "Hydrodynamic attractors for Gubser flow", *Phys. Lett. B* **806** (2020) 135481, arXiv:2001.10756 [nucl-th].

[179] A. Das, W. Florkowski, and R. Ryblewski, "Correspondence between Israel-Stewart and first-order casual and stable hydrodynamics for the boost-invariant massive case with zero baryon density", *Phys. Rev. D* **102** no. 3, (2020) 031501, arXiv:2006.00536 [nucl-th].

[180] J. Berges, M. P. Heller, A. Mazeliauskas, and R. Venugopalan, "QCD thermalization: Ab initio approaches and interdisciplinary connections", *Rev. Mod. Phys.* **93** no. 3, (2021) 035003, arXiv:2005.12299 [hep-th].

[181] S. Kamata, M. Martinez, P. Plaschke, S. Ochsenfeld, and S. Schlichting, "Hydrodynamization and nonequilibrium Green's functions in kinetic theory", *Phys. Rev. D* **102** no. 5, (2020) 056003, arXiv:2004.06751 [hep-ph].

[182] M. Shokri and F. Taghinavaz, "Conformal Bjorken flow in the general frame and its attractor: Similarities and discrepancies with the Müller-Israel-Stewart formalism", *Phys. Rev. D* **102** no. 3, (2020) 036022, arXiv:2002.04719 [hep-th].

[183] M. Martinez and M. Strickland, "Constraining relativistic viscous hydrodynamical evolution", *Phys. Rev. C* **79** (2009) 044903, arXiv:0902.3834 [hep-ph].

[184] R. Ryblewski, "Anisotropic hydrodynamics for ultra-relativistic heavy-ion collisions", *Journal of Physics G: Nuclear and Particle Physics* **40** no. 9, (Jul, 2013) 093101. https://doi.org/10.1088%2F0954-3899%2F40%2F9%2F093101.

[185] M. Alqahtani, M. Nopoush, and M. Strickland, "Relativistic anisotropic hydrodynamics", *Prog. Part. Nucl. Phys.* **101** (2018) 204–248, arXiv:1712.03282 [nucl-th].

[186] M. Alqahtani, M. Nopoush, R. Ryblewski, and M. Strickland, "(3+1)D Quasiparticle Anisotropic Hydrodynamics for Ultrarelativistic Heavy-Ion Collisions", *Phys. Rev. Lett.* **119** no. 4, (2017) 042301, arXiv:1703.05808 [nucl-th].

[187] D. Almaalol, M. Alqahtani, and M. Strickland, "Anisotropic hydrodynamic modeling of 200 gev au-au collisions", *Phys. Rev. C* **99** (Apr, 2019) 044902. https://link.aps.org/doi/10.1103/PhysRevC.99.044902.

[188] W. Florkowski, R. Ryblewski, and M. Strickland, "Anisotropic Hydrodynamics for Rapidly Expanding Systems", *Nucl. Phys. A* **916** (2013) 249–259, arXiv:1304.0665 [nucl-th].

[189] W. Florkowski, R. Ryblewski, and M. Strickland, "Testing viscous and anisotropic hydrodynamics in an exactly solvable case", *Phys. Rev. C* **88** (2013) 024903, arXiv:1305.7234 [nucl-th].

[190] W. Florkowski, E. Maksymiuk, R. Ryblewski, and M. Strickland, "Exact solution of the (0+1)-dimensional Boltzmann equation for a massive gas", *Phys. Rev. C* **89** no. 5, (2014) 054908, arXiv:1402.7348 [hep-ph].

[191] M. McNelis and U. Heinz, "Hydrodynamic generators in relativistic kinetic theory", *Phys. Rev. C* **101** no. 5, (2020) 054901, arXiv:2001.09125 [nucl-th].

[192] P. Romatschke and M. Strickland, "Collective modes of an anisotropic quark gluon plasma", *Phys. Rev. D* **68** (2003) 036004, arXiv:hep-ph/0304092.

[193] P. Romatschke and M. Strickland, "Collective modes of an anisotropic quark-gluon plasma II", *Phys. Rev. D* **70** (2004) 116006, arXiv:hep-ph/0406188.

[194] G. S. Denicol, T. Koide, and D. H. Rischke, "Dissipative relativistic fluid dynamics: A new way to derive the equations of motion from kinetic theory", *Physical Review Letters* **105** no. 16, (Oct, 2010) . http://dx.doi.org/10.1103/PhysRevLett.105.162501.

[195] G. S. Denicol, J. Noronha, H. Niemi, and D. H. Rischke, "Origin of the relaxation time in dissipative fluid dynamics", *Physical Review D* **83** no. 7, (Apr, 2011) . http://dx.doi.org/10.1103/PhysRevD.83.074019.

[196] M. Nopoush, R. Ryblewski, and M. Strickland, "Bulk viscous evolution within anisotropic hydrodynamics", *Physical Review C* **90** no. 1, (Jul, 2014) . http://dx.doi.org/10.1103/PhysRevC.90.014908.

[197] E. Molnar, H. Niemi, and D. H. Rischke, "Derivation of anisotropic dissipative fluid dynamics from the Boltzmann equation", *Phys. Rev. D* **93** no. 11, (2016) 114025, arXiv:1602.00573 [nucl-th].

[198] E. Molnár, H. Niemi, and D. H. Rischke, "Closing the equations of motion of anisotropic fluid dynamics by a judicious choice of a moment of the Boltzmann equation", *Phys. Rev. D* **94** no. 12, (2016) 125003, arXiv:1606.09019 [nucl-th].

[199] G. S. Denicol, U. W. Heinz, M. Martinez, J. Noronha, and M. Strickland, "New Exact Solution of the Relativistic Boltzmann Equation and its Hydrodynamic Limit", *Phys. Rev. Lett.* **113** no. 20, (2014) 202301, arXiv:1408.5646 [hep-ph].

[200] G. S. Denicol, U. W. Heinz, M. Martinez, J. Noronha, and M. Strickland, "Studying the validity of relativistic hydrodynamics with a new exact solution of the Boltzmann equation", *Phys. Rev. D* **90** no. 12, (2014) 125026, arXiv:1408.7048 [hep-ph].

[201] A. Behtash, S. Kamata, M. Martinez, and H. Shi, "Dynamical systems and nonlinear transient rheology of the far-from-equilibrium Bjorken flow", *Phys. Rev. D* **99** no. 11, (2019) 116012, arXiv:1901.08632 [hep-th].

[202] X. Du and S. Schlichting, "Equilibration of the Quark-Gluon Plasma at Finite Net-Baryon Density in QCD Kinetic Theory", *Phys. Rev. Lett.* **127** no. 12, (2021) 122301, arXiv:2012.09068 [hep-ph].

[203] X. Du and S. Schlichting, "Equilibration of weakly coupled QCD plasmas", *Phys. Rev. D* **104** no. 5, (2021) 054011, arXiv:2012.09079 [hep-ph].

[204] T. Dore, J. Noronha-Hostler, and E. McLaughlin, "Far-from-equilibrium search for the QCD critical point", *Phys. Rev. D* **102** no. 7, (2020) 074017, arXiv:2007.15083 [nucl-th].

[205] J.-P. Blaizot and L. Yan, "Attractor and fixed points in Bjorken flows", *Phys. Rev. C* **104** no. 5, (2021) 055201, arXiv:2106.10508 [nucl-th].

[206] A. Soloviev, "Hydrodynamic attractors in heavy ion collisions: a review", *Eur. Phys. J. C* **82** no. 4, (2022) 319, arXiv:2109.15081 [hep-th].

[207] M. Alqahtani, N. Demir, and M. Strickland, "Nonextensive hydrodynamics of boost-invariant plasmas", *Eur. Phys. J. C* **82** no. 10, (3, 2022) 973, arXiv:2203.14968 [nucl-th].

[208] C. Chattopadhyay, S. Jaiswal, L. Du, U. Heinz, and S. Pal, "Non-conformal attractor in boost-invariant plasmas", *Phys. Lett. B* **824** (2022) 136820, arXiv:2107.05500 [nucl-th].

[209] S. Jaiswal, J.-P. Blaizot, R. S. Bhalerao, Z. Chen, A. Jaiswal, and L. Yan, "From moments of the distribution function to hydrodynamics: The nonconformal case", *Phys. Rev. C* **106** no. 4, (8, 2022) 044912, arXiv:2208.02750 [nucl-th].

[210] C. Chattopadhyay, U. Heinz, and T. Schaefer, "Far-off-equilibrium expansion trajectories in the QCD phase diagram", *Phys. Rev. C* **107** no. 4, (9, 2023) 044905, arXiv:2209.10483 [hep-ph].

[211] S. Kamata, J. Jankowski, and M. Martinez, "Novel features of attractors and transseries in nonconformal Bjorken flows", *Phys. Rev. D* **107** no. 11, (5, 2023) 116004, arXiv:2206.00653 [physics.flu-dyn].

[212] X. Du, M. P. Heller, S. Schlichting, and V. Svensson, "Exponential approach to the hydrodynamic attractor in Yang-Mills kinetic theory", *Phys. Rev. D* **106** no. 1, (2022) 014016, arXiv:2203.16549 [hep-ph].

[213] J. Brewer, B. Scheihing-Hitschfeld, and Y. Yin, "Scaling and adiabaticity in a rapidly expanding gluon plasma", *JHEP* **05** (2022) 145, arXiv:2203.02427 [hep-ph].

[214] S. Jaiswal, C. Chattopadhyay, L. Du, U. Heinz, and S. Pal, "Nonconformal kinetic theory and hydrodynamics for Bjorken flow", *Phys. Rev. C* **105** no. 2, (2022) 024911, arXiv:2107.10248 [hep-ph].

[215] R. Ryblewski and W. Florkowski, "Highly anisotropic hydrodynamics – discussion of the model assumptions and forms of the initial conditions", *Acta Phys. Polon. B* **42** (2011) 115–138, arXiv:1011.6213 [nucl-th].

[216] A. Bialas and W. Czyz, "Boost Invariant Boltzmann-vlasov Equations for Relativistic Quark - Anti-quark Plasma", *Phys. Rev. D* **30** (1984) 2371.

[217] A. Bialas, W. Czyz, A. Dyrek, and W. Florkowski, "Oscillations of Quark - Gluon Plasma Generated in Strong Color Fields", *Nucl. Phys. B* **296** (1988) 611–624.

[218] J. L. Anderson and H. Witting, "A relativistic relaxation-time model for the boltzmann equation", *Physica* **74** no. 3, (1974) 466–488.

[219] G. Baym, "THERMAL EQUILIBRATION IN ULTRARELATIVISTIC HEAVY ION COLLISIONS", *Phys. Lett.* **138B** (1984) 18–22.

[220] G. Baym, "ENTROPY PRODUCTION AND THE EVOLUTION OF ULTRARELATIVISTIC HEAVY ION COLLISIONS", *Nucl. Phys.* **A418** (1984) 525C–537C.

[221] H. Heiselberg and X.-N. Wang, "Expansion, thermalization and entropy production in high-energy nuclear collisions", *Phys.Rev.* **C53** (1996) 1892–1902, arXiv:hep-ph/9504244 [hep-ph].

[222] S. Wong, "Thermal and chemical equilibration in relativistic heavy ion collisions", *Phys.Rev.* **C54** (1996) 2588–2599, arXiv:hep-ph/9609287 [hep-ph].

[223] H. Grad, "On the kinetic theory of rarefied gases", *Communications on pure and applied mathematics* **2** no. 4, (1949) 331–407.

[224] S. Chapman and T. G. Cowling, *Cambridge mathematical library: The mathematical theory of non-uniform gases: An account of the kinetic theory of viscosity, thermal conduction and diffusion in gases*. Cambridge University Press, Cambridge, England, 1991.

[225] H. Grad, "On the kinetic theory of rarefied gases", *Communications on Pure and Applied Mathematics* **2** no. 4, (1949) 331–407.

[226] G. S. Denicol, J. Noronha, H. Niemi, and D. H. Rischke, "Origin of the Relaxation Time in Dissipative Fluid Dynamics", *Phys. Rev. D* **83** (2011) 074019, arXiv:1102.4780 [hep-th].

[227] D. Teaney, "The Effects of viscosity on spectra, elliptic flow, and HBT radii", *Phys. Rev. C* **68** (2003) 034913, arXiv:nucl-th/0301099 [nucl-th].

[228] P. Bozek, "Bulk and shear viscosities of matter created in relativistic heavy-ion collisions", *Phys. Rev. C* **81** (2010) 034909, arXiv:0911.2397 [nucl-th].

[229] J.-B. Rose, J.-F. Paquet, G. S. Denicol, M. Luzum, B. Schenke, S. Jeon, and C. Gale, "Extracting the bulk viscosity of the quark–gluon plasma", *Nucl. Phys. A* **931** (2014) 926–930, arXiv:1408.0024 [nucl-th].

[230] M. Alqahtani, M. Nopoush, and M. Strickland, "Quasiparticle anisotropic hydrodynamics for central collisions", *Phys. Rev. C* **95** no. 3, (2017) 034906, arXiv:1605.02101 [nucl-th].

[231] M. Strickland. http://personal.kent.edu/~mstrick6/code/, 2017.

[232] H. Alalawi and M. Strickland, "Improved anisotropic hydrodynamics ansatz", *Phys. Rev. C* **102** no. 6, (2020) 064904, arXiv:2006.13834 [hep-ph].

[233] H. Alalawi, M. Alqahtani, and M. Strickland, "Resummed Relativistic Dissipative Hydrodynamics", *Symmetry* **14** no. 2, (2022) 329, arXiv:2112.14597 [nucl-th].

[234] G. Giacalone, A. Mazeliauskas, and S. Schlichting, "Hydrodynamic attractors, initial state energy and particle production in relativistic nuclear collisions", *Phys. Rev. Lett.* **123** no. 26, (2019) 262301, arXiv:1908.02866 [hep-ph].

[235] M. Coquet, X. Du, J.-Y. Ollitrault, S. Schlichting, and M. Winn, "Intermediate mass dileptons as pre-equilibrium probes in heavy ion collisions", *Phys. Lett. B* **821** (2021) 136626, arXiv:2104.07622 [nucl-th].

[236] Z. Chen, D. Teaney, and L. Yan, "Hydrodynamic attractor of noisy plasmas", arXiv:2206.12778 [nucl-th].

[237] R. Averbeck, J. W. Harris, and B. Schenke, *Heavy-Ion Physics at the LHC*, pp. 355–420. Springer International Publishing, Cham, 2015. https://doi.org/10.1007/978-3-319-15001-7_9.

[238] V. Dexheimer, J. Noronha, J. Noronha-Hostler, C. Ratti, and N. Yunes, "Future physics perspectives on the equation of state from heavy ion collisions to neutron stars", *J. Phys. G* **48** no. 7, (2021) 073001, arXiv:2010.08834 [nucl-th].

[239] A. Bazavov, "An overview of (selected) recent results in finite-temperature lattice QCD", *J. Phys. Conf. Ser.* **446** (2013) 012011, arXiv:1303.6294 [hep-lat].

[240] S. Borsanyi, "Frontiers of finite temperature lattice QCD", *EPJ Web Conf.* **137** (2017) 01006, arXiv:1612.06755 [hep-lat].

[241] P. Cea, L. Cosmai, and A. Papa, "Critical line of 2+1 flavor QCD: Toward the continuum limit", *Phys. Rev. D* **93** no. 1, (2016) 014507, arXiv:1508.07599 [hep-lat].

[242] C. Bonati, M. D'Elia, M. Mariti, M. Mesiti, F. Negro, and F. Sanfilippo, "Curvature of the chiral pseudocritical line in QCD: Continuum extrapolated results", *Phys. Rev. D* **92** no. 5, (2015) 054503, arXiv:1507.03571 [hep-lat].

[243] C. Bonati, M. D'Elia, F. Negro, F. Sanfilippo, and K. Zambello, "Curvature of the pseudocritical line in QCD: Taylor expansion matches analytic continuation", *Phys. Rev. D* **98** no. 5, (2018) 054510, arXiv:1805.02960 [hep-lat].

[244] C. Bonati, M. D'Elia, M. Mariti, M. Mesiti, F. Negro, and F. Sanfilippo, "Curvature of the chiral pseudocritical line in QCD", *Phys. Rev. D* **90** no. 11, (2014) 114025, arXiv:1410.5758 [hep-lat].

[245] S. Borsanyi, Z. Fodor, J. N. Guenther, R. Kara, S. D. Katz, P. Parotto, A. Pasztor, C. Ratti, and K. K. Szabo, "QCD Crossover at Finite Chemical Potential from Lattice Simulations", *Phys. Rev. Lett.* **125** no. 5, (2020) 052001, arXiv:2002.02821 [hep-lat].

[246] **HotQCD** Collaboration, A. Bazavov *et al.*, "Chiral crossover in QCD at zero and non-zero chemical potentials", *Phys. Lett. B* **795** (2019) 15–21, arXiv:1812.08235 [hep-lat].

[247] D. Toublan and J. B. Kogut, "The QCD phase diagram at nonzero baryon, isospin and strangeness chemical potentials: Results from a hadron resonance gas model", *Phys. Lett. B* **605** (2005) 129–136, arXiv:hep-ph/0409310.

[248] G. Endrodi, Z. Fodor, S. D. Katz, and K. K. Szabo, "The QCD phase diagram at nonzero quark density", *JHEP* **04** (2011) 001, arXiv:1102.1356 [hep-lat].

[249] R. Bellwied, S. Borsanyi, Z. Fodor, J. Günther, S. D. Katz, C. Ratti, and K. K. Szabo, "The QCD phase diagram from analytic continuation", *Phys. Lett. B* **751** (2015) 559–564, arXiv:1507.07510 [hep-lat].

[250] N. Haque and M. Strickland, "Next-to-next-to leading-order hard-thermal-loop perturbation-theory predictions for the curvature of the QCD phase transition line", *Phys. Rev. C* **103** no. 3, (2021) 031901, arXiv:2011.06938 [hep-ph].

[251] S. Jeon and U. Heinz, *Introduction to Hydrodynamics*, pp. 131–187. World Scientific, 2016.

[252] S. Borsányi, G. Endrődi, Z. Fodor, A. Jakovác, S. D. Katz, S. Krieg, C. Ratti, and K. K. Szabó, "The qcd equation of state with dynamical quarks", *Journal of High Energy Physics* **2010** no. 11, (Nov, 2010) . http://dx.doi.org/10.1007/JHEP11(2010)077.

[253] F. S. Bemfica, M. M. Disconzi, and J. Noronha, "First-Order General-Relativistic Viscous Fluid Dynamics", *Phys. Rev. X* **12** no. 2, (9, 2022) 021044, arXiv:2009.11388 [gr-qc].

[254] R. E. Hoult and P. Kovtun, "Stable and causal relativistic Navier-Stokes equations", *JHEP* **06** (2020) 067, arXiv:2004.04102 [hep-th].

[255] U. W. Heinz, D. Bazow, and M. Strickland, "Viscous hydrodynamics for strongly anisotropic expansion", *Nucl. Phys. A* **931** (2014) 920–925, arXiv:1408.0756 [nucl-th].

[256] L. Tinti, "Anisotropic matching principle for the hydrodynamic expansion", *Phys. Rev. C* **94** no. 4, (2016) 044902, arXiv:1506.07164 [hep-ph].

[257] D. Bazow, U. W. Heinz, and M. Martinez, "Nonconformal viscous anisotropic hydrodynamics", *Phys. Rev. C* **91** no. 6, (2015) 064903, arXiv:1503.07443 [nucl-th].

[258] M. Strickland, M. Nopoush, and R. Ryblewski, "Anisotropic hydrodynamics for conformal Gubser flow", *Nucl. Phys. A* **956** (2016) 268–271, arXiv:1512.07334 [nucl-th].

[259] M. Bluhm and T. Schäfer, "Dissipative fluid dynamics for the dilute Fermi gas at unitarity: Anisotropic fluid dynamics", *Phys. Rev. A* **92** no. 4, (2015) 043602, arXiv:1505.00846 [cond-mat.quant-gas].

[260] M. Bluhm and T. Schaefer, "Model-independent determination of the shear viscosity of a trapped unitary Fermi gas: Application to high temperature data", *Phys. Rev. Lett.* **116** no. 11, (2016) 115301, arXiv:1512.00862 [cond-mat.quant-gas].

[261] D. Almaalol, M. Alqahtani, and M. Strickland, "Anisotropic hydrodynamics with number-conserving kernels", *Phys. Rev. C* **99** no. 1, (2019) 014903, arXiv:1808.07038 [nucl-th].

[262] M. McNelis, D. Bazow, and U. Heinz, "(3+1)-dimensional anisotropic fluid dynamics with a lattice QCD equation of state", *Phys. Rev. C* **97** no. 5, (2018) 054912, arXiv:1803.01810 [nucl-th].

[263] M. Nopoush and M. Strickland, "Including off-diagonal anisotropies in anisotropic hydrodynamics", *Phys. Rev. C* **100** no. 1, (2019) 014904, arXiv:1902.03303 [nucl-th].

[264] M. McNelis, D. Bazow, and U. Heinz, "Anisotropic fluid dynamical simulations of heavy-ion collisions", *Comput. Phys. Commun.* **267** (2021) 108077, arXiv:2101.02827 [nucl-th].

[265] M. Martinez, M. McNelis, and U. Heinz, "Anisotropic fluid dynamics for Gubser flow", *Phys. Rev. C* **95** no. 5, (2017) 054907, arXiv:1703.10955 [nucl-th].

[266] G. S. Denicol, "Kinetic foundations of relativistic dissipative fluid dynamics", *J. Phys. G* **41** no. 12, (2014) 124004.

[267] S. Borsanyi, G. Endrodi, Z. Fodor, A. Jakovac, S. D. Katz, S. Krieg, C. Ratti, and K. K. Szabo, "The QCD equation of state with dynamical quarks", *JHEP* **11** (2010) 077, arXiv:1007.2580 [hep-lat].

[268] R. Ryblewski, "Thermodynamically consistent formulation of quasiparticle viscous hydrodynamics", *Acta Phys. Polon. Supp.* **10** (2017) 1073, arXiv:1708.01449 [nucl-th].

[269] M. Chojnacki, A. Kisiel, W. Florkowski, and W. Broniowski, "THERMINATOR 2: THERMal heavy IoN generATOR 2", *Comput. Phys. Commun.* **183** (2012) 746–773, arXiv:1102.0273 [nucl-th].

[270] Strickland et al, "KSU Code Repo." http://personal.kent.edu/~mstrick6/code, 2021.

[271] J. S. Moreland, J. E. Bernhard, and S. A. Bass, "Alternative ansatz to wounded nucleon and binary collision scaling in high-energy nuclear collisions", *Phys. Rev. C* **92** no. 1, (2015) 011901, arXiv:1412.4708 [nucl-th].

[272] W. Ke, J. S. Moreland, J. E. Bernhard, and S. A. Bass, "Constraints on rapidity-dependent initial conditions from charged particle pseudorapidity densities and two-particle correlations", *Phys. Rev. C* **96** no. 4, (2017) 044912, arXiv:1610.08490 [nucl-th].

[273] J. Bartels, K. J. Golec-Biernat, and H. Kowalski, "A modification of the saturation model: DGLAP evolution", *Phys. Rev. D* **66** (2002) 014001, arXiv:hep-ph/0203258.

[274] H. Kowalski and D. Teaney, "An Impact parameter dipole saturation model", *Phys. Rev. D* **68** (2003) 114005, arXiv:hep-ph/0304189.

[275] B. Schenke, P. Tribedy, and R. Venugopalan, "Fluctuating Glasma initial conditions and flow in heavy ion collisions", *Phys. Rev. Lett.* **108** (2012) 252301, arXiv:1202.6646 [nucl-th].

[276] S. Chen, "ISS Repo." https://github.com/chunshen1987/iSS, 2020.

[277] S. A. Bass *et al.*, "Microscopic models for ultrarelativistic heavy ion collisions", *Prog. Part. Nucl. Phys.* **41** (1998) 255–369, arXiv:nucl-th/9803035.

[278] M. Bleicher *et al.*, "Relativistic hadron hadron collisions in the ultrarelativistic quantum molecular dynamics model", *J. Phys. G* **25** (1999) 1859–1896, arXiv:hep-ph/9909407.

[279] **SMASH** Collaboration, J. Weil *et al.*, "Particle production and equilibrium properties within a new hadron transport approach for heavy-ion collisions", *Phys. Rev. C* **94** no. 5, (2016) 054905, arXiv:1606.06642 [nucl-th].